STUDIES OF ATOMIC HYDROGEN SPIN-EXCHANGE COLLISIONS AT 1 K AND BELOW

By

Michael Edward Hayden

MASc. (Engineering Physics), University of British Columbia

B. Eng. (Engineering Physics), University of Saskatchewan

A THESIS SUBMITTED IN PARTIAL FULFILLMENT OF

THE REQUIREMENTS FOR THE DEGREE OF

DOCTOR OF PHILOSOPHY

in

THE FACULTY OF GRADUATE STUDIES

PHYSICS

We accept this thesis as conforming

to the required standard

THE UNIVERSITY OF BRITISH COLUMBIA

1991

In presenting this thesis in partial fulfilment of the requirements for an advanced degree at the University of British Columbia, I agree that the Library shall make it freely available for reference and study. I further agree that permission for extensive copying of this thesis for scholarly purposes may be granted by the head of my department or by his or her representatives. It is understood that copying or publication of this thesis for financial gain shall not be allowed without my written permission.

Department of Physics

The University of British Columbia
Vancouver, Canada

Date Dec 13/91

DE-6 (2/88)

Abstract

Spin-exchange interactions during collisions between hydrogen (H) atoms cause the $\Delta F = 1$, $\Delta m_F = 0$ hyperfine transition of the H atom to be broadened and shifted from its unperturbed frequency. A recent theory suggests that hyperfine interactions during these collisions lead to frequency shifts in an oscillating H maser which depend in a non-linear way upon the atomic density. These non-adiabatic contributions are of considerable technological concern as they may limit the ultimate frequency stability of H masers operating at cryogenic temperatures. In the first of two experiments described here, we examine the influence of H-H spin-exchange collisions on the oscillation frequency of a H maser operating at 0.5 K. The results of this study are consistent with the theoretical predictions.

The second study involves several experiments with mixtures of H and deuterium (D) atoms at cryogenic temperatures. It makes use of the observation that for comparable H and D densities, the spin-exchange broadening of the $\Delta F = 1$, $\Delta m_F = 0$ hyperfine transition of the H atom is dominated by H-D collisions. We have used hyperfine magnetic resonance techniques on this transition to study interactions between H and D atoms confined by liquid ^{4}He (ℓ-^{4}He) walls at 1 K and zero magnetic field. The resonance signal intensity gives a measure of the H density in the mixture while the broadening of the transition gives a simultaneous measure of the D density. Measurements are made of several spin-exchange and recombination cross sections. An improved measurement of the energy required to force a D atom into ℓ-^{4}He is made. These results also set a lower bound for the effective mass of a D quasiparticle in ℓ-^{4}He.

Table of Contents

List of Tables

Chapter 3

Chapter 5

Appendix B

Appendix E

List of Figures

Chapter 6

Chapter 7

Acknowledgements

It is with great pleasure that I thank my friend and thesis advisor Walter Hardy, for his support, encouragement, and enthusiasm throughout the course of my research at UBC. I was also very fortunate to have been able to work closely with Martin Hürlimann and Meritt Reynolds; two former members of the UBC atomic hydrogen group. Martin taught me the intricacies of the UBC cryogenic hydrogen maser (CHM) and was involved with all aspects of the H-H spin-exchange work. Meritt was involved with the earliest studies of H-D spin-exchange and has been a constant source of encouragement and advice throughout the remainder of that project.

The H-H spin-exchange work would not have been possible without the CHM which was designed and built by Martin Hürlimann, Walter Hardy and Rick Cline. Mark Paetkau spent many hours assisting with the upkeep of the 1 K apparatus and with data collection for that experiment; Dennis Chow wrote the data acquisition program. George Takis lent us the pumping station which was used during the 1 K experiments and David Wineland lent us the rubidium standard which was used during both experiments. In addition, Herb Gush lent us the baratron gauge and the cathetometer used to make ^{4}He vapour pressure measurements during the 1 K experiments. Rick Cline devoted many hours to the design and upkeep of the computer system in the lab; without his contribution much of this work would have been painfully slow and difficult.

I would also like to thank Stuart Crampton for his continued interest and encouragement despite innumerable foiled attempts to cool the dilution refrigerator. Boudewijn Verhaar supplied us with detailed results of his H-H spin-exchange calculations, some of

which have been reproduced here. I have certainly enjoyed and benefited from conversations with Jook Walraven and Ted Hsu. I would also like to thank Doug Bonn for his encouragement and friendship throughout the past few years. Finally, I want to thank my parents Mike and Joan for the countless times that they have encouraged me. I am sure that without their faith in me, none of this would have come to be.

I am grateful to the Natural Sciences and Engineering Research Council of Canada and the Killam Foundation for their support in the form of postgraduate scholarships.

Chapter 1

General Introduction

Atomic hydrogen (H) is the most abundant element in the universe. Its attraction as the simplest atom has made it the subject of innumerable experimental and theoretical studies over the last century. One of the most important technological triumphs to come out of this work was the development of the atomic hydrogen maser during the 1960's [1]. This device is essentially a storage bottle containing a gas of state selected atomic hydrogen, located inside a microwave cavity tuned to a hyperfine transition of the H atom. Stimulated emission of radiation from the hydrogen produces a spectrally narrow and very stable signal at this transition frequency. The purity of this coherent radiation is due to the combined effects of a long interaction time between the atoms and their radiation field, and the use of 'non-stick' teflon coatings on the storage bottle walls. The perturbation of the atomic hyperfine interaction during collisions with these walls is very weak near room temperature. The H maser is currently the most stable atomic clock for averaging times between about 10^2 and 10^6 seconds [2]. Its extraordinary frequency stability has made it an invaluable research tool in fields as diverse as navigation, metrology, physics, and astronomy [3].

The past decade and a half has seen a resurgence of interest in the study of atomic hydrogen, this time at very low temperatures [4, 5]. It was predicted as early as 1959 [6] that spin-polarized atomic hydrogen would remain gaseous at temperatures down to absolute zero. In principle, it should be possible to cool such a gas until it reaches a state of quantum mechanical degeneracy. The truly exciting feature of this system that

sets it apart from other examples of macroscopic quantum mechanical degeneracy, is that the interactions within the condensate should still be weak enough to make comparisons between experiment and microscopic theories possible.

Along with the intensive research effort devoted to the study of H at low temperatures, many 'spin off' projects of considerable interest in their own right have been undertaken. One of the most interesting of these was the development of atomic hydrogen masers which work at cryogenic temperatures [7, 8, 9, 10]. The *intrinsic* frequency stability of a conventional hydrogen maser is determined by the background of thermal photons present in the microwave cavity. The phase of the electromagnetic field associated with these photons is random with respect to the coherent radiation produced by the maser. The frequency fluctuations caused by these photons can be reduced by going to low temperatures. Unfortunately, as the temperature of a gas of hydrogen is lowered, atoms begin to stick to the walls of the storage bottle for long periods of time. It is difficult to operate a conventional H maser below liquid nitrogen temperatures. Low temperature H masers did not become feasible until the development of new cryogenic wall coatings. The most important wall coating for low temperature H research is superfluid liquid helium [11].

The power output of a hydrogen maser is limited by collisions between atoms during which spin-exchange interactions broaden the atomic resonance. By going to temperatures near 1 K, this broadening effect is reduced by about three orders of magnitude from room temperature [12]. Cryogenic H masers can thus be run at much higher densities and power levels than conventional masers. When this effect is combined with the reduction in thermal noise, it would seem that rather dramatic improvements in frequency stability *might* be obtained by operating H masers at low temperatures.

In the time since these predictions were first made [13, 14, 15], it has been demonstrated that some improvement in the frequency stability of a hydrogen maser can indeed

be made by going to low temperatures [16, 17]. Unfortunately the same spin-exchange collisions which broaden the atomic resonance also cause it to be shifted from its unperturbed frequency. Unlike the broadening effect, there is essentially no reduction in the frequency perturbation at low temperatures. In fact, since the atomic densities in a maser operating at low temperatures are much higher, the magnitude of the spin-exchange induced frequency shifts in a cryogenic maser are typically much larger than those in a conventional maser.

These spin-exchange frequency shifts depend upon the atomic collision rate and thus fluctuations in the atomic density couple directly to the oscillation frequency of the maser. This coupling imposes very strict requirements on the stability of the atomic density. A recent theory of hydrogen spin-exchange collisions[1] was developed by B. J. Verhaar and several collaborators [19, 20]. This theory predicts that because of non-adiabatic effects caused by hyperfine interactions during these collisions, the spin-exchange induced frequency shifts depend not only on the atomic density but on the occupancy of the individual hyperfine states within the maser bulb. Cryogenic hydrogen maser research has slowed since these predictions were made, simply because it is not obvious how to overcome this problem and make further improvements in frequency stability.

Two experimental studies of hydrogen spin-exchange interactions at temperatures of 1 K and below are presented in this thesis. The first is an investigation of the effect of H-H spin-exchange collisions on the oscillation frequency of a cryogenic hydrogen maser operating at 0.5 K. In this study the first experimental evidence that the oscillation frequency of a cryogenic H maser does indeed contain contributions which seem to be explained by the Verhaar theory is presented.

From a technological standpoint this study is motivated by the obvious need to verify

[1]The first theories of hydrogen spin-exchange collisions were developed over three decades ago. In these theories it was conventional to ignore hyperfine interactions in comparison to electron spin-exchange interactions [18].

the existence of the predicted frequency shifts before further developmental work on cryogenic hydrogen masers is undertaken. A second less obvious but equally important motivation arises out of the sensitivity of the various collision cross sections of the theory to the detailed form of the interatomic potentials. These parameters are particularly sensitive to the long range parts of the potentials which are otherwise difficult to test. By measuring these parameters, it may be possible to test and further refine these potentials. In a sense, these measurements can be thought of as a form of spectroscopy.

The second study presented in this thesis also involves measurements of hydrogen spin-exchange parameters; this time at temperatures just above 1 K. It also involves the use of magnetic resonance techniques on the same hyperfine transition the H maser utilizes. While spin-exchange collisions play an integral and essential role in this work, they do not form the central theme of this part of our research. We digress for a moment to put this second experiment into historical perspective.

Recently we discovered that atomic deuterium (D) is not confined by liquid helium walls to nearly the same degree as H [21]. A deuterium atom with about 14 K of kinetic energy can penetrate a film of liquid helium. A hydrogen atom requires an estimated 35 K to penetrate the same film. This discovery was made by using magnetic resonance techniques on a hyperfine transition of the D atom at 309 MHz to study the time and the temperature dependence of the D atom density inside a sealed[2] sample bulb. It was during the course of this investigation that we observed a considerable broadening of the atomic resonance which could not be explained by spin-exchange collisions between D atoms. We postulated that this broadening was due to contamination of the samples with H. In a separate experiment, magnetic resonance techniques were used on a hyperfine transition of the H atom at 1420 MHz to verify the presence of this contamination. The second study presented in this thesis is an extension of this work.

[2]The interior walls of this bulb were coated with a film of superfluid liquid ^{4}He.

A rather striking difference exists between the magnitude of the spin-exchange broadening cross section for collisions between two H atoms, and that for collisions between an H atom and a D atom: the H-D broadening cross section was theoretically estimated [22] to be more than two orders of magnitude larger than that for H-H collisions near 1 K. This implies that if magnetic resonance techniques are used to monitor the H atoms in a mixture containing comparable densities of H and D, the broadening of the transition will be dominated by spin-exchange collisions[3] with the D atoms. In this way it is possible to monitor both atomic densities *simultaneously.* The amplitude of the magnetic resonance signal is proportional to the H density while the broadening of the transition is proportional to the D density. These techniques have allowed us to make the first study of interactions between H and D atoms in zero magnetic field at temperatures just above 1 K. Apart from the measurement of spin-exchange parameters for collisions between H and D atoms we were able to study several recombination processes and to make significant improvements in the measurement of the energy required for a D atom to penetrate a liquid helium film. All of these parameters are of considerable interest to physicists in the context of low temperature H research. They also have the same potential as the H-H spin-exchange parameters to be used in spectroscopic refinements of the various interatomic potentials.

The body of this thesis is split into eight chapters. Chapters 2 and 3 are introductory chapters. In chapter 2 the magnetic resonance techniques used throughout this work are introduced. Chapter 3 is a review of the properties of atomic hydrogen and deuterium at low temperatures which are relevant to this work. This chapter includes a discussion of spin-exchange collisions and their influence on the $\Delta F = 0, \Delta m_F = 0$ hyperfine transition of the ground state of the H atom.

[3]Other broadening mechanisms must of course be taken into consideration.

In chapters 4 and 5 the H-H spin-exchange measurements with the cryogenic hydrogen maser at 0.5 K are discussed. Chapter 4 is an introductory chapter and chapter 5 contains the results of the measurements. Chapters 6 and 7 are organized in a similar manner. Chapter 6 introduces the study of H, D mixtures at 1 K and chapter 7 contains the experimental results. Chapter 8 is the concluding chapter in which all of the measurements presented in the thesis are summarized. Several appendices have also been included. Each one describes a technique or a measurement that was in some way essential to the interpretation of the work presented in the body of the thesis. References to discussions in these appendices are made in the appropriate places in the main body of the thesis.

Chapter 2

Introduction to Zero Field Magnetic Resonance and the Hydrogen Maser

The experiments presented in this thesis all involve the use of magnetic resonance to study interactions in gaseous atomic hydrogen (H), or mixtures of H and atomic deuterium (D). In this chapter we review some the background required to understand the measurement techniques.

2.1 Hyperfine structure

At room temperature and below, gaseous atomic hydrogen (H) is found almost exclusively in its electronic ground state. This state is split into four magnetic sublevels by the hyperfine interaction between the proton spin $\mathbf{i}$ and the electron spin $\mathbf{s}$. In zero magnetic field, three of these levels are degenerate and are displaced upwards from the fourth by a frequency [23]

$$f_0 = 1420.405\,751\,773(1)\,\text{MHz}.$$

Radiation from this transition is abundant in stellar environments and is commonly referred to by astronomers[1] as the 21 cm line.

The application of a magnetic field splits the threefold degeneracy of the upper hyperfine states because of the Zeeman interaction. The effective Hamiltonian for the spin degrees of freedom of a ground state H atom in a static magnetic field $\mathbf{B}_0$ can be written

$$\mathcal{H}_0 = a\mathbf{i}\cdot\mathbf{s} - \hbar(-\gamma_e\mathbf{s} + \gamma_p\mathbf{i})\cdot\mathbf{B_0} \tag{2.1}$$

[1]The reference is to the wavelength of radiation at this frequency in free space.

where $a = 2\pi\hbar f_0$ and γ_e and γ_p are the gyromagnetic ratios of the electron and the proton. The accepted values for γ_e and γ_p are [24]

$$\begin{aligned} \gamma_e &= 1.760\,859\,2(12) \times 10^{11}\,s^{-1}T^{-1} \\ \gamma_p &= 2.675\,221\,28(81) \times 10^{8}\,s^{-1}T^{-1} \end{aligned}$$

The Hamiltonian 2.1 can be diagonalized in terms of a field dependent basis of states. This basis can in turn be written in terms of the spin states $|\, m_s\ m_i \,\rangle$, where m_s and m_i are respectively the electron and proton spin projections along the applied field $\mathbf{B}_0$. In order of increasing energy the eigenstates of the ground state of the H atom are :

$$|\,a\,\rangle = \cos\vartheta\,|\,-\tfrac{1}{2},\tfrac{1}{2}\,\rangle - \sin\vartheta\,|\,\tfrac{1}{2},-\tfrac{1}{2}\,\rangle \tag{2.2}$$

$$|\,b\,\rangle = |\,-\tfrac{1}{2},-\tfrac{1}{2}\,\rangle \tag{2.3}$$

$$|\,c\,\rangle = \sin\vartheta\,|\,-\tfrac{1}{2},\tfrac{1}{2}\,\rangle + \cos\vartheta\,|\,\tfrac{1}{2},-\tfrac{1}{2}\,\rangle \tag{2.4}$$

$$|\,d\,\rangle = |\,\tfrac{1}{2},\tfrac{1}{2}\,\rangle\,. \tag{2.5}$$

The parameter ϑ is defined by :

$$\tan(2\vartheta) = \frac{a}{\hbar(\gamma_e+\gamma_p)B_0} = \frac{50.607\,\text{mTesla}}{B_0}$$

and is used to indicate the degree of mixing (or the 'admixture') of the states $|\,-\frac{1}{2},\frac{1}{2}\,\rangle$ and $|\,\frac{1}{2},-\frac{1}{2}\,\rangle$ found in the eigenstates $|\,a\,\rangle$ and $|\,c\,\rangle$. The energies which correspond to the four eigenstates are :

$$E_a = -\frac{a}{4} - \frac{a}{2}\sqrt{1+\left[\frac{\hbar(\gamma_e+\gamma_p)B_0}{a}\right]^2} \tag{2.6}$$

$$E_b = \frac{a}{4} - \frac{\hbar}{2}(\gamma_e-\gamma_p)B_0 \tag{2.7}$$

$$E_c = -\frac{a}{4} + \frac{a}{2}\sqrt{1+\left[\frac{\hbar(\gamma_e+\gamma_p)B_0}{a}\right]^2} \tag{2.8}$$

$$E_d = \frac{a}{4} + \frac{\hbar}{2}(\gamma_e-\gamma_p)B_0 \tag{2.9}$$

The magnetic field dependence of these energy levels is shown in figure 2.1. Energies in this diagram have been expressed in the convenient units of frequency. The conversion to proper energy units is obtained by multiplying by Planck's constant h. Throughout this thesis we will also find it convenient to express energies in units of temperature. For example the zero field hyperfine splitting f_0 of the H atom is approximately 68.2 mK. In this case the conversion to proper energy units is obtained by multiplying by Boltzmann's constant k_B.

2.2 Spin $\frac{1}{2}$ analogy

If we superimpose an oscillating rf magnetic field $2B_z \cos(\omega t)$ along the static magnetic field $\mathbf{B}_0 = B_0\hat{z}$, transitions between the $|\ a\ \rangle$ state and the $|\ c\ \rangle$ state can be induced. In fact, the matrix elements of the magnetic moment operator

$$\boldsymbol{\mu} = -\hbar\gamma_e \mathbf{s} + \hbar\gamma_p \mathbf{i} \tag{2.10}$$

between the eigenstates of the H atom are such that a longitudinal field can *only* induce transitions between these two states. In practice, as long as a small static bias field[2] is present, the $|\ a\ \rangle$ state and the $|\ c\ \rangle$ state form an isolated two dimensional subspace inside the 1S manifold. Restricted to this subspace, the Hamiltonian for the H atom

$$\mathcal{H} = \mathcal{H}_0 - 2\mu_z B_z \cos(\omega t) \tag{2.11}$$

can be mapped onto the standard magnetic resonance problem for a spin $\frac{1}{2}$ system [25]. This mapping is quite general and can be applied to any two level system where the states are coupled by an rf perturbation. It is a convenient procedure since it allows

[2]The bias field is required to set a quantization axis, and to keep the neighboring (transverse) $|\ a\ \rangle$ to $|\ b\ \rangle$ and $|\ a\ \rangle$ to $|\ d\ \rangle$ transitions sufficiently far from the $|\ a\ \rangle$ to $|\ c\ \rangle$ transition. Cross relaxation between the upper three hyperfine states is also suppressed by this field. Typically only a few tens of mGauss are required.

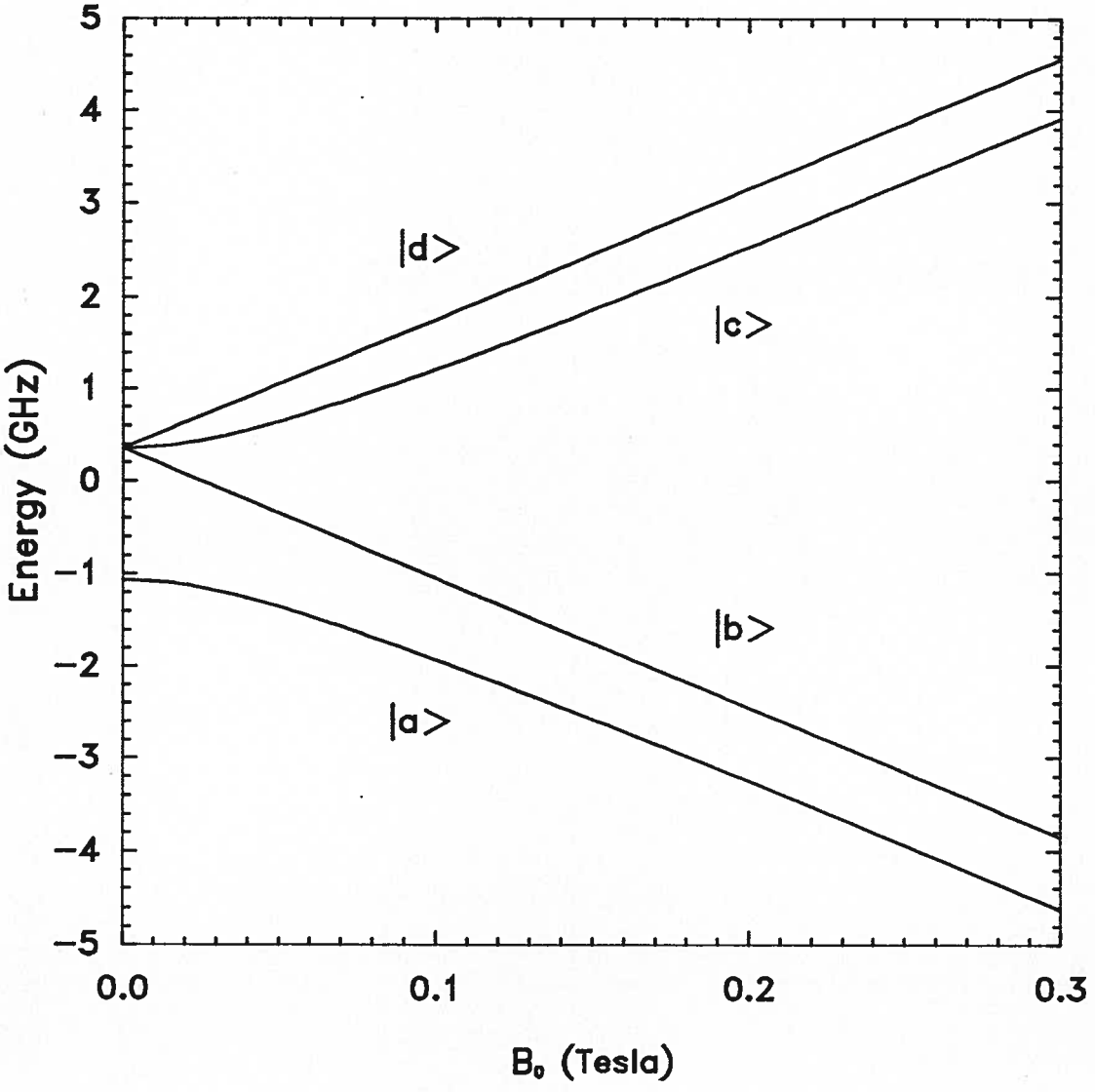

Figure 2.1: The energies of the four hyperfine levels of the ground state of the hydrogen atom as a function of magnetic field.

one to use the very well documented results pertaining to NMR theory without having to rederive any of the necessary formalism. The outline given below is only intended to give the reader a feeling for the procedure. More thorough discussions can be found in references [25, 26, 27].

The mapping is based upon the principle that any operator A acting in the two dimensional subspace can be written in terms of the Pauli matrices $\boldsymbol{\sigma}$ as

$$A = \frac{1}{2}\mathrm{Tr}(A) + 2\mathrm{Tr}(A\tilde{s}) \cdot \tilde{s} \tag{2.12}$$

where $\tilde{s} = \frac{1}{2}\boldsymbol{\sigma}$ can be associated with a fictitious spin $\frac{1}{2}$ particle. To avoid confusion, we label all quantities within the frame of this fictitious spin $\frac{1}{2}$ particle with a tilde. The density matrix and the Hamiltonian 2.11 for the H atom in a longitudinal rf field can thus be written in the form :

$$\tilde{\rho} = \frac{1}{2} + 2 < \tilde{s} > \cdot\tilde{s} \tag{2.13}$$

$$\mathcal{H} = \frac{1}{2}\tilde{E}_0 - \hbar\tilde{\gamma}\tilde{\mathbf{B}} \cdot \tilde{s} \, . \tag{2.14}$$

By comparing the matrix elements of 2.11 and 2.14 the effective gyromagnetic ratio $\tilde{\gamma}$ and the effective magnetic field $\tilde{\mathbf{B}}$ can be determined. If we choose

$$\tilde{\gamma} = \gamma_e + \gamma_p \tag{2.15}$$

the effective field $\tilde{\mathbf{B}}$ is given by[3] :

$$\tilde{B}_x = 2B_z \cos(\omega t) \tag{2.16}$$

$$\tilde{B}_y = 0 \tag{2.17}$$

$$\tilde{B}_z = \frac{a}{\hbar(\gamma_e + \gamma_p)} + \frac{\hbar(\gamma_e + \gamma_p)}{2a}B_0^2 \tag{2.18}$$

[3]Equation 2.18 is a low field approximation.

where

$$\frac{a}{\hbar(\gamma_e + \gamma_p)} = 50.607 \text{ mTesla} .$$

Furthermore, the commutator $[\mathcal{H},\tilde{\rho}]$ can be used to determine the equation of motion for the effective magnetic moment $\tilde{\boldsymbol{\mu}} = \hbar\tilde{\gamma}\tilde{\mathbf{s}}$ of the fictitious spin $\frac{1}{2}$ particle with the result:

$$\frac{d\tilde{\boldsymbol{\mu}}}{dt} = \tilde{\gamma}\tilde{\boldsymbol{\mu}} \times \tilde{\mathbf{B}} . \tag{2.19}$$

This is the classical equation of motion for a magnetic moment in a field $\tilde{\mathbf{B}}$. In effect, the mappings for $\tilde{\gamma}$ and $\tilde{\mathbf{B}}$ transform the H atom problem (the time evolution of the atomic density matrix) onto the standard NMR problem [28] (the time evolution of the magnetic moment $\tilde{\boldsymbol{\mu}}$). The correspondence between these two problems is obtained through the expectation values of the effective magnetic moment operator which are related to the elements of the full 4×4 atomic density matrix:

$$< \tilde{\mu}_x >= \frac{1}{2}\hbar(\gamma_e + \gamma_p)(\rho_{ac} + \rho_{ca}) \tag{2.20}$$

$$< \tilde{\mu}_y >= -\frac{i}{2}\hbar(\gamma_e + \gamma_p)(\rho_{ac} - \rho_{ca}) \tag{2.21}$$

$$< \tilde{\mu}_z >= \frac{1}{2}\hbar(\gamma_e + \gamma_p)(\rho_{aa} - \rho_{cc}) \tag{2.22}$$

Once this correspondence is established, it is only necessary to keep in the back of ones mind the transformations which lead to the analogy. In this thesis the real rf fields which are applied are longitudinal fields. The mapping 2.16 to the fictitious spin $\frac{1}{2}$ analogy transforms this into a transverse rf field which corresponds to the usual transverse field in the standard NMR problem. Near zero field, the real applied static field B_0 sets the quantization axis however it only makes a very small contribution to the total fictitious longitudinal field $\tilde{B}_0 = \tilde{B}_z$ given by equation 2.18. $\tilde{B}_0$ corresponds to the static longitudinal field in the conventional NMR problem.

The fictitious magnetization for many H atoms is simply $\tilde{\mathbf{M}} = n_H < \tilde{\boldsymbol{\mu}} >$ where $< \tilde{\boldsymbol{\mu}} >$ is now the average magnetic moment and n_H is the atomic density. The thermal equilibrium value of this magnetization $\tilde{M}_0$ is related to the thermal equilibrium population difference between the $|\ a\ \rangle$ state and the $|\ c\ \rangle$ state of the H atom :

$$\tilde{M}_0 = \frac{1}{2}\hbar(\gamma_e + \gamma_p)n_H \frac{1 - \exp\left(-\frac{\hbar\omega_0}{k_B T}\right)}{1 + 3\exp\left(-\frac{\hbar\omega_0}{k_B T}\right)} \approx \frac{1}{2}\hbar(\gamma_e + \gamma_p)\frac{\hbar\omega_0}{4k_B T}n_H \ . \tag{2.23}$$

The transverse[4] components of the fictitious magnetization on the other hand, are related to the off diagonal elements of the density matrix via equations 2.20 and 2.21. The fictitious transverse magnetization corresponds to a coherent superposition of the $|\ a\ \rangle$ state and the $|\ c\ \rangle$ state.

We illustrate the usefulness of this formalism with the simple example of a 'tipping pulse'. In standard NMR terminology this refers to the application of a transverse field $2B_x \cos(\omega t)$ for a length of time

$$\tau_\theta = \frac{\theta}{\gamma B_x} \ . \tag{2.24}$$

For the H atom problem this corresponds to a longitudinal rf field $2B_z \cos(\omega t)$ applied at the a-c transition frequency (the 'Larmor frequency') for a time

$$\tau_\theta = \frac{\theta}{\gamma B_z} \ . \tag{2.25}$$

The fictitious spins see an oscillating rf field along the $\hat{x}$ axis which can be decomposed in the usual way [29] into two counter rotating components in the $\hat{x}$-$\hat{y}$ plane. When we transform into the reference frame $\hat{x}'$-$\hat{y}'$ rotating in the same sense as the fictitious magnetization, the spins effectively see[5] only a static field $\tilde{B}_{x'} = B_z$ along the $\hat{x}'$ axis (all quantities within this rotating frame are so indicated with a prime). The spins precess

[4]Both the fictitious longitudinal magnetization and the fictitious transverse magnetization are directed along the $\hat{z}$ axis in real space.

[5]The counter rotating field is displaced from the frequency range of interest by twice the Larmor frequency. It leads to the Bloch-Siegert frequency shift [25] which can be neglected in our work.

about this field at an angular frequency $\tilde{\gamma}B_z$ throughout the duration of the rf pulse. After a time τ_θ the effective magnetization has been rotated through an angle θ with respect to the $\hat{z}$ axis. In the lab frame the fictitious spins are left in this canted position but precess about the effective static field $\tilde{B}_z$ at the Larmor frequency. The *real* oscillating magnetization which lies along the $\hat{z}$ axis

$$M_z = n_H \hbar \left(\gamma_p i_z - \gamma_e s_z\right) \tag{2.26}$$

is the parameter which we observe experimentally. It can conveniently be written in terms of $< \tilde{\mu}_x >$ such that

$$M_z(t) = \tilde{M}_0 \sin(\theta) \sin(\omega t) \; . \tag{2.27}$$

A rather interesting point which is made obvious by equations 2.23 and 2.27 is that in thermal equilibrium, the fictitious magnetization $\tilde{M}_0$ is non zero even though the real magnetization M_z is zero.

If a $\pi/2$ pulse is applied to a sample of H atoms initially in thermal equilibrium, $\tilde{M}_0$ is rotated into the transverse plane and left there as a *precessing* (fictitious) magnetization. The real *oscillating* magnetization is directed along $\hat{z}$ and has amplitude $\tilde{M}_0$. Physically this state corresponds to a coherent superposition of the $\mid a \rangle$ and the $\mid c \rangle$ states of the atomic sample. A π pulse on the other hand inverts the fictitious magnetization. If the system is initially in thermal equilibrium, this corresponds to an inversion of the population difference between the $\mid a \rangle$ and the $\mid c \rangle$ states. The real longitudinal magnetization associated with this state is zero. Other extensions of this analogy are obvious.

2.3 Practical hyperfine magnetic resonance

In a typical pulsed magnetic resonance experiment, rf power at the appropriate frequency is generated by a transmitter which is coupled to some form of electromagnetic resonator.

The sample is placed inside the resonator in a region of relatively high rf field homogeneity. In the usual case the rf field is transverse to a large static magnetic field about which the spins precess. Following a tipping pulse at the Larmor frequency, the real precessing magnetization of the sample induces a signal back into the resonator. This response can be detected with the appropriate circuitry.

Our experiments using pulsed magnetic resonance at the a-c hyperfine transition of H are quite similar once the fictitious spin $\frac{1}{2}$ analogy is taken into account. The real rf field is actually applied in the longitudinal direction and the bias field applied only to separate the a-c transition from the neighboring transitions.

2.3.1 The free induction decay

Quite obviously the precessing (fictitious) magnetization which exists following a tipping pulse will not persist forever. Various mechanisms will cause any magnetization $\tilde{\mathbf{M}}$ to relax towards its thermal equilibrium value $\tilde{\mathbf{M}}_0$. The time dependent decay of the real oscillating magnetization $M_z(t)$ (equation 2.27) will thus induce a *damped* sinusoidal signal in the resonator. We refer to this *undriven* response as a free induction decay or FID.

It has been found that in many instances the relaxation of the magnetization can be described very well by the phenomenological Bloch equations [25] :

$$\frac{d}{dt}\mathbf{M} = \gamma\left(\mathbf{M}\times\mathbf{B}\right) - \frac{M_x\hat{x} + M_y\hat{y}}{T_2} - \frac{M_z\hat{z} - M_0\hat{z}}{T_1} \tag{2.28}$$

where T_1 and T_2 are relaxation times for the longitudinal and transverse components of $\mathbf{M}$. We have assumed that all of the relaxation mechanisms encountered in our studies can be characterized in in this way and equate $\tilde{\mathbf{M}}$ with $\mathbf{M}$ in equations 2.28. Various mechanisms which lead to this relaxation are discussed in the following chapter.

In addition to relaxation processes it is important to consider the rf field which is

generated by the (real) oscillating magnetization of the sample. If the coupling between the magnetization and the resonator is sufficiently strong, the atomic system will precess in its own radiation field. In effect this field will cause the fictitious magnetization $\tilde{\mathbf{M}}$ to spiral back towards $\tilde{\mathbf{M}}_0$ even in the absence of other relaxation mechanisms. This effect is known as radiation damping [30]. The analysis of the influence of radiation damping on the FID's obtained in our work has played an important role in our study of spin-exchange relaxation. This topic is discussed in more detail in appendix A.

2.3.2 Power radiated by the atoms and the filling factor

In order to finally make the connection between the density of radiating spins following a tipping pulse and the rf power which is detected, we make use of the lumped element model for the resonator which is presented in appendix A. If the resonator is tuned to the atomic transition frequency, the magnetic field $\mathbf{H}$ produced by the magnetization $\mathbf{M}$ will be in quadrature with $\mathbf{M}$. Over a period of time short compared to the time scale over which the atoms diffuse, the average power radiated by the oscillating magnetization is

$$P_{rad} = \frac{\omega\mu_0}{2}\int \mathbf{H}\cdot\mathbf{M}\, dV_b \tag{2.29}$$

where the integral is carried out over the volume V_b of the sample bulb. This power must be equal to the power dissipated by the resonator and the external circuitry

$$P_{dis} = \frac{\omega\mu_0}{2Q_\ell}\int H^2 dV_c \tag{2.30}$$

where Q_ℓ is the loaded quality factor of the resonator and V_c is the volume of the resonator. Making use of this equality and realizing that at critical coupling only *half* of the power radiated by the atoms is transmitted to the external circuitry, we find

$$P_{sig} = \frac{\omega\mu_0\eta Q_\ell V_b}{4}M_z^2(0) \tag{2.31}$$

where the filling factor η is

$$\eta = \frac{[\int \mathbf{H}\cdot\mathbf{M}\, dV_b]^2}{V_b M_z^2(0) \int H^2 dV_c} \tag{2.32}$$

and $M_z(0)$ is the real oscillating magnetization at the center of the sample which we assume to be along $\hat{z}$. Following a $\pi/2$ pulse $M_z(0) = \tilde{M}_0$. Equation 2.31 expresses the signal power (which can be measured) in terms of the oscillating magnetization inside the sample bulb. In the simplest case where $\mathbf{H}$ is everywhere uniform within the resonator (as it would be in an infinitely long solenoidal coil for example), the filling factor η is simply given by the ratio V_b/V_c.

For relatively homogeneous rf fields we can neglect[6] variations in the initial amplitude of $\mathbf{M}$ over the sample volume following a $\pi/2$ pulse. Immediately following the rf pulse and before the atoms have had time to move, $\mathbf{M}$ is everywhere aligned with $\mathbf{H}$ and η is

$$\eta = \frac{[\int H dV_b]^2}{V_b \int H^2 dV_c}\,. \tag{2.33}$$

After the atoms have had time to diffuse, we assume that $\mathbf{M}$ is directed along $\hat{z}$ rather than $\mathbf{H}$ and η is given to good approximation by the usual expression [31, 32]

$$\eta = \frac{[\int H_z dV_b]^2}{V_b \int H^2 dV_c}\,. \tag{2.34}$$

In our work we have used sample bulb/resonator configurations in which most of the sample is located within a region of high rf field homogeneity. We denote this volume V'_b. The sample bulbs do have small tails $(V_b - V'_b)/V_b \ll 1$ which extend out of the resonator volume into region where the longitudinal rf fields are negligible. Only the atoms within the volume V'_b contribute to the signal power (equation 2.31) and hence the 'post homogenization' filling factor appropriate to these experiments is reduced slightly

[6]Here we only consider the case of a $\pi/2$ pulse. A more general treatment in which field inhomogeneities lead to variations in the initial tipping angle as a function of position throughout the sample is presented in references [21, 22, 27].

by the factor V'_b/V_b :

$$\eta \approx \frac{V'_b}{V_b^2} \frac{[\int H_z dV'_b]^2}{\int H^2 dV_c} . \tag{2.35}$$

In appendix B we discuss the measurement of the filling factors for the resonators and the sample bulbs used in our experiments. Both techniques which are presented are perturbation measurements in which the rf fields of the resonator are probed by putting various magnetic and dielectric materials into the resonator. One of these techniques has been used previously; however, the second is a new technique which relies on the paramagnetic susceptibility of liquid oxygen to perturb the resonant frequency of the resonator.

2.4 The hydrogen maser

The self consistent interaction of the oscillating magnetization **M** with its own radiation field **H** inside the resonator is nothing less than 'stimulated emission of radiation'.

In 1960 Goldenberg, Kleppner and Ramsey [1] built the first atomic hydrogen maser, a device whose operation is based upon the stimulated emission of radiation from H atoms. In a hydrogen maser a beam of H atoms is prepared in the upper hyperfine states and injected into a sample bulb through a small orifice. The mean residency time of the atoms within the bulb is referred to as the bulb holding time T_b which is usually of the order of 1 second. The bulb is located within the confines of an electromagnetic resonator tuned to the a-c hyperfine transition of H. Above a threshold flux of $|\ c\ \rangle$ state atoms which is required to overcome losses, the population inversion $n_H\,(\rho_{cc} - \rho_{aa})$ inside the bulb can be maintained high enough that *self sustaining* oscillations at the a-c transition are obtained. Since its invention, the unparalleled frequency stability of the hydrogen maser has made it an invaluable tool for both scientists and engineers [3]. References [33] and [31] contain excellent discussions of the theory and the operation of H masers.

Reference [32] presents a survey of the 'physics of the H maser'.

Without delving into the detailed theory of maser operation we can calculate a few parameters that will be of interest later. In appendix A, a lumped element model of the resonator is used to determine the field which is generated by the oscillating magnetization. The Bloch equations 2.28 can be solved[7] self consistently with this field. The solution is a function of the resonator detuning which is defined by

$$\Delta = Q_\ell \left(\frac{\omega_c}{\omega} - \frac{\omega}{\omega_c} \right) \approx 2Q_\ell \frac{(\omega_c - \omega)}{\omega} . \tag{2.36}$$

To second order in Δ, this self consistent solution (see appendix A) leads to the requirements :

$$-\frac{1}{\tilde{M}_r} d\tilde{M}_r dt = \frac{1}{2}\tilde{\gamma}\mu_0\eta Q_\ell \left(1 - \Delta^2\right) \tilde{M}_z + \frac{1}{T_2} \tag{2.37}$$

$$\omega - \omega_0 = -\frac{1}{2}\tilde{\gamma}\mu_0\eta Q_\ell \Delta \tilde{M}_z . \tag{2.38}$$

The first of these equations describes the instantaneous rate at which the precessing (fictitious) transverse magnetization $\tilde{M}_r$ is damped by relaxation (T_2 processes) and radiation of power. Under *steady state* operating conditions this damping must be zero and hence equation 2.38 can be rewritten in the simple form

$$\omega - \omega_0 = \frac{\Delta}{T_2} . \tag{2.39}$$

By changing the tuning of the resonator, the oscillation frequency of the maser is changed. This pulling effect is reduced by the ratio of the resonator quality factor Q_ℓ to the 'atomic quality factor'

$$Q_{atom} = \frac{1}{2}\omega_0 T_2 \tag{2.40}$$

[7]The equations must be modified in order to include the flux of atoms entering the maser bulb. The effect of this term under steady state conditions is to constantly replenish losses in the $\hat{z}$ component of the fictitious magnetization. As a result $d\tilde{M}_z/dt = 0$ and neither T_1 nor the flux term appear explicitly in the equations presented here.

i.e.

$$\omega - \omega_0 \approx \frac{Q_\ell}{Q_{atom}} (\omega_c - \omega_0) \ . \tag{2.41}$$

The atomic quality factor is usually many orders of magnitude larger than Q_ℓ and hence cavity pulling effects are strongly attenuated. It should be pointed out that the 'zero detuning' oscillation frequency ω_0 is not given exactly by $\tilde{\gamma}\tilde{B}_z$ (equation 2.18) because of other effects which perturb the a-c transition frequency. Amongst these effects (to be discussed in the next chapter) are frequency shifts due to spin-exchange collisions between H atoms. In chapters 4 and 5 we study the influence of spin-exchange induced frequency shifts on ω_0 in a hydrogen maser operating at 0.5 K by changing the parameters Δ, Q_ℓ and n_H and observing the change in $\omega - \omega_0$.

Before leaving this topic it should be noted that the steady state solution of equation 2.37 leads to an expression for the steady state value of $\tilde{M}_z$. With the aid of equation 2.22 the population inversion inside the maser bulb can be written

$$n_H (\rho_{cc} - \rho_{aa}) = \frac{4(1+\Delta^2)}{\hbar (\gamma_e + \gamma_p)^2 \mu_0 \eta Q_\ell} \frac{1}{T_2} \ . \tag{2.42}$$

We return to the discussion of H masers in chapter 4.

Chapter 3

Introduction to Atomic Hydrogen and Deuterium at Low Temperatures

In this chapter we review the various interactions between hydrogen atoms, deuterium atoms, and ^{4}He (both liquid and gas) at low temperatures. The discussion is divided into three main topics, each of which plays a role in the interpretation of the experiments presented in the later part of this thesis. General overviews of much of the material presented here as well as other aspects of atomic hydrogen research at low temperatures can be found in the reviews by Silvera and Walraven [4] and by Greytak and Kleppner [5].

The first topic discussed is the confinement of atomic hydrogen (H) and atomic deuterium (D) by superfluid liquid helium (ℓ-^{4}He) wall coatings. The use of liquid helium as a 'non-stick', yet impermeable, liquid coating to suppress the adsorption (and subsequent recombination) of H atoms to the walls of an experimental chamber at low temperatures was introduced by Silvera and Walraven [11] in 1979. This event effectively signaled the beginning of low temperature atomic hydrogen research. Its use remains an important element of most experiments with H at low temperatures to this date. Recently [21] we demonstrated that unlike the case for H, a gas of D atoms is only partially confined by ℓ-^{4}He walls at temperatures above 1 K. In chapters 6 and 7 we discuss an experiment involving mixtures of H and D atoms at 1 K in which an improved measurement of the energy required to force a D atom into ℓ-^{4}He is made.

The second topic discussed is the recombination of H and/or D into a molecular form. During our study of interactions between H and D atoms at 1 K it proved essential

to determine the rates[1] at which these reactions occur. Compared to most chemical reactions, these recombination processes are simple and they can actually be calculated from *ab initio* interatomic potentials. These potentials are already the most accurately known of all atomic systems. By measuring the rates at which the various recombination reactions occur it may be possible to further refine the potentials.

Finally we present a discussion of the influence of atomic collisions on the frequency and the width of the a-c hyperfine transition of H. These collisions are classified as 'buffer gas' (in the case of H-^{4}He collisions) and spin-exchange collisions (in the case of H-H and H-D collisions). In both cases, the perturbative effects of these collisions are calculable and provide a very sensitive means of testing the detailed form of the interatomic potentials. A recent theory [19, 20] rigorously includes hyperfine interactions in the calculation of the frequency shift and broadening cross sections for H-H spin-exchange collisions. This theory predicts the existence of frequency shifts in an oscillating hydrogen maser which depend upon the occupancy of the individual hyperfine states of the H atoms. These shifts are of relatively little consequence for existing conventional room temperature H masers; however they may limit the ultimate frequency stability of H masers operating at cryogenic temperatures. In chapters 4 and 5 we investigate these H-H spin-exchange induced frequency shifts using a cryogenic hydrogen maser.

3.1 Containment with liquid ^{4}He walls

Throughout the work presented in this thesis, van der Waals films of superfluid liquid ^{4}He (ℓ-^{4}He) have been used to coat the interior walls of the containers (sample bulbs) in which the atomic gasses are confined. These coatings are 'self-cleaning' in the sense that almost any atom or molecule *other* than H will penetrate the liquid and adsorb to the

[1]The recombination of two H atoms to form H_2 in zero magnetic field has been studied before [12, 34, 27]. In chapter 7 we present similar measurements for H-D and D-D recombination at 1 K.

underlying substrate rather than being confined [35, 36]. They are also 'self-healing' in the sense that any damage to the film (caused for example by firing an rf discharge to dissociate molecular hydrogen) is quickly repaired. This last property is a consequence of the liquid being a superfluid. The *equilibrium* thickness of the film is determined by the van der Waals attraction of the ^{4}He to the walls, and is independent of whether the film is superfluid or not.

A consequence of using saturated ℓ-^{4}He films to line the cells is that the ^{4}He vapour density above the film may in fact be much higher than the density of the hydrogen atoms which are being studied. Typically we work with H and D densities below 10^{13}cm^{-3}. At 1 K the ^{4}He density n_{He} above a saturated film is 10^{18}cm^{-3}. This density drops rapidly as the temperature is lowered, however at 0.5 K it is still about 3×10^{14}cm^{-3}.

At 1 K the motion of H and D atoms through the ^{4}He buffer gas is diffusive. The diffusion coefficient can be written

$$\mathcal{D} = \frac{3\pi\overline{v}_{ij}}{32 n_{He} Q_{diff}} \tag{3.1}$$

where $\overline{v}_{ij}$ is the mean relative velocity of the colliding atoms (H and ^{4}He or D and ^{4}He) and Q_{diff} is the effective hard core diffusion cross section. Hardy *et al.* [37] measured $\mathcal{D}$ for H atoms at T $\approx$ 1 K and inferred Q_{diff} = 20(1) Å^2. Jochemsen *et al.* [38] estimate that the corresponding cross section for D atoms is about 30 Å^2 at this temperature. The mean free paths of the diffusing H and D atoms

$$\lambda_{diff} = \frac{1}{\sqrt{2}\, n_{He} Q_{diff}} \tag{3.2}$$

are thus less than 4 microns above 1 K. At 0.5 K the ^{4}He density is much lower and the mean free path of an H atom[2] is comparable to the dimensions of the sample bulb.

The gaseous ^{4}He inside the sample bulbs influences our experiments in two other very important ways. Collisions with ^{4}He atoms can catalyze the recombination of H or D

[2] Q_{diff} is expected to drop to about half of its value at 1 K [38] and thus $\lambda_{diff} \approx$2 cm at 0.5 K.

atoms into H_2, D_2 or HD. They also cause a momentary perturbation of the hyperfine interaction during the collision which results in a shift in the frequency of the a-c hyperfine transition with which we work. Both of these points are discussed later in this chapter. We start with a discussion of the interactions between the H and/or D atoms and the ℓ-^{4}He walls.

3.1.1 Binding, sticking and thermal accommodation

Atomic H is attracted to the surface of ℓ-^{4}He by van der Waals forces which are weak because of the low polarizability [39] and the low density [40] of the liquid. There is in fact only one known bound state [41] for an H atom on the liquid surface. The most reliable measurement of this binding energy $E_B = 1.011(10)$ K was made by Hürlimann [17, 42]. The only surface to which H is more weakly bound[3] is liquid ^{3}He for which $E_B \approx 0.4$ K [44, 45]. Atomic D is more tightly bound[4] to the surface of ℓ-^{4}He than H, the measurements of Silvera *et al.* [47, 48] seeming to indicate that $E_B = 2.6(4)$ K for D on ℓ-^{4}He. There is some suspicion that this may only be an upper bound on the true binding energy [49]. Atomic tritium (T) has never been successfully studied in a cell with ℓ-^{4}He coated walls [50].

When a hydrogen atom strikes a ℓ-^{4}He surface it can either[5] scatter from, or stick to the liquid. The sticking process is characterized by a sticking coefficient 's' which is the probability that an H atom which strikes the surface will enter the bound state. Once in the bound state, H atoms form a two-dimensional gas which can interact with

[3]Traditionally it was thought that H would probably be bound to all known substrates. Recently Nacher and Dupont-Roc [43] have demonstrated that ℓ-^{4}He will not wet solid Cs. The interpretation of this result is still open to speculation. However, if it is due to some combined effect of the low occupancy of the outermost electron shells in the Cs atom and the large de Broglie wavelength of the ^{4}He atom at low temperatures, a similar effect may be seen with H.

[4]There has been some speculation that a second weakly bound state for D on ℓ-^{4}He may exist [46]. The presence of this state has not been experimentally verified.

[5]The issue of whether or not the atom can enter the liquid will be discussed in a later section.

excitations (ripplons) on the free surface of the liquid and eventually thermalize [51]. Collisions with energetic ripplons result in adsorbed atoms being desorbed and returning to the gas phase above the liquid. The thermal accommodation coefficient 'α' is a measure of the efficiency of the ℓ-^{4}He surface in thermalizing atoms which strike the surface. The details of these processes are of considerable interest at present, especially at very low temperatures where quantum mechanical effects set in. The review by Berkhout and Walraven [52] and the references therein can be consulted for further details.

3.1.2 Adsorption isotherm and the wall shift

If the H atoms adsorbed on the ℓ-^{4}He surface are in thermal equilibrium with the H atoms in the gas phase above the liquid, the chemical potentials of the two systems can be equated to relate the number density of adsorbed atoms n_σ to the bulk density n_H. In doing this one obtains the relationship

$$n_\sigma = n_H \Lambda \exp\left(\frac{E_B}{k_B T}\right) \tag{3.3}$$

where $\Lambda = \left(\frac{2\pi\hbar^2}{m_H k_B T}\right)^{\frac{1}{2}}$ is the thermal de Broglie wavelength[6] of the atoms. The assumptions behind this classical formula are valid for surface densities up to about 10^{14}cm^{-2} [53]. The surface densities encountered in our work are many orders of magnitude lower than this limit.

While adsorbed to the surface an atom is distorted slightly. This distortion is due to the combined effect of the attractive and repulsive interactions between the atom and the surface. It causes a small change in the hyperfine interaction between the nucleus and the electron to occur. This in turn causes the hyperfine transition frequency of each atom on the surface to be shifted from the unperturbed frequency ω_0 by an amount $\delta\omega_s$. In

[6] It is often convenient to remember that $\Lambda_H = 17.4\ \text{Å}\left(\frac{1\text{K}}{T}\right)^{\frac{1}{2}}$ for atomic hydrogen and $\Lambda_D = 12.3\ \text{Å}\left(\frac{1\text{K}}{T}\right)^{\frac{1}{2}}$ for atomic deuterium.

experiments with the cryogenic hydrogen maser operating at 0.5 K, this effect is manifest as a temperature dependent shift of the density independent oscillation frequency ω_0. This effect is commonly referred to as a 'wall shift'[7] A simple theory describing this shift is presented below. More detailed analyses can be found in references [54, 55].

During each sticking event an atom picks up an average phase shift $\phi = \omega_s < \tau_s >$ where $< \tau_s >$ is the average duration of a sticking event. The ratio of $< \tau_s >$ to the average time between sticking events $< \tau_b >$ is the same as the thermal equilibrium ratio of the number of atoms on the walls to the number in the bulk. In a container with surface area A and volume V this implies that

$$< \tau_s > = < \tau_b > \frac{A}{V} \Lambda \exp(E_B / k_B T) \, . \tag{3.4}$$

With the assumption that both $< \tau_s >$ and $< \tau_b >$ are distributed according to Poisson statistics, it can be shown [25] that the atomic resonance is shifted by

$$\delta\omega_w = \frac{1}{< \tau_b > 1 + \phi^2} \frac{\phi}{} \tag{3.5}$$

from the unperturbed frequency ω_0. The broadening of the resonance is

$$\Gamma_w = \frac{1}{< \tau_b > 1 + \phi^2} \frac{\phi^2}{} \, . \tag{3.6}$$

At 0.5 K the atoms do not dwell on the surface long enough to pick up a large phase shift and thus $\phi \ll 1$. In this limit the frequency shift $\delta\omega_w$ is linear in ϕ :

$$\delta\omega_w \approx \frac{\phi}{< \tau_b >} = \omega_s \frac{A}{V} \Lambda \exp\left(\frac{E_B}{kT}\right) \, . \tag{3.7}$$

Hürlimann used the UBC cryogenic H maser to measure this shift [17, 42]. He found $f_s = \omega_s / 2\pi = -7.15(30) \times 10^4$ Hz for H on ℓ-^{4}He. Similar measurements have not been made for D.

[7] In conventional room temperature H masers a similar effect is observed as atoms collide with the teflon coatings which are used to suppress wall adsorption. The difficulty in reproducing these wall coatings limits the accuracy of conventional masers to about 10^{-12}.

3.1.3 Incomplete confinement

Low concentrations of ^{3}He will dissolve into ℓ-^{4}He accompanied by the release of energy. The physics of ^{3}He in ℓ-^{4}He is a very interesting field of study and it naturally leads one to question whether or not other impurities will also dissolve into ℓ-^{4}He. From our point of view it is particularly interesting to consider the possibility of atomic hydrogen or one of its isotopes dissolving into ℓ-^{4}He.

Theoretical work

Kürten and Ristig addressed this question in a theoretical paper published in 1985 [35] They estimated the energy Δ which would be required to replace N+1 ^{4}He atoms (bulk ℓ-^{4}He) with N ^{4}He atoms and one atom or molecule of hydrogen or its isotopes. They found that the diatomic molecules of hydrogen[8] would enter the liquid accompanied by the release of energy, while energy was required to *force* the atoms H, D, and T into ℓ-^{4}He. The solvation energy E_S required to force an atom into the ℓ-^{4}He is approximately the difference between Δ and the latent heat of one ^{4}He atom :

$$E_S = \Delta - L_4 \tag{3.8}$$

Kürten and Ristig found that Δ was quite strongly dependent upon the ℓ-^{4}He density. The zero pressure density of ℓ-^{4}He in their model was 17.2×10^{-3} Å^{-3} while the true liquid density under the saturated vapour pressure is 21.7×10^{-3} Å^{-3} [40]. In table 3.1 we list estimates of the solvation energies for H, D, and T made by subtracting the known latent heat of ^{4}He ($L_4 \approx 7.2$ K) from the values of Δ presented in figure 1 of reference [35].

[8]The issue of whether the solvation process is exothermic or endothermic is determined by the detailed form of the interatomic potentials. The calculations of Kürten and Ristig suggest that H_2 is a borderline case. They felt that it would enter the liquid but perhaps that it might reside in regions of low density.

Isotope	Calculated ℓ-^{4}He Density	
	17.2×10^{-3} atoms/Å^3	21.7×10^{-3} atoms/Å^3
H	30 K	65 K
D	11 K	32 K
T	3.4 K	20 K

Table 3.1: Theoretical values for the solvation energy E_S (in temperature units) required to force hydrogen (H), deuterium (D) and tritium (T) atoms into liquid ^{4}He at two liquid densities. These results were obtained by subtracting the latent heat of ^{4}He ($\approx$7.2 K) from the theoretical energy required to replace N+1 ^{4}He atoms with N ^{4}He atoms and one impurity atom as calculated by Kürten and Ristig [35].The lower density corresponds to the zero pressure density of ℓ-^{4}He in their model while the higher density is the true liquid density under its saturated vapour pressure at 1 K.

In their calculation of the chemical potential Δ Kürten and Ristig ignored multiparticle correlations which lead to backflow effects [56]. They predicted that the inclusion of these effects would lower Δ somewhat but would not lead to a 'substantial' change in their results. They concluded that H and its isotopes would not dissolve into ℓ-^{4}He. In a later paper by Krotscheck *et al.* [57], theoretical solvation energies for H, D, and T in ℓ-^{4}He were reported[9] at 'the calculated equilibrium density of bulk ^{4}He'. These energies were 30 K, 11.5 K and 4.3 K for H, D, and T respectively.

Experimental work

In light of the calculations presented above it is not surprising that effects due to the solvation of H into ℓ-^{4}He have never been observed. Most experiments with H confined by ℓ-^{4}He have been performed at temperatures below 1.5 K where the probability of finding an atom with sufficient thermal energy to penetrate the liquid is extremely low.

[9]The main emphasis of Krotscheck *et al.*'s paper is the study of impurity states in very thin ℓ-^{4}He films where the substrate potential provides an attractive force which tends to draw the impurity atom into the liquid. The saturated films used in our work are much thicker and can be treated as bulk ℓ-^{4}He.

In the case of tritium, it is not clear from the theory whether or not a gas of T should be well confined by ℓ-^{4}He walls at these temperatures. The failure of Tjukanov *et al.* [50] to detect measurable quantities of T in a container coated with superfluid ℓ-^{4}He may indicate the latter.

For deuterium one might have expected a high degree of confinement. Nevertheless in a recent experiment [21] we observed for the first time the solvation of D atoms into ℓ-^{4}He at temperatures just above 1 K. This experiment used magnetic resonance on a hyperfine transition of the D atom to study the time and the temperature dependence of the atomic density n_D inside cells coated with ℓ-^{4}He. At temperatures just above 1 K the atomic density was observed to decay exponentially with time, and at a rate that was steeply temperature dependent. Above 1.16 K the sample lifetime was too short to measure. This decay could not be attributed to recombination processes and eventually was interpreted as being due to the solvation of D into ℓ-^{4}He.

A simple model [22, 21] was used to describe the decay of the atom density due to this solvation process. In this model, D atoms striking a ℓ-^{4}He surface were assumed to enter the liquid with thermally averaged[10] probability $\overline{\alpha}_{gl}$ if they had kinetic energy greater than E_S. It was then assumed that this D quasi particle traveled ballistically through the film with an effective mass m^* and that once it encountered the substrate (solid D_2) it was adsorbed. This model leads to an exponential decay of the atomic density

$$\frac{dn_D}{dt} = -\lambda n_D \tag{3.9}$$

where the decay rate λ for a cell with volume V and surface area A is given by

$$\lambda = \frac{A\overline{v}}{4V}\mu\overline{\alpha}_{lg}\exp\left(-\frac{E_S}{k_B T}\right) . \tag{3.10}$$

Here $\overline{v} = \left(\frac{8k_B T}{\pi m}\right)^{\frac{1}{2}}$ is the thermally averaged speed of the atoms striking the liquid surface and μ is the ratio of the quasi particle effective mass m^* to the bare atom mass m. The

[10]This probability is likely quite angle dependent at least for kinetic energies just greater than E_S.

term $\overline{\alpha}_{lg}$ is the thermally averaged transmission probability that a quasiparticle striking the liquid gas interface will leave the liquid. This reverse transmission probability is related to $\overline{\alpha}_{gl}$ through the expression

$$\overline{\alpha}_{gl} = \mu\overline{\alpha}_{lg} \exp\left(-\frac{E_S}{k_B T}\right) . \tag{3.11}$$

Analysis of the decay rate data from this experiment led to a measurement of the energy required to *force* a D atom into ℓ-^{4}He. In this original experiment we found $E_S = 13.6(6)$ K. Unfortunately, due to scatter in the data and the very narrow range of temperatures over which data could be taken, it was impossible to determine the prefactor in equation 3.10 with any precision. In chapters 6 and 7 of this thesis we present the results of a new study of the solvation of D into ℓ-^{4}He. This experiment is performed using magnetic resonance on atomic H in mixtures of H and D. This technique allows us to account for recombination processes which occur in parallel with the solvation process and thus we are able to make a considerable reduction in the scatter of the data. These result include a measurement of the prefactor associated with equation 3.10.

Before leaving this topic, the assumptions behind the simple solvation model presented above do require some comment. The assumption of ballistic transport within the film is addressed first. The thickness 'd' of a saturated ℓ-^{4}He film on a H_2 substrate is [58]

$$d = 2.5(4) \times 10^{-6} cm^{\frac{4}{3}} h^{-\frac{1}{3}} \tag{3.12}$$

where 'h' is the height above the bulk liquid at which the observation is made. The film thickness over a D_2 substrate should be similar to this. In the original measurement[11] of the solvation energy for D in ℓ-^{4}He [21] the film thickness at the site of the resonator was approximately 100 Å. The data in this experiment was recorded over the narrow temperature range 1.08 K to 1.16 K. The mean free path of a ^{3}He quasi particle in ℓ-^{4}He

[11] In the present work, the cells are smaller and hence the films are about 50% thicker.

due to scattering by rotons[12] ranges from about 1000 Å at 1.0 K down to about 250 Å at 1.2 K [59]. These mean free paths are somewhat longer than the thickness of the ℓ-^{4}He films that we use. Unless the cross section for interactions between D quasi particles and ℓ-^{4}He is much larger than that for ^{3}He - ℓ-^{4}He interactions, no attenuation due to diffusive transport in the film should be expected.

It is somewhat more difficult to address the second assumption that every D quasi particle becomes adsorbed to the substrate. The binding energy of D to bare D_2 is about 55 K [60]. Under the ℓ-^{4}He film it is necessary to balance the attraction of the substrate for the D atom against the increase in the chemical potential of the D atom as the ℓ-^{4}He density increases near the wall [35, 61]. This is complicated by the fact that very close to the substrate, the ^{4}He tends to solidify. Krotscheck *et al.* [57] noted that in the case of very thin films, D atoms on the ℓ-^{4}He surface should actually be drawn into the film and bound to the substrate by van der Waals forces. A calculation of the sticking probability for a D quasi particle striking this substrate would certainly be interesting.

3.2 Recombination processes

We turn now to a review of the recombination of atomic hydrogen and deuterium in the context of the present work.

3.2.1 Molecular potentials

At low temperatures H (or D) atoms are almost always in their electronic ground state. If we neglect hyperfine interactions then the Coulombic pair interaction between two atoms depends only upon the symmetry of the total electron spin wavefunction. This interaction can be written in terms of an attractive (except at very close range) singlet

[12]The dominant excitations in ℓ-^{4}He at this temperature are rotons.

$^1\Sigma_g^+$ potential, and an essentially repulsive triplet $^3\Sigma_u^+$ potential. The H-H interatomic potential is the most accurately known potential of any atomic system. The results of the *ab initio* calculations of these potentials made by Kolos and Wolniewicz [62, 63, 64] are shown in figure 3.1. A consequence of the accuracy to which these potentials are known is that often the cross sections for collision processes can be calculated very well from first principles.

Two H atoms interacting via the triplet potential[13] cannot recombine. On the other hand the singlet potential supports many bound states. It is difficult to test the long range part of theoretical potential energy curves at internuclear separations further than the classical turning point of the least bound molecular state.[14] For H_2 this distance corresponds to about 6 Å for the v=14 vibrational level [62]. At low temperatures the outcome of most scattering processes is governed primarily by the long range part of the interatomic potentials. In a sense, careful measurements of these processes can be used to test and refine the long range parts of calculated interatomic potentials. A tabulation of the known bound levels within 300 K of dissociation for the H_2, D_2 and HD molecules is given in appendix E.

As the temperature of a gas of H atoms is lowered, more and more atoms collide with energies comparable to the hyperfine interaction. At these temperatures it is necessary to include hyperfine interactions in the calculation of physical processes. This increases the complexity of the calculations considerably as the manifold of colliding states is enlarged. Calculations of this type have only recently been performed for H-H spin-exchange collisions in the context of the atomic H maser. These calculations are discussed in a later section. The implications of these calculations for the stability of cryogenic H

[13]There is a very shallow well (about 6.5 K) deep in the triplet potential at an internuclear separation of 4.15 Å. It is not deep enough to support any bound states.

[14]*i.e.* spectroscopic measurements of the energy of the various molecular states can be used to test the potentials at shorter separations.

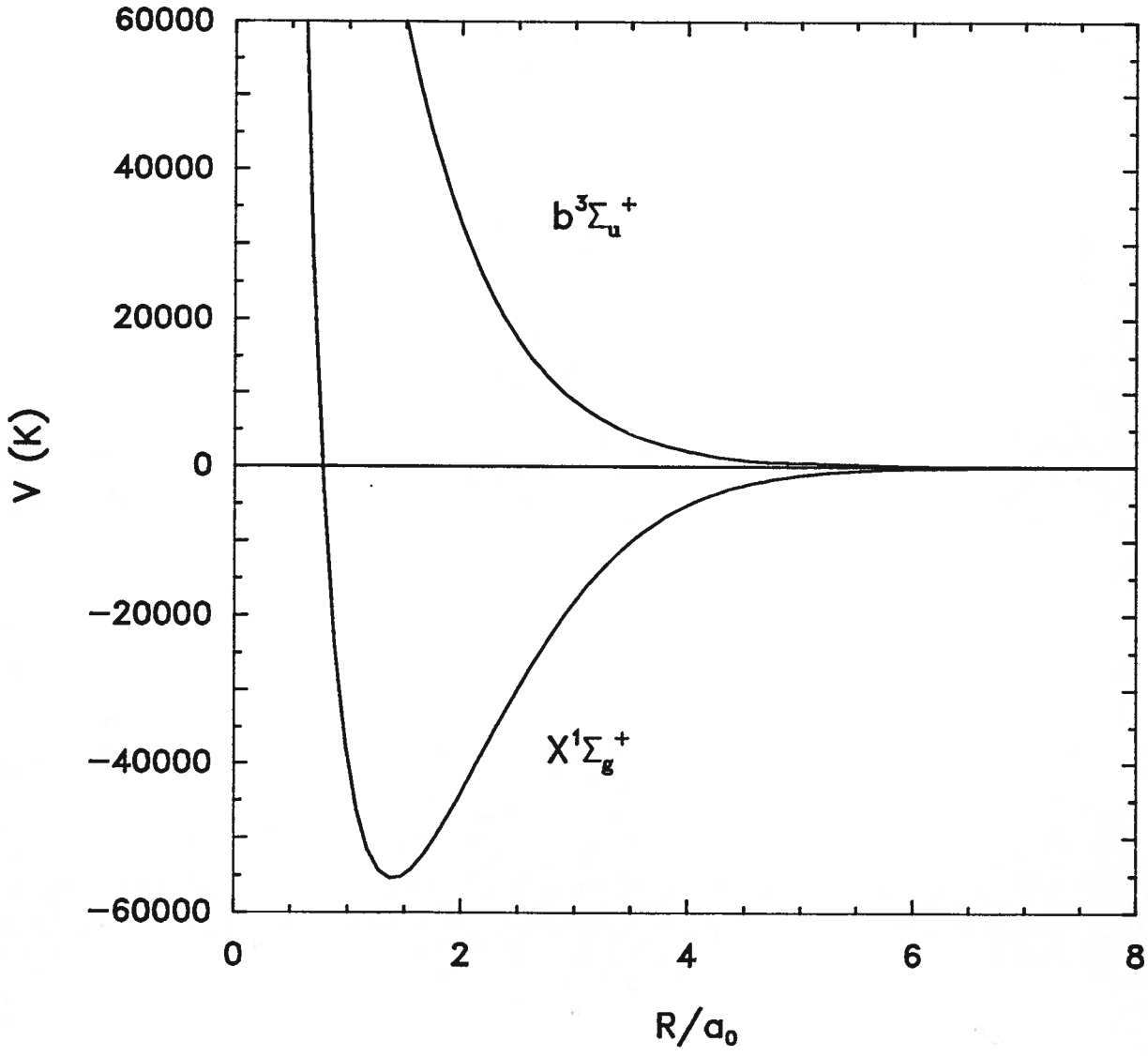

Figure 3.1: The lowest H-H interatomic singlet $^1\Sigma_g{}^+$, and triplet $^3\Sigma_u{}^+$ potentials as calculated from first principles by Kolos and Wolniewicz [62, 63, 64]. The radial separation of the nuclei has been normalized to the Bohr radius.

masers are of great technological concern. Measurements of the spin-exchange induced frequency shifts in a cryogenic H maser are presented in chapter 5.

Before leaving this topic we include a comment on notation. In the case of H_2, the two atom wavefunction describing the molecule must be antisymmetric under interchange of either the nuclei or the electrons. That is, the sum J+I must be an even number. Two possible types of states can be identified. By convention[15] the states with I=1 and J odd are labeled 'ortho' states while those with I=0 and J even are labeled 'para'. For the D_2 molecule the labeling is reversed: the states with even J are the ortho states and those with odd J are the para states.

3.2.2 Recombination of atomic H, D

The recombination of H to form molecular hydrogen H_2 (or any isotopic variation of this reaction) is an exothermic process which releases about 4.5 eV of energy. At low temperatures it is not possible to conserve both energy and momentum in this reaction unless it is catalyzed by some inert third body X. That is, recombination takes place by the reaction[16]

$$H + H + X \rightarrow H_2 + X \tag{3.13}$$

This reaction leads to a decrease of the atomic density inside a sealed container

$$\frac{dn_H}{dt} = -K_{HH} n_H^2 \tag{3.14}$$

where K_{HH} is the rate at which the decay occurs. If the initial H density is n_H^o then the time dependence of n_H is simply given by

$$n_H(t) = \frac{1}{K_{HH}} \left(\frac{1}{t + \tau} \right) \tag{3.15}$$

[15]The more practical definitions 'symmetric' and 'antisymmetric' in reference to the wavefunctions are not commonly used.

[16]The three body reaction $H + H + H \rightarrow H_2 + H$ does not contribute to the decay of the H density at the low densities considered in this thesis.

where τ is a characteristic time for the decay

$$\tau = \frac{1}{K_{HH} n_H^o} . \tag{3.16}$$

At temperatures near 1 K the dominant catalyst for this process is the 'dense'[17] ^{4}He buffer gas which is present as a consequence of the saturated ℓ-^{4}He film. In this case the decay is also proportional to the ^{4}He density n_{He} and so $K_{HH} = k_{HH} n_{He}$.

The recombination of two D atoms to form D_2 can be described in a completely analogous manner by simply replacing 'H' with 'D' throughout the above discussion. In chapter 7 we deal with mixtures of H *and* D at temperatures near 1 K. In appendix C these rate equations for the decay of the atomic densities are generalized to include H-D recombination and the solvation of D into ℓ-^{4}He as alternate density loss mechanisms.

The recombination of H by the reaction 3.13 has been studied theoretically by Greben *et al.* [65]. They found that this process could be described in terms of separate contributions from the formation of ortho and para-H_2. At zero field under the assumption that all hyperfine states are equally populated, their results can be written

$$k_{HH} = \frac{1}{16} k_{para} + \frac{3}{16} k_{ortho} . \tag{3.17}$$

Their numerical results for k_{HH} are summarized in table 3.2. The bulk of the temperature dependence of this rate constant arises from the thermal averaging of the ortho-H_2 formation rate which drops as the temperature is lowered. Measurements of k_{HH} have been made previously in this laboratory. Morrow[18] reported a value of $2.0(3)\times10^{-33}$ cm^6/s at 1 K which seems to be in excellent agreement with the rate constant 1.8×10^{-33}cm^6/s calculated by Greben *et al.* Similar calculations have not been performed for the formation of D_2 or HD. Measurements of the rate constants for D-D and H-D recombination are presented in this thesis.

[17] in the sense that $n_{He} \gg n_H$

[18] A value of $2.8(3)\times10^{-33}$ cm^6/s was originally reported in references [37, 34, 12]. It was later discovered that this value was too high by a factor of $\sqrt{2}$ [27].

v	J	D_0 (K)	Contribution to k_{HH} at various temperatures		
			1 K	0.1 K	0.01 K
14	0	210.4	0.095	0.056	0.049
14	1	185.2	0.183	0.016	
14	2	138.6	1.747	1.32	1.29
14	3	73.5	14.63	1.62	0.147
14	4	1.4	1.107	0.0015	
13	7	76.2	0.025		
Total			17.79	3.01	1.49

Table 3.2: Theoretical results of Greben *et al.* [65] for the contributions of different states of the H_2 molecule to the H-H recombination rate constant $k_{HH} = \frac{1}{16}k_{para} + \frac{3}{16}k_{ortho}$ in units of 10^{-34} cm^6/s. The molecular levels are labeled by their vibrational (v) and rotational (J) quantum numbers. The dissociation energies D_0 of these states are included as they differ slightly from the values quoted in appendix E.

At lower temperatures (T≈0.5 K or lower) where the ^{4}He buffer gas density is reduced and the H (or D) atoms spend more time adsorbed to the liquid helium wall coatings, the recombination reaction 3.13 can be catalyzed by the walls of the container. In this case the reaction is characterized by a surface recombination 'cross length'. In zero field the cross length for H-H recombination on a ℓ-^{4}He surface is[19] 0.14(2) Å .

3.3 Effects of atomic collisions on hyperfine resonance parameters

Hydrogen atoms typically undergo many collisions before finally recombining. During these collisions the hyperfine interaction between the electron and the proton is momentarily perturbed. The net effect of many such collisions can be to shift and/or to broaden the atomic resonance. These effects and their relevance to our experiments are described below. They are classified as 'buffer gas' and 'spin-exchange' collisions.

[19] A value of 0.20(3) Å was reported in references [34, 44, 12]. This was later recognized to be in error by a factor of $\sqrt{2}$ [27].

3.3.1 Shift due to collisions with ^{4}He atoms

The strength of the hyperfine interaction depends upon the local electron density at the site of the nucleus. During a collision with an inert body such as ^{4}He, polarization effects cause this density to be momentarily modified. The average effect of these perturbations is to shift the frequency of the radiation which is observed from a hyperfine transition. They do not lead to a significant broadening of the transition. Traditionally these shifts have been referred to as 'hyperfine pressure shifts' simply because the frequency shift increases as the density of the buffer gas is increased.

The calculation of these frequency shifts is a difficult theoretical problem (see for example references [66, 67, 68]). The N electron problem must first be solved (H-^{4}He is the simplest case with N=3) to determine the frequency shift as a function of the internuclear spacing, and then the necessary thermal average must be performed. At high temperatures the frequency shift for the H-^{4}He system is positive and dominated by contributions from the short range part of the interatomic potentials. Jochemsen and Berlinsky [69] extended the calculations for this system to the low temperature regime. They found that below 10 or 20 K the shift changes sign and is dominated by the long range part of the potential. The pressure shift coefficient $\delta f/n_{He}$ is essentially independent of temperature over the narrow temperature range that was examined experimentally by Hardy, Morrow and their collaborators [12, 27]. They measured

$$\frac{\delta f}{n_{He}} = -11.8 \times 10^{-18} \text{Hz cm}^3$$

for the a-c hyperfine transition of H at 1 K. We recently measured this quantity for the $\Delta F = 1$, $\Delta m_F = 0$ hyperfine transition of D in a 3.89 mTesla field [21]. The pressure shift coefficient in this case is :

$$\frac{\delta f}{n_{He}} = -3.8(1) \times 10^{-18} \text{Hz cm}^3 .$$

It is important to note that the H-^{4}He buffer gas shift leads to a frequency shift which has the same sign as the wall shift discussed earlier in this chapter (equation 3.7). This has important consequences for any cryogenic H maser which uses ℓ-^{4}He to suppress adsorption (chapters 4 and 5). The combined frequency shift due to these effects passes through a minima as a function of the temperature. The exact temperature at which the extremum occurs depends upon the area to volume ratio of the maser bulb. By operating at this temperature (typically $\sim$0.55 K) the oscillation frequency of the maser becomes insensitive to changes in the combined frequency shift. In chapter 7 we present a more accurate measurement of the pressure shift coefficient for H-^{4}He collisions at 1 K.

3.3.2 Spin-exchange induced broadening and frequency shifts

Collisions between paramagnetic atoms such as H and D also lead to perturbations of the hyperfine interaction and can lead to shifts of atomic hyperfine resonances. The effects which are induced by these collisions are dominated by electron-exchange interactions [18] and thus they are labeled 'spin-exchange' collisions. This exchange mechanism is a form of spin relaxation and hence spin-exchange collisions can broaden an atomic hyperfine resonance. Many discussions of spin-exchange can be found in the literature, however Pinard and Lalöe [70] give a particularly nice interpretation of these collisions in terms of the Pauli exclusion principle. This paper highlights the importance of spin identity in determining the outcome of a collision. Other important papers are referred to below.

Much of the theory of spin-exchange collisions as they pertain to atomic hydrogen was developed during the 1960's in the context of the atomic hydrogen maser [71, 72, 73, 74]. In the semi-classical formalism which was adopted for these studies the hyperfine interaction was deemed to play an insignificant role in determining the outcome of a collision. The frequency shift of the a-c hyperfine transition of H predicted by this theory is proportional only to the rate at which H-H collisions occur and the level population

difference between these two states. This theory has been quite successful at describing phenomena induced by H-H spin-exchange collisions at energies much higher than the hyperfine splitting of the H atom.

Recently the first fully quantum mechanical treatment of the H-H spin-exchange collision problem was published [19, 20]. The non-adiabatic effects introduced by the inclusion of hyperfine interactions result in frequency shifts and broadening of the a-c hyperfine transition of H which depend on the detailed occupancy of the individual hyperfine states.

In this thesis we will be concerned with the influence of both H-H and H-D spin-exchange collisions on the a-c hyperfine transition in a gas of atomic hydrogen at low temperatures. We begin with a review of the frequency shift and the broadening of this transition which are predicted by the semi-classical treatment of spin-exchange collisions. This is followed by a summary of the predictions which are made by the fully quantum mechanical theory [19, 20] for H-H spin-exchange collisions in an oscillating H maser. An analogous theory has not yet been developed for H-D spin-exchange collisions.

Semi-classical treatment

In the semi-classical picture used by Crampton [71, 72] and others (for example references [73, 74]) to describe H-H spin-exchange collisions, all interactions except electron spin-exchange are neglected and the initial states of the colliding atoms are considered to be identical. This is often referred to as the degenerate internal states or DIS approximation. By neglecting spin orbit coupling the (elastic) scattering process can be described in terms of independent phase shifts from the singlet and the triplet potentials of the transient molecule. Following this procedure it is possible to write down the equation of motion for the spin density matrices of the colliding atoms (see for example reference [74]). This equation depends upon whether or not the colliding atoms are identical.

In the context of a hyperfine magnetic resonance experiment, a tipping pulse (described in the previous chapter) is a small perturbation which modifies the density matrix of the atomic system. Spin-exchange collisions will cause these matrix elements to relax back to their thermal equilibrium values. We only consider the effects of spin-exchange collisions on the a-c hyperfine transition of the H atom in zero field in the discussion that follows.

In the case where the colliding atoms are identical (two H atoms), the spin-exchange relaxation rate for the *diagonal* elements of the H atom density matrix can be written [71, 72]

$$\left.\frac{1}{T_1^{se}}\right|_{HH} = n_H \overline{v}_{HH} \overline{\sigma}_{HH} \tag{3.18}$$

where $T_1^{se}|_{HH}$ is the longitudinal relaxation time due just to H-H spin-exchange collisions. The spin-exchange relaxation rate for the *off diagonal* elements of the density matrix is

$$\left.\frac{1}{T_2^{se}}\right|_{HH} = \frac{1}{2} n_H \overline{v}_{HH} \overline{\sigma}_{HH} \tag{3.19}$$

where $T_2^{se}|_{HH}$ is the corresponding transverse relaxation time. In these equations $\overline{v}_{HH}$ is the mean relative speed of the colliding H atoms and $\overline{\sigma}_{HH}$ is the thermally averaged spin-exchange (or 'spin flip') cross section for the collision. The product $\overline{G}_{HH} = \overline{v}_{HH}\overline{\sigma}_{HH}$ is often referred to as the thermally averaged spin-exchange broadening parameter or rate constant. It should be noted that in the DIS theory the ratio

$$\frac{T_1^{se}}{T_2^{se}} = \frac{1}{2} \tag{3.20}$$

is independent of the atomic density. This relationship has been verified experimentally at temperatures as low as 77 K by Desaitfuscien and Audoin [75].

If an H atom collides with heteronuclear atoms such as D rather than other H atoms, these equations become [71, 22]:

$$\left.\frac{1}{T_1^{se}}\right|_{HD} = n_H \overline{v}_{HD} \overline{\sigma}_{HD} \tag{3.21}$$

$$\left.\frac{1}{T_2^{se}}\right|_{HD} = \frac{3}{4} n_H \bar{v}_{HD} \bar{\sigma}_{HD} \tag{3.22}$$

where the notation should be obvious. In this case the ratio T_1^{se}/T_2^{se} is also independent of the atomic densities but equal to $\frac{3}{4}$. This relationship has been verified near room temperature by Berg [76].

The thermally averaged[20] cross sections for these collisions can be written in terms of the singlet and triplet phase shifts (δ_ℓ^s and δ_ℓ^t) for collisions involving angular momentum $\ell\hbar$ and relative linear momentum $\hbar k$:

$$\bar{\sigma}_{ij} = \frac{1}{\bar{v}_{ij}} \left\langle \frac{\pi\hbar}{\mu_{ij} k} \sum_{\ell=0}^{\infty} (2\ell+1) \sin^2(\delta_\ell^s - \delta_\ell^t) \right\rangle_k \tag{3.23}$$

where μ_{ij} denotes the reduced mass of the colliding atoms (not to be confused with the effective mass ratio μ introduced earlier in this chapter) and

$$\bar{v}_{ij} = \sqrt{\frac{8 k_B T}{\pi \mu_{ij}}} \tag{3.24}$$

is their mean relative speed.

H-H spin-exchange collisions also lead to a shift in the frequency of the a-c hyperfine transition of H. This shift is proportional to the population difference between the $|\, a \,\rangle$ state and the $|\, c \,\rangle$ state :

$$\omega - \omega_0 = -\frac{1}{4}(\rho_{cc} - \rho_{aa}) n_H \bar{v}_{HH} \bar{\lambda}_{HH} \tag{3.25}$$

where ω_0 is the unperturbed transition frequency and $\bar{\lambda}_{HH}$ is the thermally averaged frequency shift cross section. $\bar{\lambda}_{HH}$ can be calculated in a similar manner to $\bar{\sigma}_{HH}$ [72, 71] :

$$\bar{\lambda}_{HH} = \frac{1}{\bar{v}_{HH}} \left\langle \frac{\pi\hbar}{\mu_{ij} k} \sum_{\ell=0}^{\infty} [1 + (-1)^\ell](2\ell+1) \sin 2(\delta_\ell^s - \delta_\ell^t) \right\rangle_k \tag{3.26}$$

The product $\bar{v}_{HH}\bar{\lambda}_{HH}$ is often referred to as the thermally averaged frequency shift parameter or rate constant. Crampton has shown [71] that in the DIS limit, H-D spin-exchange collisions do not lead to a similar shift of the a-c hyperfine transition of H.

[20] The symbols $\langle \cdots \rangle_k$ are used to indicate the thermal averaging.

Temperature (K)	$\overline{\lambda}_{HH}$ (Å^2)		$\overline{\sigma}_{HH}$ (Å^2)	
	(calculated)	(measured)	(calculated)	(measured)
0.5	47.2 [77] 55 [78]		0.526 [77] 0.75 [78]	
1.1	25.9 [77]		0.387 [77] 0.55 [78] 0.31*	0.43 ± 0.03 [27]
300	3.6 [77] 3.8 ± 0.4 [80]	4.1 ± 1.0 [79]	23.4 [77] 23.5 [80]	23.1 ± 2.8 [75]

Table 3.3: Summary of measured and calculated values for the thermally averaged H-H spin-exchange frequency shift ($\overline{\lambda}_{HH}$) and broadening ($\overline{\sigma}_{HH}$) cross sections. The value of $\overline{\sigma}$ indicated with a * was reported in reference [27] after the result calculated in reference [78] was reanalyzed using the improved potentials of reference [63].

A compilation of measured and theoretical values of $\overline{\lambda}_{HH}$ and $\overline{\sigma}_{HH}$ for H-H spin-exchange collisions at temperatures relevant to the present work can be found in table 3.3. Room temperature values are also given for comparison. The theoretical results obtained by several authors have been included to illustrate the sensitivity of these parameters to the detailed form of the interatomic potentials which are used in the calculations. The calculations of Verhaar *et al.* [19, 20, 77] are believed to be the most reliable as they have used the most modern potentials.

After examining the measured broadening cross sections presented in this table, it becomes obvious why very enthusiastic predictions about the *potential* frequency stability of cryogenic hydrogen masers were once made [81, 15, 14]. The important parameter for this discussion is the spin-exchange broadening rate constant $\overline{v}_{HH}\overline{\sigma}_{HH}$. This parameter is nearly three orders of magnitude smaller at 1 K than it is at 300 K. If we only consider frequency instabilities due to the thermal photons in the maser resonator,[21] then the intrinsic instability of a maser $\delta f/f$ is proportional to $\left(\frac{k_B T}{P\tau}\right)^{\frac{1}{2}}$ where P is the output power of the maser and τ is the averaging time for the measurement. The stability of

[21]The phase of these photons will be at random with respect to the phase of the atomic coherence.

a maser obviously increases as the temperature of the resonator is lowered but it also increases as the power output is increased. The power output of a maser is limited by spin-exchange broadening and thus by going to low temperatures it *appears* that fantastic improvements in the intrinsic stability of the maser might be made.

This analysis is insufficient as it assumes that any frequency instabilities which are coupled to the atomic density can be neglected. At room temperature it is possible to tune out these density dependent shifts to a high degree of accuracy [72]. Unfortunately, as the temperature of the maser is lowered it becomes important to consider spin-exchange effects which are induced by the hyperfine interaction. These effects couple the oscillation frequency of the maser to the population of the individual hyperfine level populations in a way that cannot be simply eliminated. This point is illustrated in the next section.

Before leaving the semi-classical treatment of the hydrogen spin-exchange problem we note that Reynolds [22] has calculated the H-D spin-exchange broadening parameter $\overline{v}_{HD}\overline{\sigma}_{HD}$ in the DIS limit for temperatures in the range 1.0 to 1.5 K. He found that this rate constant was essentially independent of temperature over this narrow range and equal to[22]

$$\overline{v}_{HD}\overline{\sigma}_{HD} = 2.4 \times 10^{-10}\mathrm{cm}^3/\mathrm{s}\ . \tag{3.27}$$

This implies that the H-D spin-exchange cross section $\overline{\sigma}_{HD} = 140\ \text{Å}^2$ at 1 K. No measurements of this quantity at cryogenic temperatures have been made prior to the work presented in chapter 7.

Fully quantum mechanical picture

In the time since the first H-H spin-exchange theories were developed it was realized that non-adiabatic effects introduced by the hyperfine interaction could lead to changes

[22]There is a significant difference between the H-H and the H-D spin-exchange cross sections near 1 K. It is the H-H spin-exchange cross section which is anomalously small.

Temp (K)	$\overline{\lambda}_0$ (Å^2)	$\overline{\lambda}_1$ (Å^2)	$\overline{\lambda}_2$ (Å^2)	$\overline{\sigma}_0$ (Å^2)	$\overline{\sigma}_1$ (Å^2)	$\overline{\sigma}_2$ (Å^2)
0.39	-13.8	-2.41×10^{-2}	-1.06×10^{-2}	5.49×10^{-2}	0.560	0.554×10^{-3}
0.50	-11.8	-1.77×10^{-2}	-1.15×10^{-2}	4.09×10^{-2}	0.524	0.748×10^{-3}
0.63	-10.1	-1.29×10^{-2}	-1.25×10^{-2}	3.02×10^{-2}	0.484	0.972×10^{-3}
0.79	-8.46	-0.927×10^{-2}	-1.34×10^{-2}	2.21×10^{-2}	0.442	1.22×10^{-3}
1.00	-7.00	-0.650×10^{-2}	-1.41×10^{-2}	1.60×10^{-2}	0.400	1.49×10^{-3}
300	-0.90	0.36×10^{-2}	-0.67×10^{-2}	-0.26×10^{-2}	-0.60	12

Table 3.4: Calculated values of the thermally averaged H-H spin-exchange frequency shift and broadening cross sections in the Verhaar theory [77].

in the frequency shifts described in the previous section [82]. It was not until recently however that the fully quantum mechanical problem was addressed. B. J. Verhaar and his collaborators [19, 20] included the effects of interatomic and intraatomic hyperfine interactions as well as dipole terms in the H-H interaction Hamiltonian. Their results for spin-exchange collisions between H atoms display fundamental differences from the semiclassical picture presented above. These differences are particularly significant when applied to the operation of H masers at cryogenic temperatures. They showed that the frequency shift (equation 3.25) and the line broadening (equation 3.19) due to H-H spin-exchange collisions are actually of the form[23]

$$\omega - \omega_0 = \left[\overline{\lambda}_0(\rho_{cc} - \rho_{aa}) + \overline{\lambda}_1(\rho_{cc} + \rho_{aa}) + \overline{\lambda}_2\right] \overline{v}_{HH} n_H \tag{3.28}$$

$$\frac{1}{T_2^{se}} = \left[\overline{\sigma}_0(\rho_{cc} - \rho_{aa}) + \overline{\sigma}_1(\rho_{cc} + \rho_{aa}) + \overline{\sigma}_2\right] \overline{v}_{HH} n_H \tag{3.29}$$

Table 3.4 contains a summary of calculated values for the thermally averaged frequency shift ($\overline{\lambda}_i$) and broadening ($\overline{\sigma}_i$) cross sections at temperatures relevant to room temperature and cryogenic H masers [77].

To assess the influence of spin-exchange collisions on the oscillation frequency of a

[23]In reference [83] it is shown that in the presence of a strong magnetic field further terms $\overline{\lambda}_3$ and $\overline{\sigma}_3$ which couple to ρ_{bb} and ρ_{dd} must be added to these expressions. These additional terms are of no consequence for a hydrogen maser operating near zero field.

hydrogen maser it is necessary to add the effects of cavity pulling which were described in the previous chapter (equation 2.39) to the spin-exchange frequency shift 3.28. The combined frequency shift is

$$\omega - \omega_0 = \frac{\Delta}{T_2} + \left[\overline{\lambda}_0(\rho_{cc} - \rho_{aa}) + \overline{\lambda}_1(\rho_{cc} + \rho_{aa}) + \overline{\lambda}_2\right] \overline{v}_{HH} n_H \tag{3.30}$$

where Δ is the detuning of the resonator from the atomic resonance defined in equation 2.36. If we define

$$\beta = \frac{4\overline{v}_{HH}}{\hbar(\gamma_e + \gamma_p)^2 \mu_0 \eta Q_\ell} \tag{3.31}$$

then the population inversion $n_H\,(\rho_{cc} - \rho_{aa})$ inside the maser bulb (equation 2.42) can be written

$$(\rho_{cc} - \rho_{aa})\,\overline{v}_{HH} n_H = \beta\left(1 + \Delta^2\right)\frac{1}{T_2}\,. \tag{3.32}$$

We now assume that the only density dependent part of the linewidth is that due to spin-exchange collisions, *i.e.*

$$\frac{1}{T_2} = \frac{1}{T_0} + \left[\overline{\sigma}_0(\rho_{cc} - \rho_{aa}) + \overline{\sigma}_1(\rho_{cc} + \rho_{aa}) + \overline{\sigma}_2\right] \overline{v}_{HH} n_H\,. \tag{3.33}$$

All other contributions to the linewidth are contained in the term T_0. As a result of the dynamics of an oscillating maser the difference $(\rho_{cc} - \rho_{aa})$ is much smaller than the sum $(\rho_{cc} + \rho_{aa})$. The broadening term proportional to $(\rho_{cc} - \rho_{aa})$ is thus very small and can be neglected. The full expression describing the combined spin-exchange/cavity pulling frequency shift of an oscillating H maser can thus be written :

$$\begin{aligned} \omega - \omega_0 \;=\; & \left[\Delta + \beta\overline{\lambda}_0(1 + \Delta^2)\right]\frac{1}{T_0} \\ & + \left\{\left[\Delta + \beta\overline{\lambda}_0(1 + \Delta^2)\right]\left[\overline{\sigma}_1(\rho_{cc} + \rho_{aa}) + \overline{\sigma}_2\right] + \left[\overline{\lambda}_1(\rho_{cc} + \rho_{aa}) + \overline{\lambda}_2\right]\right\}\overline{v}_{HH} n_H\,. \end{aligned} \tag{3.34}$$

In general the dependence of this frequency shift on the atomic density is quite complicated. The essential point which should be noted is that it depends upon the density in

a nonlinear way. Various schemes which minimize the coupling between the oscillation frequency and the atomic density have been discussed [20, 84, 17]. The details of the various strategies are beyond the scope of this thesis.

The corrections to the semi-classical H-H spin-exchange frequency shift parameters are small. It is doubtful that these parameters could be measured without utilizing the narrow linewidth and the frequency stability of a hydrogen maser. In a maser operating at room temperature, the absolute spin-exchange induced frequency shifts are typically less than 1 mHz. A measurement of the various spin-exchange cross sections at room temperature by detecting *changes* in these shifts as parameters such as the tuning of the resonator are varied would be a very difficult task. At low temperatures one gains somewhat as the atomic densities are increased dramatically over those in a conventional room temperature maser. In the following two chapters we describe such a measurement using a cryogenic hydrogen maser.

Chapter 4

Apparatus used for the 0.5 K Experiments

In this chapter we describe the apparatus used to explore the influence of H-H spin-exchange collisions on the operation of the cryogenic hydrogen maser (CHM). In particular, these experiments were designed to test the H-H spin-exchange theory developed by Verhaar *et al.* [19, 20] and its applicability to the CHM. On occasion we refer to them as the '0.5 K experiments' in contrast to the higher temperature experiments presented later in the thesis.

The maser to which we refer is the CHM designed and built at the University of British Columbia (UBC) by Drs. Martin Hürlimann, Walter Hardy and Richard Cline. A complete description of the design, construction and operation of this device would be far too lengthy to be presented here. Several papers [9, 85, 42, 16] containing this, and related information have been published but by far the most complete and informative document is the PhD thesis of Martin Hürlimann [17]. In this chapter the only aspects of the maser which are addressed are those directly related to the spin-exchange measurements presented in the following chapter.

4.1 The UBC CHM: Conventional mode of operation

A conventional room temperature H maser requires a source of atomic hydrogen, a state selector (magnet) which directs atoms in the $|\ c\ \rangle$ state (often both the $|\ c\ \rangle$ and $|\ d\ \rangle$ states) into a storage bulb located within a high Q microwave cavity tuned to the a-c hyperfine transition of H. These regions are shown schematically in figure 4.1. A

minimum (threshold) flux of H atoms in the | c ⟩ state is required for stimulated emission of radiation to occur[1]. Some of the power radiated by the atoms can be extracted from the cavity and fed to external monitoring circuitry. The atoms eventually wander out of the storage bulb with a time constant typically of order a fraction of a second, and are pumped out of the system.

The UBC CHM is unlike conventional H masers in that it recirculates the H atoms. It makes use of the fact that the recombination lifetime of H atoms confined by ℓ-^{4}He walls at 0.5 K is of order hundreds of minutes at typical masing densities of 10^{12} cm^{-3}. Rather than being pumped away, atoms which have left the maser storage bulb are allowed to return to the state selection region of the maser where they are pumped to the upper (| c ⟩) state. In this way, the same atoms are repeatedly cycled through the maser.

There are 5 basic regions inside the UBC CHM (see figure 4.2). All internal surfaces are coated with a film of superfluid ^{4}He in order to suppress the recombination of atomic H. A consequence of this film being present is that the maser volume is filled with a buffer gas of ^{4}He whose density is a strong function of temperature. A low temperature atom source [27] uses a pulsed 50 MHz discharge to provide bursts of atomic H. The source contains a small Co^{60} source whose β radiation provides excess free charges which greatly facilitate initiation of the discharge. Typically, only a few pulses (of roughly 10 μs duration, 0.4W peak power) are required to obtain a H density high enough to operate the maser. A large buffer volume[2] acts as a low pass filter to 'smooth out' the bursts of atomic H produced by the source. It also reduces the area/volume ratio of the assembly which in turn increases the lifetime of the H atoms. The density within the maser can be maintained at any desired value within its operating region by modifying the discharge pulse duration and repetition rate[3]. Atoms from the source/buffer volume region are bled

[1] i.e. dissipative losses in the cavity must be overcome.
[2] This volume was added for the present experiments.
[3] A constant trickle of H is required to compensate for the loss of hydrogen due to recombination.

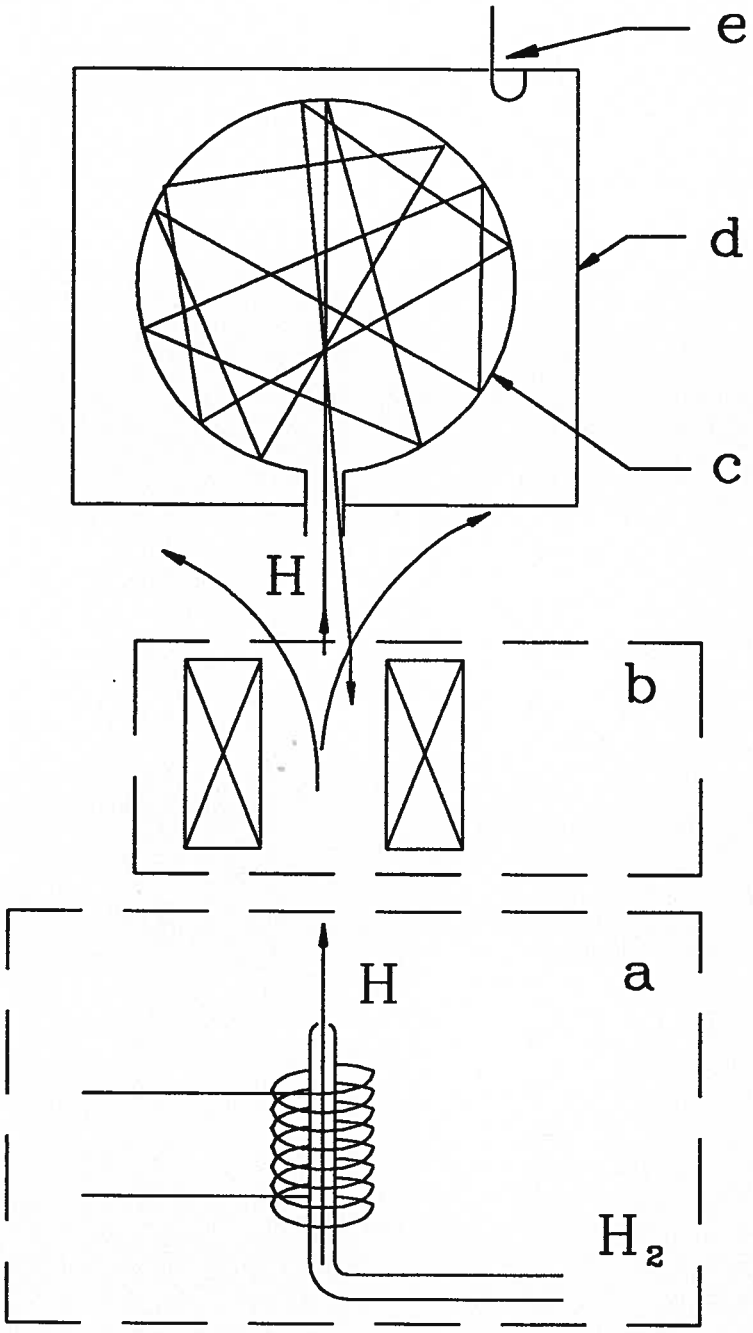

Figure 4.1: A schematic representation of the basic components of a room temperature H maser showing (a) the rf discharge/atomic source, (b) state selector, (c) storage bulb, (d) microwave cavity and (e) coupling loop.

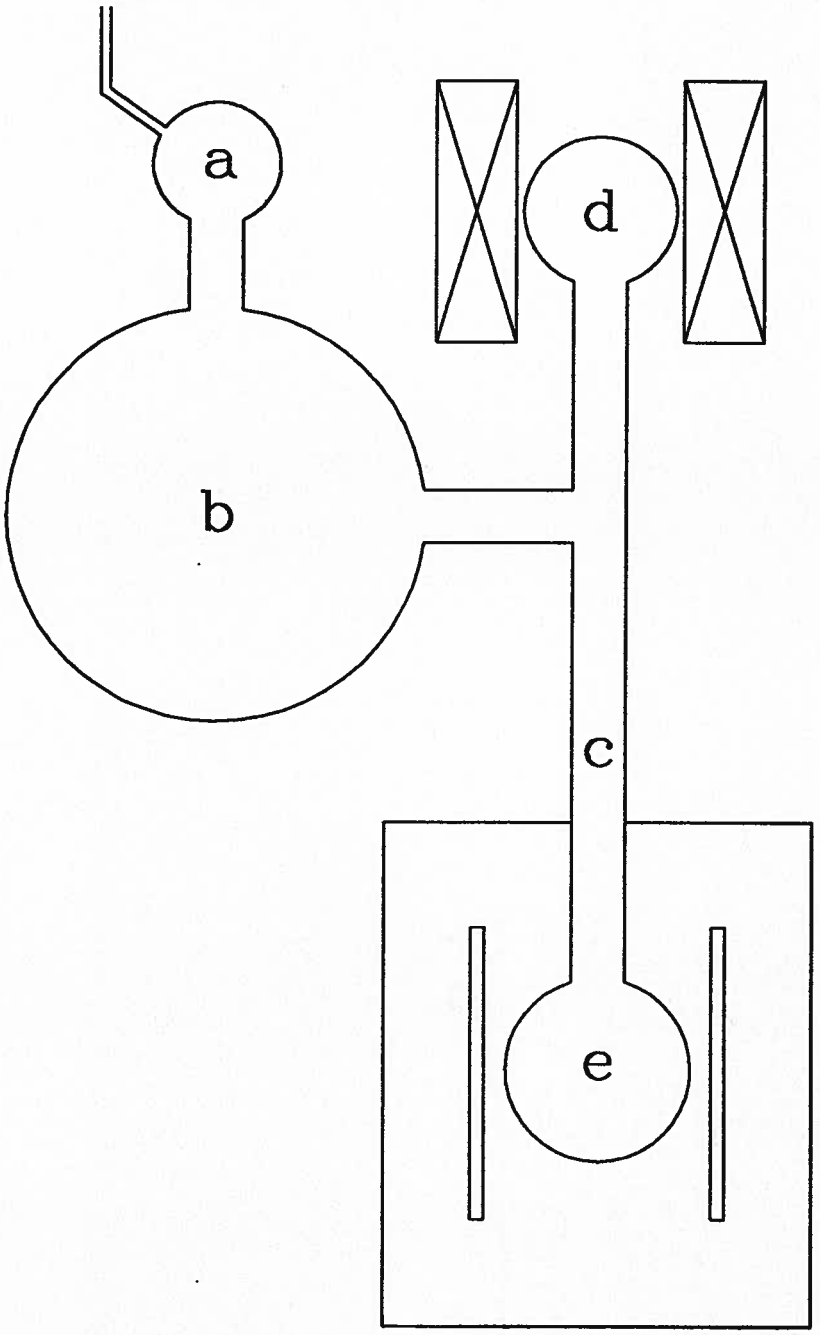

Figure 4.2: A schematic representation of the UBC cryogenic hydrogen maser showing (a) the low temperature atomic source (discharge), (b) buffer volume (added for the present experiments), (c) atom tube, (d) state selector region, and (e) the storage bulb inside the 1420 MHz split-ring resonator. The atom tube and the storage bulb are shown in more detail in figure 4.3.

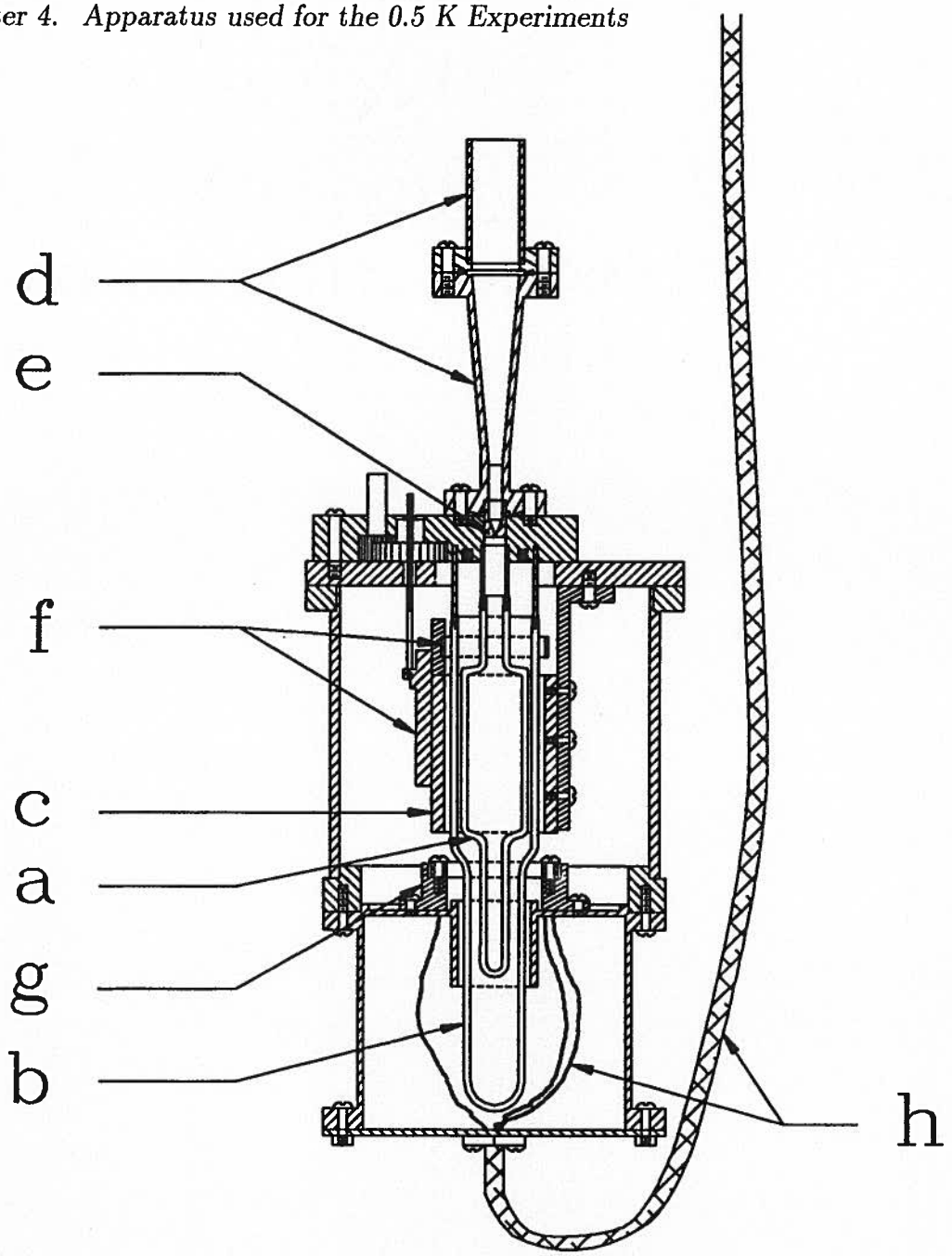

Figure 4.3: Details of the split-ring resonator and maser storage bulb region showing (a) the inner (storage) bulb, (b) outer bulb, (c) split-ring resonator, (d) atom tube and brass cone, (e) orifice, and (f) the mechanical tuning and coupling assembly (coaxial feed line not shown). Also shown is (g) the placement of the electronic Q spoiler/tuning arrangement which is detailed in figure 4.4 and (h) the bias leads for this assembly.

into the maser proper which consists of an additional three volumes. The maser bulb is a 5 cm^{-3} cylindrical pyrex bulb placed concentrically inside a slightly larger pyrex bulb which is filled with ℓ-^{4}He (see figure 4.3 for details of the maser resonator and storage bulb regions). This helium bath provides good thermal contact between the inner bulb and the resonator housing. Atoms enter the inner bulb (storage bulb) through a small orifice which results in a mean atom residency time inside the bulb of about 0.8 seconds at 0.5 K. The two bulbs are axially located inside a split-ring resonator [86] tuned to the zero field hyperfine transition of atomic hydrogen at 1420 MHz. The resonator is capacitively tuned by moving a teflon/Cu plate near the gap in the ring. This assembly is housed within a cylindrical Cu can with sealed ends to eliminate radiative electromagnetic losses from the resonator and thus maintain its Q. The temperature of this housing is regulated about 100 mK higher than the mixing chamber temperature.

The state selector region (not shown in figure 4.3) contains a 39.46 GHz cylindrical cavity operating on the TM_{010} mode. It is located inside a superconducting solenoid made from Cu clad NbTi wire which produces the longitudinal field (about 1.5 Tesla) necessary to bring the desired ($|$ b $\rangle$ to $|$ c $\rangle$ or $|$ a $\rangle$ to $|$ d $\rangle$) hyperfine transition into resonance at this frequency. The fringing fields from this solenoid draw high field seeking atoms ($|$ a $\rangle$ and $|$ b $\rangle$) into the cavity and sweep away atoms in the low field seeking states ($|$ c $\rangle$ and $|$ d $\rangle$). Atoms entering this cavity must pass near thin sheets of metallic foil impregnated with magnetic impurities having a mean spacing of a few hundred Å [17, 87, 88]. This spacing is chosen such that at typical thermal velocities, the H atoms see time varying magnetic fields with a substantial Fourier component at the $|$ a $\rangle$ to $|$ b $\rangle$ hyperfine transition frequency in the local field. In effect the magnetic impurities act as a relaxing mechanism which tries equalize the populations of the $|$ a $\rangle$ and $|$ b $\rangle$ states entering the state selector. By tuning the magnetic field to 1.43 Tesla, $|$ b $\rangle$ state atoms entering the cavity can be subsequently pumped up to the $|$ c $\rangle$ state. The geometry of

the entrance to the cavity is designed such that when atoms drift out of the state selector region, they are less likely to pass near the relaxing foil. Once out of the fringing fields of the solenoid, the $|\ c\ \rangle$ state atoms drift down the atom tube towards the storage bulb. The lower end of the tube and the storage bulb/resonator assembly are shielded from the solenoid fields by a superconducting Pb shield (not shown in figure 4.3).

Atoms entering the storage bulb eventually wander out again and, if they are in the high field seeking states, can be drawn back into the state selector and recycled. The mean free path of these atoms is determined by scattering from the ^{4}He gas within the maser. The atom tube and state selector are typically run about 100 mK colder than the maser bulb. This temperature gradient is maintained across a short, conical length of brass tubing located at the end of the atom tube where it constricts to form the orifice leading to the maser bulb (figure 4.3). As a result, H atoms leaving the maser bulb experience a mean free path which increases as they move away from the orifice. This reduces the likelihood of an atom leaving the storage bulb and reentering within a time period comparable to the mean bulb holding time.

The UBC CHM operates with atomic densities in the 10^{11}cm^{-3} to 10^{12}cm^{-3} range. Just above threshold the maser power increases linearly with n_H. As the density is increased, spin exchange collisions both broaden the resonance and reduce the population inversion (T_2 and T_1 processes). Eventually the output power of the maser reaches a maximum and then decreases to zero. The maser has been run at temperatures spanning 230 mK to 660 mK. The fractional frequency stability of the device has been measured [17] to be $6.3 \pm 3.7 \times 10^{-14}$ over an averaging time of 1 second. This is better than the performance of the best conventional masers.

4.2 The UBC CHM: Modifications for spin-exchange measurements

The spin-exchange frequency shifts and line broadening of the cryogenic hydrogen maser are characterized by 6 parameters ($\overline{\lambda}_i$ and $\overline{\sigma}_i$) in the theory developed by Verhaar *et al.* [19, 20]. In order to measure these parameters (or combinations thereof) at a given temperature, it is necessary to independently vary the atomic density, the cavity Q and the cavity tuning. The H density is easily varied[4] by changing the repetition rate and the power of the rf discharge. The buffer volume (260 cm^3) mentioned in the last section was added for the present measurements to filter out bursts of H from the source and thus to help maintain a constant n_H. The most important modifications to the maser for the purposes of making these measurements were the addition of electronic tuning and Q spoiling devices. These modifications are described below.

4.2.1 Electronic tuning/Q spoiler

The split-ring assembly is located inside a cylindrical Cu housing with sealed ends to keep electromagnetic radiative losses from degrading the resonator Q. The unloaded Q of this system was about 2800 [17] prior to the installation of the tuning/Q spoiling system described below.

For the spin-exchange measurements a 2.591 cm o.d., 1.956 cm i.d. ring with a square cross section was fabricated from OFHC Cu. This ring was cut into two semicircular halves. Enough material was removed from each face of the cut so as to form a small gap in the annulus when reassembled. The four corners of each face were rounded off in order to reduce the gap capacitance. On one half of the ring, holes were drilled and tapped on both faces in order to mount two Frequency Sources GC51105-57 varactor diodes[5].

[4]Note that while n_H can be varied, there is no control over the occupancy of the individual hyperfine states.

[5]Frequency Sources, 16 Maple Road, Chelmsford MA 01824. These devices have a nominal capacitance of 0.6 pF with a bias potential of -4 V, and 1.6 pF at -15 V.

The other half annulus was split into two equal pieces along the radius and this gap was filled with a 0.015 cm teflon spacer. Mounting holes were drilled in each Cu piece so that the ring could be reassembled on a teflon holder. This support was designed to hold the axis of the ring concentric with the split-ring and 0.874 cm below its lower end. Prior to the final assembly of this device all Cu pieces were gold plated. Small flexible strips of Cu sheet were silver epoxied between the diodes and the other two quarters of the tuning ring. These metallic strips accommodate the motion of the ring due to the thermal contraction of the teflon holder, and also provide electrical contact to the diodes so that bias potentials can be applied. This assembly is shown in figure 4.4.

The capacitive gap between the two quarter sections of the ring was bridged between the drain and the source of an NEC 720 FET packaged in a hermetically sealed PLCC package.[6] Prepackaged devices contain enough magnetic material that it was necessary to purchase the dies and do our own packaging. This assembly was then mounted on the teflon support structure adjacent to the tuning ring.

Electrical contact was made to each of the Cu section of the annulus and the gate of the FET using Fluorosint graphite leads[7] fed up from beneath the teflon support structure. These leads have a resistivity of about 2 kΩ per cm at 300 K and 3.5 kΩ per cm at 4.2 K. We have coaxially encased them in Cu braids so that they can be brought into the resonator volume without seriously degrading its Q.

The ring geometry is chosen such that the structure has its lowest resonance around 1900 MHz. By changing the bias potential V_t which is applied to the varactor diodes, the resonant frequency of the loop is changed, pulling the frequency of the split-ring resonator; the maximum attainable tuning range for our geometry is about 500 kHz (about 30% of the FWHM of the cavity resonance) at 0.5 K. By changing the bias potential V_q which

[6]Kyrocera America, 5701 NE Fourth Plain Blvd. Vancouver WA 98661 : part numbers PB45238 and KE77004-1

[7]The Polymer Corporation, 2140 Fairmont Ave, Reading PA 19603

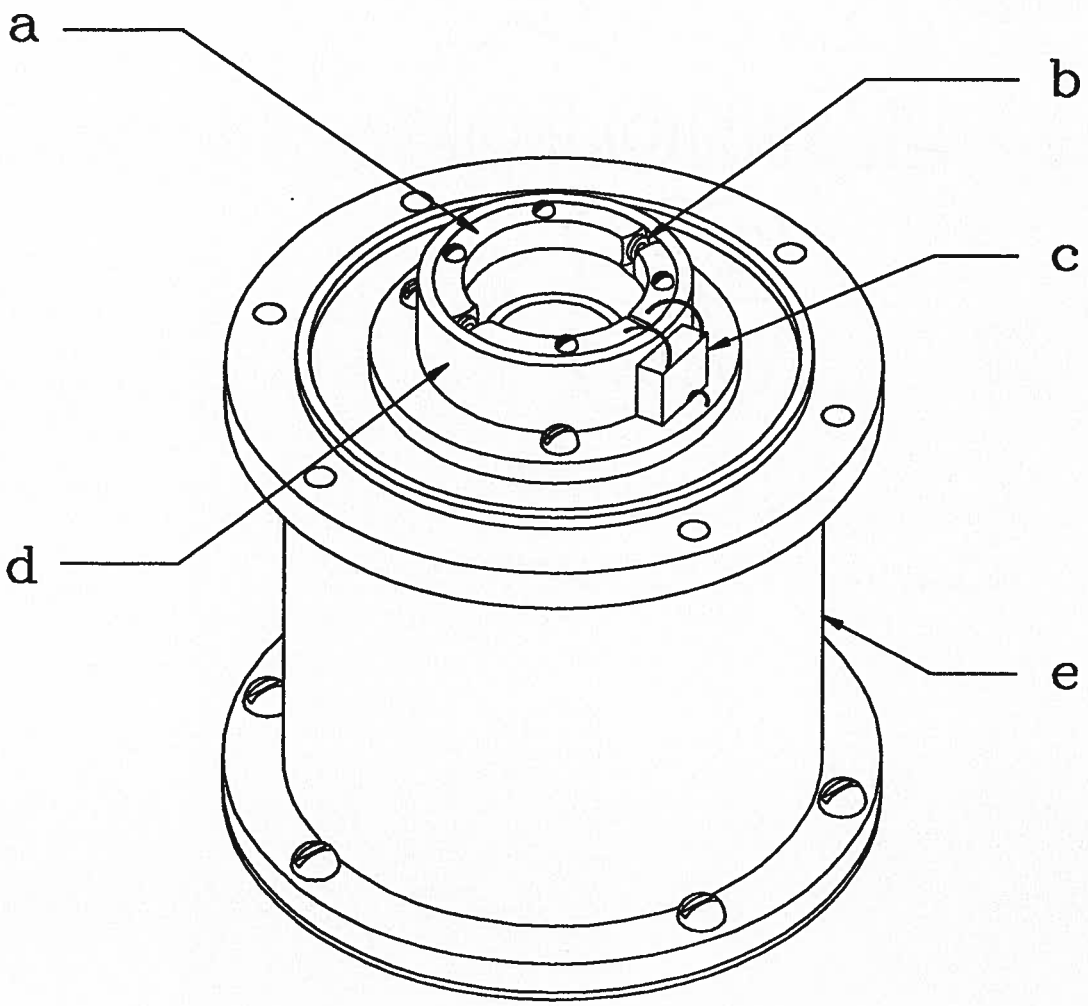

Figure 4.4: The tuning ring/Q spoiler shown mounted on the base of the Cu can which encases the split-ring structure (see figure 4.3). The Cu can below the ring is simply a housing for the graphite leads used for biasing the semiconductor devices and a thermal shield. Details show (a) the Cu ring (3 sections), (b) the varactor diodes (two), (c) the FET bridging a teflon filled capacitive gap, (d) the teflon support structure for the ring, and (e) the Cu base. The graphite bias leads individually encased in Cu braid are not shown.

is applied to the FET (essentially a variable resistance in the tuning ring) the Q of the tuning structure can be changed. This Q spoiler serves to reduce the Q of the split-ring from about 820 (the maximum low temperature Q after the modifications described above) to a minimum value around 570.

The tuning and Q spoiling functions of the ring are not completely independent of each other. By measuring both the resonator Q and tuning as a function of the two bias potentials a two dimensional mapping can be made from which lines of constant Q or constant tuning can be derived. A typical mapping is shown in figure 4.5. The reproducibility of a particular setting is better than the detection limit for both the resonator Q and the resonant frequency.

4.3 State selection

In all of the work reported prior to the present experiments the | a ⟩ to | b ⟩ to | c ⟩ pumping scheme (reliant upon the relaxing foil) described earlier was used. Computer simulations have indicated [17] that the efficiency of the state selection process was in fact bottlenecked by the production of | b ⟩ state atoms by the relaxing foil. As a result, the flux of | c ⟩ state atoms entering the maser bulb was a rather insensitive function of the tuning of the microwave radiation used to pump | b ⟩ state atoms into the | c ⟩ state.

In order to measure the atomic density inside the maser bulb[8], the pumping microwaves were swept off resonance, stopping the flux of | c ⟩ state atoms into the maser bulb and causing a cessation of maser action. Magnetic resonance techniques were then used to determine the atomic density inside the storage bulb. After this the microwave pump was swept back onto resonance and maser operation reestablished. Because of the aforementioned bottleneck, the reproducibility of the initial conditions was not limited

[8]This measurement is discussed in more detail in the next chapter.

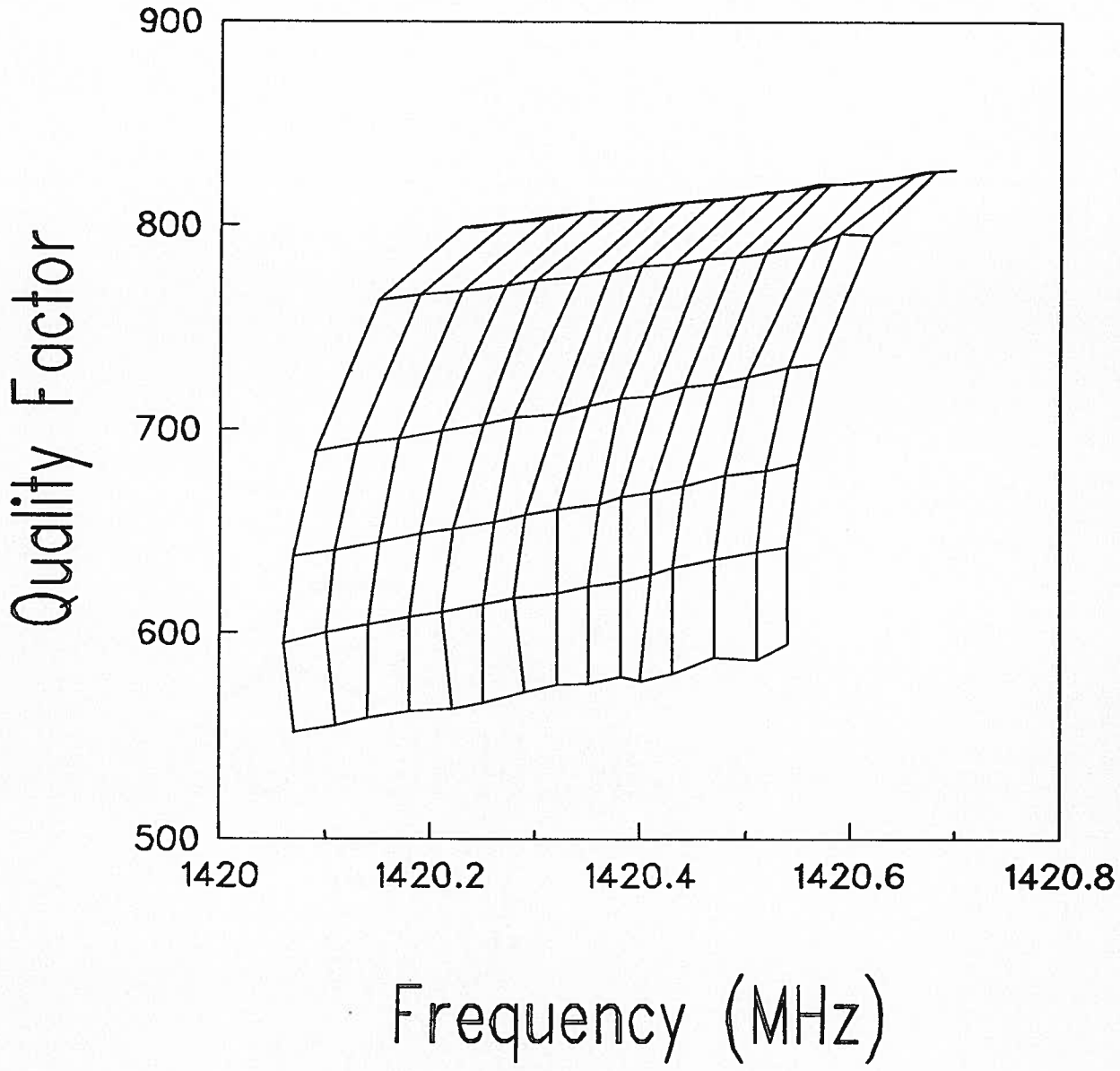

Figure 4.5: A typical mapping of the resonant frequency and the quality factor of the 1420 MHz split-ring resonator as a function of the bias potentials on the varactor diodes (V_t) and the Q spoiling FET (V_q). 'Horizontal' lines correspond to lines of constant V_q and 'vertical' lines to constant V_t. Interpolation allows one to derive combinations of V_t and V_q which produce lines of constant tuning or constant Q.

by either the stability or the reproducibility of the frequency and power of the microwave pump.

Prior to the present experiments new relaxing foil was manufactured and installed in the hopes of improving the efficiency of the state selection process. The modification indeed seemed to remove the bottleneck, however it was found that the operating conditions were now much more sensitive to the stability and the tuning of the microwave pump[9]. Several modifications were necessary in order to improve the reproducibility of the maser operating conditions after making a measurement of n_H. These modifications are outlined below.

4.3.1 New pumping scheme

It has been known for a considerable length of time [17] that the present version of the UBC CHM has considerable cross relaxation between the upper three hyperfine states due to some relaxing mechanism (magnetic impurity) believed to be located near the orifice connecting the maser bulb to the atom tube. Repeated attempts to find and eliminate the source of this relaxation have failed. In this work we have adopted a new pumping scheme which makes use of this cross relaxation. Rather than pumping the $|\,b\,\rangle$ to $|\,c\,\rangle$ transition in the state selector we have decreased the magnetic field slightly in order to pump the $|\,a\,\rangle$ to $|\,d\,\rangle$ transition. This procedure circumvents the relaxing foil as a state selection mechanism. In this situation, atoms which approach the storage bulb are predominately $|\,d\,\rangle$ state atoms, however the strong cross relaxation near the entrance to the bulb ensures that the $|\,c\,\rangle$ state is populated inside the bulb.

[9]The measured sensitivity is consistent with the estimated field inhomogeneities in the solenoidal field of the NbTi magnet ($\frac{\Delta B}{B} \approx 7 \times 10^{-4}$).

4.3.2 Frequency stability

The microwaves used in the state selector are generated by a Micro-Power model 221 backwards wave oscillator (BWO). Instead of letting this device operate under free running conditions as in previous work[10], we have frequency stabilized it using a high quality 5 MHz quartz crystal oscillator[11] (see figure 4.6). This was done by generating a 2.47 GHz signal (LO) with a HP 8662A frequency synthesizer phase locked to the output of the quartz crystal and then mixing this with the output of the BWO at 39.5 GHz (RF). The 16th harmonic of the LO signal is offset from the RF by 50 MHz and produces an IF signal which is fed into a HP 5342A microwave frequency counter with a digital to analogue converter. The analogue output of the counter was used to lock the output frequency of the BWO to within a few tens of kHz. The output power of the BWO was monitored using a directional coupler and a diode detector at the top of the cryostat. Power levels were maintained constant to within about 1% throughout the experiments.

Rather than stopping the maser by sweeping the microwaves off resonance as done previously, in the present work a resistive attenuator card could be inserted through a slot in the broad wall of the Ka band waveguide leading down into the refrigerator. This gave about 20 dB of attenuation which is more than sufficient to stop the pumping action in the state selector. The insertion of this card was actuated by a mechanical relay.

4.4 Refrigeration, temperature monitoring and control

The UBC CHM is mounted inside an Oxford Instruments (Special) Model 400 dilution refrigerator with a home made dilution unit. Typically it runs at temperatures around 0.5 Kelvin (at or near the temperature at which the frequency shifts due to the wall and

[10]Previously this procedure was not necessary as the state selection process was bottlenecked by the relaxing foil and thus n_H was insensitive to the frequency of the pump microwaves.

[11]Oscilloquartz OSA model 8600.03 BVA very high stability model

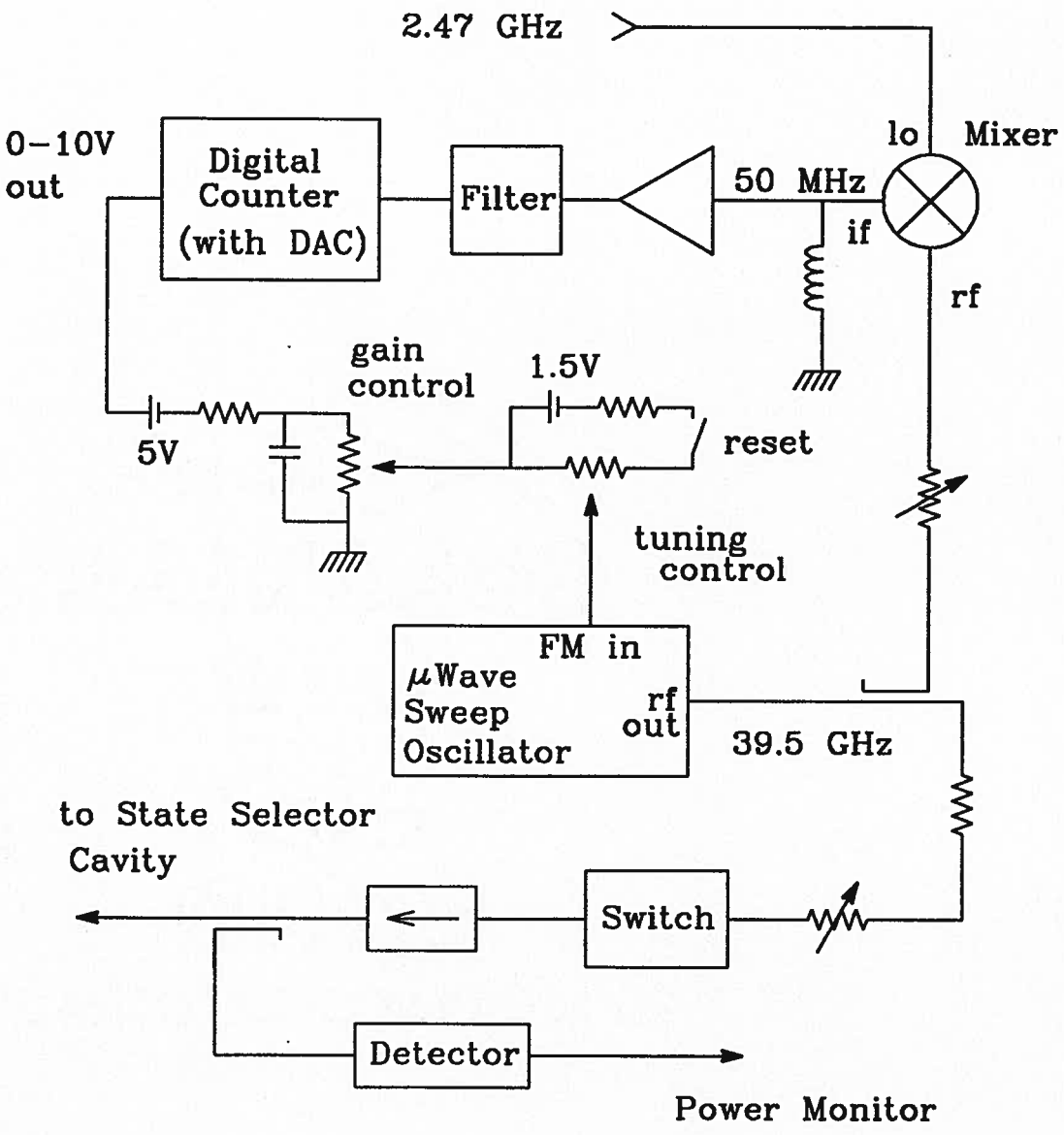

Figure 4.6: Method used to stabilize the microwave pump frequency used in the atomic state selection process. Details are described in the text.

the buffer gas shifts pass through a minima). The atom source is thermally attached to a special heat exchanger and run at temperatures near 0.4 K. The state selector is mounted on the mixing chamber (MC) of the refrigeration unit and run at temperatures about 100 mK lower than the actual maser bulb (discussed previously). The temperature of the state selector is monitored by a carbon resistance thermometer. The temperature of the state selector is also regulated using this resistor. The temperature of the MC is monitored and regulated using a calibrated germanium resistance thermometer. The temperature of the inner maser bulb is governed by the temperature of the ^{4}He bath in the outer bulb which is in turn thermally linked to the Cu resonator and housing via a volume of Ag sinter. This temperature is also monitored and regulated with a calibrated germanium resistance thermometer.

4.5 1420 MHz spectrometer

The magnetic resonance experiments described in this thesis were all performed using a two stage heterodyne detection system combined with a gated pulse generator. This system was originally designed by W. N. Hardy and has been used in other experiments with atomic H [17, 27]. The spectrometer design is sketched in figure 4.7. We describe the basic principle of operation in the text below. Details specific to the experiments performed at 0.5 K are described in the next section. Details pertaining to the experiments with H, D mixtures near 1 K are given in chapter 6.

The system is based upon two local oscillator signals derived from either a 10 MHz Rb frequency standard[12] or a high quality quartz crystal oscillator[13]. A signal at 1420 MHz is obtained by direct frequency multiplication ($\times 2$, $\times$ 71) of the frequency reference. The 405 kHz signal is synthesized from the same reference using a phase locked HP3330A

[12]Efratom model FRK-L Rb frequency standard, on loan from D. Wineland, NIST Boulder CO.
[13]Oscilloquartz OSA model 8600.03 BVA ultra high stability

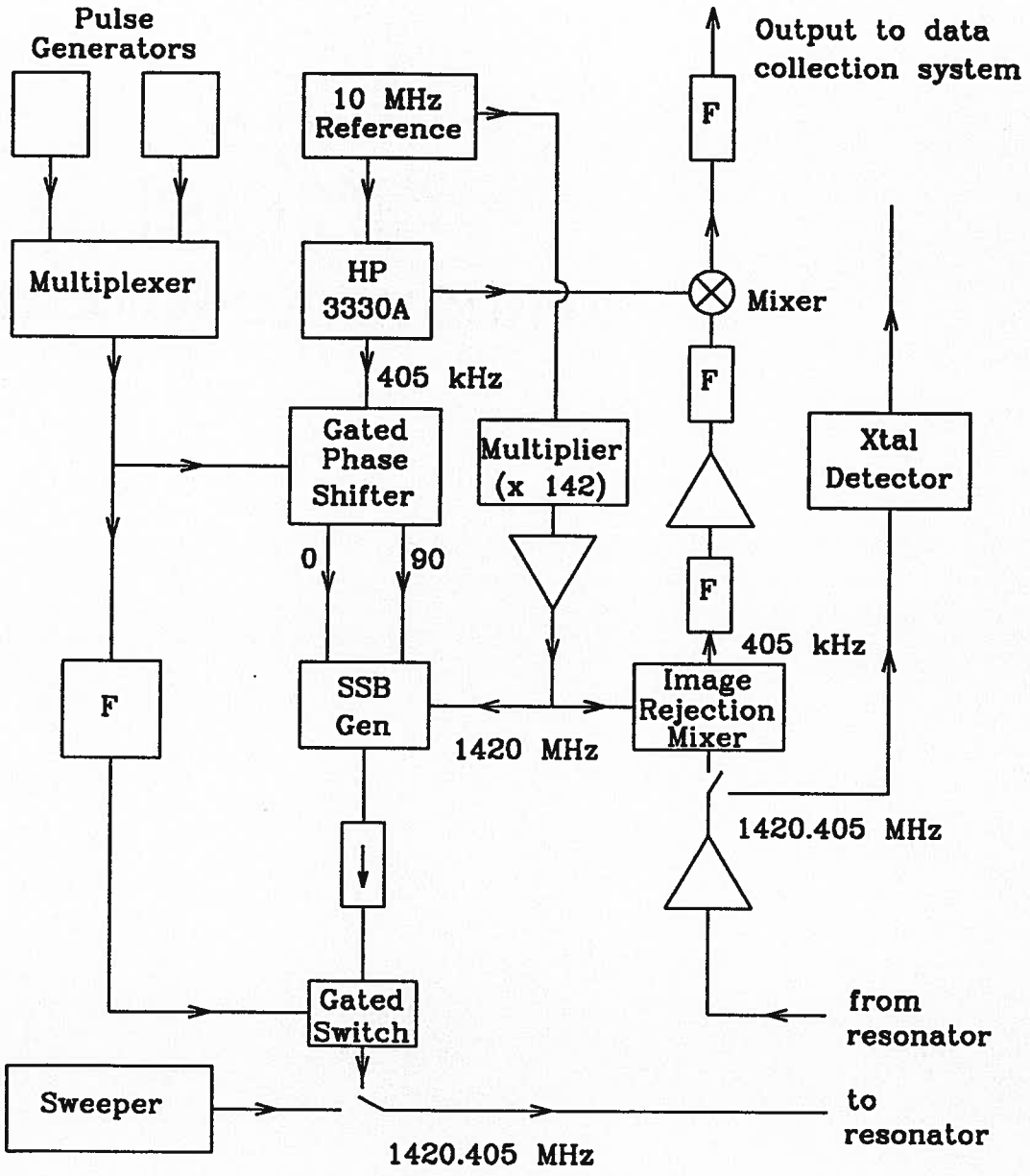

Figure 4.7: A schematic diagram of the 1420 MHz pulsed magnetic resonance spectrometer used in these experiments. 'F' is used to label the various filters. The operation of this device is described in the text.

frequency synthesizer.

An rf signal at the hyperfine frequency of atomic H is derived from these two local oscillator signals using a single sideband generator. Externally generated pulses of varying widths are then multiplexed and used to gate this signal. In order to avoid the possibility of interference at the sum frequency (1420.405 MHz) the phase shifter which is used to produce the two phases of the 405 kHz for the SSB is also gated. As a result, the 1420.405 MHz signal is only produced during the application of the external pulses. This system allows one to produce coherent pulse sequences such as $\pi/2$ pulses or π-$\pi/2$ sequences.

Rf power emitted by the atomic system[14] is first amplified and then mixed with the LO at 1420 MHz in an image rejection mixer[15]. This signal is then filtered, amplified, and mixed with the second LO at 405 kHz. The frequency of this LO is adjusted to produce a convenient beat frequency (near 10 Hz) which is fed to the data acquisition system.

In order to set the tuning and the coupling of the resonator, provision is made to inject a swept frequency signal into the cavity. The reflected signal is monitored using a crystal detector. Absolute power calibrations are performed using a HP435B power meter.

4.5.1 Data acquisition

In the experiments performed at 0.5 K the reference frequency we used was derived from a second 5 MHz high quality quartz crystal oscillator[16] loosely phase locked to a Rb time standard. The crystal oscillators are (commercially) packaged in temperature regulated dewar flasks and have fractional frequency stabilities better than 5×10^{-13}

[14]This is either the free induction response of the atoms to some pulse sequence, or a cw maser signal.

[15]Using this procedure the response signal at 405 kHz does not contain noise from the rf signal at 1419.595 MHz.

[16]Oscilloquartz OSA model 8600.03 BVA ultra high stability

for averaging times in the 0.1 to 10 second range. We have packaged these devices in a second temperature regulated/insulated Al can which can be evacuated and sealed in order to pressure regulate the devices. Cooling and temperature regulation is provided by a temperature regulated water bath which circulates water through a heat exchanger. By using the Rb time standard as a flywheel we were able to improve the long term stability of the combination without seriously degrading the short term stability of the quartz crystal. The stability of the combination is about 1 part in 10^{12} over time periods comparable to the duration of the experiments and hence limits our practical frequency resolution to about 1 mHz.

The gated output from the spectrometer is derived from the crystal oscillator/Rb clock combination. The pulsed signal is fed down a coaxial line to a 20 dB directional coupler mounted on top of the main vacuum can of the dilution refrigerator (T$\approx$4.2 K). This coupler feeds the signal down to the maser cavity through another coaxial line. The reflected and/or emitted signal from the maser cavity is amplified using a GaAs based preamplifier[17] operating at 4.2 K before being brought up to room temperature. The gain of this device is 18.1 dB at 4.2 K with a 3 dB bandwidth of 395 MHz and a noise temperature of 20 K. A second directional coupler is used to inject calibrated signals for absolute power calibrations of the system. These components are shown in figure 4.8

The output of the final mixer stage of the spectrometer is fed to a Nicolet 1170 signal averager, an HP 5345A frequency counter and an HP 3478A ac voltmeter. The signal averager is used for general purpose data acquisition including FID's from pulsed magnetic resonance experiments and Q curves from swept frequency reflection measurements of the 1420 MHz resonator response. Both types of signals are subsequently transferred to a computer for further analysis. The maser output power is determined from the amplitude of the ($\approx$ 10 Hz) beat frequency between the maser signal and the two LO's in the

[17]based on a design by Williams *et al.* [89].

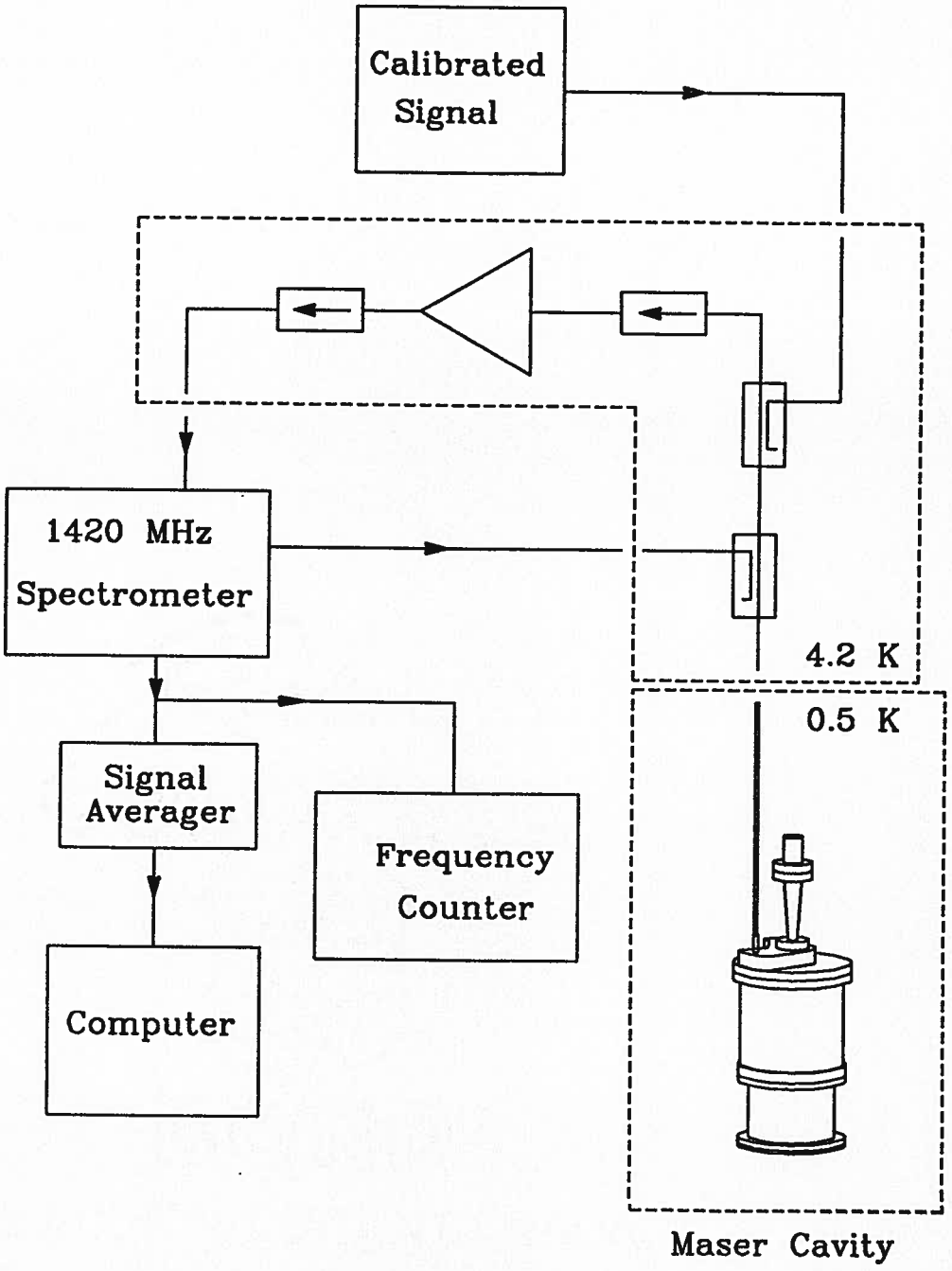

Figure 4.8: A schematic diagram of the rf wiring and data acquisition system for the 0.5 K experiments.

1420 MHz spectrometer. This measurement is made with the ac voltmeter. This beat signal is also fed to the frequency counter in order to determine the oscillation frequency of the maser.

4.5.2 Measurement of Q and Δ

Due to limited access to the maser we were forced to measure the resonator Q and resonant frequency in reflection rather than in transmission. Swept frequency measurements of the reflected signal were fed to a HP 8473B crystal detector operated in the square law region. The curves were numerically fit to a single Lorentzian lineshape with a sloping background, the width and position of which gave the Q of the cavity and its detuning from the atomic resonance.

This technique is inherently susceptible to distortion induced by standing waves in the external circuitry. In order to evaluate these measurements we have performed extensive computer simulations of the measurement technique using a commercial simulation program[18]. The s parameters of all components in the circuit were measured using an HP 8754A/H26 RF Network Analyzer and used as input parameters to the models. Care was taken to evaluate effects due to the changing ℓ-^{4}He level in the main bath of the refrigerator as well as the effects of room temperature changes of the effective length of (teflon dielectric) coaxial cables in the measurement circuit. The results of this study suggest that our measurements of Q are accurate to about 1%. The reproducibility of individual measurements is considerably better than this. Estimates of the accuracy and the precision of the measurement of the cavity tuning are discussed in the next chapter.

[18]EESOF Inc. (5795 Lindero Canyon Rd, Westlake Village, CA 91362 USA) 'Touchstone' and 'Libra' microwave simulation programs.

Chapter 5

The 0.5 K H-H Spin-Exchange Measurements

The results described in this chapter represent the culmination of a considerable effort at UBC to attempt to test the predictions of the H-H spin-exchange theory proposed by B. J. Verhaar *et al.* [19, 20]. These predictions impose rather severe limits on the ultimate frequency stability of the CHM. At the same time, the sensitivity of the predicted shifts to the details of the H-H interaction potential suggests that by studying the shifts, delicate refinements to the potentials might be possible. For these reasons an experimental verification of the sensitivity of the oscillation frequency of the CHM to the atomic density is of considerable technological importance as well as theoretical interest.

Unfortunately much of this work was frustrated by poor workmanship in the construction of the commercial dilution refrigerator in which the CHM was housed. Several attempts to study these frequency shifts were made over a period of a few years and in each case the experimental runs were thwarted by problems associated with the refrigeration system. After several rather drastic measures aimed at repairing the malfunctioning refrigerator, it was possible to stage a one month concentrated effort to obtain experimental data. This run was not carried out without technical difficulties (which will be discussed in the next section), however at the time it was feared that attempts to correct these problems might cause further damage and bring further delays to the program. Rather than risk never obtaining data[1], we made every attempt to obtain the best data possible given the circumstances.

[1]This run effectively signaled the end of the CHM program at UBC due to the lack of manpower and resources.

In the time since this work was carried out, techniques developed in the lab and additional studies have given us far more confidence in the original work. The results of that investigation are presented here in light of these new findings. The measurements are significant in that they demonstrate that that formalism which Verhaar *et al.* have introduced appears to be valid and certainly merits further evaluation. This is, to our knowledge, the only experimental verification of this theory to date. Unfortunately as a consequence of these frequency shifts, it is not likely that the CHM will ever attain frequency stabilities in the 10^{-18} range as was once predicted [15].

5.1 Summary of technical problems

We begin the discussion of these measurements by quickly outlining a few of the technical difficulties which were encountered during the experimental run. These points initially led to some concern about the interpretation of the data and have delayed its presentation until now.

1. The cooling power and the base temperature of the refrigerator were limited by a thermal 'touch' between one of the Cu braids used to bias the semiconductor devices in the tuning/Q spoiling system, and a thermal shield surrounding the maser cavity. This touch also initially led to some concern as to the actual temperature of the maser bulb. During the run it was discovered that the heat leak could be alleviated somewhat by forcing the main vacuum jacket of the refrigerator off centre, causing it to push against the vacuum can which housed the maser and ultimately relieving some of the pressure between the Cu braid and the thermal shield. It was not possible to completely alleviate the problem. Eventually it was decided that any temperature gradients which might have been introduced by this heat leak were small enough to be neglected. The temperatures which are reported here are those

which were measured during the experiment. No corrections have been applied.

2. As mentioned in the last chapter, we were forced to measure the resonator Q and centre frequency in the reflection mode. This technique is inherently quite sensitive to the standing wave patterns in the microwave circuitry. These standing waves led to some concern about the absolute accuracy of the measured Q's and cavity frequencies. This problem was compounded during the experimental run by the changing ℓ-^{4}He level[2] in the main bath of the refrigerator. The resulting change in the temperature gradient along the coaxial lines leading to the resonator causes shifts to occur in the standing wave pattern via the change in the electrical length of the lines. Our concerns surrounding these measurements were alleviated after additional measurements of the electrical parameters of the system were made and used in a computer model of the measurement technique. This additional work has allowed us to place reasonable limits on the uncertainties incurred during the measurements.

3. The measurements of the maser output power as a function of density made during this run did not initially seem to be consistent with earlier measurements. In particular the threshold density for maser oscillations seemed to be too low. This observation led us to question the absolute power/density calibration measurements and the absolute measurement of the resonator Q. Since that time the filling factor of the maser bulb inside the split-ring resonator has been carefully measured (appendix B). In addition, the techniques outlined in appendix A were used to include radiation damping in the numerical fit to the FID data used for determining the

[2]It was not possible to regulate the ℓ-^{4}He level during the spin-exchange measurements because of the sensitivity of the maser to mechanical vibrations. This sensitivity was not normal and was related to the thermal touch.

atomic densities. The extent to which radiation damping influences the data provides a check on the power calibration. No discrepancy between these methods of determining n_H was observed during the data analysis. The result of the numerical fits to the FID's are entirely consistent with the measured power/density calibration. They are also consistent with results obtained later on a different system (see chapters 6 and 7). As a result, we are confident in the measurements reported here; any discrepancies between this run and earlier reports must be due to the use of the new pumping scheme used in the present work and the fact that the filling factor for the maser bulb with the modified tuning arrangement was actually higher than for previous work. This last point is discussed in the section on the determination of the atomic density.

5.2 Cooldown procedure (standard)

After the system is cooled below 1 K for the first time, a small quantity of H_2 is admitted to the source region through a heated capillary. Sufficient ^{4}He to coat the internal walls of the maser is then admitted via the same capillary. The discharge is fired several times to create a sample of H gas from the frozen H_2, and pulsed magnetic resonance techniques (usually $\pi/2$ pulses at the a-c hyperfine transition frequency) are used to detect the presence of these atoms.

The maser cavity is axially located inside a cylindrical superconducting Pb shield which itself is located inside a high μ metal shield ('Co-netic foil'[3]). The Co-netic foil is demagnetized at room temperature and again at 77 K. Using a solenoid located between the two shields a small longitudinal bias field at the site of the maser bulb is then applied to set the quantization axis and to split the degeneracy of the upper three hyperfine

[3]Perfection Mica Company - Magnetic Shield Division, 740 Thomas Dr, Bensenville Ill.

levels of the H atoms. As this field is increased, cross relaxation between the upper three hyperfine levels is reduced. At the same time the sensitivity[4] of the oscillation frequency of the maser to fluctuations in the bias field is increased. The magnitude of the bias field is chosen as a compromise between these effects. The field is set while the Pb shield is driven normal. The shield is then cooled in order to trap the field. In the present experiments, a field of 1×10^{-5} Tesla was applied, resulting in an upwards shift of about 30 Hz in the oscillation frequency of the maser.

5.3 Characterization of the maser

5.3.1 Magnetic relaxation

During earlier studies [17] it was established that H atoms in the UBC CHM are subjected to strong magnetic relaxation somewhere near the orifice which leads to the maser bulb. This relaxation is predominantly cross relaxation between the upper three hyperfine levels[5]. This relaxation affects the evolution of the longitudinal magnetization of the H atoms during magnetic resonance experiments. It is necessary to characterize this relaxation if the techniques outlined in appendix A are to yield reliable fits to free induction decays. We proceed by assuming that the relaxation rates between the $|\,c\,\rangle$ and the $|\,d\,\rangle$ and between the $|\,c\,\rangle$ and the $|\,b\,\rangle$ states are equal and denote this rate by Γ_c. Longitudinal relaxation between the upper three states and the $|\,a\,\rangle$ state is considerably less efficient. Again we assume that all three of these relaxation processes occur at the same rate, which is denoted by Γ_a.

At low densities where spin-exchange relaxation can be be neglected, the relaxation

[4]The oscillation frequency is essentially independent of the bias field when the field is zero and increases as the bias field is increased.

[5]In fact, the new pumping scheme which we have used in these experiments is made possible because of this relaxation.

of the longitudinal component of the magnetization (using the spin $\frac{1}{2}$ analogy introduced in chapter 2) towards its thermal equilibrium value

$$n_H(\rho_{aa} - \rho_{cc})_{eq} \approx \frac{1}{4} n_H \frac{\hbar\omega_0}{k_B T} \tag{5.1}$$

following a π-$\pi/2$ pulse sequence, is such that the time dependent deviation $\delta n_H(\rho_{aa} - \rho_{cc})(t)$ from this value is represented very well by a sum of exponentials. When this deviation is normalized to the thermal equilibrium value given by equation 5.1 we can write

$$\frac{\delta M_z(t)}{\delta M_z(0)} = -2\left(\frac{2}{3}\exp(-\Gamma_1 t) + \frac{1}{3}\exp(-\Gamma_2 t)\right) \tag{5.2}$$

where $\Gamma_1 = \Gamma_b + 4\Gamma_a \approx \Gamma_b$ and $\Gamma_2 = \Gamma_b + \Gamma_a + 3\Gamma_c \approx \Gamma_b + 3\Gamma_c$. Here Γ_b represents the rate at which atoms are lost from the maser bulb due to effusion from the orifice. In figure 5.1 we show the measured amplitude of the atomic response to a $\pi/2$ pulse which occurs at a time t following a π pulse. The signals have been normalized to an initial amplitude of 1 so that the data is proportional to $\frac{\delta M_z(t)}{2\delta M_z(0)}$. The measurements were made at a density $n_H = 4.9 \times 10^{10}$ cm^{-3} where contributions due to spin-exchange are expected to be small.

When the amplitude of these decays is fitted to the form given in equation 5.2 we obtain $\Gamma_1 = 1.14$ s^{-1} and $\Gamma_2 = 7.73$ s^{-1}. With the assumption that $\Gamma_a \approx 0$ [17] we obtain $\Gamma_c = 2.20$ s^{-1} and $\Gamma_b = 1.14$ s^{-1}. These values are consistent with earlier observations [17].

In appendix A, the phenomenological differential equations describing the evolution of the spin magnetization are presented along with a discussion of the procedure used to fit these equations to magnetic resonance data. These equations are presented only for the case in which there is a single T_1 process. It is a relatively simple matter to modify these equations to include the additional relaxation processes described above. That is, the relaxation of the z component is assumed to occur at a rate which is the

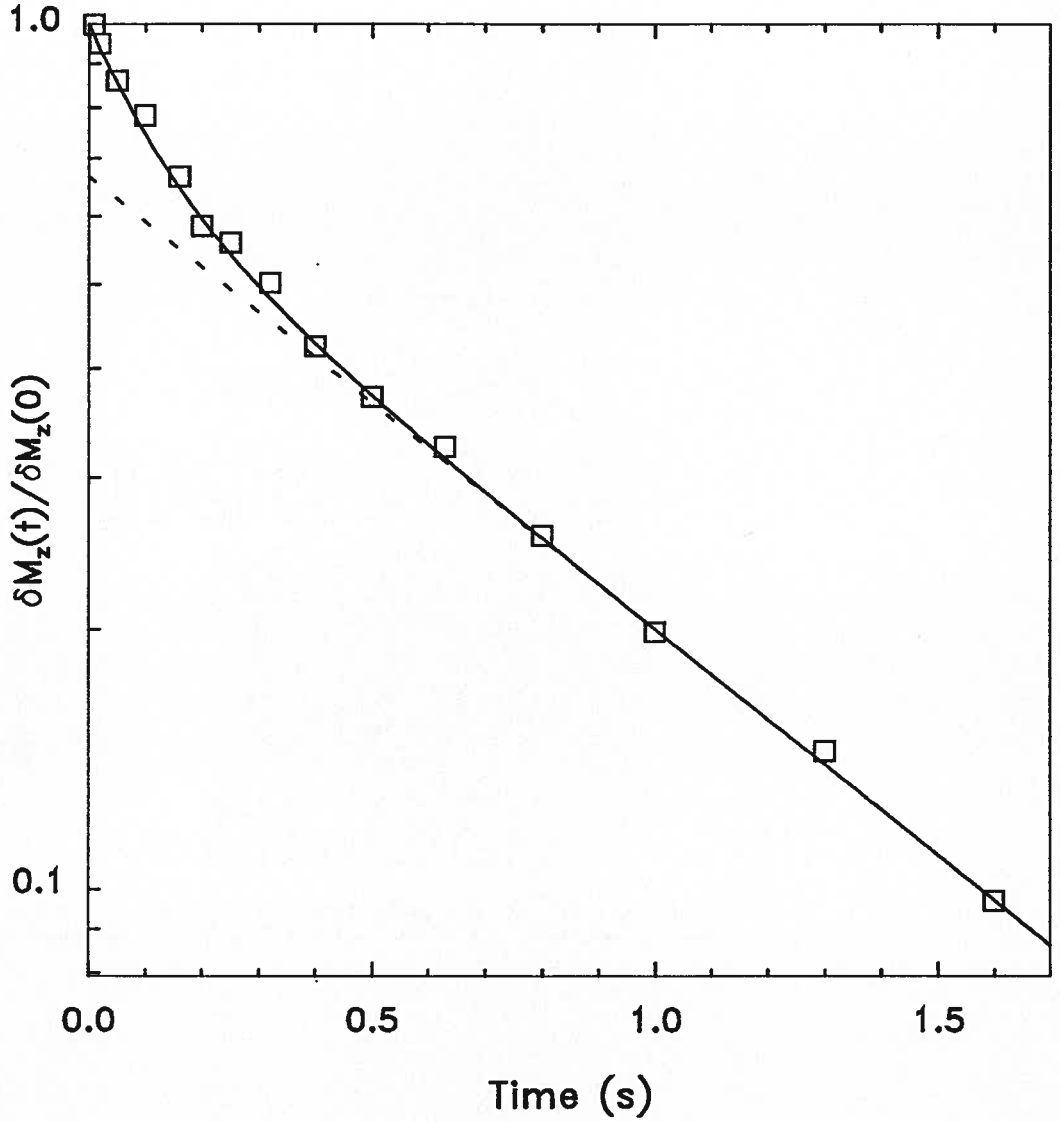

Figure 5.1: The normalized amplitude recovery of the longitudinal magnetization following a $\pi - \pi/2$ pulse sequence, as a function of the interpulse spacing. This information is used in the fits which are made to the FID's using the techniques described in appendix A. The atomic density is $n_H = 4.9 \times 10^{10}$ cm^{-3} and the temperature is 0.500(3) K.

sum of the processes described by Γ_b and Γ_c and an additional, as yet unspecified T_1^{-1} which accounts for additional relaxation due to processes such as spin-exchange. The free induction decays obtained during the course of the experiment have all been fitted using this modification to the radiation damping equations.

5.3.2 Determination of the atomic density

In order to measure the spin-exchange frequency shift parameters it is necessary to have an absolute calibration of the atomic density. For a collection of spins in thermal equilibrium this measurement can be made using magnetic resonance techniques as outlined in chapter 2 and appendix A. Under thermal equilibrium conditions the static (longitudinal) magnetization $\tilde{M}_0$ is proportional to the H density[6]. Following a $\pi/2$ pulse this magnetization is converted into a precessing (transverse) magnetization $\tilde{M}_r$ which (initially) has the same amplitude. The time evolution of this response gives rise to the free induction decay. It is observed experimentally as a damped oscillatory signal which is compared with the local oscillator of the 1420 MHz spectrometer. The power emitted by the atoms immediately following the pulse is given by[25, 27]

$$P = \frac{\mu_0 \omega_0 V_b \eta Q_\ell}{2} \left|\tilde{M}_r\right|^2 = \frac{\mu_0 \omega_0 V_b \eta Q_\ell}{2} \left[\frac{\hbar^2(\gamma_e + \gamma_p)\omega_0}{8 k_B T}\right]^2 n_H^2 \,. \tag{5.3}$$

Half of this power is absorbed by the detection circuitry when it is critically coupled to the resonator. The gain of the detection system is carefully measured so that absolute power measurements can be made. The FID data is fit to the numerically integrated differential equations outlined in appendix A, with the free parameters T_1, T_2, n_H, frequency, and an initial phase angle. Measured quantities such as the power calibration factor, bulb holding time, cross relaxation rate, cell volume and filling factor are included as known parameters in the appropriate equations.

[6] We are using the fictitious spin $\frac{1}{2}$ analogy again.

An example of a fit to a FID is shown in figure 5.2. The H density determined from the power calibration is 7.1 $\times 10^{11}$ cm^{-3}. The decay is not obviously non-exponential; however radiation damping does account for about one quarter of the observed damping. Radiation damping also influences the data in more subtle ways. In this particular example, a fit to a single damped sinusoid would overestimate the frequency of the signal by 9 mHz and underestimate the atomic density by 4%. These effects have been studied in detail by Bloom [30].

An essential part of this procedure is to have a proper measurement of the filling factor η. Prior to the present work the filling factor for the UBC CHM was only known indirectly. Estimates placed this value at 0.2 [17] with a rather large uncertainty. In appendix B of this thesis we present a new technique for measuring magnetic filling factors which is based on the use of the paramagnetic properties of liquid O_2. We have used this technique to measure the filling factor of the unmodified CHM resonator and find η=0.24(1). The modified resonator used in the present experiments contains a considerable amount of teflon located below the actual split-ring resonator. This dielectric material increases the effective length of the resonator can. At the same time it tends to enhance the longitudinal fields near the lower part of the maser bulb and thus increases η. The filling factor of the modified resonator assembly used in this work is 0.27(1).

There is some corroborative evidence that our measurements of the filling factor are quite reliable. Throughout this work radiation damping makes a significant contribution to the FID envelope. If we try to fit the differential equations given in appendix A to the FID's at high n_H using larger values of η, we find that the damping quickly becomes excessive and that a good fit is not possible. That is, the measured values of η appear to be the largest values consistent with the observed damping. Decreasing the value of η and accounting for the additional damping with a smaller value of T_2^* leads to a more exponential decay. If we use χ^2 as a measure of the goodness of the fit to the data, we

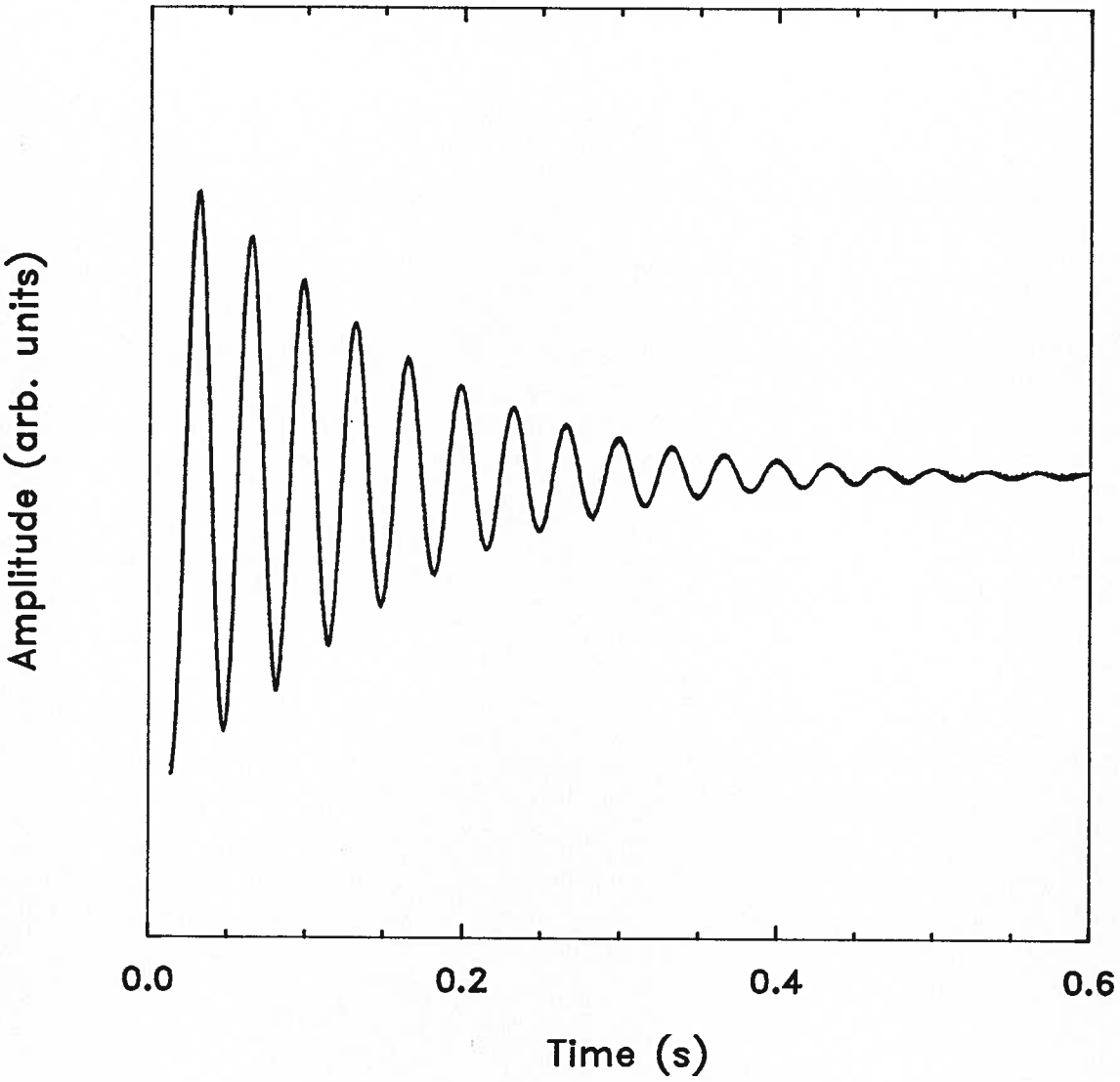

Figure 5.2: An example FID and the numerical fit to the data using the techniques outlined in appendix A. The decay was taken with $n_H = 7.1 \times 10^{11} cm^{-3}$ at a temperature of 0.50 K. Radiation damping accounts for about one quarter of the observed damping. The residual T_2^* due to processes other than radiation damping is 0.18 s.

find that χ^2 doubles if η is decreased to 0.22. This is a somewhat less stringent lower bound on η but still rather suggestive.

It should be noted that implicit in the power/density calibration is the assumption of thermal equilibrium. The translational degrees of freedom for the H atoms are very quickly thermalized by collisions with ^{4}He atoms and the ℓ-^{4}He walls. The spin degrees of freedom on the other hand are only thermalized by spin exchange interactions and magnetic field gradients. At low H densities, magnetic relaxation is likely to be the dominant thermalizing process. During the normal operation of the CHM the atoms are in contact both with maser bulb volume and with the slightly cooler state selector region. At the lowest densities where spin-exchange relaxation is not efficient, the spin temperature in the maser bulb may be lower than the measured temperature. This effect would lead to an overestimation of the atomic density inside the maser bulb for low densities.

5.3.3 Computer simulation

The dynamics of the operation of the maser are quite complicated and cannot be directly monitored. In particular, it is not possible to measure (or control) the occupation of any one (or any combination) of the hyperfine states at any point within the maser while it is operating. To determine the atomic density inside the maser bulb, it is necessary to stop the maser oscillations and then probe the system with magnetic resonance techniques. A prerequisite for the use of these techniques[7] is that the system be in a state of thermal equilibrium (including the spin degrees of freedom which are thermalized predominantly by spin exchange and magnetic relaxation). While the maser is operating, there is a constant flux of low field seeking atoms approaching the storage bulb. When the state

[7] A $\pi/2$ pulse measures the population difference between the $|\,a\,\rangle$ and $|\,c\,\rangle$ states. In the derivation of equation 3.30 it is explicitly assumed that the atomic system is in thermal equilibrium.

selector is turned off, this flux is stopped almost completely, causing the net H atom density inside the bulb to decrease. As a result, the density measured when the maser is not operating is less than that when it is masing.

In order to overcome this obstacle we rely upon the result of a computer simulation of the quasi-steady state operation of the UBC CHM which was developed by M. D. Hürlimann [17, 16, 90] who looked at the dependence of the atomic density in the various maser volumes as a function of numerous factors such as the efficiency of the relaxing foil. The results of his study suggests that the 'correction' or 'density enhancement' factor which must be applied in order to relate the non-operating and operating atomic densities is about 1.4. There is of course some uncertainty in this value. However reasonable assumptions [17], suggest that this uncertainty is likely of the order of 5%. In the present work we have made no attempt to refine the results of this study and use the factor of 1.4 for determining n_H in the operating maser. We also assume that this factor is independent of density within the 5% uncertainty. This is again consistent with the computer simulation results.

The simulation also allows one to predict the density dependence of the populations of the various hyperfine levels. Of particular interest for the measurement of the spin exchange frequency shifts in the CHM is the dependence of $\rho_{cc}+\rho_{aa}$ on the atomic density inside the maser bulb. Hürlimann finds that changes in this sum are not expected to be more than about 5% across the operating range of the maser. The uncertainties associated with the measurement of the spin-exchange parameters are too large to warrant the use of this model to attempt to extract further information. For our purposes it can be assumed that $\rho_{cc} + \rho_{aa} = 0.5$ inside the maser bulb [17].

5.3.4 Output power of the maser

The output power of the CHM was measured as a function of the atomic density inside the maser bulb using the new pumping scheme outlined in the previous chapter. The results of this measurement are shown in figure 5.3. The resonator Q was 809(8) and the bulb temperature was 0.500(3) K. The threshold for masing is slightly lower than expected when compared with earlier experiments [17]. This discrepancy *may* indicate an error in the density enhancement factor determined from the computer simulation, either in this work or the previous work.

5.4 The measurements

The equation describing the combined frequency shifts due to spin-exchange and cavity detuning for the CHM as predicted by Verhaar *et al.* [19, 20] is repeated here for the sake of convenience :

$$\begin{aligned} f - f_0 &= \frac{1}{2\pi}[\Delta + \beta\overline{\lambda}_0(1+\Delta^2)]\frac{1}{T_0} \\ &\quad + \frac{1}{2\pi}\left\{[\Delta + \beta\overline{\lambda}_0(1+\Delta^2)][\overline{\sigma}_1(\rho_{cc}+\rho_{aa}) + \overline{\sigma}_2] + [\overline{\lambda}_1(\rho_{cc}+\rho_{aa}) + \overline{\lambda}_2]\right\}\overline{v}_{HH}n_H \end{aligned} \tag{5.4}$$

where

$$\beta = \frac{4\overline{v}_{HH}}{\hbar(\gamma_e+\gamma_p)^2\mu_0\eta Q_\ell} \tag{5.5}$$

and the detuning

$$\Delta = Q_\ell\left(\frac{\omega_c}{\omega} - \frac{\omega}{\omega_c}\right) \tag{5.6}$$

is a measure of the offset between the resonator (ω_c) and atomic (ω) resonances. It is possible to identify eight types of shift terms in this equation which depend in different ways upon the resonator quality factor Q, detuning Δ, and the atomic density n_H. Four of

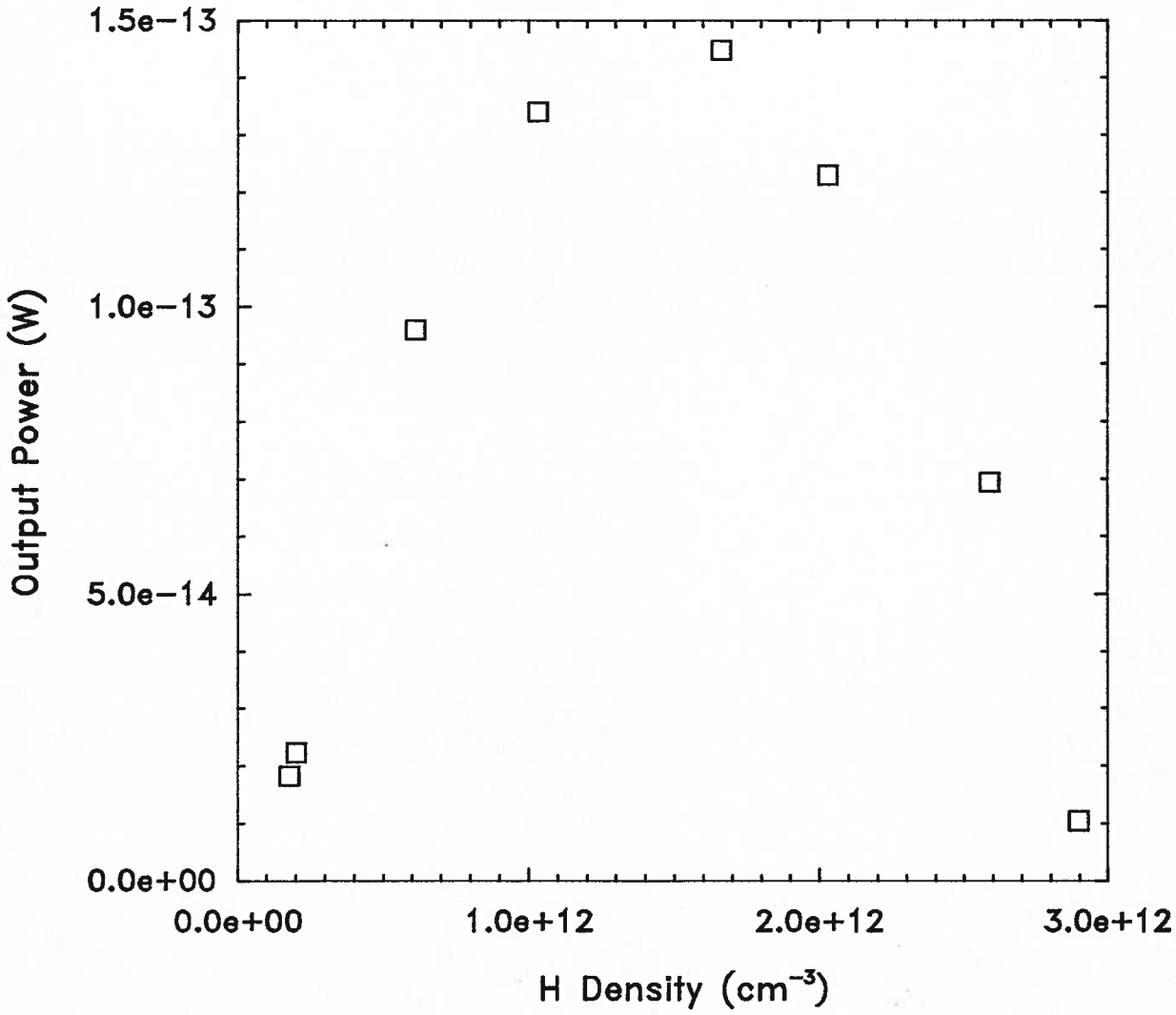

Figure 5.3: The output power of the UBC CHM utilizing the new pumping scheme ($|\ a\ \rangle$ to $|\ d\ \rangle$) which relies on cross relaxation near the bulb orifice. Measurements were made with a resonator Q of 809(8) and a bulb temperature of 0.500(3) K.

these terms are independent of density while four are proportional to the density. Of the density independent terms there is one which depends solely on Δ, one solely on Q, and one on both Δ and Q. There are three density dependent terms with similar dependencies on Q and Δ. In addition there is one density independent shift f_0 (due to factors such as the wall shift, buffer gas shift and the bias field), and a density dependent shift (involving λ_1 and λ_2), both of which are independent of Q and Δ. In this experiment we aim to identify and measure each of these shifts. The most important shift from the point of view of trying to establish the influence of hyperfine interactions during spin-exchange collisions is the shift which depends upon λ_1 and λ_2 (see chapter 3, equations 3.25 and 3.28). In the absence of these effects we do not expect to find a density dependent shift which is independent of both Q and Δ. The contribution of the hyperfine interaction to the total frequency shift can be measured with the dimensionless ratio [20]:

$$\Omega = -\frac{\lambda_1(\rho_{cc} + \rho_{aa}) + \lambda_2}{\sigma_1(\rho_{cc} + \rho_{aa}) + \sigma_2} \tag{5.7}$$

5.4.1 Procedure and data

Prior to making the frequency shift measurements, the resonator Q and tuning were mapped out as a function of the bias potentials V_t and V_q as described in the last chapter. From these measurements, a series of potentials were derived which enabled us to change the resonator tuning at a constant Q (near the maximum attainable $Q \approx 800$) and to change the Q at a constant detuning (near $\Delta = 0$). The Q's and tunings at each of these settings were then individually measured. Note that unless explicitly stated otherwise, the quality factors we report refer to the loaded values. All work was performed under conditions of critical coupling.

Atomic densities were set by varying the discharge pulse duration and repetition rate. The pulse widths were typically 1 μsec and the repetition rates were of order 1 every

10 seconds. Densities produced in this manner did not fluctuate measurably within the detection noise limit of about 1% of the measured density.

The maser output was beat down to a 10 Hz signal in the 1420 MHz spectrometer[8] as described in the previous chapter. Once stable maser operation was established at a given density, this frequency was measured repeatedly with the frequency counter using a 10 second averaging time. This frequency measurement was then repeated as a function of the preset Q's and Δ's. At each setting the frequency was measured a minimum of three times. Multiple checks of the unperturbed oscillation frequency (maximum Q, Δ=0) were made throughout the measurements. Finally the microwaves used to pump the $|\ a\ \rangle$ to $|\ d\ \rangle$ transition were stopped by inserting the resistive card switch and the atomic density within the maser bulb was measured using several $\pi/2$ pulses. The original operating condition of the maser was reestablished before moving on to a new density. At the end of the run the Q's and Δ's at each of the canonical settings were remeasured.

The maser oscillation frequency measured in this way is shown as a function of density at constant Q in figure 5.4 and and as a function of Q^{-1} at constant $\Delta \approx 0$ in fig 5.5. It should be noted that a small but measurable shift in the absolute detuning occurred part of the way through the measurements. This effect is most obvious in the data at constant Δ (figure 5.5) where the data appears to be grouped into two clusters. This shift is presumably due to an abrupt change in the mechanical tuning.

5.5 Analysis

In the following sections we present our analysis of the frequency shift data presented in figures 5.4 and 5.5.

[8]The LO of this spectrometer was derived from one of the quartz crystal oscillators. The long term stability of this oscillator was enhanced by using the Rb clock as a flywheel.

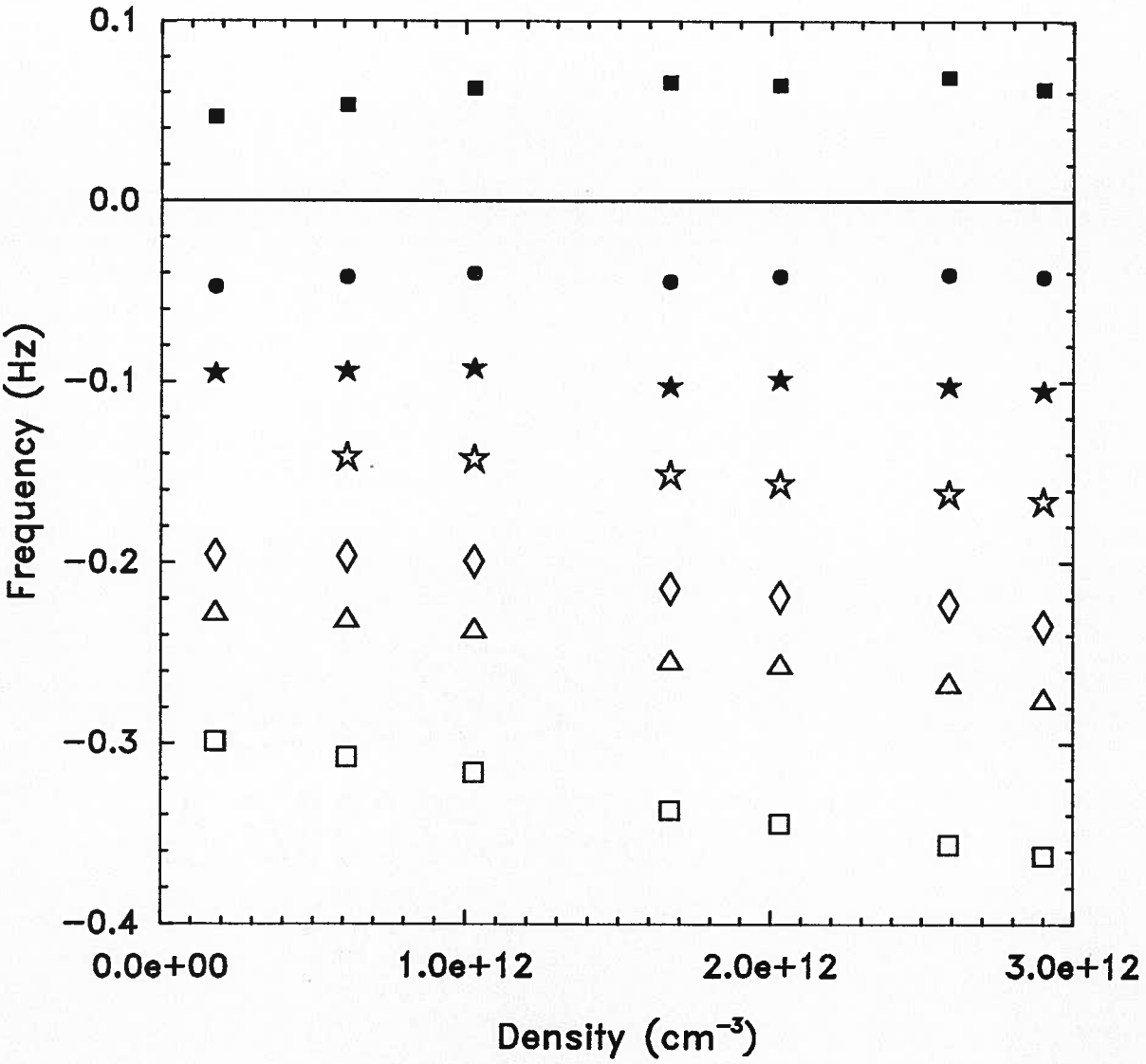

Figure 5.4: The measured frequency shift of the oscillation frequency of the UBC CHM as a function of the H density inside the maser bulb for various cavity detunings. The frequencies have been converted to absolute shifts from the density independent oscillation frequency f_0. The resonator Q=809(8) and the temperature of the maser bulb T=0.500(3) K were held constant through these measurements. The lowest set of data corresponds to $\Delta \approx -0.2$ and the highest set to $\Delta \approx 0.2$.

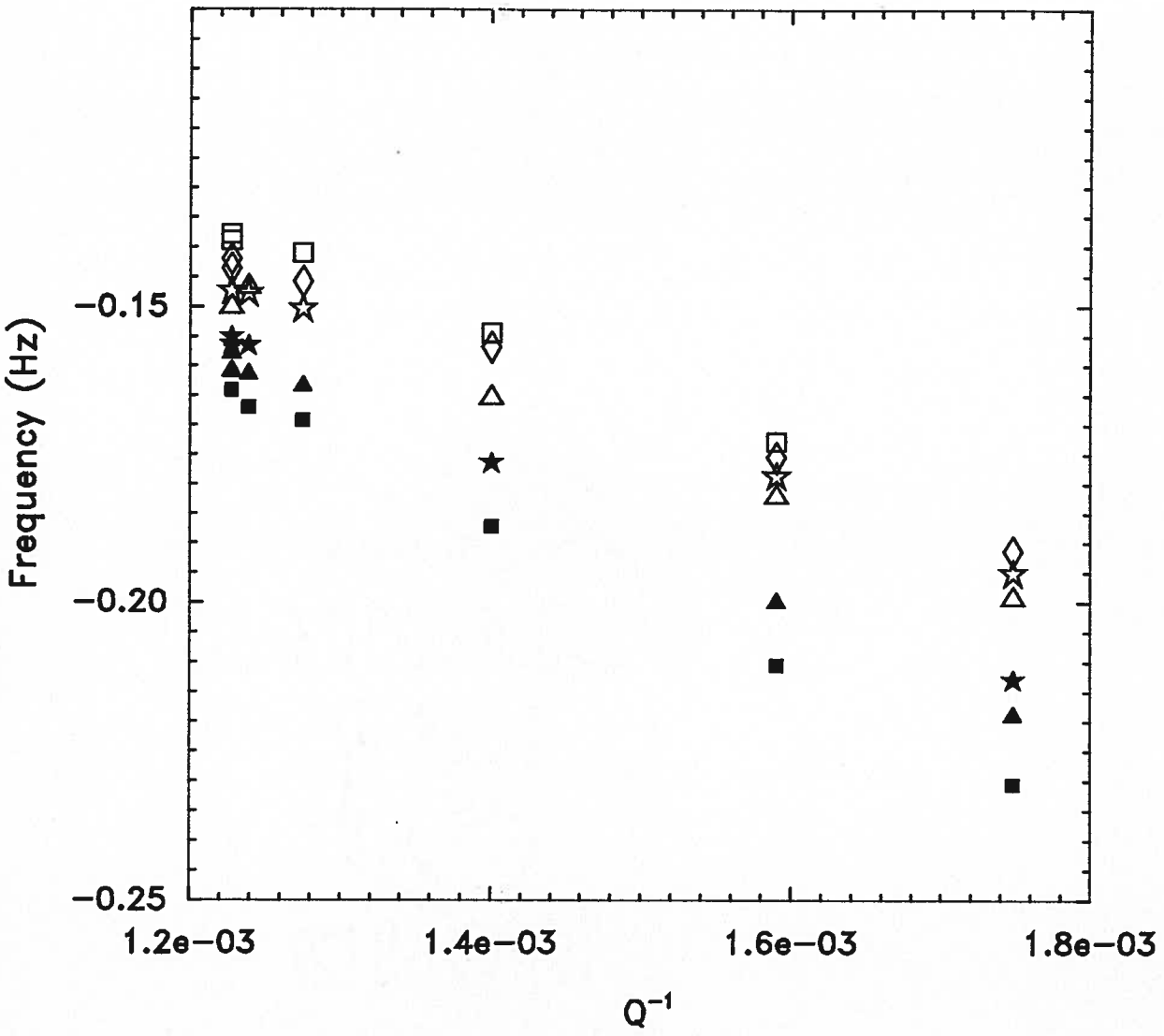

Figure 5.5: The measured frequency shift of the oscillation frequency of the UBC CHM as a function of Q^{-1} for various H densities. The frequencies have been converted to absolute shifts from the density independent oscillation frequency f_0. The resonator detuning was set near zero and the temperature of the maser bulb was held constant at 0.500(3) K. The lowest set of data corresponds to $n_H = 2.6 \times 10^{12} cm^{-3}$ while the highest set corresponds to $n_H = 2.0 \times 10^{11} cm^{-3}$.

5.5.1 Density independent frequency shift and absolute detuning

The analysis of the frequency shifts requires a careful establishment of the density independent oscillation frequency f_0 and the absolute resonator detuning. In figure 5.6 we plot the frequency of the FID used to determine the H density during the spin-exchange measurements, as a function of n_H. The data extrapolates to a zero density frequency shift[9] f_0 = 1420.405 783 434 (1) MHz. All other frequency shifts mentioned in this chapter are reported with respect to this value.

The cavity tuning is determined by fitting the cavity resonance to a single Lorentzian lineshape with a sloping background. Since this measurement is made in reflection it is very susceptible to apparent shifts caused by standing waves in the external circuitry. In figure 5.7 we show the initial phase of several FID's as a function of the measured cavity detuning Δ from the atomic resonance. Changing the cavity tuning by Δ should lead to a change of 2Δ in this phase. The experimentally determined slope obtained from this data is 1.983(23) which indicates that our measurements of relative detunings are good to about 1%.

We have employed two independent methods to determine the absolute detuning of the resonator from the atomic resonance. In figure 5.8 we show the normalized measured power output of the maser as a function of the measured detuning. This data has been fit[10] to a quadratic of the form

$$\frac{P}{P_0} = 1 - \alpha(\Delta - \Delta_0)^2 \tag{5.8}$$

with the result that Δ_0 = -0.014(30).

[9]This frequency is measured against the combination of the quartz crystal oscillator and the Rb clock. We are only interested in relative shifts from this value. The absolute frequency measured directly against the calibrated Rb clock is about 400 mHz lower. This offest is due to the oscillation frequency of the x-tal oscillator and is of no consequence in these measurements.

[10]P_0, α, Δ variable.

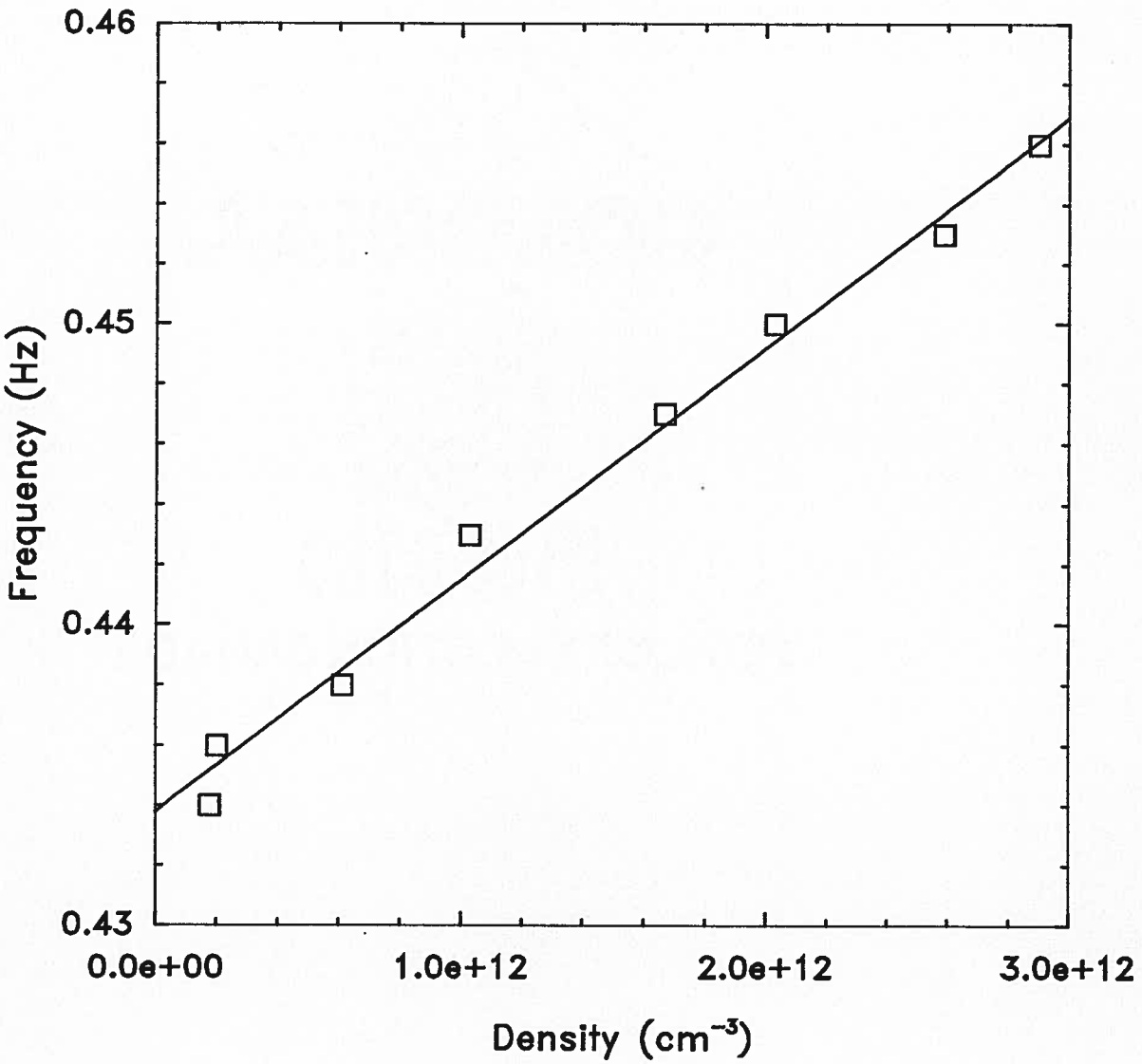

Figure 5.6: The frequency of the free induction decays used to determine the atomic density during the spin-exchange measurements, as a function of n_H. A frequency of 1420.405 783 MHz has been subtracted from this data. The zero density frequency f_0 obtained from this plot is 1420.405 783 434 (1) MHz.

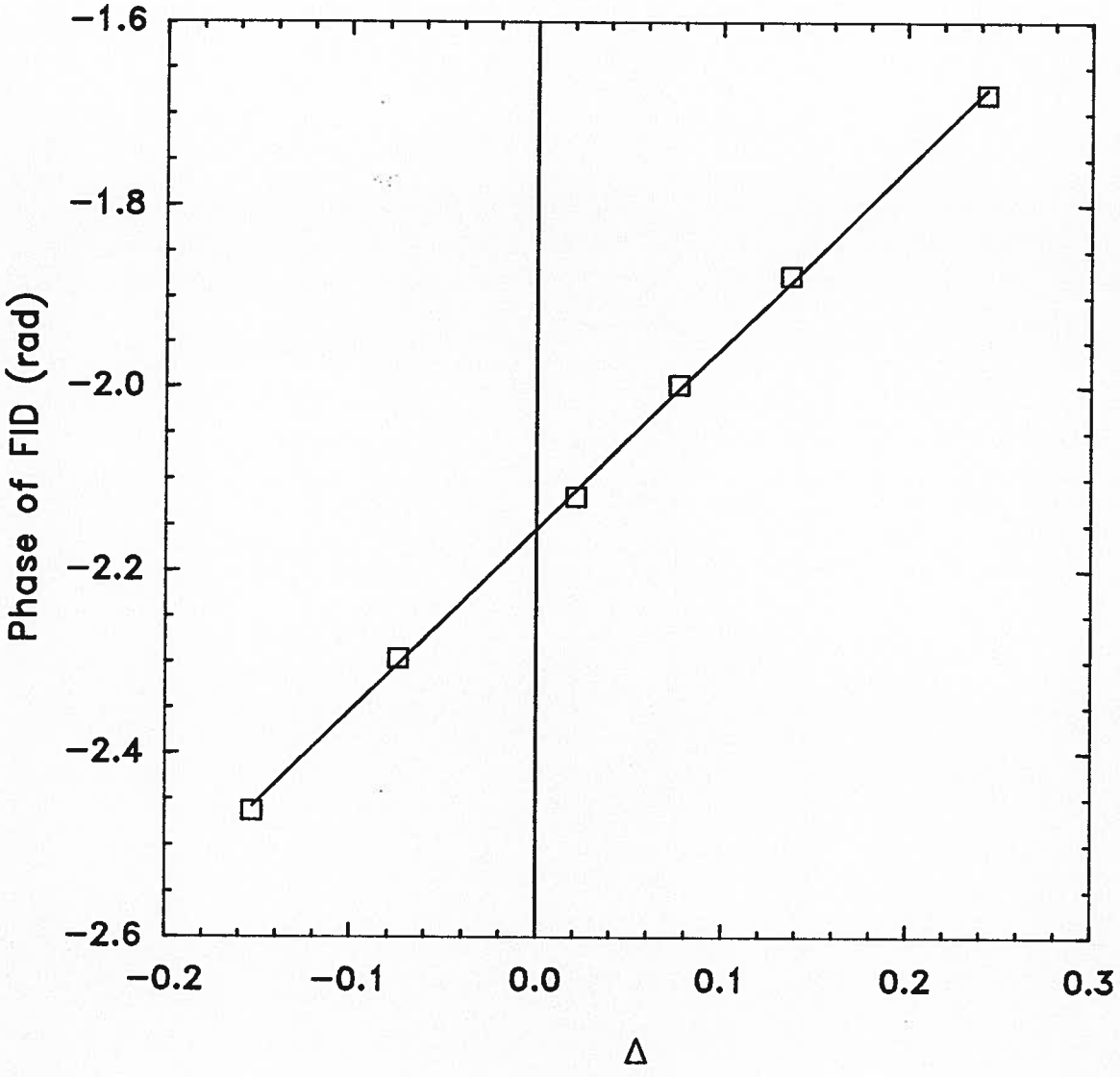

Figure 5.7: The initial phase of a free induction decay as a function of the measured resonator detuning. The slope of this plot is 1.983(23) (theoretically 2) which indicates that relative changes in detuning measured in reflection agree with the changes felt by the H atoms to within 1%.

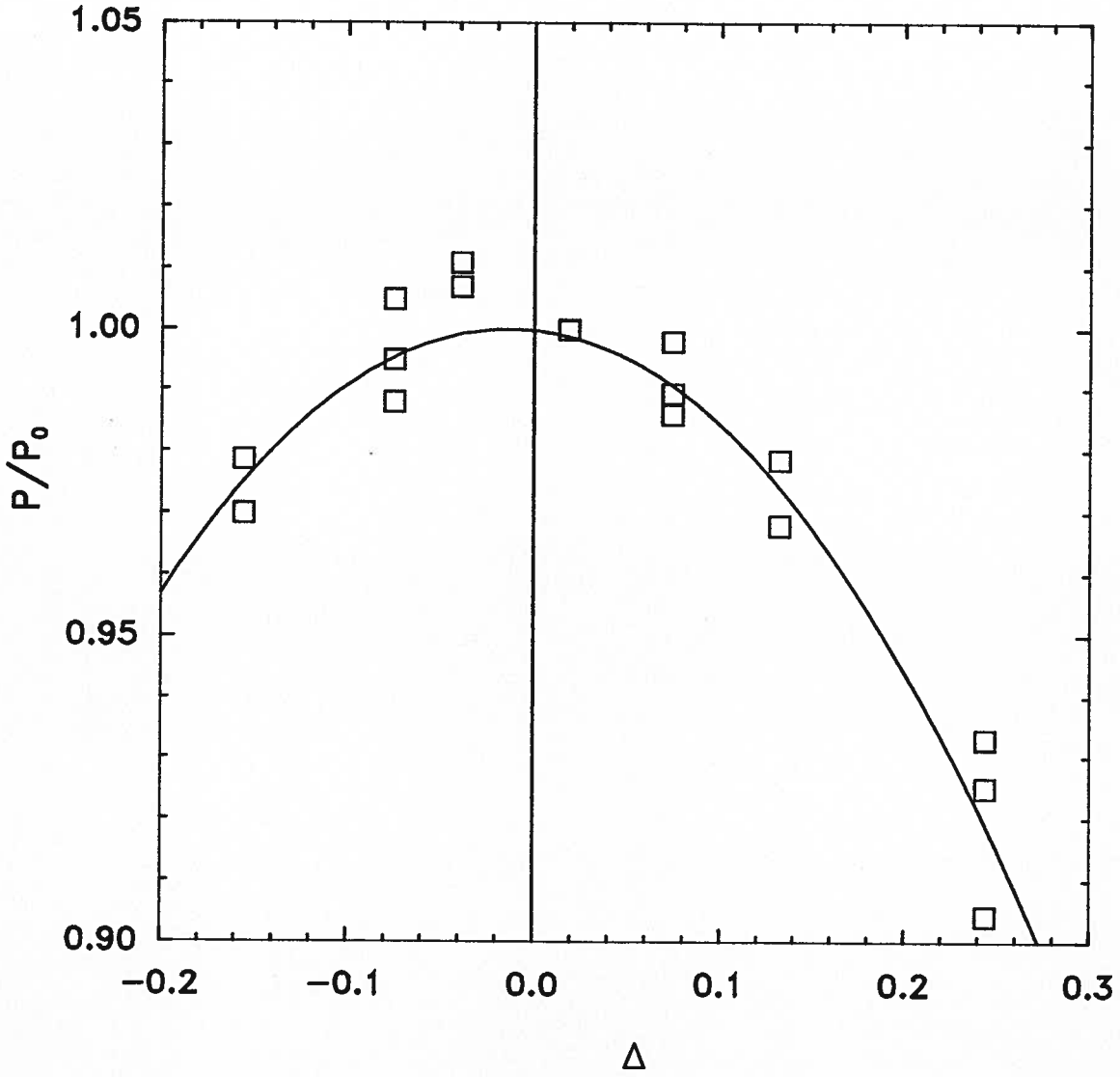

Figure 5.8: The output power of the maser arbitrarily normalized to a value at $\Delta = 0.019$ as a function of the measured resonator detuning. When fit to a quadratic of the form in equation 5.8 it appears that there is an offset Δ_0=-0.014(30) in the absolute measure of Δ.

The second determination of the absolute detuning is based upon an analysis of the data shown in figure 5.5 which was taken at a constant $\Delta \approx 0$. According to equation 5.4 we would expect this data to depend linearly upon $\beta \propto Q^{-1}$ at constant n_H. In figure 5.9 we reproduce this data along with the results of a linear fit to each data set. In the limit of zero detuning (we ignore terms in Δ^2) and infinite Q, the residual frequency shift is expected to be

$$f - f_0 = \frac{1}{2\pi}\left\{\frac{\Delta}{T_0} + \overline{v}_{HH} n_H \left(\Delta[\overline{\sigma}_1(\rho_{cc}+\rho_{aa}) + \overline{\sigma}_2] + [\overline{\lambda}_1(\rho_{cc}+\rho_{aa}) + \overline{\lambda}_2]\right)\right\} \qquad (5.9)$$

The data in figure 5.9 has been extrapolated to Q^{-1}=0 and the residual shift plotted as a function of n_H in figure 5.10. The shift in the absolute detuning which occurred part of the way through the run is quite obvious as a discontinuity in the data. In the following section we determine a value for T_0 (which is independent of the absolute value of Δ to first order). As we have measured values for Δ before and after the shift, we can correct for it. This correction has been applied to the data marked by the triangles. The residual shift does not have an obvious dependence upon density and hence we attribute it solely to an offset Δ_0 between our measured values of Δ and the absolute detuning[11]. Using the value of T_0 determined in the next section we find Δ_0 = -0.046(1). This value is in agreement with the value determined from the tuning dependence of the maser power and is the value that we have chosen to use throughout the remainder of this analysis.

5.5.2 The parameters λ_0 and T_0

The frequency shifts measured at constant Q (figure 5.4) have been replotted in figure 5.11. In this figure a straight line has been fit to each data set (lines of constant detuning) and used to determine the zero density residual shift and the rate of change of this shift

[11]Note that neither the numerical results calculated by Verhaar *et al.* [19, 20], nor the measured values for the spin-exchange parameters that we present later in this chapter suggest that a significant contribution from the density dependent shifts ***should*** be expected in figure 5.10.

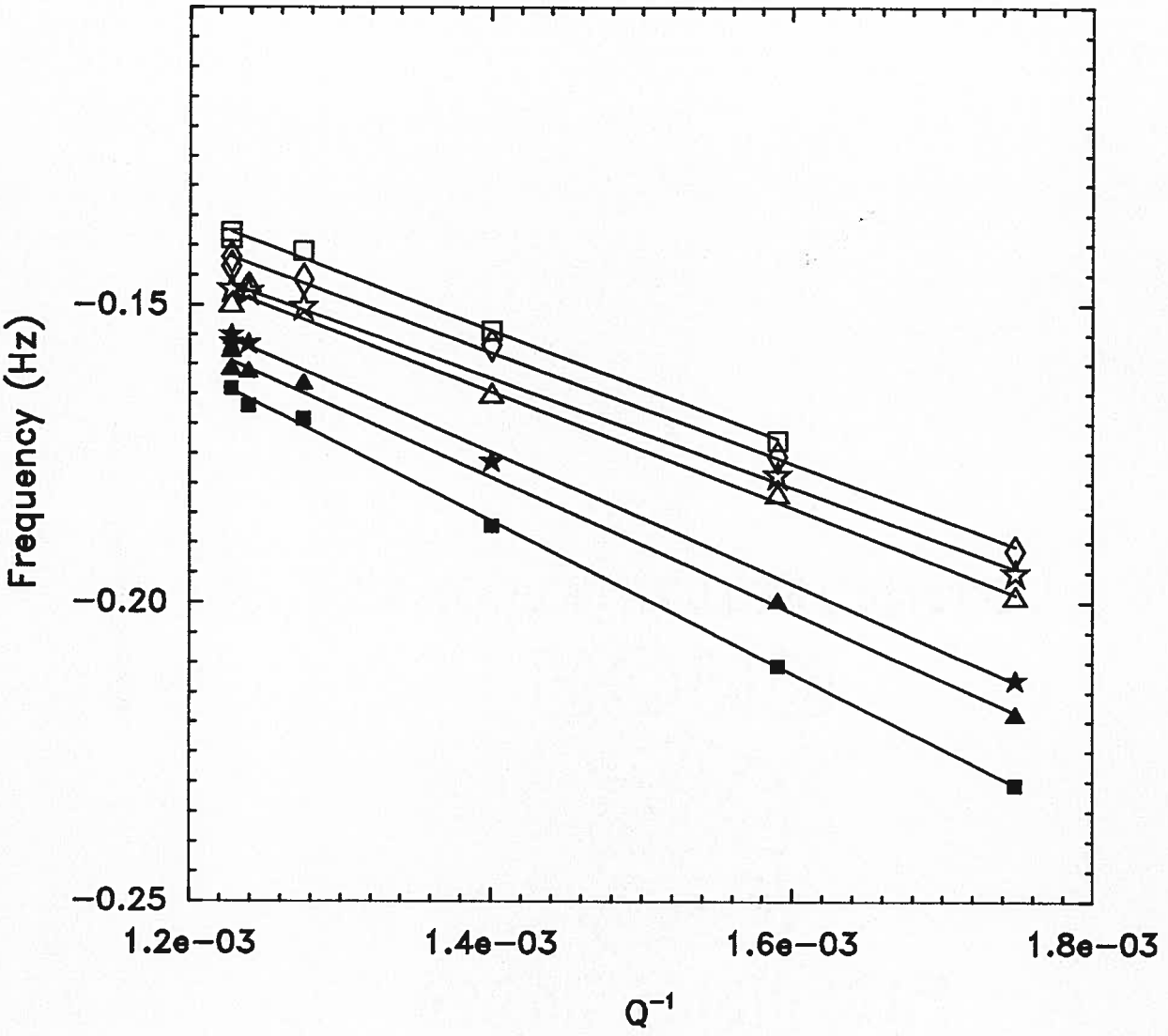

Figure 5.9: The data taken near $\Delta = 0$ as a function of Q^{-1} reproduced from figure 5.5. A straight line has been fitted to the data set at each density in order to extrapolate to the residual shift at infinite Q.

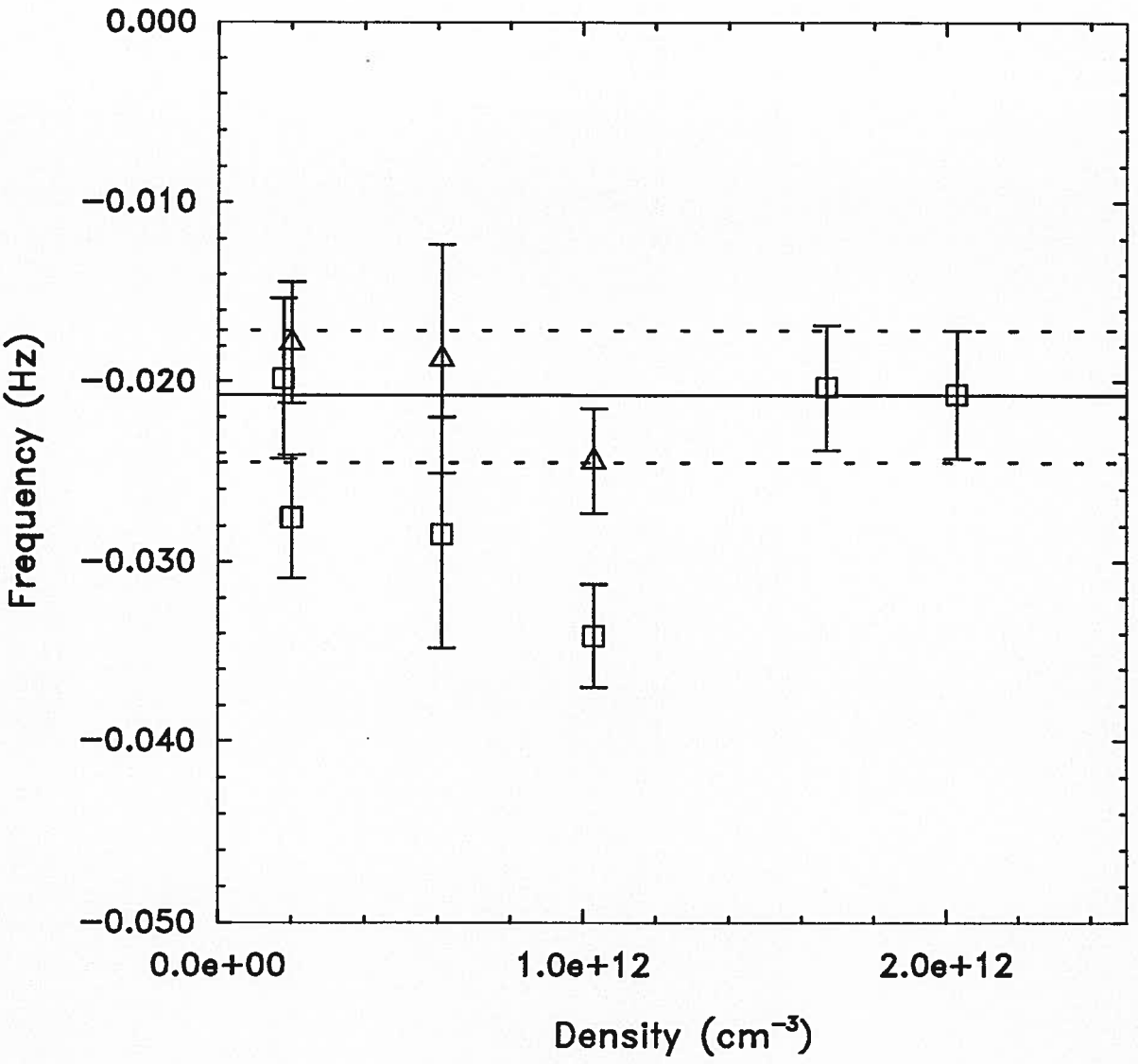

Figure 5.10: The Q^{-1}=0 intercept of the data taken near zero detuning plotted as a function of the H density (squares). The shift which occurred in the absolute detuning is quite obvious. This measured shift has been corrected for and the shifted data indicated by the triangles. The residual shift is $f_0 = -0.021(4)$ Hz which corresponds to a detuning offset Δ_0 = -0.046(1).

with density for each detuning. The zero density intercept is quadratic in Δ (see equation 5.4) and should be given by

$$\lim_{n_H \to 0} f - f_0 = \frac{1}{2\pi}\left[\Delta + \beta\lambda_0(1+\Delta^2)\right]\frac{1}{T_0}\,. \tag{5.10}$$

The intercept obtained from the data in figure 5.11 has been plotted in figure 5.12 along with a fit to the quadratic $a_0 + a_1\Delta + a_2\Delta^2$. Even though it is slight, the curvature in this plot is significant and indicates that the sign of λ_0 is negative. The linear term in this fit depends only upon the relative measure of Δ to first order and can be used to determine T_0. The value a_1=0.850(19) Hz yields a value T_0=0.187(4) seconds. This value was used in the previous section to establish the absolute cavity detuning.

The ratio of the linear term to the constant term can be used to determine λ_0:

$$\lambda_0 = \frac{a_1}{\beta a_0} \tag{5.11}$$

We obtain a value λ_0 = -21.7(2.8) Å^2 where this error reflects all of the experimental uncertainties including the uncertainty in the absolute detuning. We note that both parameters determined in this way (T_0 and λ_0) are quite insensitive to the absolute atomic densities, however λ_0 is sensitive to the absolute detuning.

5.5.3 The parameters $\sigma_1(\rho_{cc}+\rho_{aa})+\sigma_2$ and $\lambda_1(\rho_{cc}+\rho_{aa})+\lambda_2$

The rate of change of the frequency shift with respect to the H density predicted by equation 5.4 is

$$\frac{\partial(f-f_0)}{\partial n_H} = \frac{\bar{v}_{HH}}{2\pi}\left\{\left[\Delta+\beta\lambda_0(1+\Delta^2)\right]\left[\sigma_1(\rho_{cc}+\rho_{aa})+\sigma_2\right]+\left[\lambda_1(\rho_{cc}+\rho_{aa})+\lambda_2\right]\right\} \tag{5.12}$$

In figure 5.13 we have plotted the *slope* of the data shown in figure 5.11 along with a fit[12] to

[12]A similar analysis can be performed by fitting the data to a quadratic however the error bars are large enough so as to make the determination of the term b_2 quite uncertain.

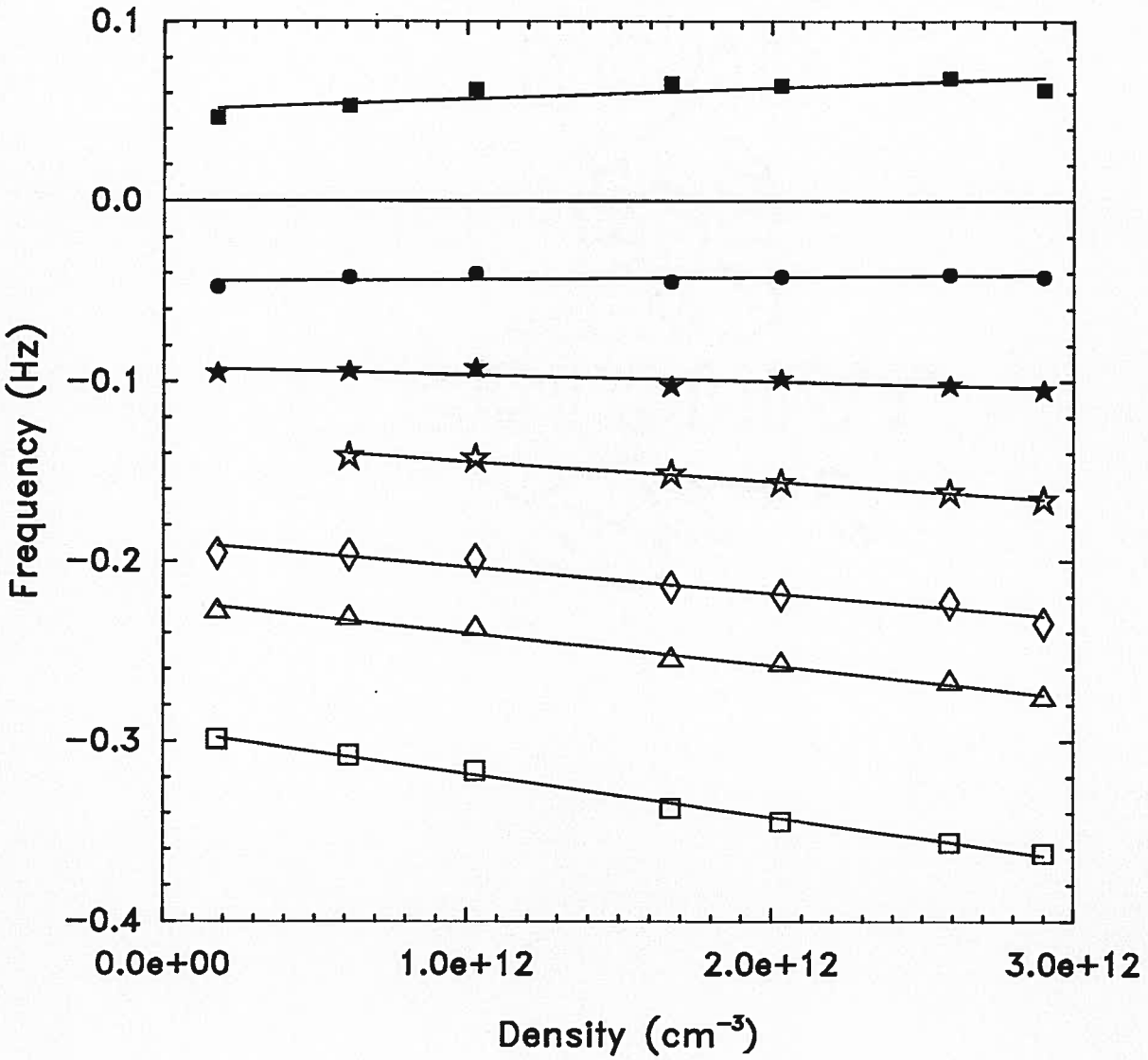

Figure 5.11: The data taken at constant Q reproduced from figure 5.4. A straight line has been fit to the data set at each detuning in order to determine the zero density intercept (figure 5.12) and the rate of change of the frequency shift as a function of n_H (figure 5.13).

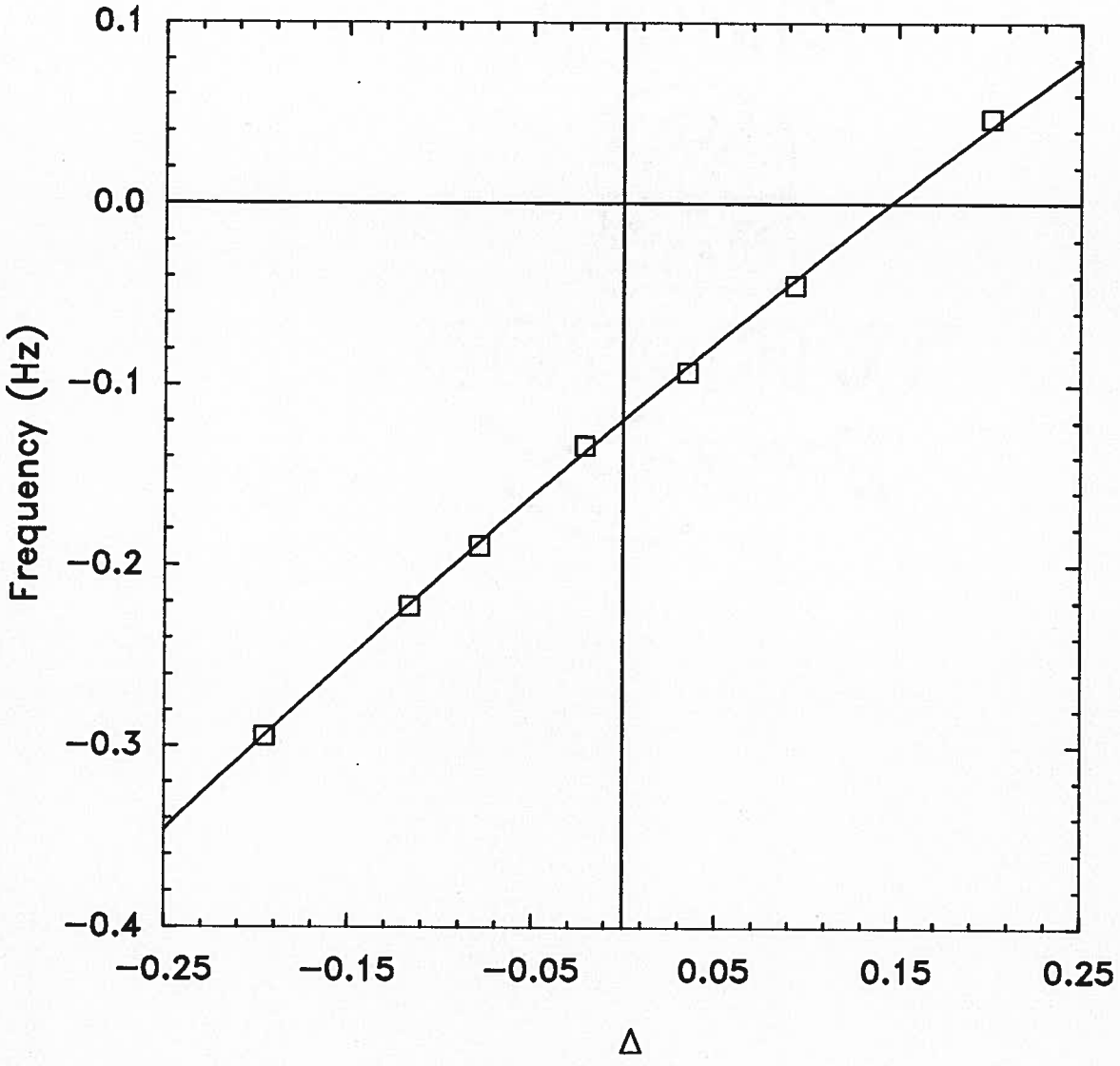

Figure 5.12: The zero density frequency shift as a function of the absolute detuning at Q=809(8). Error bars are smaller that the symbols used to indicate the data. The negative curvature is significant and indicates that λ_0 is negative. This data has been fit to the quadratic $a_0 + a_1\Delta + a_2\Delta^2$ to determine T_0 and λ_0.

$b_0 + b_1\Delta$. Here b_0 is simply the $\Delta = 0$ intercept of equation 5.12

$$b_0 = \left.\frac{\partial(f - f_0)}{\partial n_H}\right|_{\delta=0} = \frac{\overline{v}_{HH}}{2\pi}\{\beta\lambda_0[\sigma_1(\rho_{cc} + \rho_{aa}) + \sigma_2] + [\lambda_1(\rho_{cc} + \rho_{aa}) + \lambda_2]\} \tag{5.13}$$

and if terms in Δ^2 are neglected

$$b_1 = \frac{\partial}{\partial\Delta}\left(\left.\frac{\partial(f - f_0)}{\partial n_H}\right|_{\delta\approx 0}\right) = \frac{\overline{v}_{HH}}{2\pi}[\sigma_1(\rho_{cc} + \rho_{aa}) + \sigma_2] \ . \tag{5.14}$$

The slope of the data in figure 5.13 gives a direct measure of $\sigma_1(\rho_{cc} + \rho_{aa}) + \sigma_2$ which is sensitive to the absolute atomic density but depends only upon the relative measure of Δ. We find $\sigma_1(\rho_{cc} + \rho_{aa}) + \sigma_2 = 0.385(30)$ Å^2. The uncertainty which is reported here includes a relative error of 5% which was added because of the uncertainty to due with the choice of the density enhancement factor (determined by computer simulation [17]).

Finally we note that the residual shift due to the term $\lambda_1(\rho_{cc} + \rho_{aa}) + \lambda_2$ (if present) is given by the difference

$$\lambda_1(\rho_{cc} + \rho_{aa}) + \lambda_2 = \frac{2\pi}{\overline{v}_{HH}}b_0 - \beta\lambda_0 \tag{5.15}$$

We find from this data that $\lambda_1(\rho_{cc}+\rho_{aa})+\lambda_2 = 0.021(14)$ Å^2. The error in this quantity is large as it depends upon the difference between two frequency shifts. The result depends both upon the absolute atomic density and the absolute resonator detuning. It does however appear to make a significant contribution to the total observed frequency shift. This (density dependent) frequency shift (which does not depend on either Δ or Q) is the first indication that hyperfine interactions influence the oscillation frequency of the CHM as predicted by Verhaar *et al.* [19, 20].

5.5.4 Summary of measured quantities

A global fit to all of the data taking into account the small (measured) deviations from constant Q and Δ does not lead to an improvement of the uncertainties associated with

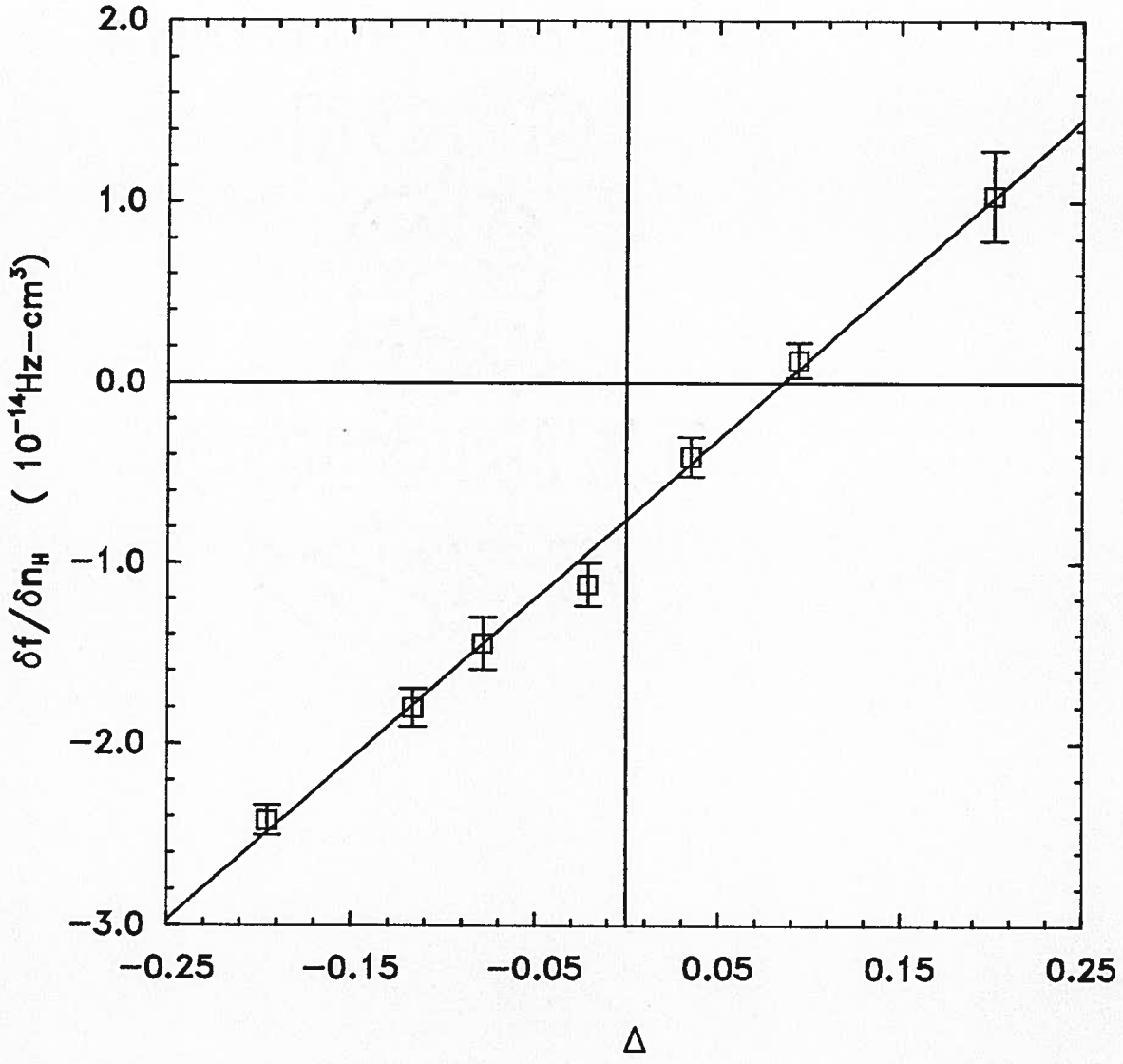

Figure 5.13: The rate of change of the observed frequency shift with n_H as a function of the absolute resonator detuning. The data has been fit to the straight line $b_0 + b_1\Delta$ with b_0 = -7.56(8)$\times 10^{-15}$Hz cm^3 and $b_1 = 8.87(24)\times 10^{-14}$Hz cm^3. This data is used to determine the parameters $\sigma_1(\rho_{cc} + \rho_{aa}) + \sigma_2$ and $\lambda_1(\rho_{cc} + \rho_{aa}) + \lambda_2$

Parameter	Theoretical value [77]	Measured value
	$\AA^2$	$\AA^2$
λ_0	-11.8	$-21.7(2.8)$
$\sigma_1(\rho_{cc}+\rho_{aa})+\sigma_2$	0.262	0.385(30)
$\lambda_1(\rho_{cc}+\rho_{aa})+\lambda_2.$	-0.0204	0.021(14)
Ω	0.0779	$-0.055(35)$

Table 5.1: Summary of measured and calculated [77] spin-exchange frequency shift and broadening cross sections at a temperature of 0.5 K. We have assumed that $\rho_{cc}+\rho_{aa}=0.5$ in reporting the theoretical values.

the quantities $\lambda_0, T_0, \sigma_1(\rho_{cc}+\rho_{aa})+\sigma_2$, and $\lambda_1(\rho_{cc}+\rho_{aa})+\lambda_2$. The measured values determined in the previous sections are summarized in table 5.1 along with a few of the numerical results of Verhaar *et al.* [77].

We note several significant discrepancies between the measured values and the calculated values. The measured amplitude of λ_0 is nearly twice as big as that of the corresponding theoretical value. As determined, this quantity does not depend upon the absolute density calibration and hence should be quite reliable. The value determined for the combination of the σ's is also somewhat larger than the numerical value. This value does depend upon the absolute density calibration, however a 5% uncertainty has already been added due to the uncertainty regarding the density enhancement factor. The possible density dependence of this factor has not been included in the analysis. The numerical results [20] suggest that $\sigma_2 \ll \sigma_1$. If we assume $\rho_{cc}+\rho_{aa}=0.5$ as predicted [17] for the UBC CHM, we obtain $\sigma_1=0.770(60)$ $\AA^2$. There are however no experimental results which allow us to distinguish the relative sizes of $\overline{\sigma}_1$ and $\overline{\sigma}_2$ in this way.

Finally we note that the term depending upon the combination of λ_1 and λ_2 appears to be significantly different from zero but that it has the *opposite* sign from the numerically determined value. The calculations of Verhaar *et al.* [77] yield a *negative* value for this

combination of terms for all temperatures in the range 10^{-3} K to 10^{3} K if we assume that $\rho_{cc} + \rho_{aa} = 0.5$. In this experiment we observed a *positive* frequency shift. If we use the dimensionless ratio Ω (equation 5.7) as a measure of the contribution of the contribution of the hyperfine interaction to the total spin exchange induced frequency shift we find that Ω = -0.055(35) at a temperature of 0.500(3) K rather than the value 0.078 predicted in references [20, 77]. The theoretical spin-exchange cross sections are quite sensitive to the detailed form of the interatomic potentials used in the calculation. It is difficult to infer what effect the discrepancies between our measurements and the theoretical results listed in table 5.1 might have on the interatomic potentials. This is a question that could be best answered by the Eindhoven group led by Professor Verhaar.

Chapter 6

Background and Technical Aspects of the 1 K Experiments

We turn now to a study of mixtures of atomic hydrogen (H) and deuterium (D) confined by superfluid ℓ-^{4}He walls at cryogenic temperatures. This study comprises the first investigation of interactions between two different isotopes of hydrogen in zero field at these temperatures. At the same time we have also been able to make significant improvements in our understanding of the solvation of D into ℓ-^{4}He.

In this chapter we describe the apparatus used to perform the experiments. The results which were obtained are presented in the following chapter. The historical basis for the design of this experiment played an important role in the evolution of these studies and warrants mention before further details are discussed.

6.1 Historical context

Recently we observed for the first time the solvation of atomic D into ℓ-^{4}He [21, 22]. These experiments were performed using magnetic resonance on the β-δ hyperfine transition[1] of the D atom at 309 MHz in a 39 Gauss magnetic field. Atomic D densities were observed to decay exponentially with time which was quite unlike the two body decay rate (equation 3.14) which had been expected by analogy with the gas phase or surface recombination of two H atoms [37, 12]. The rate at which the atomic density decayed was also a very steep function of temperature, making the observation of D nearly impossible above 1.16

[1]This is the $\Delta F = 1, \Delta m_F = 0$ hyperfine transition. It passes through an extremum as a function of field at 39 Gauss.

K. On the other hand, the base temperature of the (pumped ^{4}He) cryostat was 1.08 K, so that the range of observation was very narrow. The decay of the D atom density was attributed to the solvation of D into the ℓ-^{4}He film coating the walls and subsequently adsorbing to the underlying substrate which was composed of solid D_2. The data was analyzed in terms of the simple theory presented in chapter 3 whereby the sample decay rate is:

$$\lambda = \frac{A}{4V}\overline{\alpha}_{l_g}\mu\overline{v}\exp\left(-\frac{E_S}{k_B T}\right). \tag{6.1}$$

In equation 6.1, E_S is the energy required to force a D atom into the ^{4}He liquid and μ is the ratio of the effective mass m^* of the D quasi particle inside the ℓ-^{4}He to the bare D mass m. $\overline{\alpha}_{l_g}$ is the thermally averaged probability that a D quasi particle striking the ℓ-^{4}He surface will leave the liquid and $\overline{v}$ is the mean thermal speed of the D atoms in the gas phase. This study indicated that E_S=13.6(6) K. Unfortunately the very narrow temperature range and the limited accuracy of the data made the determination of the prefactor to the exponential uncertain to more than an order of magnitude.

During these studies we observed startlingly strong broadening of the D atom magnetic resonance line: under some circumstances it could be more more than an order of magnitude larger than expected for a D atom gas. It was postulated that this excess broadening was due to spin exchange collisions between the D atoms, and H atoms which were present in the sample as a contaminant. Reynolds [22] calculated numerically the relevant broadening cross sections in the DIS limit (see chapter 3) and used this to infer the density of H atoms which were in the cell. In a separate experiment we used magnetic resonance on the a-c hyperfine transition of atomic H at 1420 MHz in order to verify this contamination by direct observation of the H. This work was done with a similar but considerably smaller cell filled with the same D_2 gas. The levels of contamination which were observed were roughly consistent with the broadening which had been observed

during the 309 MHz experiment. Work up to this point has already been reported in references [21] and [22].

Over time it was realized that a better measurement of the solvation energy opposing the penetration of ℓ-^{4}He by D might in fact be made by using the 1420 MHz apparatus to monitor the H atoms inside the cells (and indirectly the D atoms). The key to this experiment is the fact that at 1 K the thermally averaged spin-exchange broadening cross section for H-D collisions is more than two orders of magnitude larger[2] than the corresponding quantity for H-H collisions. As a result we found that it was possible to monitor both the H and the D densities simultaneously: following a $\pi/2$ tipping pulse, the initial power radiated by the spin system is related to the H density whereas the broadening of the transition is related to the D density[3]. Effectively we obtain the same type of information that a double resonance experiment[4] would yield. Note that it is more difficult to perform the analogous experiment (inferring the H density from the broadening of the β-δ transition of D) at 309 MHz since the broadening cross section for D-D collisions is expected to be comparable to that for H-D collisions [22].

The motivation for pursuing the 1420 MHz experiments further was twofold. Initially we hoped to reproduce and perhaps improve upon the original measurement of the solvation energy for D in ℓ-^{4}He. The 309 MHz experiment had originally been designed to study resonance recombination of D in magnetic fields [21], not to study the solvation of D into ℓ-^{4}He! Apart from this fact, the 309 MHz experiments were technically very demanding and the amount of attention which could be devoted to actually making measurements was rather limited. It was quite obvious that the 309 MHz apparatus

[2]This was predicted by Reynolds [22]. It has been verified by the experimental results presented in the next chapter.

[3]The determination of the absolute D density was initially dependent on the numerical calculations [22] for the broadening cross section. Later we were able to measure this cross section and thus obtain an absolute calibration.

[4]1420 MHz and 309 MHz simultaneously. An experiment of this type would be a rather daunting undertaking.

would have to be redesigned if further studies of the solvation of D into ℓ-^{4}He were to be performed with it. Modifications to the 1420 MHz apparatus were much easier to make.

As time passed, it became apparent that the 1420 MHz experiment would also yield a much richer variety of information about interactions between H and D atoms. In particular it was possible to study the various processes by which the D atoms in the sample recombine. By accounting for these alternate decay mechanisms which occur in parallel with the solvation process, it was possible to make a much 'cleaner' measurement of the solvation energy. It was also possible to make absolute measurements of the H-D spin exchange broadening and frequency shifts parameters. These measurements form an important complement to the study of H-H spin exchange presented earlier.

6.2 Experimental design

The apparatus and techniques used to carry out the experiments reported here were similar in many ways to earlier experiments performed in this laboratory using hyperfine magnetic resonance techniques [27, 22, 37]. These types of experiments have been summarized in reference [12]. In the following discussion we concentrate on the elements of the experimental design and the data analysis which were most essential to the studies presented in the next chapter.

6.2.1 The cryostat

These experiments were performed in a 8.9 cm inner diameter (i.d.) glass dewar with a second glass ℓ-N_2 jacket. The experimental cell and resonator housing were suspended in the main ℓ-^{4}He bath from above by a stainless steel tube incorporating several radiation baffles. During the experiments the entire resonator volume was flooded with ℓ-^{4}He from the main bath. This bath was cooled below 4.2 K by evaporative cooling. A roots

blower[5] backed by a rotary piston pump[6] were combined to achieve a pumping speed of about 600 cfm near the base temperature of the system. The dewar was elevated and moved to within 1.5 m of the pumping system in order to make maximum use of the available pumping speed. Bellows were used to mechanically decouple the experiment from the pumping system. The lowest temperature obtained in this way was 0.990(3) K. This represents a significant improvement[7] over the base temperature obtained in the 309 MHz experiments.

Two concentric high permeability metal shields[8] were wrapped around the outer dewar in order to shield out the earth's magnetic field. These shields were demagnetized using a 10 turn coil and AC currents up to 10 A. The residual field was subsequently mapped out using a Hall probe. Typically it was less than 5×10^{-7} Tesla. Fluctuations in this residual over the resonator volume were less than 1×10^{-7} Tesla.

6.2.2 The resonator

The 1420 MHz resonator used in this work was a Cu split-ring resonator [86]. It is illustrated in figure 6.1. It was 4.6 cm high and had an outer diameter of 2.54 cm. Two overlapping holes with different diameters were bored parallel to (but offset from) the axis of this cylinder. The larger hole (1.8 cm diameter) was used to contain the pyrex experimental cells (bulbs) described later. The second hole formed a relief volume between the capacitive gap in the split-ring and the sample bulb. The idea behind this design is to keep the fringing **E** fields near the gap away from the pyrex ($\epsilon \approx 5$) walls of the cells.

This assembly was located inside a 3.8 cm i.d. Cu rf shield such that the axis of the

[5]Leybold-Heraeus WA1000: 685 cfm displacement.
[6]Leybold-Heraeus E250: 162 cfm displacement.
[7]The effective range over which data could be taken was more than doubled.
[8]Co-netic foil: Perfection Mica Company-Magnetic Shield Division, 740 Thomas Dr, Bensenville Ill.

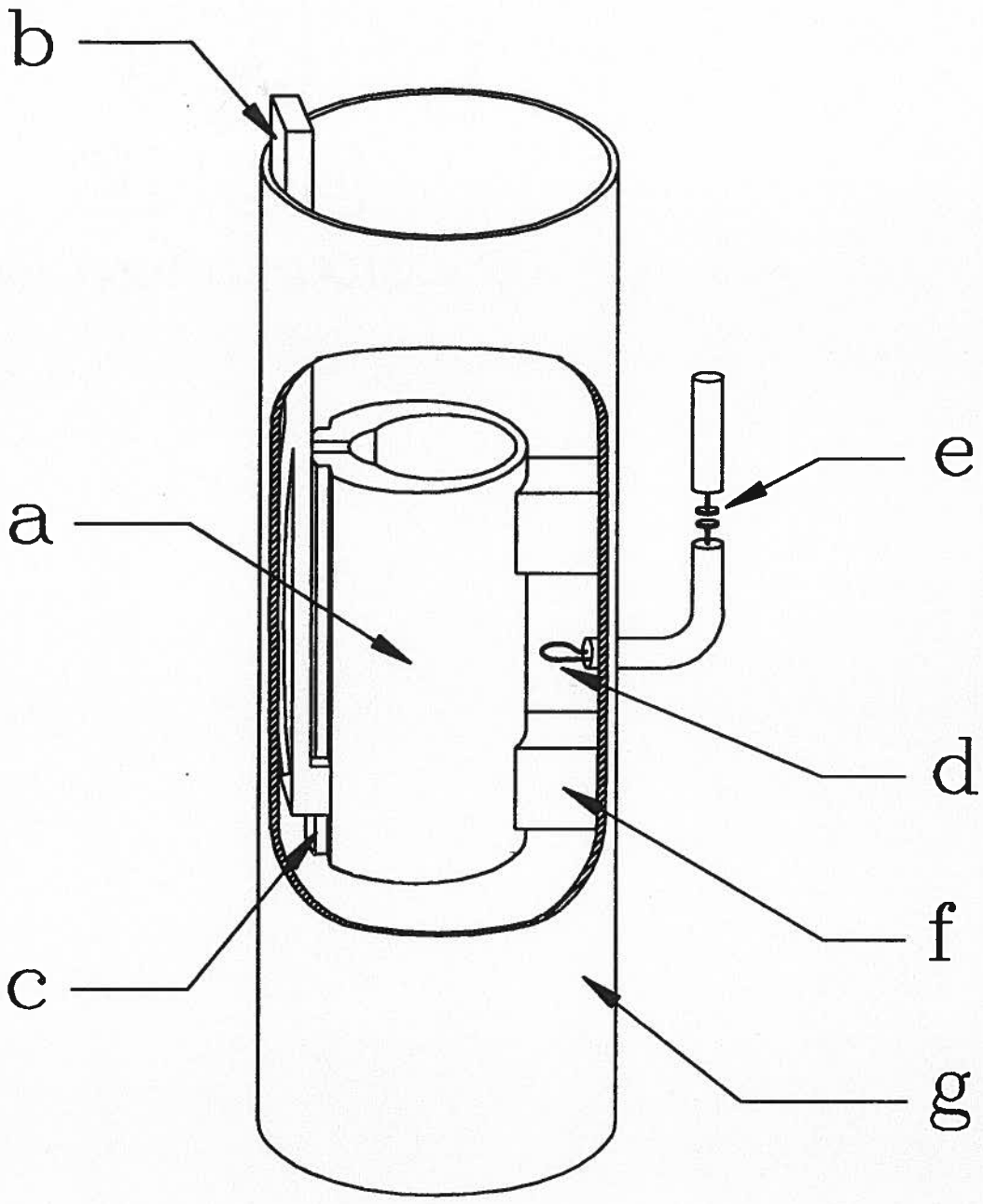

Figure 6.1: The 1420 MHz resonator used in order to study H, D mixtures at 1 K. Details show (a) the split-ring resonator [86] into which the sample bulb is inserted, (b) the teflon tuning bar and , (c) its tracking grooves, (d) the rf coupling loop and , (e) the adjustable coupling mechanism (schematic), (f) the teflon supports for the resonator, and (g) the resonator housing (rf shield). Further details are shown in figure 6.2.

bulb is aligned with the axis of the shield. This shield acts as a barrier to electromagnetic radiation and confines the rf energy to the resonator volume. The resonator was held in place by two teflon supports. It should be noted that a parasitic TEM mode is often encountered when using split-ring resonators. It is believed that some of the earlier studies of atomic H carried out in this lab [27] may have been affected by this problem. The much narrower shielding can used here ensures that this mode is pushed far from the frequencies of interest.

Grooves on either side of the 2.3 mm gap in the split-ring acted as a guide for the teflon slab which is used to capacitively tune the resonator. This bar was made slightly thicker than the available distance between the resonator and the shield. A cut in this bar made perpendicular to the split-ring gap allowed it to be squeezed into position and be held positively against the resonator. The tuning bar was moved along the length of the resonator by a mechanical linkage driven by a micrometer at room temperature.

A single rf coupling loop was brought into the resonator volume opposite the split-ring gap. A mechanically adjusted capacitance (shown schematically in figure 6.1) allowed adjustments to the coupling between the resonator and the external circuitry to be made. All work reported here was performed under conditions of critical coupling. Correspondingly, all reported quality factors are equal to one half the unloaded values (Q_0).

The quality factors of similar split-ring resonators at this frequency are generally about 6×10^3 at critical coupling. The Q of this resonator was intentionally lowered to about 1.5×10^3 to reduce the effects of radiation damping on the envelope of the FID's.

Prior to its use in these experiments the filling factor of the resonator was measured using a type I perturbation measurement as described in appendix B. A pyrex sleeve was placed inside the resonator during these measurements to mimic the walls of the sample bulb. This measurement was essential if the techniques outlined in appendix A were to be used to analyze the broadening of FID's. A filling factor $\eta = 0.37(4)$ was measured

for this geometry. The parameter of interest for determining the influence of radiation damping on a FID at a given atomic density is the quantity[9] $\eta Q \frac{\hbar\omega_0}{k_B T}$. This parameter was about 25% larger for this experiment than it was for the H-H spin-exchange experiments described in chapters 4 and 5.

6.2.3 The discharge

A cross sectional view of the resonator and its housing is shown in figure 6.2 with the sample bulb in place. The rf discharge is located in a separate encasement below the resonator volume. These regions are connected via a short Cu tube. This tube acts as a waveguide beyond cutoff and effectively isolates the two chambers. The discharge is a simple LC parallel resonant circuit tuned to 50 MHz. A coaxial line is tapped into the inductor about 1 turn away from its lower end (which is grounded) in order to form a step-up voltage transformer. The impedance of this circuit is roughly matched to the impedance of the external circuitry. RF power is supplied by an Arenberg pulsed oscillator[10]. Typical power levels of 400 W were used with 10 to 20 μsec discharge pulse durations.

A central access port is located above the sample bulb and opens into the resonator housing. This port allows for visual confirmation of the firing of the discharge. During several runs a 'stinger'[11] was passed down through this access hole and moved near to the sample bulbs in order to help initiate the first discharge inside the cell. On other occasions a ^{60}Co β source was used for this purpose. Generally no difficulties were encountered in firing the discharge after it had been fired for the first time.

---

[9] In the high temperature limit the thermal equilibrium population difference between the $|\, a \,\rangle$ state and the $|\, c \,\rangle$ state scales as $\frac{\hbar\omega_0}{k_B T}$. In the spin $\frac{1}{2}$ analogy this difference is related to the effective magnetization of the radiating spins.

[10] Arenberg Ultrasonic Laboratories, Boston MA. Model PG-650C

[11] A tungsten wire axially encased in an evacuated pyrex tube. Both ends of the wire pass through the sealed ends of the tube. High voltages are applied to the wire using a Tesla coil.

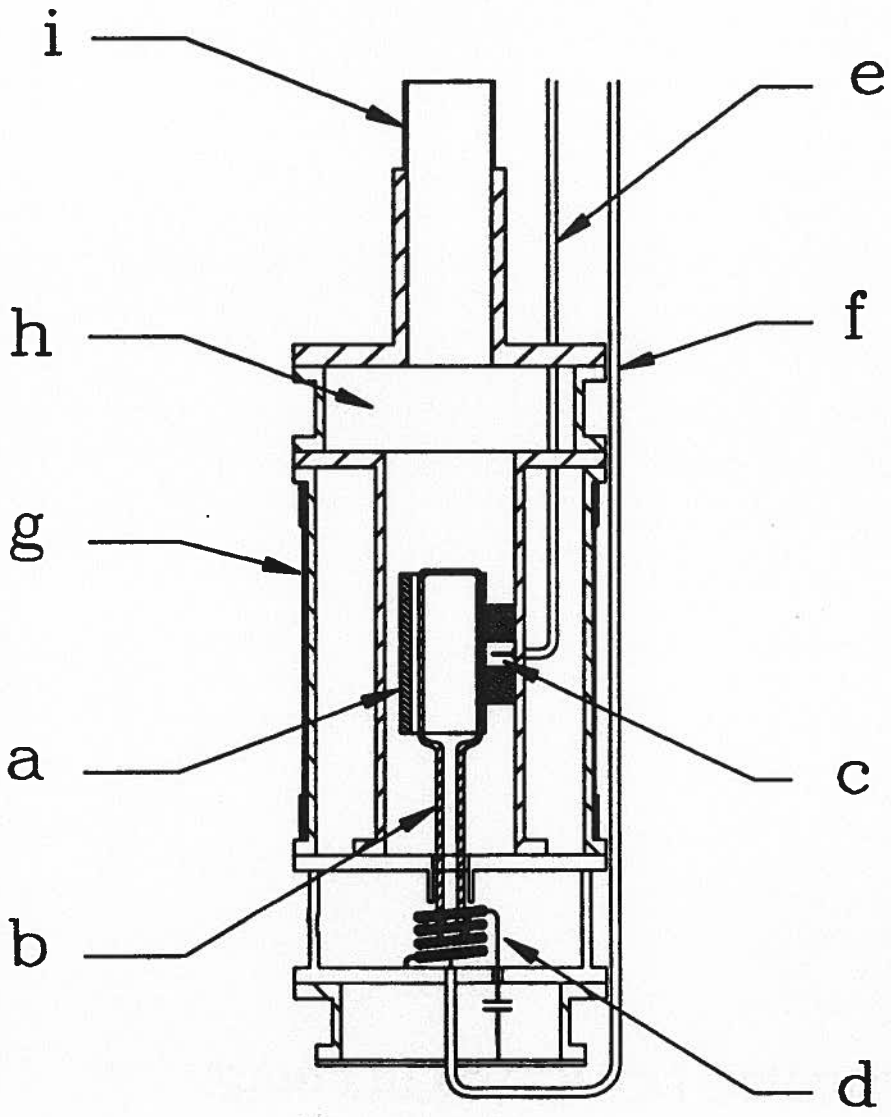

Figure 6.2: A cross sectional view of the low temperature experimental assembly which is submerged in the main ℓ-^{4}He bath. Details show (a) the Cu split-ring resonator (see figure 6.1), (b) the pyrex bulb containing the atomic samples, (c) the rf coupling loop, (d) the 50 MHz discharge, the coaxial lines leading to (e) the 1420 MHz spectrometer, and (f) the pulsed oscillator, (g) the bias solenoid and gradient coils, (h) the encasement for the variable tuning and coupling linkages (which are not shown), and (i) the support tube and central access port.

6.2.4 The bulbs

The cells used to confine the gases in this work were pyrex cylinders typically 1.7 cm in diameter and 4.6 cm long with a 0.5 mm wall thickness. One end of each tube was sealed and the other necked down to form a narrow tail. The main body of the cells filled the centre bore of the split-ring resonator while the tail extended into the rf discharge region (figure 6.2). The bulbs were held in place with nylon set screws (not shown).

Prior to filling the cells they were heated to 200 C and pumped on through a cold trap for 24 hours with a diffusion pump. The bulbs were then filled with 99.65% isotopically pure D_2 and UHP ^{4}He and sealed with a torch. The D_2 gas was from the same bottle[12] used in the 309 MHz experiments [21]. The hydrogen which is the central object in the present magnetic resonance experiments, either enters the cells as a contaminant in the D_2 gas or is liberated during the sealing process (exchange between D and some proton bearing material in the glass). On one occasion the H level inside the bulb was intentionally raised by adding some H_2 gas before sealing the cell. Typically cells were filled to a room temperature pressure of between 20 and 100 Torr of D_2 and 500 Torr of ^{4}He. At the temperatures of interest the D_2 forms a solid which coats the pyrex substrate. The ^{4}He forms a saturated superfluid ℓ-^{4}He layer which coats the inner walls of the cell. Any excess forms a pool in the tail of the bulb.

The A/V ratio of a sealed bulb was typically 3.5 cm^{-1}. This is about double the corresponding factor for the 309 MHz experiments. The tails comprised only about 5% of the total cell volume. It is important to realize that diffusion of atoms into the tail volume following a $\pi/2$ tipping pulse leads to a time dependent decrease in the effective filling factor for the cell. Radial diffusion times for both H and D [12, 38] lie in the range 30 to 150 msec in this experiment depending on the ^{4}He density. Longitudinal

[12]Bio-Rad Laboratories, Richmond CA

diffusion times are somewhat longer. Immediately following a $\pi/2$ pulse and before the atoms have had time to move, the appropriate filling factor is the full measured value. At times much longer than the spin homogenization time, the filling factor must be reduced by the appropriate ratio of volumes (see chapter 2). While this correction was minimized by keeping the tail volumes small, we felt it necessary to examine the effect of spin homogenization in the final analysis. All data was analyzed with both the pre- and post-homogenization values for η. In general, pre-homogenization values were used for work involving short T_2's and post homogenization values for work involving long T_2's. Uncertainties have been reported accordingly.

Once the cells have been cooled to 1 K, the thermal link between the cooling bath and the gas of H and D atoms passes through the glass walls, the solid D_2 substrate and the ^{4}He film. The dominant time constant for thermal diffusion through a slab of material of thickness L, density ρ, specific heat C, and thermal conductivity κ is given by

$$\tau = \frac{C\rho L^2}{\kappa\pi^2} \tag{6.2}$$

Using typical values for pyrex (C$\approx 3.1 \times 10^{-6}$J/g K [91], $\kappa = 1.2 \times 10^{-4}$W/cm K [92], and $\rho \approx 2.5$g/cm^3) we find that $\tau < 20$ μsec for our cells. The implication of this is that we can consider the inner wall of the pyrex cell to be at the temperature of the main ℓ-^{4}He (superfluid) cooling bath. The thermal time constant associated with the Kapitza resistances and thermal conduction through the ℓ-^{4}He film are about the same as τ. Radial thermal diffusion times in the ^{4}He buffer gas inside the cells are slightly longer but are only about 60 msec. All of these time constants are short and thus we did not expect to observe any heating phenomena associated with firing the discharge. None were observed.

6.2.5 Temperature measurement and regulation

Throughout this work temperatures were inferred from a measurement of the ^{4}He pressure above the main bath. In the first studies we report, pressures were measured using a McLeod gauge. Temperatures were maintained simply by regulating the pumping speed of the ^{4}He evaporation system. This was sufficient for measurements of *relatively* temperature independent quantities such as the H-D recombination cross section. Over time the vapour pressure measurement evolved into a much more accurate and precise measurement centred around the use of a capacitance pressure gauge. This technique also made it possible to implement temperature regulation based upon the ^{4}He vapour pressure above the main bath. This system proved indispensable in the final studies of the solvation of D into ℓ-^{4}He and the H-D spin-exchange frequency shift cross section. The details and characterization of this system are described in appendix D.

All temperature uncertainties which are reported are uncertainties in absolute temperature. Vapour pressure measurements were made through open stainless steel tubes extending to just above the ℓ-^{4}He bath. Where necessary small corrections due to thermomolecular pressure gradients [93] have been applied. In the later work, the uncertainties in relative temperatures (important in the measurement of the solvation energy and the ^{4}He buffer gas shift) are typically less than 100 μK.

6.2.6 Data collection

The rf electronics associated with this experiment are essentially the same as the system described in chapter 5. The data acquisition system is diagramed in figure 6.3. The 1420 MHz spectrometer was operated using the Rb frequency standard as the frequency reference. The low frequency beat signal between the atomic FID and the spectrometer LO's was fed to an analogue to digital converter and then passed to a computer for

storage. This system allowed us to accumulate data at sample rates up to one per 75 μsec. Typically a single FID was sampled 1000 times and then plotted on the computer screen along with simple diagnostics. The rate at which data (FID's) could be acquired was set by the thermal equilibration time for the spin degrees of freedom of the H system. The dominant equilibration process in these experiments was H-D spin exchange and hence T_2 for the FID, (related to T_1) gave a rough measure of this time. This was of course not true in experiments where the D density was low and H-H spin-exchange and magnetic relaxation were the dominant spin relaxation mechanisms. Detailed analysis of the FID's was performed after the experiment was completed.

Resonator Q's were measured in reflection as described in chapter 4. Absolute power calibrations of the detection circuitry were also made during each run.

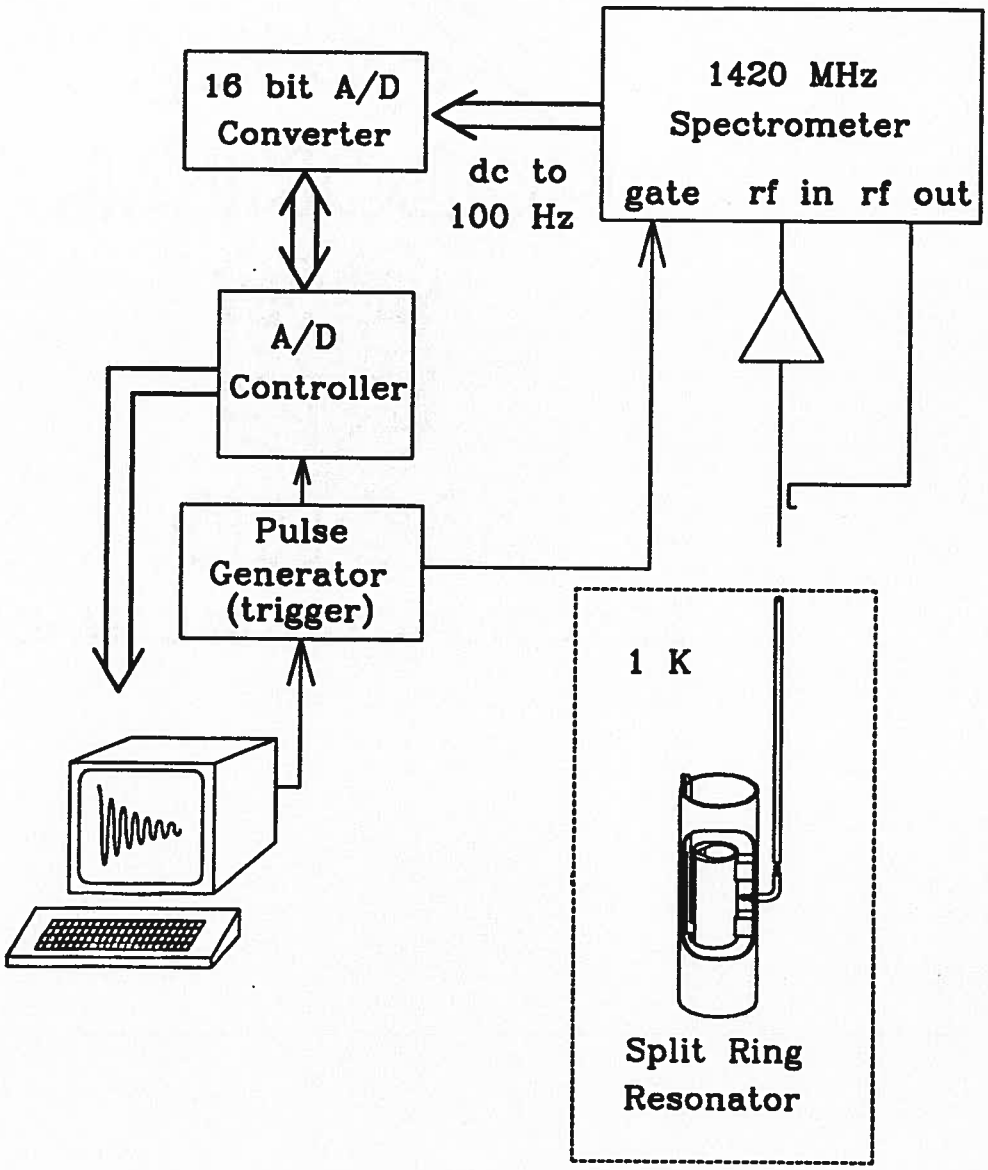

Figure 6.3: An outline of the data acquisition system used to generate trains of $\pi/2$ tipping pulses and to record the ensuing free induction decays. The 1420 MHz spectrometer is described in chapter 4.

Chapter 7

Experiments with H, D Mixtures at 1 K

In this chapter we summarize the experimental results of our studies of atomic hydrogen (H) and deuterium (D) confined by liquid helium (ℓ-^{4}He) walls at 1 K. They are carried out using magnetic resonance at the a-c hyperfine transition of atomic H at 1420 MHz. The evolution of these experiments from first being a means of verifying the contamination of samples of D with H, to their present state was described in the previous chapter. It was noted that by using magnetic resonance techniques to observe the H contamination in our D samples, it was possible to monitor, and to make absolute measurements of both the H and the D densities simultaneously and with a single resonator. This procedure, which is much less complicated than a double resonance technique, allowed us to study for the first time, interactions between two hydrogen isotopes confined by ℓ-^{4}He walls in zero field at 1 K.

The key to this experiment is the fact that the thermally averaged spin exchange broadening cross section[1] of the a-c hyperfine transition[2] of H due to H-D spin exchange collisions is more than two orders of magnitude larger than the corresponding cross section for H-H collisions. The broadening of the a-c hyperfine transition of atomic H due to

[1]Throughout this chapter we refer to spin exchange cross sections and rate constants without specifically indicating that these are thermally averaged quantities. All thermally averaged quantities are indicated with a line drawn above the appropriate symbol.

[2]The phrase 'of the a-c hyperfine transition of H (at 1420 MHz)' will often be omitted. It should be understood that all spin exchange parameters which are referred to here are with respect to this transition at zero magnetic field.

both H-H and H-D spin exchange collisions is [71, 22] :

$$\frac{1}{T_2^{se}} = \frac{1}{2}\overline{G}_{HH}n_H + \frac{3}{4}\overline{G}_{HD}n_D \tag{7.1}$$

$$\frac{1}{T_1^{se}} = \overline{G}_{HH}n_H + \overline{G}_{HD}n_D \ . \tag{7.2}$$

Reynolds [22] has calculated theoretical values for the broadening rate constants $\overline{G}_{ij}$ in the degenerate internal states (DIS) approximation at 1 K :

$$\overline{G}_{HH} = 7.8 \times 10^{-13}\text{cm}^3/\text{s} \tag{7.3}$$

$$\overline{G}_{HD} = 2.4 \times 10^{-10}\text{cm}^3/\text{s} \ , \tag{7.4}$$

values essentially independent of temperature between 1.0 and 1.5 K. Dividing by the appropriate mean relative speeds for the colliding atoms ($\overline{v}_{HH}$ or $\overline{v}_{HD}$) at 1 K, we obtain

$$\overline{\sigma}_{HH} = 0.38\text{Å}^2 \tag{7.5}$$

$$\overline{\sigma}_{HD} = 140\text{Å}^2 \ . \tag{7.6}$$

The result for H-H collisions is in agreement with the more sophisticated coupled channel calculations by Verhaar *et al.* [20] which yield $\overline{\sigma}_{HH} = 0.40$ Å^2. The only experimentally determined value[3] for $\overline{\sigma}_{HH}$ at 1.1 K is 0.43(3) Å^2 [27].

The result of this large difference in spin-exchange cross sections is that for comparable H and D densities, the broadening of the a-c hyperfine transition of H is completely dominated[4] by H-D spin exchange collisions. Consequently the amplitude of a free induction decay (FID) following a $\pi/2$ tipping pulse at the a-c transition frequency gives a measure of the H density in the cell (n_H) while the decay time of the envelope provides a simultaneous measure of the D density (n_D). Under the right conditions $\overline{G}_{HD}$ can be

[3]The value reported in references [37, 12] was in error (high) by a factor of $\sqrt{2}$.
[4]Other broadening mechanisms being neglected.

measured and thus it is not necessary to rely on the numerical prediction (equation 7.4) to calibrate n_D.

It is important to realize throughout the presentation that follows, that the conclusions which are drawn were often based upon inferences from several experiments, including our earlier studies of D at 309 MHz [21] and studies of pure H at 1420 MHz [12].

7.1 The basic experiment

The sample bulbs are filled with a mixture[5] of D_2 and ^{4}He gases as described in the previous chapter, and cooled to 1 K. As the temperature is lowered the D_2 first forms a solid on the inner walls of the bulb and is then covered by a layer of superfluid ℓ-^{4}He. We start the experiment by firing the rf discharge. This liberates both H and D from the molecular ice underlying the ℓ-^{4}He film. These atoms interact with each other and with the ℓ-^{4}He coated walls: recombination processes (H-H, H-D, and D-D) reduce the atomic densities inside the cell; the D atom density also decreases due to the solvation of D atoms into the ℓ-^{4}He film and subsequent adsorption to the substrate.

At any instant in time the fraction of D atoms in the cell with sufficient energy to penetrate the film is low; however collisions with ^{4}He atoms ensures that a thermal distribution of kinetic energies is maintained. As a result there is a constant flux of D atoms passing through the film. At high temperatures ($T > 1.2$ K) essentially all of the D atoms penetrate the film within seconds of the discharge. At lower temperatures this decay rate is slower but solvation is *usually* the dominant mechanism by which the D density decays in the experiments reported here.

In their simplest form, our measurements consist of the application of a train of

[5]Generally H is present in the cells only as a contaminant.

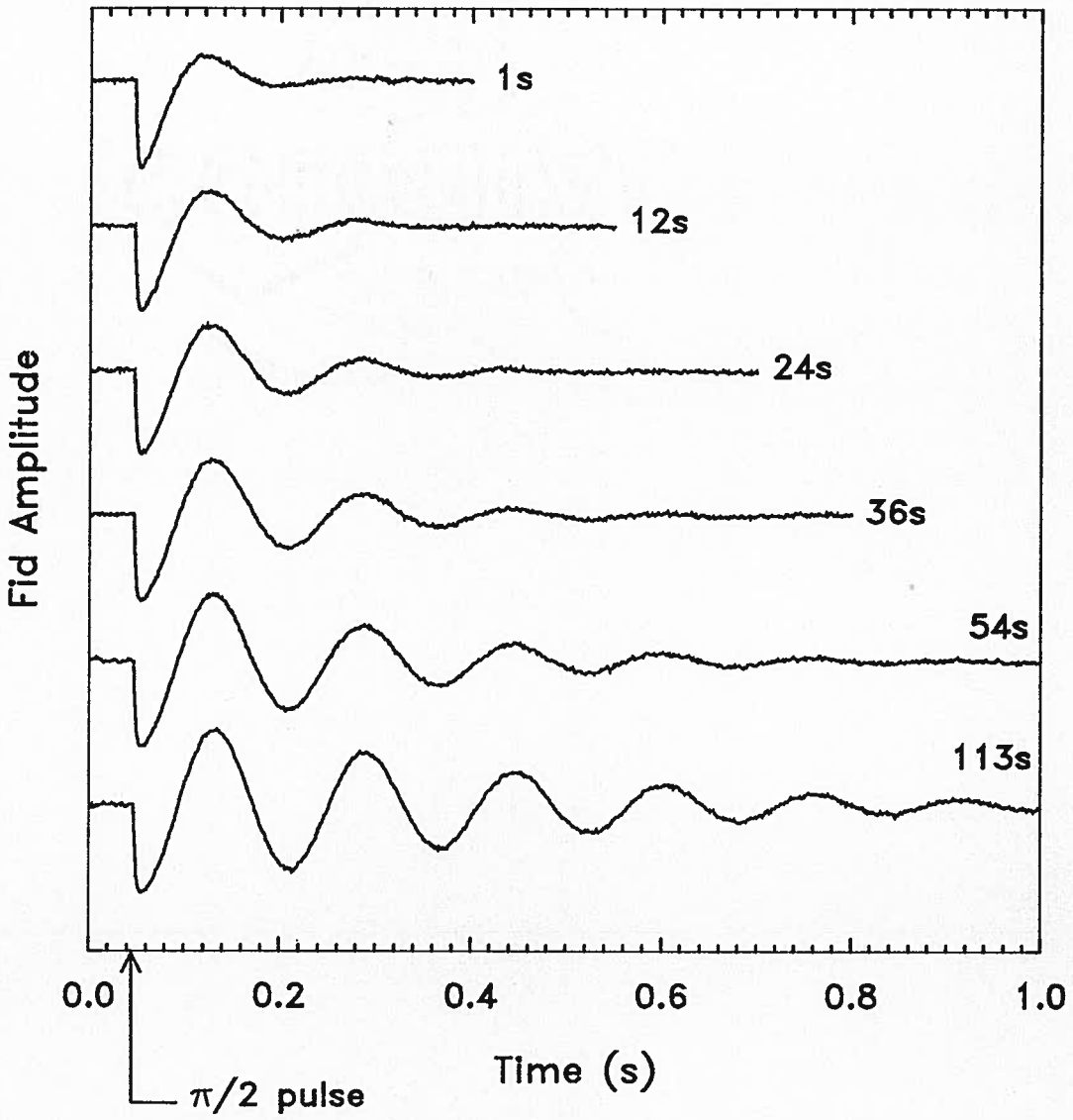

Figure 7.1: The FID's resulting from the application of a series of $\pi/2$ tipping pulse at the a-c hyperfine transition of H (1420 MHz) to a mixture of H and D at 1.001(3) K. The labels on the right hand side of the decays indicate the time following the discharge pulse at which the $\pi/2$ pulse was applied. An arbitrary constant has been added to each decay in order to display the data in this fashion. The beat frequency is arranged to be at a convenient value via the synthesizer setting.

$\pi/2$ tipping pulses at the a-c hyperfine transition of H to the sample. These pulses are separated by a variable time interval. Each pulse interrogates the atomic system, returning information about both the number of H and D atoms in the cell at that time. In figure 7.1 we show an example of the FID's which result from such a pulse train. This particular data was taken at a temperature of 1.001(3) K where the lifetime of the D atoms in this cell due to solvation is about 30 seconds. An arbitrary constant has been added to each decay in order to display them in this fashion. The label on the right hand side of each decay indicates the time at which the $\pi/2$ pulse was applied following the discharge pulse. The most obvious change in the data over this period of time is the increase in the apparent decay time T_2^* associated with the envelope of the FID. It was this type of observation which initially piqued our interest in this system and led to the present studies. We attribute this time dependent broadening to the presence of D atoms in the cell. A simple analysis shows that the rate at which the D atoms disappear is roughly exponential and that the temperature dependence of this rate is about what one would expect due to the solvation of D in the ℓ-^{4}He film [21]. A more detailed analysis indicates that the data also contains contributions from recombination processes.

7.2 Analysis of the data

The notation in this chapter deviates somewhat from that in the magnetic resonance literature and thus requires special mention at this point. We refer to the *apparent* decay time of the FID as T_2^*. T_2 is used for the *effective* relaxation time once the effects of radiation damping have been accounted for. In the strictest sense this latter quantity should be denoted T_2^* as it may still contain a contribution from magnetic field inhomogeneities. We reserve the notation T_2^{se} for the *true* spin-spin relaxation time due to spin exchange collisions, once all other effects have been accounted for.

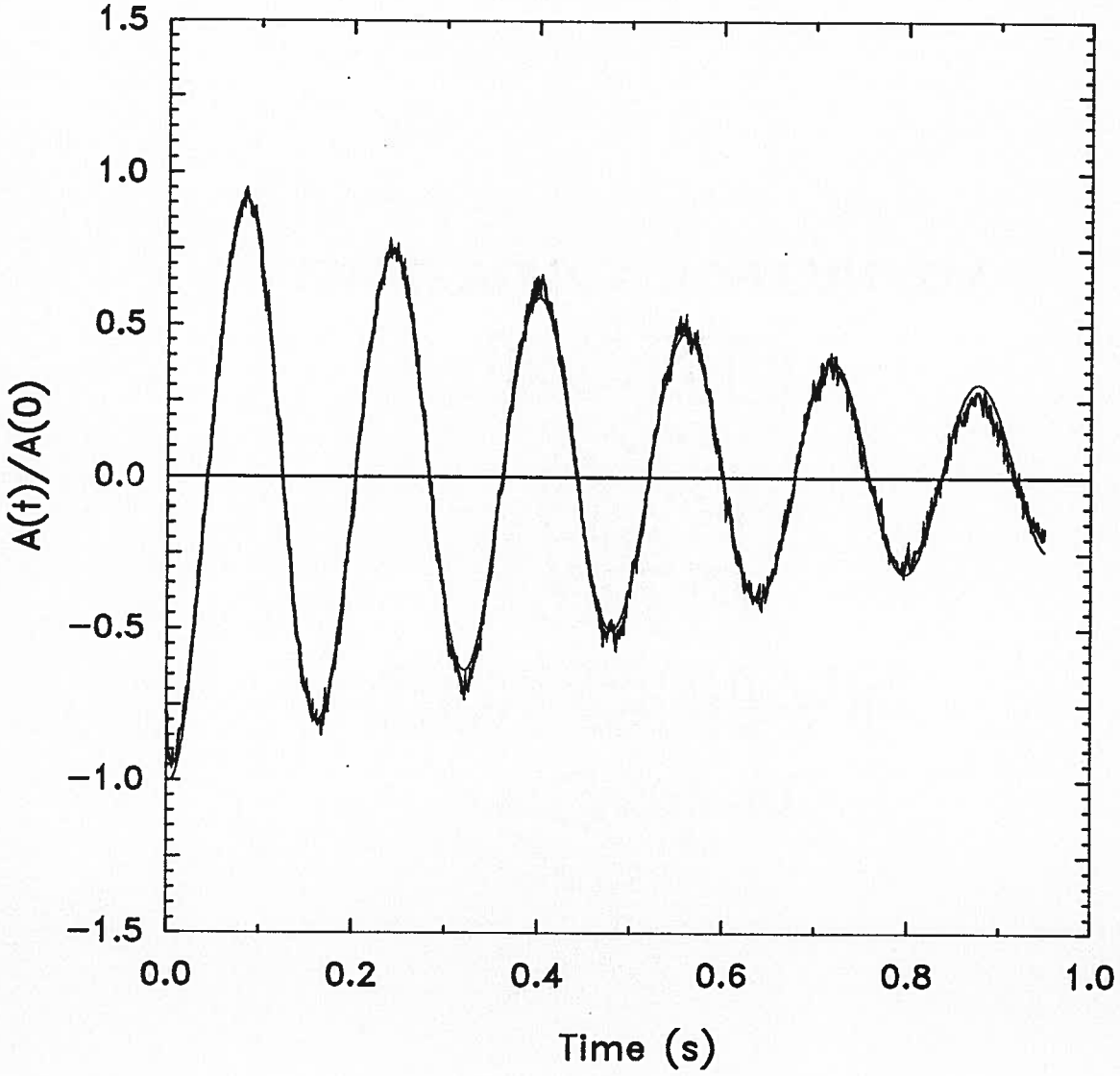

Figure 7.2: A FID taken at 1.000(3) K and the numerical fit to the data. The H density is $n_H = 8.6 \times 10^{10} cm^{-3}$. Radiation damping accounts for about one third of the of the decay of the FID envelope. In the example chosen here, T_2^{-1} is approximately equal to the residual broadening which, as explained in the text, sets the detection threshold for the D atom density. The normalization is such that the amplitude of the fit to the data is initially one.

Immediately following the discharge pulse T_2^* is dominated by H-D spin exchange collisions and the FID envelope is roughly exponential. As time progresses and the broadening due to H-D collisions decreases, radiation damping begins to play an increasingly more important role in determining T_2^*. We have analyzed all of the FID data by fitting the decays to the numerically integrated differential equations outlined in appendix A in order to properly account for the effects of radiation damping. In these fits, the filling factor, resonator Q, and the power calibration of the signal are entered as measured quantities. The free parameters in the fits are T_2, T_1, the beat frequency, the H density (signal amplitude) and an initial phase angle. If the data is not analyzed in this way it becomes difficult to determine n_H and T_2 accurately when the D density is low and radiation damping is beginning to influence the FID's.

In figures 7.2 and 7.3 we show examples of the numerical fits to the FID's in different regimes. In figure 7.2 $n_H = 8.6 \times 10^{10}$ cm^{-3} at a temperature of 1.000(3) K. Radiation damping accounts for about one third of the observed damping. The residual T_2 (≈ 1 s) is very close to the 'infinite time' relaxation time T_2^∞ (*i.e.* long after the discharge pulse when all of the D atoms are expected to have left the gas phase). The observed residual broadening is in general greater than that expected from H-H spin exchange alone [27]. The excess is due to factors such as field inhomogeneities, magnetic relaxation, and the diffusion[6] of H atoms out of the resonator volume. In general this residual broadening is not well reproduced between cooldowns, however it is reproducible throughout a given run. It is a weak function of the H density. In essence, the combined effects of the processes which lead to this residual broadening set the practical detection threshold on the D atom density. At this level, 10% changes in the broadening are easily detected. Using the numerical results [22] for $\overline{G}_{HD}$ and equation 7.1 we infer a threshold detection

[6]Diffusion does not strictly give rise to an exponential FID; however it does lead to a shortening of the effective T_2 determined in the fit.

limit near[7]

$$n_D\,|_{\text{thresh.}} = \frac{1}{10}\left(\frac{4}{3}\right)\frac{(T_2^{\infty})^{-1}}{\overline{G}_{HD}} \approx 2 \times 10^9 \text{cm}^{-3}\,. \tag{7.7}$$

This is comparable to the H atom detection limit with the present system.

In the second example of a fit to a FID, shown in figure 7.3, the H density has been increased to $1.8\times10^{11}\text{cm}^{-3}$ but more importantly there is considerable broadening due to H-D spin-exchange collisions. The FID envelope yields $T_2 = 60$ ms. This broadening (T_2^{-1}) is well above the detection limit and we infer[8] that $n_D \approx 9 \times 10^{10}\text{cm}^{-3}$. In the following sections we examine the various parameters determined from these numerical fits in more detail.

The dominant decay of the FID's is set by T_2 however T_1 also makes a contribution and can be determined from the numerical fits to the data. This procedure is outlined in appendix A. T_1 is a measure of the time taken for the longitudinal component of the (fictitious) magnetization to relax to its thermal equilibrium value following a tipping pulse. Information about T_1 is contained[9] in the rate at which the instantaneous damping of the FID changes as a function of time. This relationship is described explicitly in appendix A.

The parameter T_1 is not determined to the same precision as T_2 in this type of analysis. In particular the relative error in T_1 is large both when the number of zero crossings in the FID's is small, and when radiation damping dominates the FID. The first situation occurs when the dominant decay time of the FID (*i.e.* T_2) is comparable to, or shorter than, the oscillation period of the beat frequency between the radiating atoms and the local oscillator of the spectrometer. T_1 is determined from the *rate* at which the instantaneous damping of the FID changes. Without any zero crossings in the data the

[7]H-H spin exchange broadening is completely neglected in this simple estimate.

[8]Again we have used the numerical values for $\overline{G}_{HD}$.

[9]Radiation damping also causes the longitudinal component of the magnetization to relax and and must be taken into account.

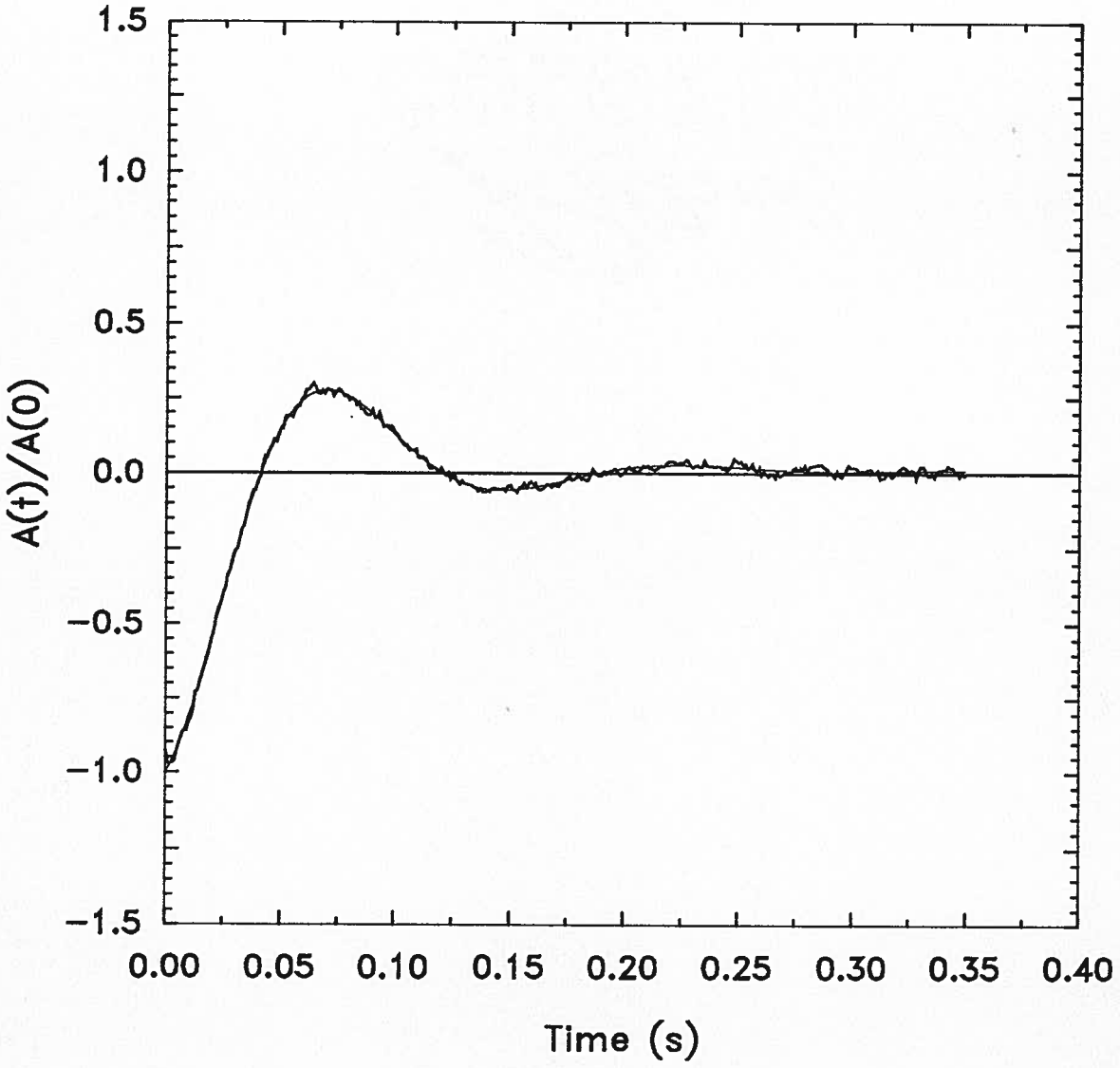

Figure 7.3: A FID taken at 1.001(3) K shown with the numerical fit to the data. The data has been normalized to the fit amplitude at t=0. Considerable broadening due to H-D spin exchange collisions is apparent. The numerical results [22] for $\overline{G}_{HD}$ imply a D atom density $n_D \approx 9 \times 10^{10}$ cm^{-3}. The H density is $n_H = 1.8 \times 10^{11}$ cm^{-3}.

damping of the FID is easily confused with an *apparent* frequency shift. On the other hand when radiation damping dominates the FID, T_1 makes very little contribution to the relaxation of the longitudinal magnetization and thus it is only poorly determined.

7.2.1 T_1 and T_2

An example of the simultaneous time evolution of T_1 (squares) and T_2 (triangles) as determined from the fits to a series of FID's following a single discharge pulse is shown in figure 7.4. Initially the FID decay time is much shorter than that caused by radiation damping. In this case T_2 is set quite accurately by the envelope decay time. The relative error in T_1 on the other hand can be large if the number of zero crossings in the data is of order 1. Care has been taken in the analysis of all data in this regime to ensure that the zero crossings are well represented by the fits.

Both T_1 and T_2 increase with time and eventually 'saturate'. This saturation occurs at different times for the two parameters. Just as was the case with T_2, the saturation limit for T_1 sets a threshold limit on the lowest D densities which can be inferred using equation 7.2. In general we find that the practical range over which T_1 data can be used to infer n_D is less than the useful range over which T_2 can be used.

A π-$\pi/2$ pulse sequence can be used to verify the determination of T_1 from the FID data. In the spin $\frac{1}{2}$ analogy, a π pulse inverts $\tilde{\mathbf{M}}_z$ which subsequently relaxes back to its thermal equilibrium value by T_1 processes. Radiation damping does not play a role in this relaxation since the transverse magnetization remains zero. A $\pi/2$ pulse which interrogates the relaxing magnetization after a time τ yields a measure of the amplitude of $\tilde{\mathbf{M}}_z$ at that time. If $\tau = T_1/\ln(2)$ then $\left|\tilde{\mathbf{M}}_z\right| = 0$ and no FID is observed after the $\pi/2$ pulse. By changing τ until a null signal is observed, a measurement of T_1 can be made. We have measured T_1 in this way following several $\pi/2$ pulse trains. In each case the results are in agreement with the values of T_1 determined from the FID data.

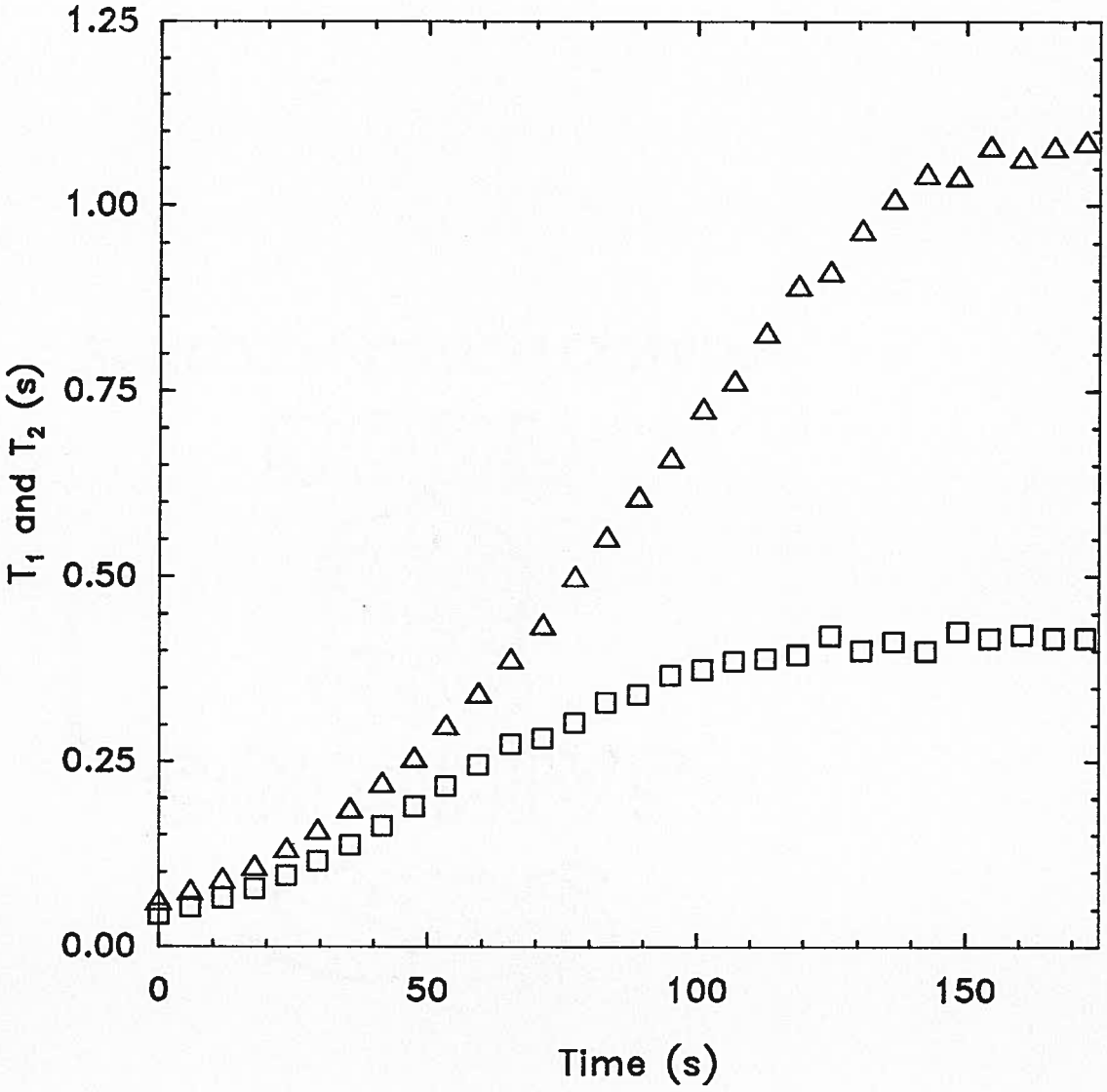

Figure 7.4: The fit parameters T_1 (squares) and T_2 (triangles) determined from a sequence of FID's following a single discharge pulse at t=0. The results for T_1 are in agreement with measurements made using a π-$\pi/2$ pulse sequence in the saturated limit. This data was taken at 1.001(3) K.

The long time limiting values of these relaxation rates ($1/T_1^{\infty}$ and $1/T_2^{\infty}$) are subtracted from the relaxation rate data obtained from the fit to the FID's ($1/T_1$ and $1/T_2$) and the residual relaxation is attributed to H-D spin-exchange collisions. The residual broadening rates are denoted $1/T_1^{se}$ and $1/T_2^{se}$. The ratio of T_1^{se} to T_2^{se} determined in this way is essentially $\frac{3}{4}$; the ratio which is expected due to spin-exchange collisions between heteronuclear species of H (see chapter 3). A typical example of this ratio immediately following a single discharge pulse[10] is shown in figure 7.5. This is an important check that the residual broadening is indeed due to H-D spin-exchange collisions. Repeated measurements of this ratio indicate that $T_1^{se}/T_2^{se} = 0.74(2)$. This is the only measurement of this ratio for H-D spin-exchange collisions that we are aware of below room temperature [76].

An example of the broadening $1/T_2^{se}$ which remains after the subtraction of the residual $1/T_2^{\infty}$, and which is attributed wholely to H-D spin-exchange, is shown in figure 7.6. This broadening is proportional to the D atom density n_D inside the cell: using the numerical result 7.4 for $\overline{G}_{HD}$ we infer an initial D density of 6.6×10^{10} cm^{-3}. This is about 40% of the H density in the cell at the same time.

7.2.2 The H density

An example of the time dependence of the H density inside the cell as determined from the power emitted by the H atoms following a series $\pi/2$ pulses is shown in figure 7.7. This data is from the same decay as that from which the broadening data of figure 7.6 is derived. It has been plotted separately in order to expand the vertical scale.

Before proceeding further we want to point out the existence of three different time scales. The first of these is associated with the drop observed in the H density immediately following the discharge. The amplitude of this drop depends upon the D density inside

[10] In this example the relative error in T_1 becomes too large to determine T_1^{se}/T_2^{se} at longer times.

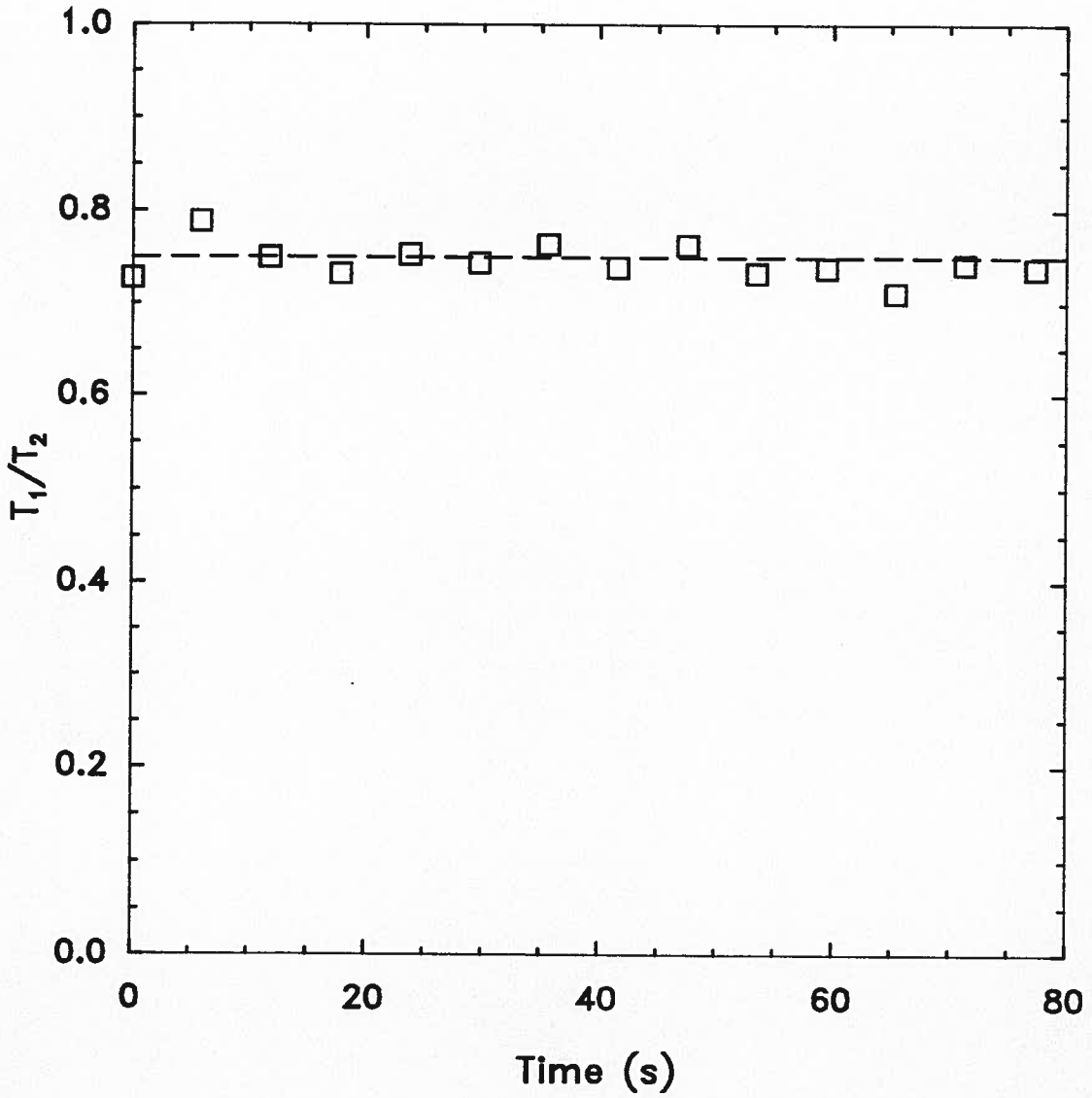

Figure 7.5: The ratio T_1^{se}/T_2^{se} as a function of time following the discharge pulse. The dashed line indicates the ratio $\frac{3}{4}$ which is expected due to spin-exchange collisions between H and D in the DIS limit. The average value of this ratio determined from repeated measurements is 0.74(2).

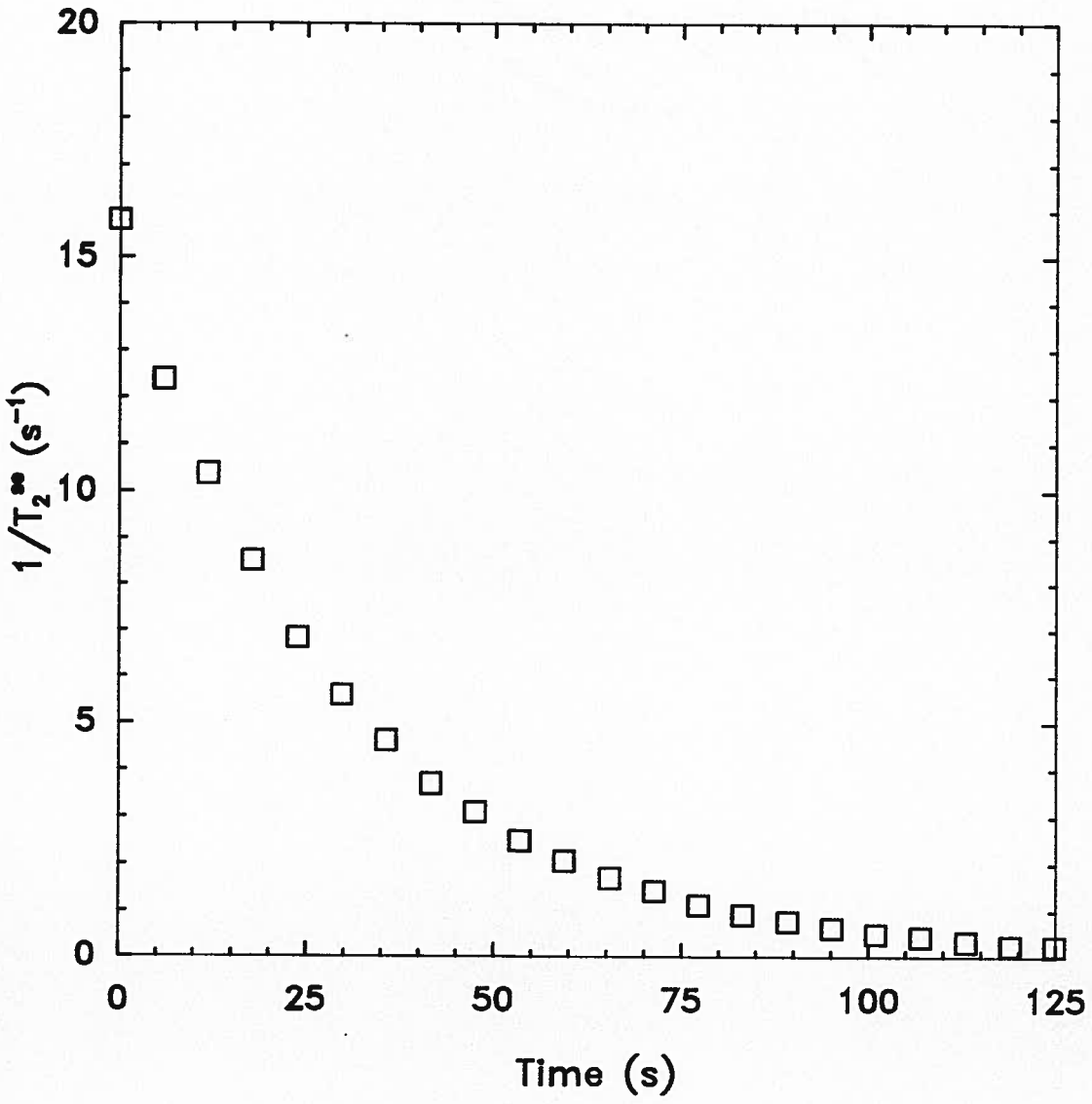

Figure 7.6: An example of the time dependence of the broadening $1/T_2^{se}$ which is wholely attributed to H-D spin exchange collisions (*i.e.* residuals have been subtracted). The decay of $1/T_2^{se}$ (which is proportional to the D atom density) is approximately exponential. Using the theoretical result $\overline{G}_{HD} = 2.4 \times 10^{-10}$ cm^3/s [22] the initial D density is 6.6×10^{10} cm^{-3}. The measured H density is about 9×10^{10} cm^{-3} (see figure 7.7). The temperature of the cell is 1.001(3) K.

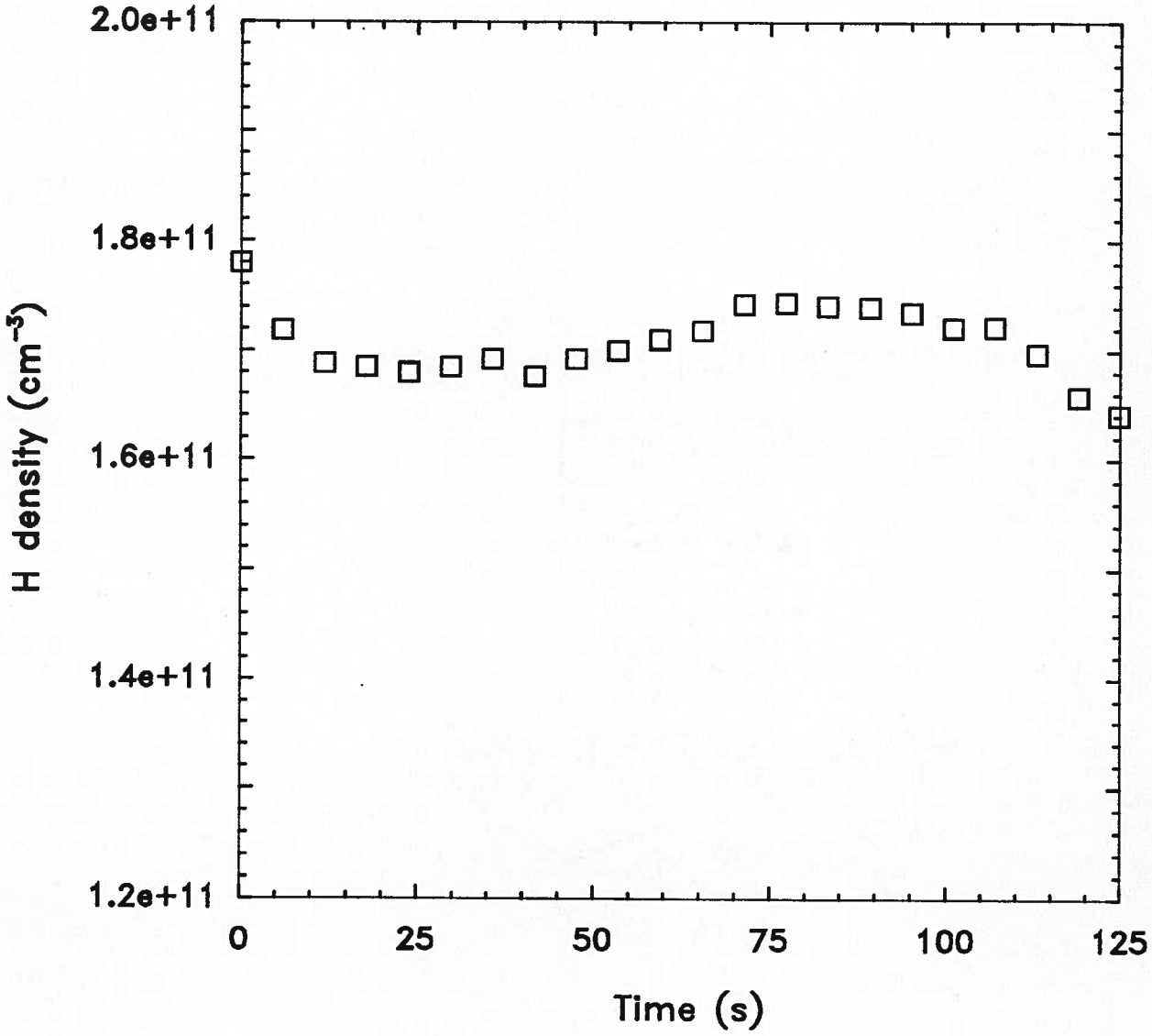

Figure 7.7: The H density in the sample bulb during the broadening measurements shown in figure 7.6. Three time scales are distinguished. The first period lasts tens of seconds and is associated with the recombination of H and D immediately following the discharge. The second time scale lasts hundreds of seconds and is associated with the delayed source of H atoms. This 'peak' is thought to be due to H liberated in a chemical exchange reaction occurring on the substrate. The third time scale is governed by H-H gas phase recombination. The characteristic time for this reaction is measured in thousands of seconds.

the cell and we attribute it to the recombination of H and D to form molecular HD. This reaction is discussed in the next section. The second time scale is associated with the *increase* in n_H, which follows the initial decrease. In figure 7.7 this increase begins about 50 s after the discharge. During other cool downs, the time at which this increase begins is delayed for as long as 200 s. This unusual feature was quite unexpected. It seems to be a source of atomic H which is delayed from the initial discharge. A analogous feature is not observed in samples containing only H_2. The third time scale is set by the gas phase recombination of two H atoms to form H_2. This process has been studied previously by Hardy *et al.*[11] and is known to occur on a time scale of thousands of seconds at these temperatures and densities. For a short period of time following the apparent source of H atoms, the decay of the H atom density is somewhat faster than expected based on the rate reported by Hardy *et al.* After a few hundred seconds the decay rate slows down and is consistent with the earlier report. We have not studied this part of the decay in detail: it is not understood why the decay of the H atom density initially seems to be faster over this time period.

The bulk of the H impurity in our samples is likely present as HD. In addition, the gas phase recombination of H and D ensures that the surface of the substrate [12] underlying the ℓ-^{4}He film is covered with HD. We postulate that D atoms, which penetrate the film and adsorb to the surface, encounter and react chemically with this HD :

$$HD + D \rightarrow D_2 + H \, . \tag{7.8}$$

A similar (exothermic) reaction has been observed before in D_2-HD mixtures when atoms are produced by irradiation [94, 95]. In this picture the H atom which is liberated is subsequently ejected from beneath the film and returned to the gas phase. These atoms

[11]The recombination rate constant k_{HH} determined by Hardy and his coworkers was 0.20×10^{-32}cm^6/s at 1 K. The value reported in [37] and [12] was in error by a factor of $\sqrt{2}$. The proper value was reported in [27].

[12]All molecular isotopes of hydrogen pass easily through the ℓ-^{4}He film unlike H [35].

appear in our data as a delayed source of H. Simple estimates made by balancing the van der Waals attraction of the D_2 substrate to a D atom [96] against the repulsive force due to the increasing ℓ-^{4}He density near the substrate [35, 61] seem to indicate that the D atom is bound to the surface. Similar estimates made for H atoms suggest that the H atom is not bound. These calculations are rather speculative since the solidification of the ℓ-^{4}He near the substrate is likely to play an important role. For this reason we do not present the details of this calculation here.

Details of the diffusion of D on the substrate have not been studied systematically however a few observations are worth noting. If the sample bulb is cooled slowly (10 to 20 K/hour) below 20 K, the delayed source of H atoms occurs within 50 to 100 seconds of the discharge. We also note that the lower the temperature at which the data is taken (and hence the slower the D solvation process) the further the peak is delayed. Faster cooling of the bulb seems to delay the release of H from the surface for up to several hundred seconds. In the later case the fast cooling rates may result in a more convoluted substrate. If a 'cold spot' were to develop at some point on the walls of the cell during the cooling procedure, a large fraction of the D_2 might concentrate at this point. Faster cooling rates also tend to result in lower (maximum) H densities at a given discharge power; this may be a result of less fractionation of the HD during cooling. Under these conditions we have been able to obtain $n_D^o \gg n_H$ and we find that the integrated number of atoms from the delayed source is equal to the number of H atoms which are lost due to H-D recombination. This seems to suggest several things. First of all, it would appear that each H atom which is scavenged from the gas phase is eventually liberated from the surface by a D atom (in this case). As there are many D atoms which reach the surface and yet only a limited number of H atoms which return to the gas phase, it is likely that there are very few H atoms near the substrate surface immediately following the discharge. Finally, as the source of H atoms appear to be delayed from the time at which

the D atoms penetrate the liquid, it would seem that the D atoms are at least somewhat mobile on the surface of the substrate. In situations in which the sample was cooled slowly, we do not see the same agreement between the number of H atoms scavenged by D and the number which are eventually released from the surface. Likely there is much more HD on or near the substrate in this case. The observation of this delayed source of H gives important support to our picture of the solvation process in that it shows that D atoms and not D_2 molecules have actually penetrated the film.

7.2.3 H-D recombination: Measurements with $n_H \gg n_D$

The decay of the D atom density due to H-D recombination in the cell occurs at the rate:

$$\frac{\dot{n}_D}{n_D} = -K_{HD} n_H \ . \tag{7.9}$$

If this reaction is predominantly catalyzed by gaseous ^{4}He atoms in the cell (as opposed to atoms in the ℓ-^{4}He walls) then we expect $K_{HD} = k_{HD} n_{He}$. In order to study this recombination process a bulb was prepared with additional hydrogen added in the form of H_2 gas. The isotopic ratio of H atoms to D atoms in the resulting mixture was 0.06. Using this cell it was found that following a discharge pulse at low temperatures, $n_H \gg n_D$. Typical densities were $n_H \approx 5 \times 10^{12}$ cm^{-3} and $n_D^o \approx 6 \times 10^{10}$ cm^{-3}. Measurements of T_1 for the H atoms using a π-$\pi/2$ pulse sequence were made as a function of time after firing the discharge. Data for each series of T_1 measurements was fit to the form

$$\frac{1}{T_1} = \alpha \exp(-\zeta t) + \beta \tag{7.10}$$

In effect the first term in this equation represents $1/T_1^{se}$ while the second is $1/T_1{}^{\infty}$. In figure 7.8 the exponential decay rate ζ is plotted as a function of the H density in the cell for a series of measurements made at constant temperature (and hence constant ^{4}He density). In a later section it is shown that these decay rates are much faster than the

rate at which D atoms are lost due solvation at this temperature. A straight line fit to the data gives an H-D recombination rate constant $K_{HD} = 4.0(2) \times 10^{-14}$ cm^{-3}/s.

By changing the temperature of the atomic gas only slightly, the ^{4}He density above the ℓ-^{4}He film can be changed quite dramatically. In figure 7.9 the ratio ζ/n_H is plotted as a function of the ^{4}He density inside the cell. Again a linear relationship is observed which further indicates that this recombination is occurring in the gas phase catalyzed by ^{4}He atoms (H + D + ^{4}He $\rightarrow$ HD + ^{4}He). From the slope of this plot we find $k_{HD} = 2.5(1) \times 10^{-32}$ cm^6/s. We have assumed that k_{HD} is independent of temperature over the narrow range of temperatures at which data was taken. The value obtained for k_{HD} is more than an order of magnitude larger than the corresponding value $k_{HH} = 0.20(3) \times 10^{-32}$ cm^6/s for H-H gas phase recombination at this temperature [27]. The H-H-^{4}He recombination problem has been tackled theoretically by Greben *et al.* [65] with remarkable success.[13] No calculations of the H-D rate constant have been made.

7.2.4 H-D and D-D recombination: An absolute calibration of n_D

The measurement of k_{HD} presented in the previous section was independent of the absolute D density inside the cell. In this section a second measurement of k_{HD} which does depend on n_D is presented. By comparing these two measurements we arrive at an absolute calibration for the D density or in effect, a measurement of the H-D spin exchange broadening rate constant $\overline{G}_{HD}$.

This study was carried out on a cell which was cooled quickly below 20 K. This resulted in a much lower H density and further delayed the source of H atoms from the chemical reaction of equation 7.8 occurring on the substrate. Throughout this experiment we operated with $n_D^o \gg n_H$ where n_D^o is the D density immediately following the discharge. After a typical discharge pulse $n_D^o \approx 5\times10^{11}$ cm^{-3} while $n_H \approx 5\times10^{10}$ cm^{-3}. The observed

[13] They calculated a value $k_{HH} = 0.18 \times 10^{-32}$cm^6/s at this temperature.

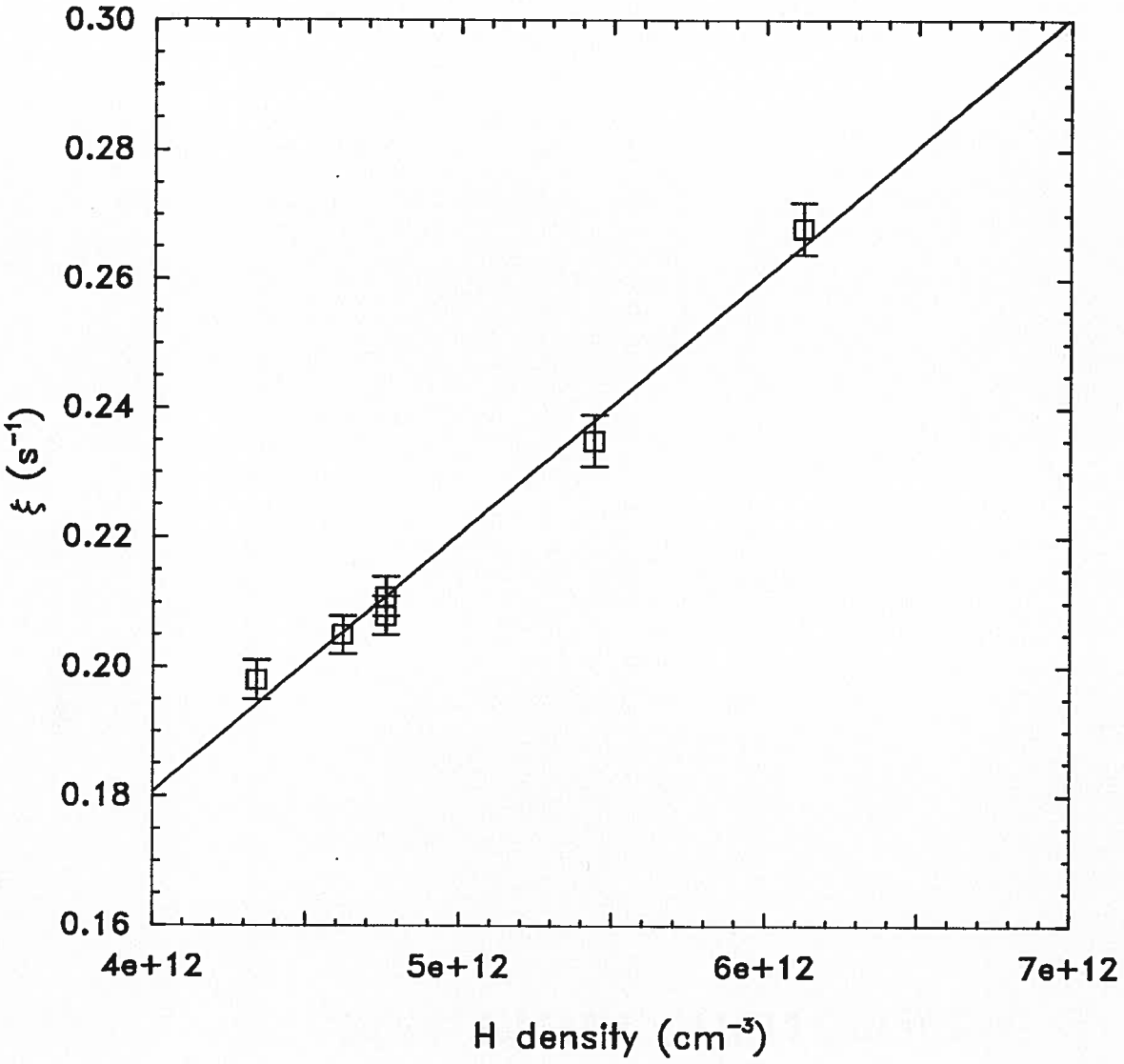

Figure 7.8: The rate constant ζ with which T_1^{-1} decays following a discharge pulse under the condition $n_H \gg n_D$. The data has been plotted as a function of the H density inside the cell. The slope of the data gives an H-D recombination rate $K_{HH} = 4.0(2) \times 10^{-14}$ cm^3/s at this temperature (1.043(3) K).

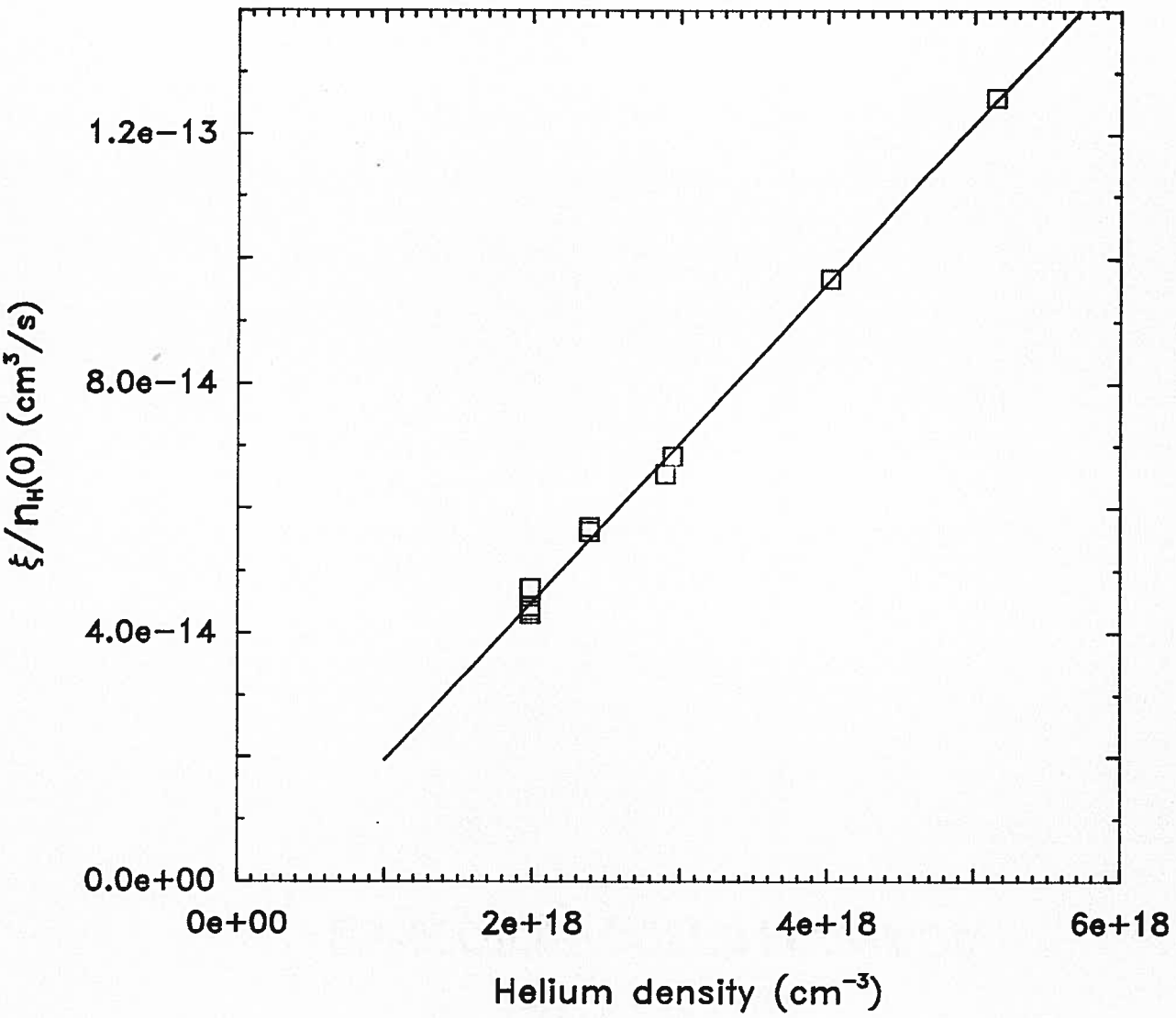

Figure 7.9: The rate constant ζ for the D atom density decay, normalized to the H density n_H in the cell and plotted as a function of the ^{4}He density. The fact that the data lies along a straight line indicates that H-D recombination is occurring in the gas phase catalyzed by ^{4}He atoms (*i.e.* H + D + ^{4}He $\rightarrow$ HD + ^{4}He). The rate constant for this process $k_{HD} = 2.5(1) \times 10^{-32}$ cm^6/s is more than an order of magnitude larger than the corresponding rate constant k_{HH} for H-H recombination reported in [27]. Here contributions due to the solvation of D into the ℓ-^{4}He are small and can be neglected.

initial drop in n_H was more pronounced than in the example shown in figure 7.7, with up to half[14] of the H atoms being lost due to H-D recombination over the first 10 to 30 seconds following the discharge. The H density then remained relatively constant until a time of about 200 seconds when the delayed source of H began to appear. n_D on the other hand initially decayed more rapidly than expected simply due to solvation. This excess decay was correlated strongly with n_D (rather than n_H) and was attributed to D-D recombination.

In appendix C the rate equations for the decay of both the H and the D densities in the presence of solvation (D only) are presented. In the limit where H-D recombination can be neglected as a means of reducing n_D (*i.e.* $K_{DD}n_D \gg K_{HD}n_H$ and $\lambda \gg K_{HD}n_H$) and H-H recombination can be neglected as a means of reducing n_H (*i.e.* $K_{HD}n_H \gg K_{HH}n_H$), these rate equations can be solved analytically. The equations do not include a term for the delayed source of H atoms; however at times short compared to the reappearance of these atoms, the use of this formalism is justified. The key point to be made here is that in this limit the H and the D densities are analytically related via

$$\frac{n_D(t)}{n_D^o} = \left(\frac{n_H(t)}{n_H^o}\right)^{\frac{K_{DD}}{K_{HD}}} \exp(-\lambda t) \ . \tag{7.11}$$

This relationship is independent of the absolute atomic densities. Furthermore, the initial drop in the H density due to the scavenging of H by D is given by

$$\frac{n_H(\infty)}{n_H^o} = \left(\frac{\lambda\tau_{DD}}{1+\lambda\tau_{DD}}\right)^{\frac{K_{HD}}{K_{DD}}} \tag{7.12}$$

where τ_{DD} is a characteristic time for D-D recombination:

$$\tau_{DD} = \frac{1}{K_{DD}n_D^o} = \frac{4\overline{G}_{HD}T_2^{se}(0)}{3K_{DD}} \ . \tag{7.13}$$

In equation 7.13 we have made use of the fact that n_D is proportional to $(T_2^{se})^{-1}$. $T_2^{se}(0)$ is the value of T_2^{se} immediately following the discharge. It is evident that the drop in

[14]Less than 5% of the D atoms were lost due to H-D recombination during this period.

the initial H density contains information about the number of D atoms which are lost due to H-D recombination and in effect gives a measure of the calibration between the D density and T_2^{se-1}. The simultaneous decays of n_H and n_D immediately following the discharge (where the use of the formalism outlined above is justified) were used in order to determine τ_{DD} and the ratio K_{HD}/K_{DD} as a function of temperature[15]. In figure 7.10 the ratio $T_2^{se}(0)/\tau_{DD}$ is plotted as a function of the ^{4}He density in the cell. From equation 7.13 we see that

$$\frac{T_2^{se}(0)}{\tau_{DD}} = \frac{3K_{DD}}{4\overline{G}_{HD}} \tag{7.14}$$

$\overline{G}_{HD}$ is expected to be essentially independent of temperature near 1 K and should not be related to the ^{4}He density in any way. Quite obviously K_{DD} is proportional to n_{He} thus D-D recombination is occurring in the gas phase, just as was the case for the H-D recombination observed in the last experiment. From the slope of this plot we obtain

$$\frac{3k_{DD}}{4\overline{G}_{HD}} = 1.9(1) \times 10^{-22}\text{cm}^3 \, . \tag{7.15}$$

In addition the analysis yields the ratio $K_{HD}/K_{DD} = k_{HD}/k_{DD} = 1.03(4)$ (independent of temperature). Combining these results with the measured value of k_{HD}, we find $k_{DD} = 2.4(2) \times 10^{-32}$ cm^6/s and $\overline{G}_{HD} = 1.7(2) \times 10^{-10}$ cm^3/s.

The value for the D-D gas phase recombination cross section is essentially the same as that for H-D recombination. Just as was the case for H-D recombination, there are no known calculations of this quantity. The value $\overline{G}_{HD} = 1.7(2) \times 10^{-10}$ cm^3/s is 30% smaller than the value calculated by Reynolds in the DIS limit [22]. If we take the experimental values as being the correct one, all D densities which were inferred from the theoretical result and mentioned up to this point should be increased by 40%. The thermally averaged H-D spin exchange broadening cross section at 1 K which is implied

[15]The solvation rate λ is also determined in this analysis. We delay the presentation of these results until the next section.

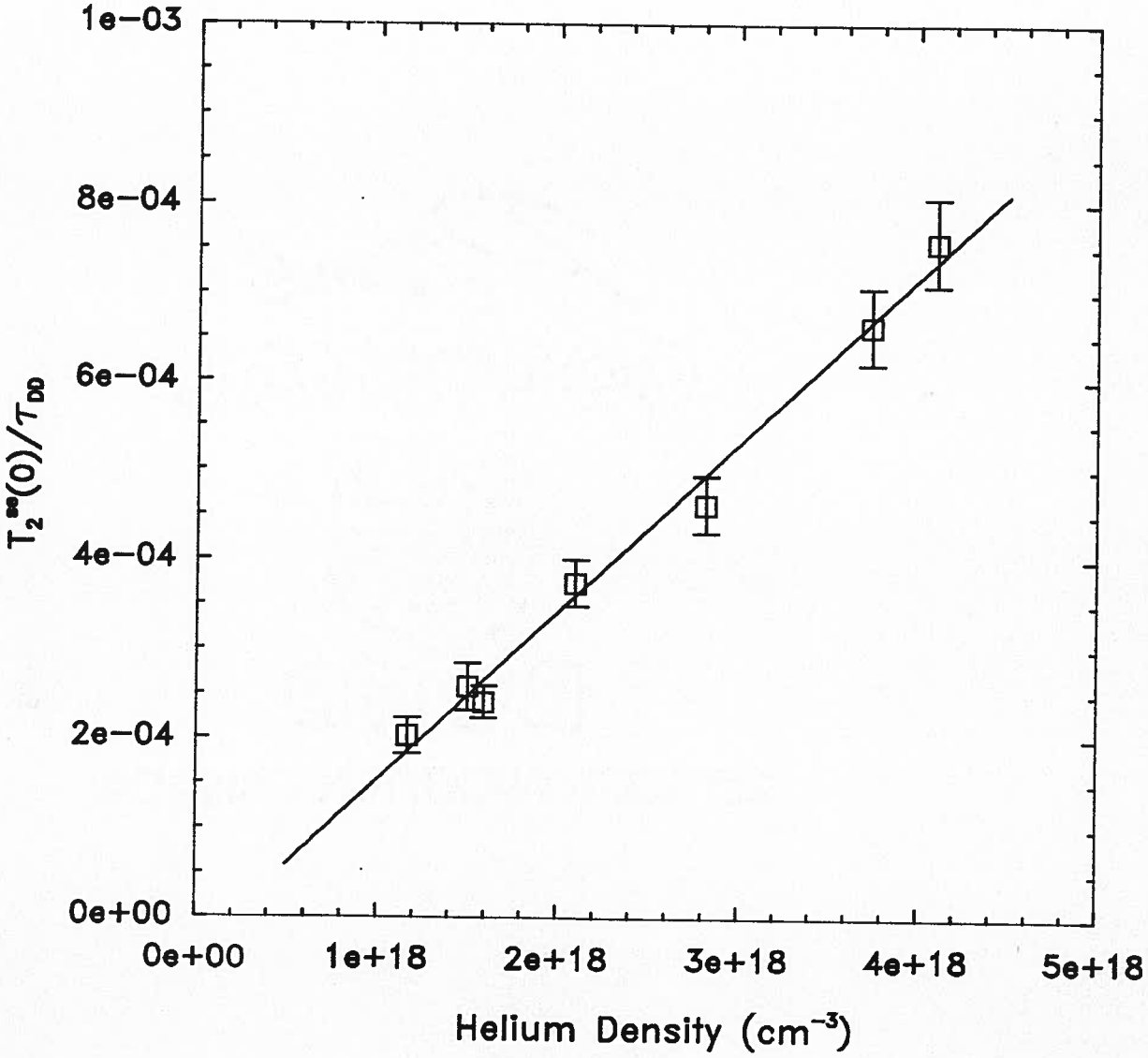

Figure 7.10: The ratio of the H-D spin exchange broadening T_2^{se} immediately following the discharge pulse to the characteristic time τ_{DD} for D-D recombination plotted as a function of the ^{4}He density inside the cell. $T_2^{se}(0)/\tau_{DD}$ is proportional to the D-D recombination rate K_{DD}. The linear relationship between K_{DD} and n_{He} indicates that D-D recombination is taking place in the gas phase rather than on the ℓ-^{4}He surfaces. The slope of this plot relates the the D-D recombination rate to the H-D spin exchange broadening rate constant. We find $4k_{DD}/3\overline{G}_{HD} = 1.9(1) \times 10^{-22}$ cm^3.

by this result is obtained by dividing by the mean collision speed of the colliding atoms. We find $\overline{\sigma}_{HD} = 96(11)$ Å^2. This is the only known measurement of this quantity. Note that the experimentally determined ratio $\overline{\sigma_{HD}}/\overline{\sigma_{HH}} = 2.2(4) \times 10^2$ is indeed large as was predicted in reference [22].

7.2.5 Measurement of the solvation energy

Up to this point we have dealt with situations in which the H and the D densities were quite different. In this section we present results obtained in the intermediate regime where these densities are comparable. The cell used in this work was prepared in the standard way but cooled slower than in the previous section. Typically $n_H \approx n_D^o \approx 10^{11}$ cm^{-3} following a discharge pulse. In this regime the decay of the D atom density contains small contributions due to both H-D and D-D recombination which make the decay non-exponential. In order to analyze the data we make use of the measured recombination rate constants k_{HD} and k_{DD}, the measured spin exchange broadening rate constant $\overline{G}_{HD}$, and the H and ^{4}He densities. The rate equation for the decay of the D density (see appendix C)

$$\frac{d}{dt}n_D(t) = -k_{HD}n_{He}n_H(t)n_D(t) - k_{DD}n_{He}n_D^2(t) - \lambda n_D(t) \tag{7.16}$$

or equivalently the H-D spin exchange broadening seen by the H atoms

$$\frac{d}{dt}\left(\frac{1}{T_2^{se}(t)}\right) = -k_{HD}n_{He}n_H(t)\left(\frac{1}{T_2^{se}(t)}\right) - \frac{4k_{DD}n_{He}}{3\overline{G}_{HD}}\left(\frac{1}{T_2^{se}(t)}\right)^2 - \lambda\left(\frac{1}{T_2^{se}(t)}\right) \tag{7.17}$$

is then numerically integrated and fit to the data with the solvation rate λ as the only free parameter.

In figure 7.11 an example of an extreme case in which both H-D and H-H recombination play an important role in determining the rate at which $T_2^{se\,-1}$ changes is shown. The initial D density[16] implied by the broadening is $n_D^o = 2.5 \times 10^{11}$ cm^{-3}. The H density

[16]This data could have equivalently been plotted as n_D. We choose to plot the measured broadening.

is about 10^{11} cm^{-3} throughout the decay. The dashed line is drawn such that it has the same slope as the decay due to solvation plus the *average* rate[17] due to H-D recombination. The amplitude of this line has no significance. It is simply intended as a guide for the eye. Initially the slope of the decay is steeper than the dashed line due primarily to D-D recombination. As n_D drops, only H-D recombination and solvation contribute to the decay of n_D and the two lines are essentially parallel. Near the end of this time period the H density drops below its average value and H-D recombination contributes slightly less to the decay of n_D. The slope indicated by the data is correspondingly less steep than that of the dashed line.

The solvation rate λ determined in this manner for a series of decays spanning the full range of accessible temperatures is shown in figure 7.12 (squares). In general the H and D densities were kept lower than the example outlined in figure 7.11 to try to minimize the decay of the D density due to H-D and D-D recombination. Also plotted in this figure (triangles) are the results of our earlier measurements of λ made by direct observation of the D atoms [21]. This earlier set of data has been scaled by the appropriate ratio to account for the fact that the A/V ratio of the two cells were different.

The first point to be noted is that the agreement between the absolute values of the two sets of data is quite good. We find similar agreement between measurements made on the same cell during different cooldowns and also between different cells. Throughout this work we were concerned that the actual area of the ℓ-^{4}He film seen by the D atoms could have been substantially larger than the geometrical area of the bulb. This would occur if the D_2 substrate underlying the film had a 'snow-like' texture. The data shown in figure 7.12 indicates that the ratio of the area of the ℓ-^{4}He film to the geometrical area of the bulb appears to have remained constant throughout these studies. Variations in

[17]Recall that the H density is also changing due to H-D recombination and due the delayed source of H atoms.

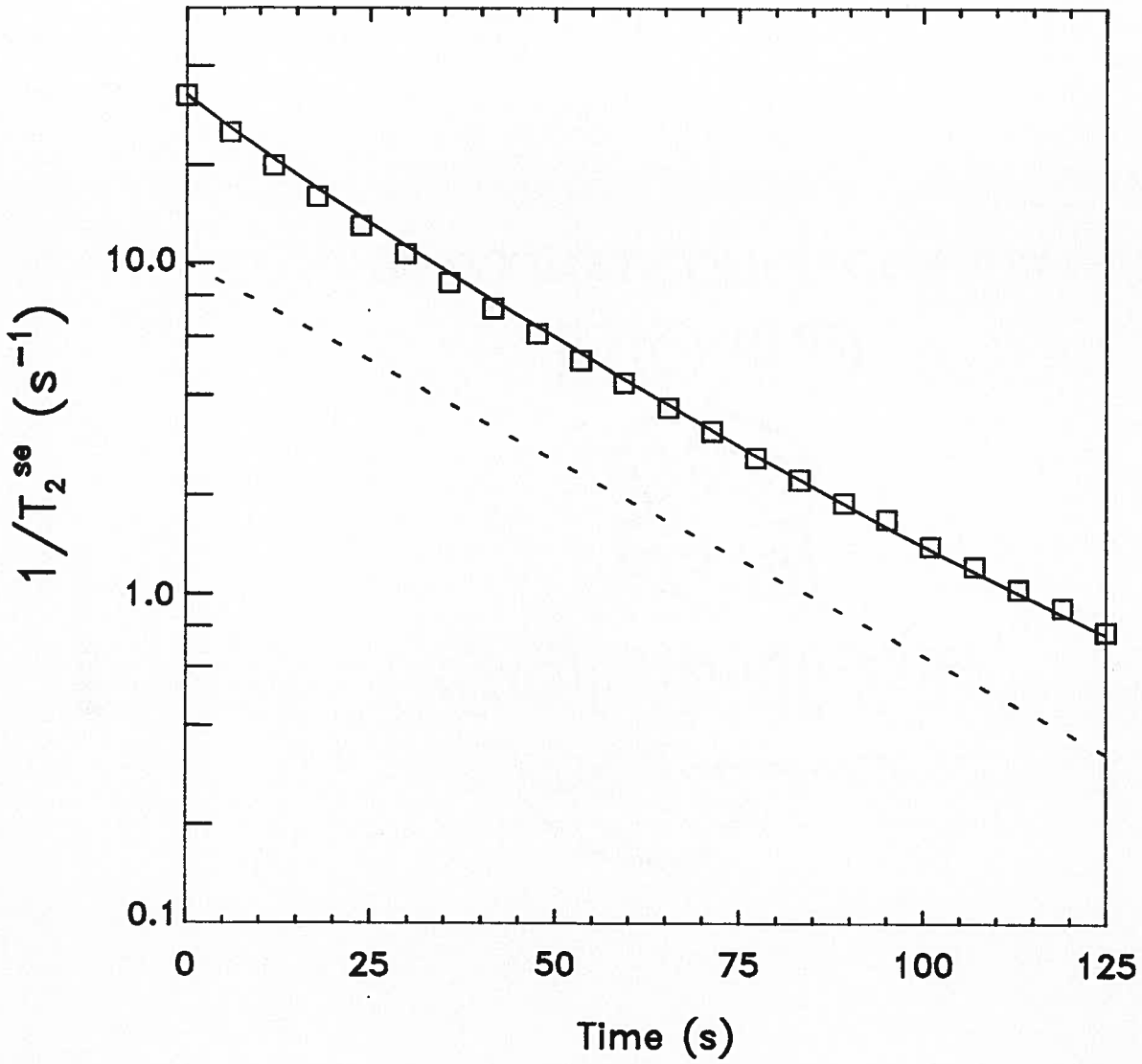

Figure 7.11: A measurement of $T_2^{se\,-1}$ as a function of time following a discharge pulse at a temperature of 1.000(3) K. The line passing through the data is a fit to a numerical integration of equation 7.17 with the solvation rate λ as the only free parameter. The dashed line indicates the rate at which $T_2^{se\,-1}$ (or n_D) changes due to solvation and the average H-D recombination rate. Immediately following the discharge D-D recombination also contributes to the decay. Near the end of this time period n_H is decreasing and the H-D recombination rate drops below its average value.

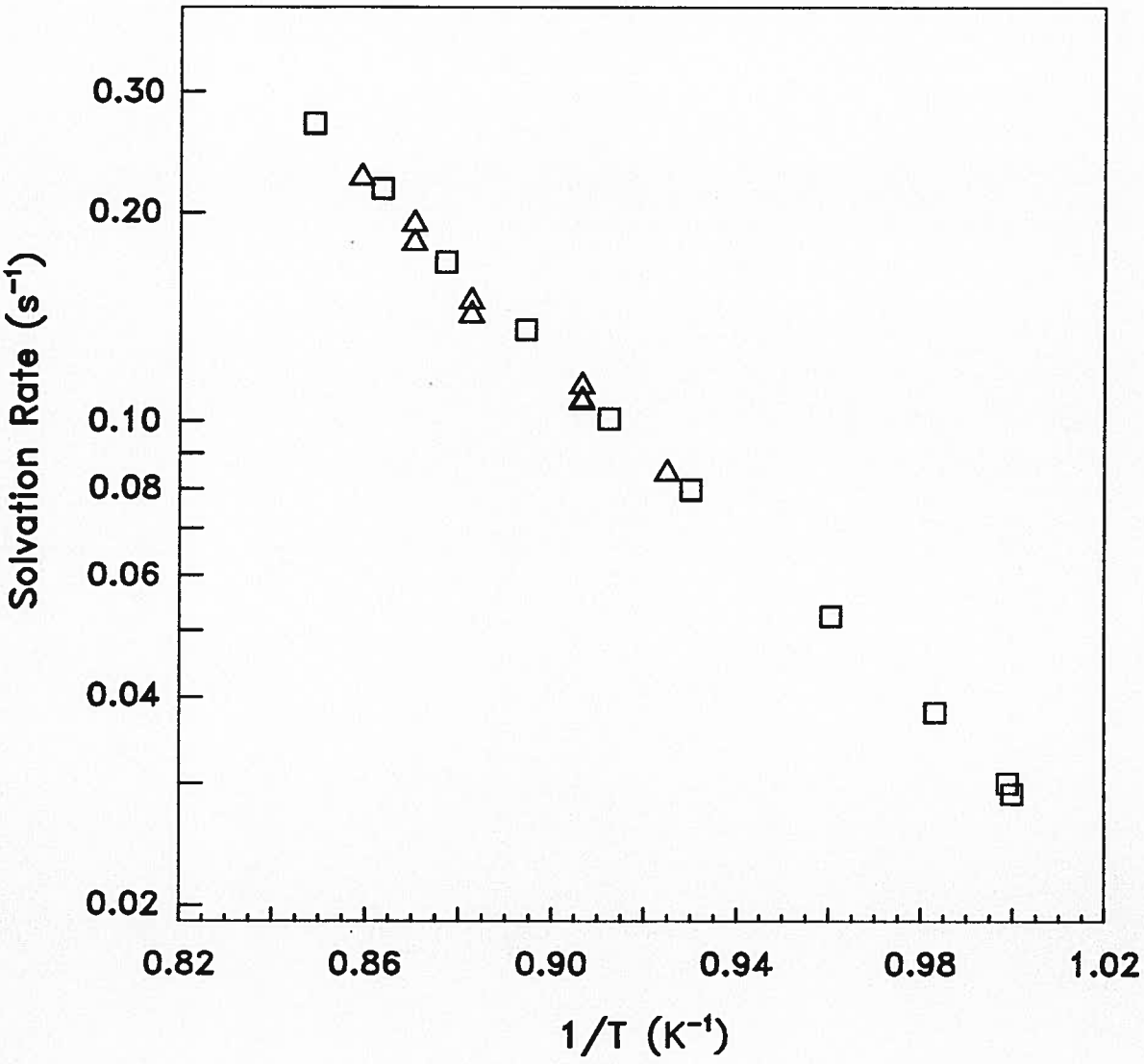

Figure 7.12: The solvation rate λ at which the D atoms penetrate the ℓ-^{4}He lined walls of the sample bulb plotted as a function of the inverse temperature. Squares indicate data obtained in this work using a bulb with A/V = 3.4 cm^{-1}. The triangles represent data obtained earlier using magnetic resonance on the β-δ hyperfine transition of D [21]. This earlier data has been scaled to the appropriate A/V ratio.

the quantity of D_2 admitted to the cells does not appear to change the absolute value of the solvation rate and thus we equate the the area of the ℓ-^{4}He film with the geometrical area of our cells. The second observation which is readily visible in figure 7.12 is that slopes of the two sets of data are consistent. On the other hand the scatter[18] in the present data is much less.

The solvation rate data shown in figure 7.12 has been fit to the form[19] (refer to chapter 2 for details)

$$\lambda = \frac{A}{4V}\overline{\alpha}_{lg}\mu\overline{v}\exp\left(-\frac{E_S}{k_B T}\right) \tag{7.18}$$

and replotted in figure 7.13. The free parameters in the fit were E_S and the product $\mu\overline{\alpha}_{lg}$. If we assume that $\mu\overline{\alpha}_{lg}$ is independent of temperature we obtain a value $E_S = 14.0(1)$ K for the energy required to force a D atom into the ℓ-^{4}He film coating the inner walls of our cells. This value is consistent with our earlier [21] measurement $E_S = 13.6(6)$ K. The experimental uncertainty associated with E_S has been reduced considerably in the present work. We also find $\mu\overline{\alpha}_{lg} = 4.0(5)$. This represents a remarkable[20] improvement over the earlier experiment in which this quantity was uncertain to more than an order of magnitude. This last result is quite interesting as it sets a lower limit on the effective mass m^* of a D quasi particle in ℓ-^{4}He.[21] The thermally averaged transmission probability for ejecting a D quasi particle from the liquid $\overline{\alpha}_{lg}$ can be at most 1 and thus m^* must be at least 4.0 ± 0.5 times the bare D mass or about 8 mass units. This is the first known measurement of the effective mass of a massive neutral particle inside ℓ-^{4}He other than ^{3}He. The experimental value for μ for ^{3}He in ℓ-^{4}He extrapolated to the zero concentration

[18] In light of the recombination rate constants measured during these studies it seems fair to say that much of the scatter in the 309 MHz data was due to H-D and D-D recombination. The remaining scatter was likely due to fluctuations in the temperature of the cell.

[19] Remember that $\overline{v}$ is a function of temperature.

[20] The relatively small temperature range of the data makes it quite difficult to determine the prefactor accurately.

[21] The films used in this work are likely thick enough to be treated as bulk ℓ-^{4}He.

limit is 2.34(18) [97] (m^* for ^{3}He is about 7 mass units).

7.2.6 The ^{4}He buffer gas frequency shift

The ^{4}He buffer gas shift of the a-c hyperfine transition of atomic hydrogen has been measured previously in this laboratory. This shift is more than an order of magnitude smaller and has the opposite sign from the room temperature value [98]. Hardy and coworkers report [12]

$$\delta f = -(1.18 \times 10^{-17}\mathrm{Hz\,cm^3})\mathrm{n_{He}}\ . \tag{7.19}$$

This measurement was made using a McLeod gauge to measure the pressure of the ℓ-^{4}He bath. We expect our measurements to be considerably more accurate because of the method in which the ^{4}He density was determined (see appendix D). In figure 7.14 the frequency of a FID is plotted as a function of $\mathrm{n_{He}}$ inside the cell. The frequency measurement is made against a Rb frequency standard. The slope of this plot indicates that

$$\delta f = -(1.150(2) \times 10^{-17}\mathrm{Hz\,cm^3})\mathrm{n_{He}} \tag{7.20}$$

which is 3% less than reported in [12, 27]. If we assume that the higher ^{4}He pressures in the earlier work were correct this discrepancy suggests that the measured values of pressure may have been out by as much as 10% near 1 K.[22]

The buffer gas shift is quite sensitive to the detailed form of the H-^{4}He potential. Jochemsen and Berlinsky [69] used existing H-^{4}He potentials in order to calculate this shift and found moderate agreement between their numerical result (0.7×10^{-17}Hz cm^3) and the experimental value at 1 K. There is certainly room for improvement in these calculations.

[22] A temperature error of about 10 mK.

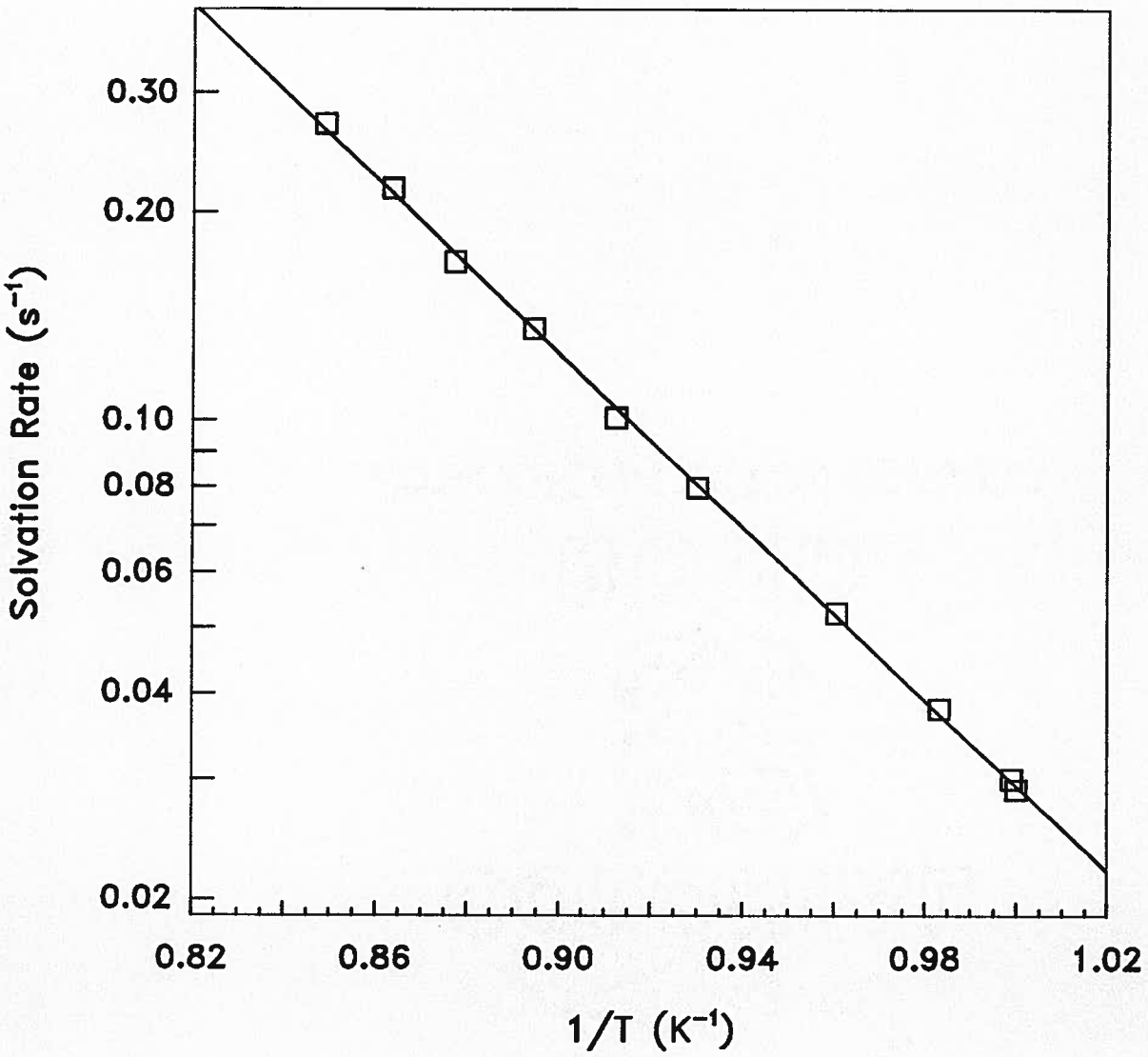

Figure 7.13: The solvation rate data obtained in this work. Uncertainties in the solvation rate are typically about half the height of the symbols. The data has been fit to the form 7.18 with E_S and $\mu\overline{\alpha}_{lg}$ as free parameters. If $\mu\overline{\alpha}_{lg}$ is assumed to be independent of temperature we find E_S = 14.0(1) K and $\mu\overline{\alpha}_{lg}$ = 4.0(5). This measurement solvation energy E_S is in agreement with our earlier result [21]. If we assume that the ejection probability $\overline{\alpha}_{lg}$ is 1 the effective mass of the D quasi particle implied by this data is 4 times the bare D mass.

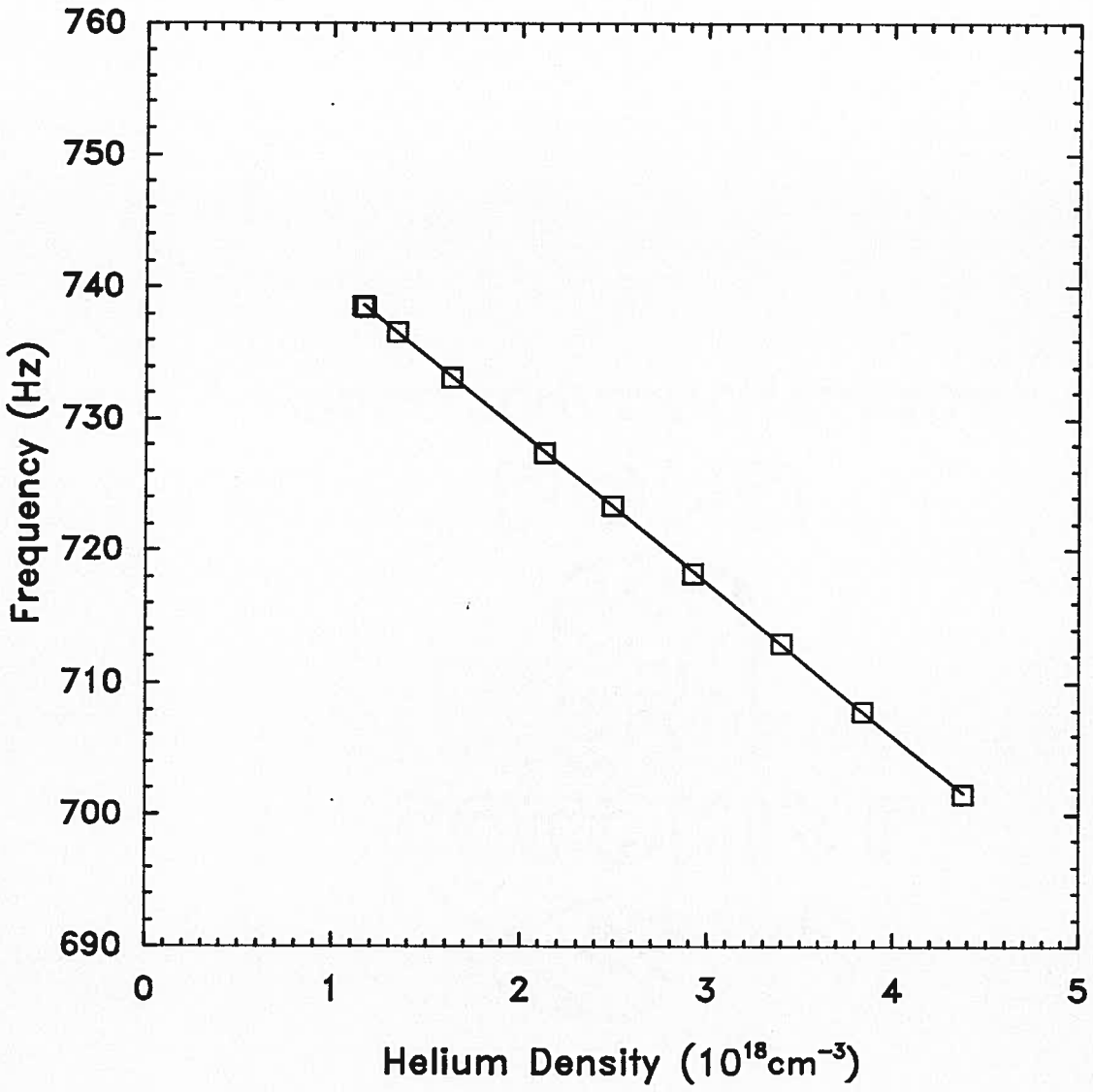

Figure 7.14: The ^{4}He buffer gas shift measured in this work. Uncertainties in the frequency and the ^{4}He density are discussed in appendix D. They are insignificant on this scale. The slope of this plot implies a pressure shift coefficient of -1.150(2)$\times 10^{-17}$ Hz cm^3. A frequency of 1420.405 MHz has been subtracted from the measured frequency of the FID's.

7.2.7 Frequency shift due to H-D collisions

During the study of H, D mixtures at 1 K, a shift in the frequency of the a-c hyperfine transition of H proportional to the D density in the cell was observed. In figure 7.15 this frequency shift is plotted as a function of the absolute D density in the cell (determined from the measured value of $\overline{G}_{HD}$). The maximum shift due to H-D collisions observed here is very small in comparison to the temperature dependent (*i.e.* ^{4}He density dependent) buffer gas shift. The error bar which is drawn on this plot indicates the frequency shift which would be expected from a 1 mK change in the temperature of the cell. The success of this measurement relied heavily on the temperature stability of our experimental cell.

It has already been mentioned that when the number of zero crossings in a FID become small, there exists the potential to misinterpret the broadening due to T_1^{se} as a frequency shift during the numerical fitting procedure. This point is discussed further in appendix A. The data presented in figure 7.15 has been checked carefully to correlate the frequency shift with the zero crossings in the frequency data. This frequency shift is not an artifact of the fitting procedure.

Crampton [71] has shown that in the DIS limit, the a-c hyperfine transition of H should not be shifted by H-D spin-exchange collisions. This does not mean that a fully quantum mechanical treatment of this problem will not lead to such a shift. Unfortunately the solution of this problem is rather involved. It has only been performed for the H-H spin-exchange problem [19, 20] and thus there is no framework in which to analyze this data.

To proceed further we *define* an H-D spin-exchange frequency shift cross section by

$$\delta f = \overline{\lambda}_{HD}\overline{v}_{HD}n_D \tag{7.21}$$

where $\overline{v}_{HD}$ is the mean relative velocity between H and D atoms in the gas. The slope of the data plotted in figure 7.15 is $-1.15(3) \times 10^{-12}$Hz cm^3 at 1.017(3) K. This in turn

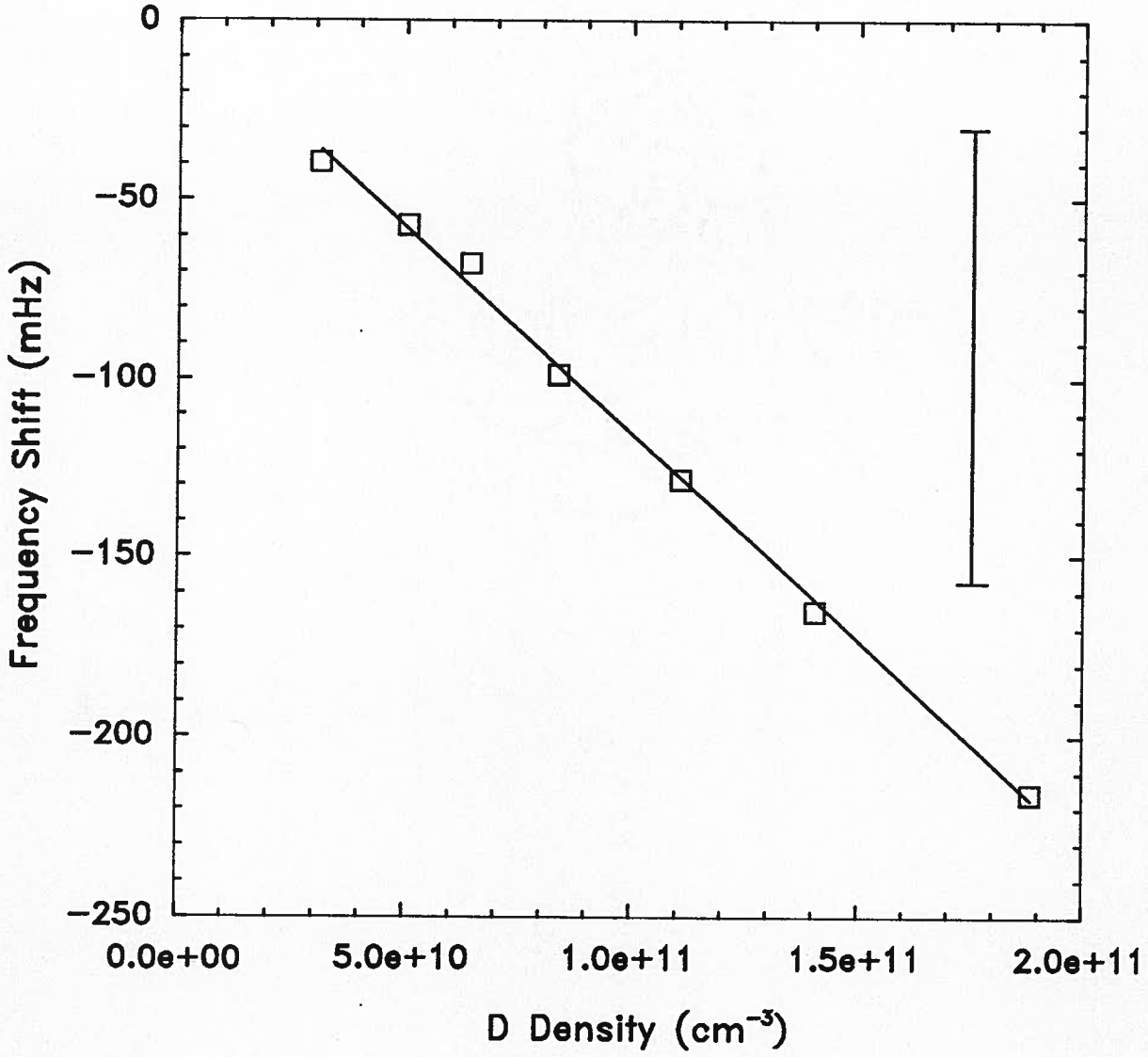

Figure 7.15: The frequency shift of the a-c hyperfine transition frequency of H attributed to H-D spin exchange collisions at 1.017(3) K. The frequency shift has been plotted as a function of the D density inside the cell inferred from the measured H-D spin exchange broadening rate constant. The slope of the data indicates that the thermally averaged spin exchange frequency shift cross section (defined by equation 7.21) is $\overline{\lambda}_{HD} = -1.1(2)$ Å^2. The ratio $\overline{\lambda}_{HD}/\overline{\sigma}_{HD} = -1.21(3) \times 10^{-2}$ is determined independently of any other measurement. The error bar drawn on the right hand side of the plot indicates the magnitude of the ^{4}He buffer gas frequency shift that would be expected from a 1 mK change in temperature.

implies that $\overline{\lambda}_{HD}$ = -1.1(2) Å^2. Note that in essence, the data in figure 7.15 is a measure of the ratio of the H-D spin exchange frequency shift cross section for the a-c transition of H (defined by equation 7.21) to the corresponding broadening cross section. This ratio is determined independently of any other parameters. We find that at 1.017(3) K, this ratio is:

$$\frac{\overline{\lambda}_{HD}}{\overline{\sigma}_{HD}} = -1.21(3) \times 10^{-2} \tag{7.22}$$

Chapter 8

Discussion and Conclusions

8.1 Summary

The unifying theme throughout this thesis has been the study of spin-exchange collisions and their perturbing influence on the a-c hyperfine transition of atomic hydrogen (H) at 1420 MHz in zero magnetic field. During the first set of experiments we used a cryogenic hydrogen maser (CHM) as a very sensitive probe of this transition, to study spin-exchange collisions between H atoms at 0.5 K. This technique allowed us to observe, effects induced by hyperfine interactions acting during these collisions. The implications of this first study are of considerable technological interest since the frequency shifts induced by these collisions will most certainly impose very strict design constraints on attempts to improve the frequency stability of the CHM. At the same time, discrepancies between our results and a theory [19, 20] which attempts to predict these frequency shifts may suggest that a reevaluation of the H-H interatomic potentials is necessary.

During the second set of experiments we examined the influence of spin-exchange collisions between hydrogen and deuterium (D) atoms on the a-c hyperfine transition of H at temperatures around 1 K. The key to the success of these experiments was the fact that the broadening cross section for H-D collisions is more than two orders of magnitude larger than the corresponding cross section for H-H collisions at this temperature. Pulsed magnetic resonance techniques were used to monitor the density of H atoms in a gaseous mixture of H and D. The broadening of the transition was almost wholly determined by

H-D spin-exchange collisions and in effect gave a simultaneous measure of the density of D atoms in the mixture. This allowed us to study for the first time interactions between two isotopes of H in zero field at cryogenic temperatures. Measurements were made of the broadening and frequency shift cross sections for H-D spin-exchange collisions as well as the gas phase recombination rate constants for H-D and D-D recombination. All of these parameters are quite sensitive to the detailed form of the interatomic potentials. They should certainly be useful in any future attempts to reevaluate the various potentials involved. These techniques also allowed us to study the solvation of D into ℓ-^{4}He. Our findings make important contributions to the experimental picture of solvation [22, 21] and provide an improved measurement of the energy required to force a D atom into ℓ-^{4}He. The results also impose a lower bound on the effective mass of a D quasi particle in ℓ-^{4}He.

8.2 Spin-exchange measurements

The study of H-H spin-exchange induced frequency shifts in the CHM was made by independently varying the resonator Q, detuning, and the atomic density, while monitoring the oscillation frequency of the maser. The deviation of this frequency from the density independent frequency of the hyperfine transition was analyzed in the context of a theory developed by B. J. Verhaar and his collaborators [19, 20]. In this theory the influence of the hyperfine interaction has been rigorously included in the calculation of the H-H spin-exchange frequency shifts and broadening parameters for this transition. We had no means by which to independently vary or control the occupation of individual hyperfine states inside the maser bulb. As a consequence we were able to distinguish only three[1] parameters (or combinations of parameters) of the theory. Experimental and theoretical

[1] out of a total of 5 parameters which are believed to be of any consequence for our CHM

results for the parameters[2]

$$\overline{\lambda}_0$$

$$\overline{\lambda}_1 (\rho_{cc} + \rho_{aa}) + \overline{\lambda}_2$$

$$\overline{\sigma}_1 (\rho_{cc} + \rho_{aa}) + \overline{\sigma}_2$$

are summarized in table 5.1 of chapter 5. Implicit in our analysis is the assumption that $\rho_{cc} + \rho_{aa}$ is independent of the atomic density in the maser bulb.

In the *absence* of any hyperfine induced effects during H-H spin-exchange collisions, $\overline{\lambda}_1 (\rho_{cc} + \rho_{aa}) + \overline{\lambda}_2$ is expected to be zero. The dimensionless ratio

$$\Omega = -\frac{\overline{\lambda}_1 (\rho_{cc} + \rho_{aa}) + \overline{\lambda}_2}{\overline{\sigma}_1 (\rho_{cc} + \rho_{aa}) + \overline{\sigma}_2}$$

is a measure of the contribution of hyperfine interactions to the total spin-exchange frequency shift. Our measurements indicate that $\Omega = -0.055(35)$. The magnitude of the observed effect is in agreement with the theoretical predictions made by Verhaar *et al.* We interpret this as a signature of hyperfine interactions during H-H spin-exchange collisions. This measurement represents the first observation of this effect at cryogenic temperatures.

The technological implication of this measurement is rather sobering. The early 1980's saw the development of a good deal of enthusiasm based on the potential frequency stability of a H maser operating at cryogenic temperatures. The theory developed by Verhaar *et al.* was first published in 1987 [19], soon after the first CHM's were realized [8, 9, 10]. It bore with it the unsettling revelation that hyperfine interactions coupled the oscillation frequency of a H maser to the atomic density in a way that depends upon the individual[3] hyperfine level populations. Theoretically the dominant thermally

[2]Recall that ρ_{aa} and ρ_{cc} are two of the diagonal elements of the H density matrix.

[3]In the semi-classical approach to this problem in which hyperfine effects are neglected, the oscillation frequency is only coupled to the population difference between the $|\, a \,\rangle$ and the $|\, c \,\rangle$ states.

averaged frequency shift rate constant $\overline{\lambda}_0\overline{v}_{HH}$ for H-H spin-exchange collisions [19, 20] is smaller at 0.5 K than it is at 300 K by a factor of two. On the other hand, the typical atomic densities in a CHM are several orders of magnitude higher than those in a conventional room temperature H maser. The resulting potential frequency instabilities due to fluctuations in the level populations are correspondingly greater at 0.5 K than at 300 K. Our measurements form an experimental verification of the effects predicted by Verhaar *et al.* It remains to be seen whether or not any new and innovative CHM designs[4] can attain significant improvements in frequency stability.

The results summarized in table 5.1 are interesting from another point of view as well. While there is qualitative agreement between the magnitudes of the measured and the theoretical values for the various parameters, discrepancies are obvious. The most striking of these is the fact that the measured sign of the term $\overline{\lambda}_1(\rho_{cc}+\rho_{aa})+\overline{\lambda}_2$ is positive while the numerical calculations[5] indicate that it is negative. The parameters of the theory are quite sensitive to the detailed form of the atomic potentials used in the calculations. These discrepancies will likely form an important indicator in any future refinements of these potentials. They also may be an indication that a reevaluation of the role of hyperfine interactions during spin-exchange collisions is warranted. Certainly corroborative experimental evidence[6] is required before such steps are taken.

A few words of caution are required at this point. The most serious drawback of our experiment was the fact that we simply had no way to monitor the occupancy of the individual hyperfine states in the maser bulb *nor* the actual atomic density while the maser was oscillating. Our results rely on a computer simulation [17, 90] in order to

[4] A full treatment of the design constraints imposed by these frequency shifts is far beyond the scope of this thesis. Cursory discussions of these requirements can be found in references [19, 20, 17].

[5] The numerical calculations indicate that this term is negative over a very broad range of temperatures regardless of the value chosen for $\rho_{cc}+\rho_{aa}$.

[6] The only other study of H-H spin-exchange at these temperatures was a measurement of the broadening cross section at 1.1 K made in this laboratory[27]. No attempt was made to investigate hyperfine induced effects. The results of this earlier study are consistent with our findings.

infer this information from measurements made while the maser was not operating. We have tried to place reasonable uncertainties on these estimates; however their accuracy is difficult to verify. We do note that unlike the other combinations of parameters, the determination of $\overline{\lambda}_0$ is only weakly dependent upon the actual atomic density in the maser. The second uncertainty which was of some concern during this experiment was the establishment of the absolute resonator detuning. We have placed what we believe to be generous limits on this uncertainty.

Currently we are aware of two proposals to study the role of the hyperfine interaction during H-H spin-exchange collisions in a similar manner. If successful, these investigations will provide additional information near[7] 10 K and near[8] 300 K. The results of these studies are certainly eagerly awaited. They should form an essential complement to our work.

During our second set of experiments with H, D mixtures at 1 K we were able to measure the frequency shift and the broadening of the a-c hyperfine transition of H due to H-D spin-exchange collisions. The sensitivity of this experiment was in no way comparable to that of the CHM experiment and hence no attempt was made to directly account for effects induced by hyperfine interactions. On the other hand, these results do represent an interesting complement to the H-H spin-exchange measurements.

The H-D spin-exchange broadening cross section is $2.2(4)\times10^2$ times as big as the corresponding cross section for H-H collisions[9] [27] at 1.1 K. In chapter 7 we noted that a discrepancy between the experimental and the only theoretical value [22] for the

[7]Dr S. B. Crampton (Williams College, Williamstown MA, USA) has proposed a study of spin-exchange collisions in a H maser with neon coated walls operating near 10 K.

[8]Drs R. L. Walsworth and R. F. C. Vessot (Harvard-Smithsonian Center for Astrophysics, Cambridge MA, USA) have proposed a new study of H-H spin-exchange collisions using room temperature H masers.

[9]The amplitudes of the spin-exchange cross sections depend upon the phase shifts introduced by the singlet and the triplet molecular potentials. It is the H-H cross section which is anomalously small at low temperatures. For convenience a tabulation of the ro-vibrational levels of the H_2 and HD molecules close to the dissociation limit is given in appendix E. The calculation of the spin-exchange cross sections are sensitive to the exact placement of these levels.

broadening cross section does exist. This is likely an indication that the long range part of the potential used in the calculation of the cross section needs to be modified. The measurement of a frequency shift due to H-D spin-exchange collisions is an interesting observation. This shift is not predicted by the semi-classical theories of spin-exchange [71]. Unfortunately the H-D spin-exchange problem has not been treated in the same fully quantum mechanical manner as the H-H spin-exchange problem and there are no theoretical estimates with which to compare our result. The H, D system examined in this thesis may prove to be[10] an important testing ground for the formalism used by Verhaar *et al.* [19, 20] to calculate the H-H cross sections.

8.3 Recombination measurements

During the experiments at 1 K, measurements were made of the rate constants for H-D and D-D recombination catalyzed by ^{4}He atoms. Interestingly enough, both rate constants are about an order of magnitude larger than the rate constant for the H-H reaction [27]. This observation is consistent with the relative abundance of low angular momentum molecular levels close to dissociation (the spectrum of the D_2 molecule near dissociation is also tabulated in appendix E). The H-H recombination rate constant at this temperature has been calculated with remarkable success[11] [65]. Similar calculations for the H-D and D-D reactions have not been performed though they would certainly be enlightening. This is especially so given the apparent discrepancy between the calculated and the measured H-D spin-exchange broadening cross section discussed earlier.

A rather interesting comparison can be made between our results for D-D recombination and those of Mayer and Seidel [60]. Using ESR they set a lower bound on the *surface*

[10]Interest in examining the H-D system theoretically has been expressed by the Eindhoven group led by Professor Verhaar : private communication.

[11]The rate constant reported in references [37] and [12] were too high by a factor of $\sqrt{2}$. The proper experimental value is reported in reference [27].

D-D recombination rate at 0.5 K in a magnetic field of 0.3 Tesla. They then scaled their result to set a lower bound of 300 Å on the effective cross length for the surface catalyzed two body D-D recombination reaction in zero magnetic field. Their result is consistent with the data of Silvera and Walraven [47] which was scaled in the same manner. This scaling procedure[12] has been used moderately successfully in the case of H to relate high field recombination data [100, 101, 102] to low field data. The recombination cross length obtained for D however, seems anomalously large in comparison to the corresponding H-H cross length. In zero field the H-H cross length is 0.14(3) Å [27]. There has been some controversy regarding the reason for this difference with speculations as to the possibility of additional recombination channels for D [49]. If we scale Mayer and Seidel's results to our conditions using a binding energy of 2.6(4) K for D on ℓ-^{4}He we would expect to observe a two body recombination rate constant of $K_{DD} > 3 \times 10^{-13}$ cm^3/s at 1 K due just to recombination on the surface. We measure[13] $K_{DD} = 3 \times 10^{-14}$ cm^3/s at this temperature. This is an order of magnitude smaller than expected based on Mayer and Seidel's data! Furthermore we find that the D-D recombination above 1 K appears to be occurring in the *gas phase* rather than on the surface. This result either implies that the surface recombination cross length is very temperature dependent or it casts further doubt on the validity of scaling high field surface recombination rates to zero field in the case of D. Applying the converse argument to the comparison of these two experiments our results place an *upper* limit of 30 Å on the D-D surface recombination cross length in zero field. As we have not seen an obvious indication of surface recombination in our data, the actual zero field cross length is likely to be somewhat shorter than this. This limit is much more in keeping with the H-H cross length.

[12]In the case of H, the recombination rate scales as the admixture coefficient between the | a ⟩ state and the | b ⟩ state in high field [99]. For D there are two such coefficients due to the larger nuclear spin.

[13]This information is taken from figure 7.10 of chapter 7 where we have used the measured H-D spin exchange rate constant $\overline{G}_{HD}$ to obtain the absolute rate constant.

8.4 Solvation measurements

Our study of H, D mixtures at 1 K has allowed us to make an improved measurement of the energy required to force a D atom into ℓ-^{4}He. We determined $E_S = 14.0(1)$ K. The improvement over our earlier report $E_S = 13.6(6)$ K [21] made by direct observation of D using magnetic resonance on the D atom, is due primarily to the fact that we were able to account for H-D and D-D recombination as alternate mechanisms by which the D atom density inside our cells decayed. The theoretical calculation of this quantity by Kürten and Ristig [35] is in fair agreement with our results if we assume that the appropriate ℓ-^{4}He density is that corresponding to zero pressure in their model [21]. If we use the true ℓ-^{4}He density, their calculation results in a value of E_S which is too high by more than a factor of two.

Two ancillary observations which were made during our studies are of considerable interest. The first of these was the inferred chemical-exchange reaction

$$D + HD \rightarrow D_2 + H$$

occurring on the substrate underneath the ℓ-^{4}He films in our cells. This is an indication that the D atoms which 'disappear' during the pulsed magnetic resonance experiment actually reach the substrate. The second observation was that the roughness of the D_2 substrate did not appear to enhance the effective area to volume ratio of our cells. This second observation combined with our improved solvation rate data has allowed us to set a lower bound on the effective mass of a D quasi particle inside liquid helium. We find $m^*/m_p > 8(1)$ (m_p is the proton mass) which can be compared to a value of $m^*/m_p = 7.0(5)$ for ^{3}He in ℓ-^{4}He in the limit of zero concentration [97]. This is the first time information regarding the effective mass of a neutral atom in ℓ-^{4}He other than ^{3}He has been obtained. We only claim that our measurement is a lower bound as we do not know the actual thermally averaged probability that a D atom with kinetic energy $> E_S$ striking

the ℓ-^{4}He surface will enter the liquid (likely an angle dependent problem). In addition we have assumed that all of the D atoms which enter the liquid subsequently adsorb to the substrate with certainty. If a theory which describes these processes adequately is developed[14] it will be possible to set an absolute value on m* for D in ℓ-^{4}He. This information would certainly be useful in any attempts to further refine the calculations of the solvation energy for D in ℓ-^{4}He.

As a final note in passing, we have looked for indications of the solvation of H into ℓ-^{4}He in our cells at temperatures up to 2 K. We have not observed any indication of this effect.

[14]Even better of course would be an experimental determination of these probabilities.

Bibliography

[1] H. M. Goldenberg, D. Kleppner, and N. F. Ramsey. Atomic hydrogen maser. *Phys. Rev. Lett.*, **5**(8):361, (1960).

[2] D. W. Allan. In search of the best clock - an update. In A. De Marchi, editor, *Frequency Standards and Metrology*, page 29. Springer Verlag, (1989).

[3] N. F. Ramsey. Experiments with separated oscillatory fields and hydrogen masers. *Rev. Mod. Phys.*, **62**(3):541, (1990).

[4] I. F. Silvera and J. T. M. Walraven. Spin polarized atomic hydrogen. In D. Brewer, editor, *Progress in Low Temperature Physics X*, page 139. North Holland, (1986).

[5] T. J. Greytak and D. Kleppner. *New Trends in Atomic Physics.* North Holland, (1984).

[6] C. E. Hecht. The possible superfluid behavious of hydrogen atom gases and liquids. *Physica*, **25**:1159, (1959).

[7] S. B. Crampton, K. M. Jones, G. Nunes, and S. P. Souza. In *Proceedings of the Sixteenth Annual Precise Time and Time Interval (PTTI) Conference*, volume NASA Techn. Memorandum No 8756, page 339, (1985).

[8] H. F. Hess, G. P. Kochanski, J. M. Doyle, T. J. Greytak, and D. Kleppner. Spin-polarized hydrogen maser. *Phys. Rev. A*, **34**(2):1602, (1986).

[9] M. D. Hürlimann, W. N. Hardy, A. J. Berlinsky, and R. W. Cline. Recirculating cryogenic hydrogen maser. *Phys. Rev. A*, **34**(2):1605, (1986).

[10] R. L. Walsworth, I. F. Silvera, H. P. Godfried, C. C. Agosta, R. F. C. Vessot, and E. M. Mattison. Hydrogen maser at temperatures below 1 K. *Phys. Rev. A*, **34**(3):2550, (1986).

[11] I. F. Silvera and J. T. M. Walraven. Stabilization of atomic hydrogen at low temperature. *Phys. Rev. Lett.*, **44**(3):164, (1980).

[12] W. N. Hardy, M. Morrow, R. Jochemsen, and A. J. Berlinsky. Magnetic resonance of atomic hydrogen at low temperatures. In *Physica*, volume **109** & **110B**, page 1964, (1982). Proc. 16th Int. Conf. on Low Temperature Physics.

[13] S. B. Crampton, W. D. Phillips, and D. Kleppner. Proposed low temperature hydrogen maser. *Bull. Am. Phys. Soc.*, **23**:86, (1978).

[14] R. F. C. Vessot, M. W. Levine, and E. M. Mattison. Comparison of theoretical and observed hydrogen maser stability limitation due to low-temperature operation. In *Proceedings of the Ninth Annual Precise Time and Time Interval (PTTI) Applications and Planning Meeting*, volume NASA Technical Memorandum No 78104, page 549, (1978).

[15] A. J. Berlinsky and W. N. Hardy. Cryogenic masers. In *Proceedings of the Thirteenth Annual Precise Time and Time Interval (PTTI) Applications and Planning Meeting*, volume NASA Conference Publication No 2220, page 547, (1982).

[16] M. D. Hürlimann, W. N. Hardy, M. E. Hayden, and R. W. Cline. Performance of the UBC cryogenic hydrogen maser. In A. De Marchi, editor, *Frequency Standards and Metrology*, page 95. Springer Verlag, (1989).

[17] M. D. Hürlimann. *Cryogenic Hydrogen Maser.* PhD thesis, University of British Columbia, (1989).

[18] J. P. Wittke and R. H. Dicke. Redetermination of the hyperfine splitting in the ground state of atomic hydrogen. *Phys. Rev.*, **103**:620, (1956).

[19] B. J. Verhaar, J. M. V. A. Koelman, H. T. C. Stoof, O. J. T. Luiten, and S. B. Crampton. Hyperfine contribution to spin-exchange frequency shifts in the hydrogen maser. *Phys. Rev. A*, **35**(9):3825, (1987).

[20] J. M. V. A. Koelman, S. B. Crampton, H. T. C. Stoof, O. J. T. Luiten, and B. J. Verhaar. Spin-exchange frequency shifts in cryogenic and room temperature hydrogen masers. *Phys. Rev. A*, **38**:3535, (1988).

[21] M. W. Reynolds, M. E. Hayden, and W. N. Hardy. Hyperfine resonance of atomic deuterium at 1 K. *J. Low Temp. Phys.*, **84**(1/2):87, (1991).

[22] M. W. Reynolds. *Resonant Recombination of Atomic Hydrogen and Deuterium at Low Temperatures.* PhD thesis, University of British Columbia, (1989).

[23] P. Petit, M. Desaintfuscien, and C. Audoin. Temperature dependence of the hydrogen maser wall shift in the temperature range 295-395 K. *Metrologia*, **16**(6):7, (1980).

[24] E. Richard Cohen and Barry N. Taylor. The 1986 adjustment of the fundamental physical constants. *Rev. Mod. Phys.*, **59**(4):1121, (1987).

[25] A. Abragam. *Principles of Nuclear Magnetism.* Clarendon Press, Oxford, (1978).

[26] Richard Marsolais. *Spin Relaxation and Recombination in Atomic Hydrogen Gas at Temperatures around 1 K.* MSc thesis, University of British Columbia, (1980).

[27] M. R. Morrow. *Magnetic Resonance on Atomic Hydrogen Confined by Liquid Helium Walls.* PhD thesis, University of British Columbia, (1983).

[28] Charles P. Slichter. *Principles of Magnetic Resonance.* Harper and Row, New York, 1963.

[29] I. I. Rabi, N. F. Ramsey, and J. Schwinger. Use of rotating coordinates in magnetic resonance problems. *Rev. Mod. Phys.*, **26**(2):167, (1956).

[30] S. Bloom. Effects of radiation damping on spin dynamics. *J. Appl. Phys.*, **28**:800, (1957).

[31] D. Kleppner, H. C. Berg, S. B. Crampton, N. F. Ramsey, R. F. C. Vessot, H. E. Peters, and J. Vanier. Hydrogen-maser principles and techniques. *Phys. Rev.*, **138**(4A):A972, (1965).

[32] C. Audoin, J. P. Schermann, and P. Grivet. Physics of the hydrogen maser. In *Advances in Atomic and Molecular Physics: volume 7.* Academic Press, (1971).

[33] Daniel Kleppner, H. Mark Goldenberg, and Norman F. Ramsey. Theory of the hydrogen maser. *Phys. Rev.*, **126**(2):603, (1962).

[34] M. Morrow, R. Jochemsen, A. J. Berlinsky, and W. N. Hardy. Zero-field hyperfine resonance of atomic hydrogen for $0.18 \leq T \leq 1K$: the binding energy of H on liquid ^{4}He. *Phys. Rev. Lett.*, **46**(3):195, (1981). Erratum: *Phys. Rev. Lett.* **47**, 455 (1981).

[35] K. E. Kürten and M. L. Ristig. Atomic and molecular hydrogen isotopes in liquid helium. *Phys. Rev. B*, **31**(3):1346, (1985).

[36] K. E. Kürten and J. W. Clark. Variational monte carlo study of heavy atom impurities in liquid ^{4}He. *Phys. Rev. B*, **32**(5):2952, (1985).

[37] W. N. Hardy, M. Morrow, R. Jochemsen, B. W. Statt, P. R. Kubik, R. M .Marsolais, A. J. Berlinsky, and A. Landesman. Magnetic-resonance studies of gaseous atomic

hydrogen confined at 1 K and zero magnetic field. *Phys. Rev. Lett.*, **45**(6):453, (1980).

[38] R. Jochemsen, A. J. Berlinsky, and W. N. Hardy. The diffusion cross section for atomic hydrogen in helium gas at low temperature and the H-He potential. *Can. J. Phys.*, **62**(8):751, (1984).

[39] J. Dupont-Roc, M. Himbert, N. Pavloff, and J. Treiner. Inhomogeneous liquid ^{4}He: A density functional approach with a finite-range interaction. *J. Low Temp. Phys.*, **81**(1/2):31, (1990).

[40] J. Wilks. *The Properties of Liquid and Solid Helium.* Clarendon Press, Oxford, 1967.

[41] I. B. Mantz and D. O. Edwards. Binding of spin-polarized hydrogen to the free surface of liquid helium. *Phys. Rev. B*, **20**(11):4518, (1979).

[42] W. N. Hardy, M. D. Hürliamnn, and R. W. Cline. Application of atomic hydrogen at low temperatures: The recirculating cryogenic hydrogen maser. In *Jap. J. of Appl. Phys.*, volume **26**, page 2065, (1987). Proc. 18th Int. Conf. on Low Temperature Physics.

[43] P. J. Nacher and J. Dupont-Roc. Experimental evidence for nonwetting with superfluid helium. preprint, (1991).

[44] R. Jochemsen, M. Morrow, A. J. Berlinsky, and W. N. Hardy. Interaction of atomic hydrogen with helium films: Sticking probabilities for H on ^{3}He and ^{4}He, and the binding energy of H on ^{3}He. *Phys. Rev. Lett.*, **47**(12):852, (1981).

[45] G. H. I. van Yperen, A. P. M. Mathey, J. T. M. Walraven, and Isaac F. Silvera.

Adsorption energy and nuclear relaxation of H↓ on ^{3}He-^{4}He mixtures. *Phys. Rev. Lett.*, **47**:800, (1981).

[46] W. C. Stwally. Simple long-range model and scaling relations for the binding of isotopic hydrogen atoms to isotopic helium surfaces. *Chem. Phys. Lett.*, **88**(4):404, (1982).

[47] Issac. F. Silvera and J. T. M. Walraven. Spin-polarized atomic deuterium: Stabilization, limitations on density, and adsorption energy on helium. *Phys. Rev. Lett.*, **45**(15):1268, (1980).

[48] A. P. M. Mathey, J. T. M. Walraven, and Issac F. Silvera. Measurements of pressure of gaseous H↓: Adsorption energies and surface recombination rates on helium. *Phys. Rev. Lett.*, **46**(10):668, (1981).

[49] M. Papoular. On the dynamical stability of D↓. *J. Low Temp. Phys.*, **50**(3/4):253, (1983).

[50] E. Tjukanov, P. C. Souers, and W. N. Hardy. Zero field magnetic resonance studies of atomic tritium. In *Proc. 3rd Int. Conf on Spin Polarized Quantum Systems*, (1989).

[51] D. S. Zimmerman and A. J. Berlinsky. Diffusion of H atoms on the surface of liquid ^{4}He. *Can. J. Phys.*, **62**:590, (1984).

[52] J. J. Berkhout and J. T. M. Walraven. Sticking and thermal accomodation of atomic hydrogen on liquid helium surfaces. In *Proc. 3rd Int. Conf on Spin Polarized Quantum Systems*, (1989).

[53] Victor V. Goldman. Kapitza conductance between gaseous atomic hydrogen and liquid helium. *Phys. Rev. Lett.*, **56**(6):612, (1986).

[54] S. B. Crampton, J. J. Krupczak, and S. P. Souza. Temperature dependence of hydrogen atom adsorption on molecular hydrogen surfaces. *Phys. Rev. B*, **25**:4383, (1982).

[55] M. Morrow and W. N. Hardy. The magnetic resonance lineshape for atomic hydrogen confined by liquid helium walls. *Can. J. Phys.*, **61**(6):956, (1983).

[56] R. P. Feynman. Atomic theory of the two-fluid model of liquid helium. *Phys. Rev.*, **94**(2):262, (1954).

[57] E. Krotscheck, M. Saarela, and J. L. Epstein. Impurity states in liquid-helium films. *Phys. Rev. B*, **38**(1):111, (1988).

[58] J. G. Brisson. PhD thesis, Harvard University, (1990).

[59] P. T. Ptukha. Thermal conductivity and diffusion in weak He^3-He^4 solutions in the temperature range from the λ point to 0.6 K. *Sov. Phys. JETP*, **13**(6):1112, (1961).

[60] R. Mayer and G. Seidel. Electron-spin resonance of atomic hydrogen and deuterium at low temperatures. *Phys. Rev. B*, **31**(7):4199, (1985).

[61] S. Franchetti. On the problem of the static helium film. *Nuovo Cimento*, **IV**(6):1504, (1956).

[62] W. Kolos and W. Wolniewicz. Potential-energy curves for the $X^1\Sigma_g^+$, $b^3\Sigma_u^+$, and $C^1\Sigma_u$ states of the hydrogen molecule. *J. Chem. Phys.*, **43**(7):2429, (1965).

[63] W. Kolos and W. Wolniewicz. Variational calculation of the long range interaction between two ground-state hydrogen atoms. *Chem. Phys. Lett.*, **24**(4):457, (1974).

[64] W. Kolos and W. Wolniewicz. Improved potential energy curve and vibrational energies for the electronic ground state of the hydrogen molecule. *J. Mol. Spectry.*, **54**:303, (1975).

[65] J. M. Greben, A. W. Thomas, and A. J. Berlinsky. Quantum theory of hydrogen recombination. *Can. J. Phys.*, **59**:945, (1981).

[66] G. A. Clarke. Effects of helium buffer gas atoms on the atomic hydrogen hyperfine frequency. *J. Chem. Phys.*, **36**:2211, (1962).

[67] W. D. Davison and Y. C. Liew. A calculation of the interaction potential and hyperfine shift in HeH. *J. Phys. B*, **5**:309, (1972).

[68] S. Ray. Molecular theory of hyperfine pressure shifts in H caused by Ar and He buffers. *Phys. Rev. A*, **12**:2031, (1975).

[69] R. Jochemsen, M. Morrow, and A. J. Berlinsky. The hyperfine frequency shift of atomic hydrogen in the presence of a helium buffer gas. *Can. J. Phys.*, **60**:252, (1982).

[70] M. Pinard and F. Laloë. The role of the Pauli principle in spin exchange collisions. *J. Physique.*, **41**:769, (1980).

[71] S. B. Crampton. *Hyperfine and Spin Exchange Experiments with the Atomic Hydrogen Maser.* PhD thesis, Harvard University, (1964).

[72] S. B. Crampton. Spin-exchange shifts in the hydrogen maser. *Phys. Rev.*, **158**(1):57, (1967).

[73] P. L. Bender. Effect of hydrogen-hydrogen exchange collisions. *Phys. Rev.*, **132**(5):2154, (1963).

[74] L. C. Balling, R. J. Hanson, and F. M. Pipkin. Frequency shifts in spin-exchange optical pumping experiments. *Phys. Rev.*, **133**(3A):A607, (1964).

[75] M. Desaintfuscien and C. Audoin. Temperature dependence of the hydrogen-hydrogen spin-exchange cross section. *Phys. Rev. A*, **13**(6):2070, (1976).

[76] Howard C. Berg. Spin exchange and surface relaxation in the atomic hydrogen maser. *Phys. Rev.*, **137**(6A):A1621, (1965).

[77] Values obtained in a private communication from B. J. Verhaar. All values correspond to results published in reference [20].

[78] A. J. Berlinsky and B. Shizgal. Spin-exchange scattering cross sections for hydrogen atoms at low temperatures. *Can. J. Phys.*, **58**:881, (1980).

[79] S. B. Crampton, J. A. Duvivier, G. S. Read, and E. R. Williams. Frequency shifts due to hydrogen-hydrogen spin-exchange collisions. *Phys. Rev. A*, **5**(4):1752, (1972). This measurement was made at 308 K. Allison [80] has calculated $\overline{\lambda}(308\text{K}) = 4.0\text{Å}^2$.

[80] A. C. Allison. Spin-change frequency shifts in H-H collisions. *Phys. Rev. A*, **5**(6):2695, (1972).

[81] W. N. Hardy and M. Morrow. Prospects for low temperature h masers using liquid helium coated walls. *Journal de Physique*, **42**(12):C8–171, (1981).

[82] S. B. Crampton and H. T. M. Wang. Duration of hydrogen-atom spin-exchange collisions. *Phys. Rev. A*, **12**(4):1305, (1975).

[83] A. C. Maan, H. T. C. Stoof, and B. J. Verhaar. The cryogenic H maser in a strong B field. *Phys. Rev. A*, 41(5):2614, (1989).

[84] J. M. V. A. Koelman, S. B. Crampton, H. T. C. Stoof, and O. J. Luiten. Frequency instability of cryogenic and room temperature hydrogen masers. In *Proc. 3rd Int. Conf on Spin Polarized Quantum Systems*, (1989).

[85] Martin D. Hürliamnn, A. John Berlinsky, Richard W. Cline, and Walter N. Hardy. A recirculating cryogenic hydrogen maser. *IEEE Trans. on Instr. and Measurement*, **IM-36**(2):584, (1987).

[86] W. N. Hardy and L. A. Whitehead. Split-ring resonator for use in magnetic resonance from 200-2000 MHz. *Rev. Sci. Instrum.*, **52**(2):213, (1981).

[87] M. Abe, M. Gomi, and F. Yokoyama. Magneto-optical effect in anodized Al_2O_3 film with micropores electrodeposited with Co. *J. Appl. Phys.*, **57**(1):3909, (1985).

[88] F. Keller, M. S. Hunter, and D. L. Robinson. Structural features of oxide coatings on aluminum. *J. Electrochem. Soc.*, **100**:411, (1953).

[89] D. R. Williams, W. Lum, and S. Weinreb. L-band cryogenically cooled GaAs FET amplifier. *Microwave Journal*, **23**:73, (1980).

[90] M. D. Hürlimann. to be published.

[91] R. J. Corruccini and J. J. Gniewek. Specific heats and enthalpies of technical solids. In *NBS Monograph 21*. US Department of Commerce, (1960).

[92] G. K. White. *Experimental Techniques in Low Temperature Physics*. Oxford University Press, London, 1968.

[93] Thomas R. Roberts and Stephen G. Sydoriak. Thermomolecular pressure ratios for He^3 and He^4. *Phys. Rev.*, **102**(2):304, (1956).

[94] Tetsuo Miyazaki and Kwang-Pill Lee. Direct evidence for the tunneling reaction HD + D → H + D_2 in the radiolysis of a D_2-HD mixture at 4.2 K. *J. Phys. Chem.*, **90**:400, (1986).

[95] Kwang-Pill Lee, Tetsuo Miyazaki, Kenji Fueki, and Kenji Gotoh. Rate constant for tunneling reaction D_2 + D → D + D_2 in radiolysis of D_2-HD mixtures at 4.2 and 1.9 K. *J. Phys. Chem.*, **91**:180, (1987).

[96] L. Pierre, H. Guignes, and C. Lhuillier. Adsorption states of light atoms (H,D,He) on quantum crystals(H_2,D_2,He,Ne). *J. Chem. Phys.*, **82**(1):496, (1985).

[97] Ray Radebaugh. Thermodynamic properties of HE^3-HE^4 solutions with applications to the HE^3-HE^4 dilution refrigerator. In *NBS Technical Note 362*. US Department of Commerce, (1967).

[98] G. Das, A. F. Wagner, and A. C. Whal. Calculated longe-range interactions and low energy scattering in He+H, Ne+H, Ar+H, Kr+H and Xe+H. *J. Chem. Phys.*, **68**:4917, (1978).

[99] Isaac F. Silvera. Spin-polarized hydrogen and deuterium: Quantum gases. In *Physica*, volume **109** & **110B**, page 1499, (1982). Proc. 16th Int. Conf. on Low Temperature Physics.

[100] R. W. Cline, T. J. Greytak, and D. Kleppner. Nuclear polarization of spin-polarized hydrogen. *Phys. Rev. Lett.*, **47**:1195, (1981).

[101] R. Sprik, J. T. M. Walraven, G. H. van Yperen, and Isaac F. Silvera. State dependent recombination and suppressed nuclear relaxation in atomic hydrogen. *Phys. Rev. Lett.*, **49**:153, (1982).

[102] B. Yurke, J. S. Denker, B. R. Johnson, N. Bigelow, L. P. Levy, D. M. Lee, and J. H. Freed. NMR-induced recombination of spin polarized hydrogen. *Phys. Rev. Lett.*, **50**:1137, (1983).

[103] J. C. Slater. Microwave electronics. *Rev. Mod. Phys.*, **18**:441, (1946).

[104] D. J. Wineland and N. F. Ramsey. Atomic deuterium maser. *Phys. Rev. A*, **5**(2):821, (1972).

[105] R. A. Waldron. *The Theory of Waveguides and Cavities.* Gordon and Breach Science Publishers, New York, 1967.

[106] J. C. Amato and H. Herrmann. Improved method for measuring the electric fields in microwave cavity resonators. *Rev. Sci. Instrum.*, **56**(5):696, (1985).

[107] L. C. Maier and J. C. Slater. Field strength measurements in resonant cavities. *J. Appl. Phys.*, **23**(1):68, (1952).

[108] C. Kittel. *Introduction to Solid State Physics.* John Wiley and Sons, 5th edition, 1976.

[109] J. A. Osborne. Demagnetizing factors of the general ellipsoid. *Phys. Rev.*, **67**(11 and 12):351, (1945).

[110] J. Wong. *Filling Factor of a Microwave Resonant Cavity.* Undergraduate thesis, University of British Columbia, (1989).

[111] H. M. Roder, R. D. McCarty, and V. J. Johnson. Liquid densities of oxygen, nitrogen, argon and para hydrogen. In *NBS Technical Note 361 - Revised.* US Department of Commerce, (1972).

[112] Victor J. Johnson, editor. US National Bureau of Standards: *The Properties of Materials at Low Temperatures.* Pergammon Press, (1959).

[113] G. Föex. Diamagnétisme et paramagnétisme. In *Constantes Sélectionées* Volume 7. Masson & C^{ie}, Paris, (1957).

[114] B. A. Younglove. Measurements of the dielectric constant of liquid O_2. In K. D. Timmerhaus, editor, *Advances in Cryogenic Engineering: Proc. 1969 Conf. on Cryogenic Engineering*, volume 15, New York, (1989). Plenum.

[115] A. P. Brodyanskii and Yu A. Freiman. The short range structure and properties of liquid oxygen. *Sov. J. Low Temp. Phys.*, **12**(11):684, (1986).

[116] I. S. Gradshteyn and I. M. Ryzhik. *Table of Integrals, Series, and Products.* Academic Press, Toronto, 1980.

[117] D. A. Bonn, D. C. Morgan, and W. N. Hardy. Split-ring resonators for measuring microwave surface resistance of oxide superconductors. *Rev. Sci. Instrum.*, **62**(7):1819, (1991).

[118] John F. Cochrane and D. E. Mathoper. Superconducting transition in aluminum. *Phys. Rev.*, **111**(1):132, (1958).

[119] J. Bardeen, L. N. Cooper, and J. R. Schrieffer. Theory of superconductivity. *Phys. Rev.*, **108**:1175, (1957).

[120] G. Herzberg. The dissociation energy of the hydrogen molecule. *J. Mol. Spectry.*, **33**:147, (1970).

[121] Robert J. Le Roy and Margaret G. Barwell. Ground state D_2 dissociation energy from the near-dissociation behavior of rotational level spacings. *Can. J. Phys.*,

53:1983, (1975).

[122] I. Dabrowski. The Lyman and Werner bands of H_2. *Can. J. Phys.*, **62**:1639, (1984).

[123] H. Bredohl and G. Herzberg. The Lyman and Werner bands of deuterium. *Can. J. Phys.*, **51**(9):867, (1973).

[124] I. Dabrowski and G. Herzberg. The absorption and emission spectra of HD in the vacuum ultraviolet. *Can. J. Phys.*, **54**:525, (1976).

[125] W. C. Stwally. The dissociation energy of the hydrogen molecule using long-range forces. *Chem. Phys. Lett.*, **6**(3):241, (1970).

Appendix A

Radiation Damping and the FID

We have made repeated use of the free induction decay (FID) response of a gas of hydrogen atoms (H) to a $\pi/2$ tipping pulse at the a-c hyperfine transition of H to measure the spin relaxation times of the atomic system. In this appendix we discuss the formalism used to model the evolution of the effective magnetization of the atomic system. Throughout this discussion we make use of the spin $\frac{1}{2}$ analogy introduced in chapter 2.

The free evolution of the net magnetization of a spin $\frac{1}{2}$ system in a magnetic field is a standard topic in most books on magnetic resonance [25]. One finds that in many situations the magnetization $\mathbf{M}$ evolves according to the phenomenological Bloch equations:

$$\frac{\mathrm{d}}{\mathrm{dt}}\mathbf{M} = \gamma\,(\mathbf{M}\times\mathbf{B}) - \frac{\mathrm{M_x}\hat{\mathrm{x}} + \mathrm{M_y}\hat{\mathrm{y}}}{\mathrm{T_2}} - \frac{\mathrm{M_z}\hat{\mathrm{z}} - \mathrm{M_0}\hat{\mathrm{z}}}{\mathrm{T_1}} \tag{A.1}$$

where $\mathrm{M_0}\hat{\mathrm{z}}$ is the thermal equilibrium magnetization in the static magnetic field and γ is the gyromagnetic ratio of the spins. In the spin $\frac{1}{2}$ analogy for H described in chapter 2, $\gamma_e = \gamma_e + \gamma_p$ or $\tilde{\gamma}$ and $\mathbf{M}$ is equated with $\tilde{\mathbf{M}}$. $\mathrm{T_2}$ and $\mathrm{T_1}$ are the well known transverse and longitudinal ('spin-lattice') relaxation times. $\mathrm{T_2}^{-1}$ characterizes the rate at which spins become dephased with respect to each other. $\mathrm{T_1}^{-1}$ is a measure of the coupling between the spin system and some external bath of spins (the 'outside world').

If we start with a system in thermal equilibrium and momentarily perturb it by applying a $\pi/2$ tipping pulse, the thermal equilibrium magnetization $\mathrm{M_0}\hat{\mathrm{z}}$ is rotated into the $\hat{\mathrm{x}} - \hat{\mathrm{y}}$ plane and becomes a precessing transverse magnetization

$$\mathbf{M_r} = \mathrm{M_x}\hat{\mathrm{x}} + \mathrm{M_y}\hat{\mathrm{y}} \tag{A.2}$$

with

$$M_x = M_r \cos(\omega t)$$

$$M_y = -M_r \sin(\omega t)$$

which eventually relaxes back to $M_0\hat{z}$ according to equations A.1. These precessing atoms radiate power which can be detected by coupling the atomic system to an electromagnetic resonator. In the regime of atomic densities and resonator Q's encountered in our work, the coupling between the radiating atoms and the resonator is strong enough that the atomic precession following a $\pi/2$ pulse can no longer be considered 'free'.[1] That is, the spins feel, and begin to precess in, their own radiation field. This effect was studied in detail by Bloom [30] and is commonly referred to as radiation damping.

A.1 Electrical model for the resonator

The calculation of the rf magnetic field produced by an oscillating magnetization inside a resonant cavity was first done by Slater [103]. The analysis of the coupling between these spins and the resonator is considerably more transparent than the original derivation if we use lumped circuit elements to model the resonator. This procedure was first outlined by Wineland *et al.* [104]. The results are equivalent to those obtained by Slater.

We assume that near resonance the resonator and the external electronics (as seen by the atomic system) can be modeled by the series LCR circuit shown in figure A.1. The precessing magnetization of the atomic system is coupled to the oscillating magnetic field in the inductor L. Physically the oscillating field in the inductor (or the split-ring resonator) is longitudinal. In the spin $\frac{1}{2}$ analogy for the H atom this field is mapped onto the transverse plane and is written H_x. The external circuitry (with characteristic

[1] In spite of this coupling we continue to refer to the response of the atomic system following a $\pi/2$ pulse as a FID.

impedance Z_0) is coupled to the resonator via an ideal transformer. The impedance Z_ℓ seen looking into the transformer is

$$Z_\ell = n^2 \left[R + j\left(\omega L - \frac{1}{\omega C}\right)\right]. \tag{A.3}$$

The coupling parameter

$$\beta = \frac{Z_0}{n^2 R} \tag{A.4}$$

is equal to one at critical coupling.

Using Faraday's law and Ampere's law the voltage induced across the inductor can be written[2]:

$$V = L\left(\frac{d}{dt}H_x + \eta M_x\right) \tag{A.5}$$

where η is the filling factor

$$\eta = \frac{\int H_x^2 dV_b}{\int H^2 dV_c}. \tag{A.6}$$

and V_b and V_c are the volumes of the sample bulb and the resonator. When the voltages around around the circuit in figure A.1 are summed up and differentiated with respect to time we obtain :

$$-\eta\frac{d}{dt}M_x = \frac{d^2}{dt^2}H_x + \frac{\omega_c}{Q_\ell}\frac{d}{dt}H_x + \omega_c^2 H_x \tag{A.7}$$

where :

$$\omega_c = \frac{1}{\sqrt{LC}} \tag{A.8}$$

$$Q_0 = \frac{\omega_c L}{R} \tag{A.9}$$

$$Q_\ell = \frac{Q_0}{1+\beta} \tag{A.10}$$

This is the classical equation which couples the field in the resonator to the magnetization of the spin system and is essentially the result derived by Slater.

[2]L is assumed to remain unchanged by the presence of the atomic sample.

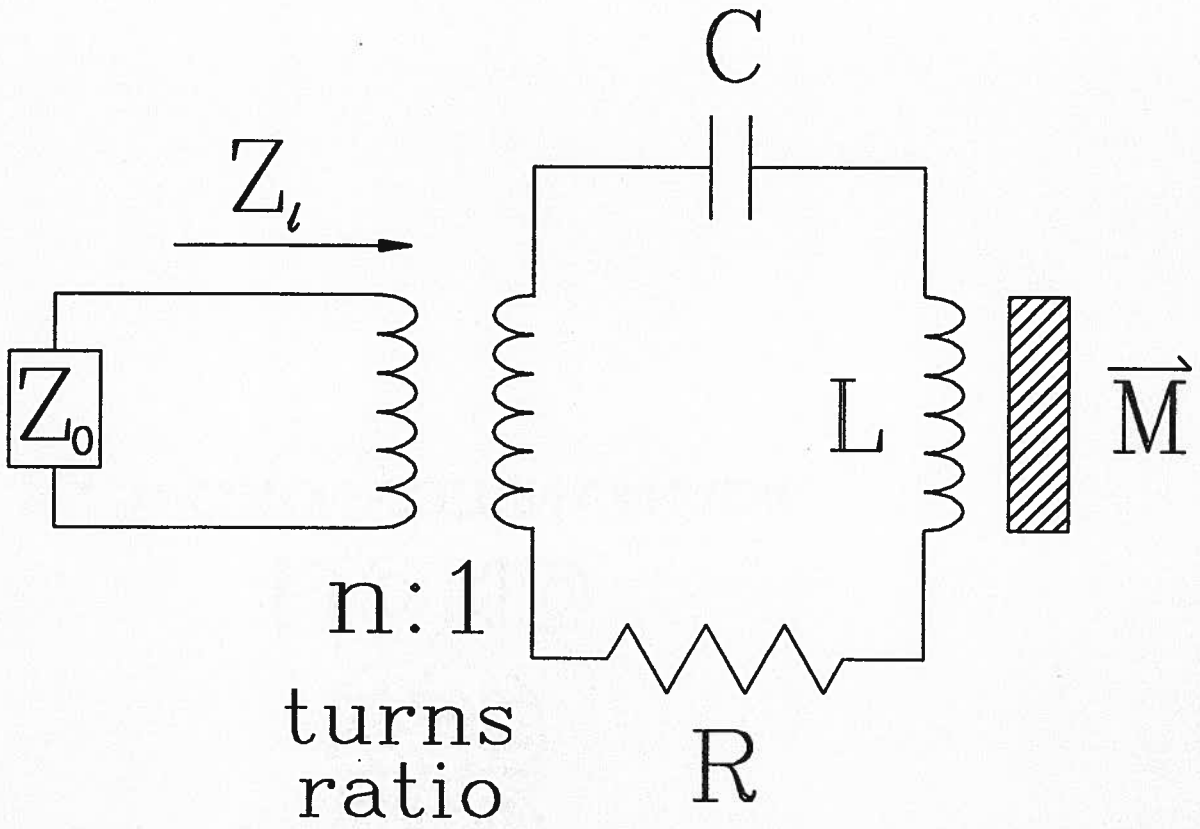

Figure A.1: The lumped parameter circuit used to model the coupling between the atomic system and the detection circuitry.

The response time $\frac{2Q}{\omega_c}$ of the resonators used in this work are much shorter than any of the relaxation times associated with the spin system. Thus the ringing field B_x due to the radiating spins can be assumed to respond instantaneously to changes in the magnetization. The steady state solution to equation A.7 for the oscillating field (an $e^{-j\omega t}$ time dependence is implicit) due to the spins is :

$$B_x = \mu_0 H_x = \mathrm{Re}\{KM_x\} \tag{A.11}$$

where the complex coupling constant K

$$K = K' + jK''$$

is given by

$$K = \left[\frac{\mu_0 \eta Q_\ell \left(\frac{\omega}{\omega_c}\right)}{1+\Delta^2}\right](\Delta - j) \tag{A.12}$$

and

$$\Delta = Q_\ell \left(\frac{\omega_c}{\omega} - \frac{\omega}{\omega_c}\right) \approx 2Q_\ell \frac{(\omega_c - \omega)}{\omega} \tag{A.13}$$

is a measure of the detuning of the resonator from the free angular precession frequency ω of the magnetization.

A.2 Radiation damping equations

Following a $\pi/2$ pulse the precessing transverse magnetization A.2 produces a ringing field B_x which is related to the magnetization via equation A.11. This field can can be decomposed into components rotating and counter rotating with respect to $\mathbf{M}_r$. The counter rotating field does not make a contribution to radiation damping and can be neglected. The next step is to transform into the frame $\hat{x}'$-$\hat{y}'$ rotating with angular velocity $\omega_0 = \gamma B_0$ and in the same sense as $\mathbf{M}_r$, and use the constraint A.11 to eliminate the magnetic field in the transformed equivalent of equations A.1. The algebra involved

in this transformation and substitution is straightforward. We omit the details. The resulting equations are:

$$\frac{d}{dt}M_z = \frac{\gamma}{2}K''M_r^2 - \frac{M_z - M_0}{T_1} \tag{A.14}$$

$$\frac{d}{dt}M_{x'} = -\frac{M_{x'}}{T_2} - \frac{\gamma}{2}M_z\left[K''M_{x'} + K'M_{y'}\right] \tag{A.15}$$

$$\frac{d}{dt}M_{y'} = -\frac{M_{y'}}{T_2} + \frac{\gamma}{2}M_z\left[K'M_{x'} - K''M_{y'}\right] \tag{A.16}$$

where

$$M_{x'} = M_r \cos\left[(\omega - \omega_0)t\right] \tag{A.17}$$

$$M_{y'} = -M_r \sin\left[(\omega - \omega_0)t\right] \tag{A.18}$$

are the transverse components of **M** in the rotating frame. These equations describe the evolution of the spin magnetization in the presence of radiation damping. Limiting approximations to these equations (such as the case where both T_1 and T_2 are infinitely long) have been studied previously [27]. In general, for work with H in which spin-exchange collisions cause T_1 and T_2 to be comparable to the apparent decay time of the FID, these simplifications are not justified.

It is worth examining these equations further in order to get a feeling for the the relevant parameters of the theory. Substituting A.17 into A.15 and A.18 into A.16 the equations involving the transverse magnetization can be rewritten[3] :

$$\frac{1}{M_r}\frac{d}{dt}\tilde{M}_r = -\frac{1}{T_2} - \frac{\gamma}{2}M_zK'' \tag{A.19}$$

$$\omega - \omega_0 = -\frac{\gamma}{2}M_zK' \,. \tag{A.20}$$

When the resonator is tuned close to the atomic resonance ($\Delta \ll 1$) K' is small and there are essentially no frequency pulling effects due to radiation damping. The precession is fully described by the remaining equations A.14 and A.19. These are in effect the

[3]In writing these equations we make the assumption that $\frac{d\omega}{dt} = 0$.

equations that were studied by Bloom [30]. The instantaneous damping rate for the transverse magnetization

$$\Gamma = -\frac{1}{M_r}\frac{dM_r}{dt} \tag{A.21}$$

is obtained from equation A.19. If the coupling K″ between the resonator and the spins is turned off, T_2 processes lead to an exponential decay of M_r following a $\pi/2$ pulse. This decay is accentuated as the coupling is turned back on. This additional damping is due to the precession of the magnetization about its own radiation field. The *rate* at which this additional damping is incurred depends upon the coupling, $1/T_2$, and in part $1/T_1$.

A.3 Data analysis

Keep in mind that the quantity which is measured in these experiments is the voltage amplitude of the rf power coupled from the atomic system, via the resonator, to the external circuitry. It is relatively simple to show [25] that the power which is detected is

$$P = \frac{\mu_0 \omega \eta Q_0 V_b}{4(1+\beta)} M_r^2 \,. \tag{A.22}$$

The FID amplitude is proportional to $P^{\frac{1}{2}}$ and is thus proportional to M_r. The constant of proportionality consists solely of measured parameters and hence the FID represents an absolute measurement of $M_r \cos[(\omega - \omega_{LO})t + \phi]$ where $\omega_{LO} \approx \omega_0$ is the angular frequency of the local oscillator (LO) of the spectrometer against which the FID is compared. ϕ is a phase angle which accounts for the relative phase between the precessing spins and the LO.

The FID data is fit to a numerically integrated solution of equations A.14, A.15, and A.16 with the initial conditions appropriate to a $\pi/2$ pulse

$$M_{x'}(0) = M_0 \cos(\phi)$$

$$M_{y'}(0) = -M_0 \sin(\phi)$$

$$M_z(0) = 0$$

where the thermal equilibrium magnetization is

$$M_0 = \hbar(\gamma_e + \gamma_p)n_H. \tag{A.23}$$

The precession frequency of the rotating frame is that of the LO rather than ω_0 in this case. The free parameters of the fit are T_1, T_2, $\omega - \omega_{LO}$, ϕ, and the amplitude of the FID (or in effect via equations A.22 and A.23, the H density).

A note of caution is required regarding the determination of T_1 from the FID data in this manner. As the effective damping time of the FID becomes comparable to, or shorter than the period of the beat frequency between the LO and the atomic precession it becomes difficult to determine T_1 precisely. The T_1 information is in the data as part of the rate at which the instantaneous damping of the FID is changing. This rate information is easily confused with an *apparent* frequency shift as the number of zero crossings in the FID data becomes small. Care has been taken throughout the data analysis to ensure that the zero crossings are well represented by the fits.

Appendix B

Measurement of Filling Factors

In this appendix we discuss the measurement of the filling factor η which was introduced in chapter 2. Two techniques for measuring this quantity are discussed; both are cavity perturbation measurements in which some perturbing body is introduced into the electromagnetic resonator so as to distort the rf field pattern. The change in the resonant frequency of the resonator is then used to infer the rf field strength at the site of the perturbation. A general discussion of these types of measurements can be found in reference [105].

The first technique has been used previously to study rf electric fields in microwave cavity resonators for particle accelerator applications [106] and rf magnetic fields in split-ring resonators [27]. It is based on a technique developed by Maier and Slater [107]. The second is a new technique which we have developed in the context of the low temperature studies of atomic hydrogen presented in this thesis. This measurement is introduced in the second part of this appendix. A detailed description of this technique including a discussion of its adaptability to other applications will be reported elsewhere.

Before reviewing cavity perturbation measurements, an important distinction between dielectric media and magnetic media must be pointed out. Dielectric materials can be used to distort rf electric fields without distorting the rf magnetic fields. In general it is difficult to find materials which will distort rf magnetic fields and not rf electric fields. Consequently it is easier to study rf electric fields by cavity perturbation methods than it is to study rf magnetic fields. The latter measurement must be performed in two

steps. First a magnetic substance must be introduced to the cavity to distort both the rf magnetic and electric fields. A second purely dielectric body must then be introduced to determine the contribution of the dielectric properties of the first body to the total perturbation.

B.1 Cavity perturbation measurements

Cavity perturbation measurements usually fall into one of two categories [105]. If the local change in the material parameters (electric and magnetic susceptibilities) during the measurement is large, the volume of the perturbing bodies must be small. If on the other hand the change in these parameters is small, the total volume which the bodies may occupy can be large. We refer to the first type of measurement as a type I perturbation and the latter as a type II measurement. Morrow's [27] determination of magnetic filling factors falls into the class of type I cavity perturbation measurements. The new technique which we describe later in this appendix is a type II measurement.

The distortion of the rf fields inside the resonator due to the insertion of the perturbing medium must be small enough that the electromagnetic mode structure is not changed significantly. In effect, we require the energy which is stored inside the perturbing body to be small in comparison to the total energy stored in the resonator in its perturbed condition. The perturbation condition can be stated in terms of the shift $\delta\omega$ which is observed in the resonant frequency ω_c of the resonator when the perturbing body is introduced. In general we require $\frac{\delta\omega}{\omega_c} \ll 1$ for the perturbation assumptions to be valid.

For both type I and type II perturbation measurements the changes in the fields ($\mathbf{E}_1$ and $\mathbf{H}_1$) and their inductions ($\mathbf{D}_1$ and $\mathbf{B}_1$) due to the perturbation must be small in comparison to the unperturbed quantities ($\mathbf{E}_0$,$\mathbf{H}_0$,$\mathbf{D}_0$, and $\mathbf{B}_0$) over *most* of the volume

V_c of the cavity.[1] The fractional frequency shift which is observed when a dielectric with magnetic properties is used to perturb the cavity resonance is[2] [105]

$$\frac{\delta\omega}{\omega_o} = \frac{\int_{V_s} [(\mathbf{E_1}\cdot\mathbf{D_0} - \mathbf{E_0}\cdot\mathbf{D_1}) - (\mathbf{H_1}\cdot\mathbf{B_0} - \mathbf{H_0}\cdot\mathbf{B_1})]\,dV}{\int_{V_c} (\mathbf{E_0}\cdot\mathbf{D_0} - \mathbf{H_0}\cdot\mathbf{B_0})\,dV} \tag{B.1}$$

where V_s is the volume occupied by the perturbing body. The first term in this expression represents the dielectric contribution to the frequency shift while the second term represents the magnetic contribution. It is the second term upon which we will focus most of our attention. Under the proper conditions it can be related to the filling factor η which was introduced in chapter 2.

We begin by writing equation B.1 in terms of the unperturbed fields. It is assumed that the dielectric constant ϵ and the permeability μ of the perturbing body are known and homogeneous throughout the material. This allows one to rewrite the electric displacement $\mathbf{D}$ and the magnetic induction $\mathbf{B}$ in terms of the fields $\mathbf{E}$ and $\mathbf{H}$. The depolarizing field $\mathbf{E_1}$ and the demagnetizing field $\mathbf{H_1}$ can also be written in terms of $\mathbf{E_0}$ and $\mathbf{H_0}$ with the aid of a well known property of homogeneous ellipsoidal bodies; namely that exposure to a uniform polarizing or magnetizing field will in turn produce a uniform polarization or magnetization within that body. If the polarization (or magnetization) along some axis within the body is $\mathbf{P}$ ($\mathbf{M}$), then the depolarization (demagnetization) field is related to it by [108, 109]

$$\mathbf{E_1} = -\frac{\mathbf{N_e P}}{\epsilon\epsilon_o} \qquad\qquad \mathbf{H_1} = -\frac{\mathbf{N_m M}}{\mu\mu_o}\,. \tag{B.2}$$

where N_e (N_m) is the depolarizing (demagnetizing) factor in that direction. The material polarization (magnetization) on the other hand, exists as a consequence of the total field

[1] For example the perturbed electric field $\mathbf{E_0} + \mathbf{E_1}$ must be very nearly equal to the unperturbed field $\mathbf{E_0}$ most places within the resonator, and likewise for the other electromagnetic quantities.

[2] The convention that $\mathbf{E} = E_0 \exp(j\omega t)$ and $\mathbf{H} = H_0 \exp(j\omega t)$ has been adopted and thus the terms $\mathbf{E_0}\cdot\mathbf{D_0}$ and $-\mathbf{H_0}\cdot\mathbf{B_0}$ have the same sign.

$\mathbf{E} = \mathbf{E_0} + \mathbf{E_1}$ (or $\mathbf{H} = \mathbf{H_0} + \mathbf{H_1}$) and thus :

$$\mathbf{E_1} = -\frac{N_e(\epsilon - 1)}{1 + N_e(\epsilon - 1)}\mathbf{E_0} \qquad \mathbf{H_1} = -\frac{N_m(\mu - 1)}{1 + N_m(\mu - 1)}\mathbf{H_0}\,. \tag{B.3}$$

Using these relationships the fractional frequency shift B.1 cab be rewritten in the more useful form :

$$\frac{\delta\omega}{\omega_o} = -\frac{\frac{1}{2}(\epsilon - 1)}{1 + N_e(\epsilon - 1)}\frac{\int_{V_s}\mathbf{E_0}\cdot\mathbf{E_0^*}dV}{\int_{V_c}\mathbf{E_0}\cdot\mathbf{E_0^*}dV} - \frac{\frac{1}{2}(\mu - 1)}{1 + N_m(\mu - 1)}\frac{\int_{V_s}\mathbf{H_0}\cdot\mathbf{H_0^*}dV}{\int_{V_c}\mathbf{H_0}\cdot\mathbf{H_0^*}dV}\,. \tag{B.4}$$

As would be expected, an increase in either of the material parameters ϵ or μ results in a drop in the resonant frequency of the cavity which is being investigated.

B.1.1 Type I perturbations

For a type I perturbation measurement where the volume of the perturbing body V_s is much smaller than the volume V_b of the sample bulb used to confine the gasses of atomic H, we define a reduced magnetic filling factor η_{mr} such that

$$\eta_{mr} = \frac{V_c}{V_s}\frac{\int_{V_s}\mathbf{H_0}\cdot\mathbf{H_0^*}dV}{\int_{V_c}\mathbf{H_0}\cdot\mathbf{H_0^*}dV} \tag{B.5}$$

and

$$\eta_m = \frac{\int_{V_b}\eta_{mr}(\mathbf{r})dV}{V_c}\,. \tag{B.6}$$

The rf magnetic fields inside the split-ring resonators used in our work with atomic gasses are homogeneous and uniform[3] over the sample volume. In this situation we are justified in associating the true filling factor η with η_m.

Similar quantities η_{er} and η_e can be defined for the electric fields. The frequency shift (equation B.4) can thus be written :

$$\frac{\delta\omega}{\omega_o} = -\frac{\frac{1}{2}(\epsilon - 1)\eta_{er}}{1 + N_e(\epsilon - 1)} - \frac{\frac{1}{2}(\mu - 1)\eta_{mr}}{1 + N_m(\mu - 1)}\,. \tag{B.7}$$

[3]The sample bulbs consist of two distinct volumes. The main body of the bulb is located within the bore of the split-ring resonator. The fields here are uniform and longitudinal. The tails of the bulb extend into regions where the rf field intensity is essentially zero. The volume associated with the transition region is small and can be neglected.

Both η_{er} and η_{mr} can be determined at a given position within the resonator by measuring the fractional frequency shifts for two different perturbing bodies placed in that location. The bodies must have well known but different dielectric and magnetic properties. By passing these bodies throughout the volume of interest, the filling factors η_e and η_m are easily determined.

This technique was used to measure the filling factor of the resonator used in our studies of mixtures of H and D described in chapters 6 and 7 [110]. The measurements were made using small teflon ($\epsilon_t \approx 2, \mu_t = 1$) sphere as the dielectric body and a similar aluminum sphere ($\epsilon_m = -j\infty, \mu_m = 0$) as the other. Each sphere was suspended from a fine silk thread which was held taught between mechanical locating devices. The dielectric constant of the teflon sphere was first measured by perturbing the resonant frequency of a microwave cavity with a known mode structure. The two spheres were then passed (individually) throughout the entire volume of the split-ring resonator normally occupied by the sample bulb. During this measurement a cylindrical pyrex sleeve was used to mimic the walls of the sample bulb. The shift $\delta\omega$ of the resonant frequency of the split-ring resonator was recorded as a function of the position of the sp eres. As the demagnetizing and the depolarizing factors for a sphere are both equal to $\frac{1}{3}$ it is a simple matter to determine η_{er} and η_{mr} at each position inside the resonator at which measurements were made. The filling factor η is determined by performing the sum indicated by equation B.6.

The main drawbacks associated with this technique are that it is quite time consuming to perform the measurement and that often (substantial) changes need to be made to the resonator to allow access to the sample volume. The accuracy of the technique is limited by the reproducibility of the sample placement within the resonator volume. The new technique which is introduced in the following section was developed to eliminate some of these problems.

B.1.2 Type II perturbations

In contrast to a type I measurement, the perturbing body in a type II measurement occupies the entire volume of interest.[4] This means that detailed information about the local field homogeneity is not available. On the other hand the complexity of the sample and the resonator geometries can be quite intricate.

To interpret the frequency shift predicted by equation B.4 in terms of a magnetic filling factor, we again assume that the rf magnetic fields are homogeneous and uniform[5] over the sample bulb volume. The resulting frequency shift is :

$$\frac{\delta\omega}{\omega_o} = -\frac{\frac{1}{2}(\epsilon-1)}{1+N_e(\epsilon-1)}\frac{\int_{V_b}\mathbf{E_0}\cdot\mathbf{E_0^*}dV}{\int_{vc}\mathbf{E_0}\cdot\mathbf{E_0^*}dV} - \frac{\frac{1}{2}(\mu-1)\eta_m}{1+N_m(\mu-1)}\,. \tag{B.8}$$

We do not make any assumptions about the electric field homogeneity and leave the first term in this equation unevaluated. We have implicitly assumed that the frequency shifts scale as if *effective* depolarizing and demagnetizing factors[6] can be associated with the sample volume.

The choice of perturbing media for a type II measurement is very limited. The first trick is to find a material with a relatively large permeability μ and at the same time a relatively low dielectric constant ϵ within the constraint that both of these parameters must be close to unity. That is, the frequency shift due to the magnetic properties should not be swamped by the dielectric contribution to the shift. The total shift must of course be small. The second trick is to find another material which has essentially the same dielectric properties as the first but which is non-magnetic. The measurement is then made by filling the entire sample bulb alternately with each material and measuring the fractional frequency shift $\frac{\delta\omega}{\omega_c}$ of the cavity resonance. As long as the dielectric constants

[4] *i.e.* the sample bulb volume

[5] As mentioned previously the sample volume can be thought of as being composed of two distinct volumes. The assumption of field homogeneity in both regions is confirmed by the type I measurements described above.

[6] Strictly speaking these quantities are only defined for ellipsoidal bodies.

Temperature (K)	Liquid	Density [111] (g/cm^3)	$\epsilon - 1$	$\mu - 1$
77.35 (liquid N_2)	N_2	0.80739	0.4430 [112]	-8.7×10^{-6} [113]
	O_2	1.2027	0.51716 [114]	3.93×10^{-3} [113, 115]
87.28 (liquid Ar)	Ar	1.3939	0.519 [112]	-8.65×10^{-6} [113]
	O_2	1.1553	0.49411 [114]	3.55×10^{-3} [113, 115]

Table B.1: Various material parameters of liquid oxygen, argon, and nitrogen at the boiling points of the liquid N_2 and liquid Ar under 1 atmosphere of pressure. Permeabilities and permittivities are in MKS units.

of the two media are matched[7] the 'depolarizing factor' in equation B.8 is irrelevant. In addition, for practical materials $\mu - 1 \ll 1$ and demagnetizing effects can be ignored altogether. The difference between the two fractional frequency shifts thus gives a measure of the filling factor η_m.

We have made use of the rather unique properties of liquid O_2, and Ar in our measurement of the filling factor of the UBC cryogenic hydrogen maser bulb. Liquid oxygen is very strongly paramagnetic and at the same time has a relatively low dielectric constant. Liquid Ar has very nearly the same dielectric constant as liquid O_2. As our work with atomic gasses is cryogenic by nature, the adaptations required to use liquid O_2 and Ar were minimal. Furthermore, as both of these liquids have been studied in detail by others, no measurements of the relevant material properties had to be made. The permeabilities, permittivities and densities of liquid O_2, Ar and N_2 are presented in table B.1 along with references to the source of the data. The reason for including the properties of liquid N_2 will become obvious below.

The measurement of η was made by admitting the various cryogens to the maser bulb one at a time and observing the shift in the resonant frequency of the split-ring

[7]If they are not perfectly matched then it is possible to measure the effective depolarizing factor. This procedure is described below.

resonator. To make use of the temperature dependence of the dielectric properties of the liquids, the liquid O_2 was condensed into the maser bulb at the temperature of boiling liquid N_2 and the liquid Ar at the temperature of boiling Ar. The difference in $\epsilon - 1$ for the two liquids under these conditions is only 0.4%. The fractional shift $\frac{\delta\omega}{\omega_c}$ of the cavity resonance which is measured when the resonator is loaded with liquid O_2 is larger than when it is loaded with liquid Ar due to the paramagnetic susceptibility of the O_2. The difference between the two shifts is *essentially* that due to the magnetic properties of the O_2.

If the small difference between the dielectric constants of liquid O_2 and Ar is taken into account the dielectric contribution to the liquid O_2 shift is

$$\left(\frac{\delta\omega}{\omega_0}\right)_{\ell O_2}\Bigg|_{\text{dielectric}} = \frac{(\epsilon_{O_2}-1)}{(\epsilon_{\ell Ar}-1)}\left[\frac{1+N_e(\epsilon_{\ell Ar}-1)}{1+N_e(\epsilon_{\ell O_2}-1)}\right]\left(\frac{\delta\omega}{\omega_0}\right)_{\ell Ar} \tag{B.9}$$

where N_e is the effective depolarizing factor for the particular geometry. This factor can be estimated by also filling the cell with liquid N_2 at its boiling temperature. The dielectric shift of the resonance when the cell is loaded with liquid N_2 is somewhat smaller than the dielectric shift caused by either of the other cryogens. The ratio of two purely dielectric shifts (N_2 and Ar) can be used to determine the effective N_e from equation B.8. We find

$$N_e = \frac{1}{1-r}\left(\frac{r}{\epsilon_{\ell N_2}-1} - \frac{1}{\epsilon_{\ell Ar}}\right) \tag{B.10}$$

where

$$r = \frac{\left(\frac{\delta\omega}{\omega_0}\right)_{\ell N_2}}{\left(\frac{\delta\omega}{\omega_0}\right)_{\ell Ar}} < 1 \tag{B.11}$$

is the ratio of the fractional shifts in the cavity resonance when the cell is filled with liquid N_2 and with liquid Ar.

The Ar and N_2 frequency shifts determine N_e and ultimately the dielectric contribution to the liquid O_2 shift (equation B.8). The magnetic contribution to this shift is

given by

$$\left(\frac{\delta\omega}{\omega_0}\right)_{\ell O_2}\Bigg|_{\text{magnetic}} = \left(\frac{\delta\omega}{\omega_0}\right)_{\ell O_2} - \left(\frac{\delta\omega}{\omega_0}\right)_{\ell O_2}\Bigg|_{\text{dielectric}} \tag{B.12}$$

and hence the filling factor η_{m} can be written[8]

$$\eta_{\text{m}} = \frac{2}{(\mu - 1)}\left(\frac{\delta\omega}{\omega_0}\right)_{\ell O_2}\Bigg|_{\text{magnetic}} . \tag{B.13}$$

Again because of the homogeneity of the magnetic fields in the particular geometries we have used, η_{m} can be associated with the filling factor η.

[8] N_m has been neglected as $\mu - 1 \ll 1$ for liquid O_2.

Appendix C

Rate Equations for the Atomic Densities

In chapter 3 we discussed the recombination of two hydrogen atoms (H) catalyzed by a third body :

$$H + H + X \rightarrow H_2 + X\,. \tag{C.1}$$

The H atom density (n_H) inside a sealed container filled with a gas of H decays as

$$\left.\frac{d}{dt}(n_H)\right|_{\text{HH recomb.}} = -K_{HH} n_H^2 \tag{C.2}$$

where K_{HH} is the rate constant for this reaction. The recombination of two D atoms to form D_2 can be described in a completely analogous manner by simply replacing 'H' with 'D' in the above equations. In both cases, if no other processes lead to a change in the atomic density n_i, the time dependence of n_i is given by

$$n_i(t) = \frac{1}{K_{ii}}\left(\frac{1}{t+\tau}\right) \tag{C.3}$$

where n_i° is the initial atomic density and

$$\tau = \frac{1}{K_{ii} n_i^\circ} \tag{C.4}$$

is a characteristic time for the recombination process. When a gas consisting of a mixture of H *and* D is considered, the additional reaction

$$H + D + X \rightarrow HD + X \tag{C.5}$$

also contributes to the decay of both the H and the D densities :

$$\left.\frac{d}{dt}(n_H)\right|_{\text{HD recomb.}} = \left.\frac{d}{dt}(n_D)\right|_{\text{HD recomb.}} = -K_{HD} n_H n_D \tag{C.6}$$

The symmetry of these rate equations is broken by the fact that the solvation of D atoms through the ℓ-^{4}He coated walls of a cell at temperatures near 1 K [21] leads to an additional decay mechanism

$$\left.\frac{d}{dt}(n_D)\right|_{solvation} = -\lambda n_D \tag{C.7}$$

for the D atoms. In this equation λ is the solvation rate constant. The complete rate equations for the atomic densities inside a sealed bulb containing a mixture of both H and D near 1 K are thus :

$$\dot{n}_H = -K_{HH}n_H^2 - K_{HD}n_H n_D \tag{C.8}$$

$$\dot{n}_D = -K_{DD}n_D^2 - K_{HD}n_H n_D - \lambda n_D \tag{C.9}$$

where the dots indicate differentiation with respect to time. In general there is no known analytic solution to these equations and they must be integrated numerically.

C.0.3 Simplified equations

In chapter 7 we encountered a situation[1] in which two simplifying assumptions in the rate equations C.9 and C.8 were justified. The solution to the rate equations C.8 and C.9 with these approximations is discussed below.

The first assumption[2] we make is that H-D recombination makes a negligible contribution to the decay of the D atom density. That is, we assume $K_{DD}n_D \gg K_{HD}n_H$ and that $\lambda \gg K_{HD}n_H$. In this approximation equation C.9 becomes :

$$\dot{n}_D = -K_{DD}n_D^2 - \lambda n_D \tag{C.10}$$

[1]This situation occurred during the studies with $n_D^o \gg n_H$.

[2]There is in fact no need to make any assumptions at this point. The derivation of equation C.12 is equally valid without this assumption except that λ needs to be replaced everywhere with $K_{HD}n_H + \lambda$. The solution of equation C.13 however does require this assumption to be made. We make it here only to simplify the notation.

This equation has the same form as the Ricatti equation [116]

$$\frac{dz}{dt} = a(t)z + b(t)z^2 + c(t) \tag{C.11}$$

with $c(t) = 0$. With the initial condition $n_D(0) = n_D^\circ$ we obtain :

$$n_D(t) = n_D^\circ \left[\frac{\lambda\tau \exp(-\lambda t)}{(1+\lambda\tau) - \exp(-\lambda t)}\right] \tag{C.12}$$

where τ is the characteristic time for D-D recombination given by C.4. The decay of n_D is exponential in the limit $\tau^{-1} \to 0$ as it should be due to solvation. On the other hand at high D densities $\tau^{-1} \gg \lambda$ and equation C.12 reduces to equation C.3 as it should for D-D recombination.

The second assumption which we make is that H-H recombination makes a negligible contribution to the decay of the H density. That is, we assume that $K_{HD} n_D \gg K_{HH} n_H$. Substituting equation C.12 into C.8 with this approximation, the differential equation

$$\dot{n}_H(t) = -K_{HD} n_D^\circ \left[\frac{\lambda\tau \exp(-\lambda t)}{(1+\lambda\tau) - \exp(-\lambda t)}\right] \tag{C.13}$$

for n_H is obtained. This equation can be solved analytically with the initial condition $n_H(0) = n_H^\circ$. The result is :

$$n_H(t) = n_H^\circ \left[\frac{\lambda\tau}{(1+\lambda\tau) - \exp(-\lambda t)}\right]^{\frac{K_{HD}}{K_{DD}}} \tag{C.14}$$

At short times ($t \approx \lambda^{-1}$) the H density is a decreasing function of time as some H atoms are scavenged from the gas phase by D atoms. On a longer time scale the H density levels off at a fraction

$$\lim_{t\to\infty} \frac{n_H(t)}{n_H^\circ} = \left[\frac{\lambda\tau}{(1+\lambda\tau)}\right]^{\frac{K_{HD}}{K_{DD}}} \tag{C.15}$$

of its initial value. This ratio is valid only for as long as any other processes which cause n_H to change can be neglected. Eventually H-H recombination must reduce n_H further.

An interesting point which should be noted is that the H and the D densities are related :

$$\frac{n_D(t)}{n_D^o} = \left(\frac{n_H(t)}{n_H^o}\right)^{\frac{K_{DD}}{K_{HD}}} \exp(-\lambda\tau) \qquad (C.16)$$

This relationship is independent of any calibration of the H or D densities and can provide a means of measuring the ratio of the D-D and H-D recombination rates.

The approximations discussed in this appendix are illustrated in figure C.1. We have chosen to set $K_{HD} = K_{DD}$ and $\lambda = \tau^{-1} = 0.1s^{-1}$. The initial conditions are such that $n_D^o = 10n_H^o$. The functions describing the approximate H and D densities (equations C.14 and C.12) are plotted as solid lines in this figure. The H density is plotted on a linear scale while the D density is plotted on a logarithmic scale. The dashed lines (short dashes) adjacent to the solid lines indicate the densities obtained by numerical integration of equations C.8 and C.9 with $K_{HH} = 0$. The discrepancies between these pairs of curves are due to the neglect of H-D recombination as a means of reducing the D density. The relative error in n_D gets progressively worse with time as the decay rate for n_D is underestimated by equation C.12. The error in the effective solvation rate which is inferred from these decays is 4%. The approximations also lead to an underestimation of the residual H density by about 3%. The third dashed line which is plotted in figure C.1 (long dashes) indicates the decay that would be expected for n_D neglecting recombination (solvation only).

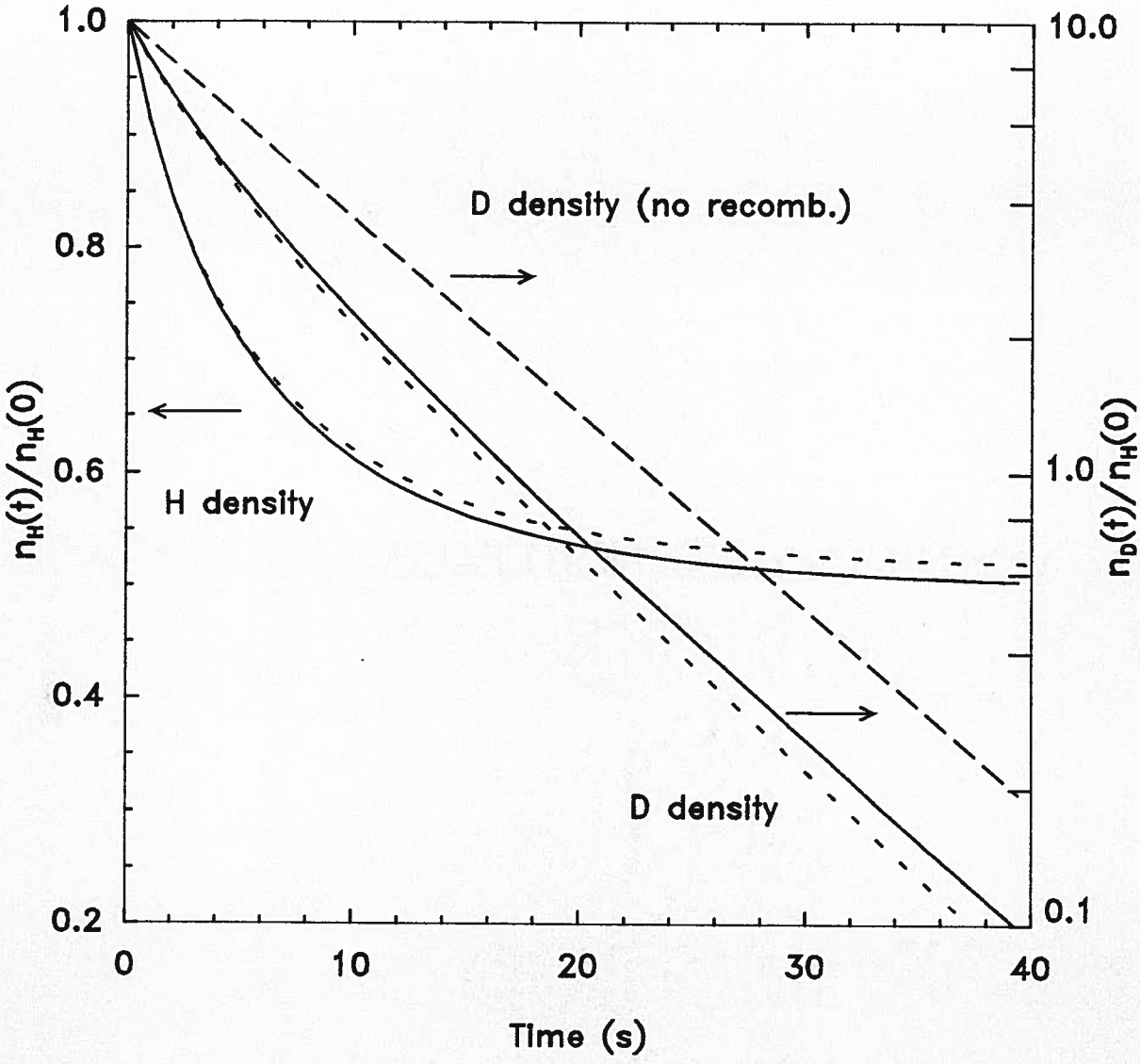

Figure C.1: An illustration of the approximations used for the H and the D densities. We have chosen to set $K_{HD} = K_{DD}$ and $\lambda = \tau^{-1} = 0.1s^{-1}$ with the initial condition $n_D^o = 10n_H^o$. The solid lines indicate the approximations C.12 and C.14 for n_D and n_H. The short dashed lines are obtained by numerical integration of equations C.9 and C.8 with $K_{HH} = 0$. The long dashed line indicates the decay of n_D which is expected due to solvation alone. Note that the H density is plotted on a linear scale while the D density is plotted on a logarithmic scale.

Appendix D

Temperature Measurement and Control of a ^{4}He Bath at 1 Kelvin

The measurement and control of absolute temperatures near 1 K played an important role in the studies of H, D mixtures presented in chapters 6 and 7 of this thesis. *Accurate* temperature measurements were needed to reliably determine the solvation energy required to force a D atom into a ℓ-^{4}He film. This is a consequence of the narrow (170 mK) temperature range over which measurements could be made[1]. *Precise* temperature control was needed in order to measure the H-D spin-exchange induced frequency shift of the a-c hyperfine transition of atomic hydrogen. This stability requirement was imposed by the strong temperature dependence of the ^{4}He buffer gas shift upon which the spin-exchange shift is superimposed[2].

In order to meet these requirements we used a commercial capacitance pressure gauge calibrated against a column of oil to measure the ^{4}He vapour pressure at the surface of the ℓ-^{4}He cooling bath in which the experiment was staged. This measurement was made through an open stainless steel tube placed just above the liquid surface; this avoids errors due to pressure gradients in the gas above the bath. The tube was equipped with a 'film burner' and a 'knife edge' in order to inhibit the flow of superfluid ^{4}He up its inner walls. The vapour pressure reading was then converted to a temperature using the

[1]The upper temperature limit is set by the rapid solvation of the D atoms into the ℓ-^{4}He film while the lower limit is set by the base temperature of the ^{4}He evaporation system.

[2]The change in the ^{4}He buffer gas shift which results from a 1 mK change in temperature is comparable to the maximum observed H-D spin-exchange shifts.

approximation [81]

$$P_{^4He}(T) = 155.827 \text{ Torr} \times \left(\frac{T}{1K}\right)^{\frac{5}{2}} \exp\left(-\frac{7.16888K}{T}\right) \quad \text{(D.1)}$$

Finally the voltage output of the capacitance gauge was used to temperature regulate the bath using a heater immersed in the bath.

D.1 Pressure gauge calibration

This work was performed using a 1 Torr full scale MKS Baratron gauge[3]. We encased this device in 5 cm of R10 styrofoam insulation to enhance its temperature stability. Prior to making ^4He vapour pressure measurements, the baratron was calibrated against a column of Inland TW vacuum pump fluid[4]. This oil was chosen simply because of its relatively low vapour pressure and its availability. Before using the oil it was vacuumed degassed at 90 C by pumping[5] on it through a liquid N_2 cold trap. After one day the residual vapour pressure was below 10^{-4} Torr.

The density of the oil was measured to be 0.8571(7) g/cm^3 at 22.7 C using a volumetric flask. The volume of the flask was measured independently using demineralized distilled H_2O which had been allowed to come to equilibrium (in air) at the same temperature. In both cases care was taken to account for weight changes due to the adsorption of moisture on the flask. The error in this density measurement due to gasses which dissolved into the oil during the measurement is estimated to be considerably less than the reported uncertainty.

The inner surfaces of the manometer were first cleaned with hydrofluoric acid and

[3]Model 220-2A1-1. MKS Instruments Ltd. Nepean Ont. Canada

[4]Inland Vacuum Co. New York, USA.

[5]Heating the fluid reduces its surface tension and expedites the formation of gas bubbles. A magnetic stirrer was also used to ensure that all of the oil reached the free surface where the pressure head due to the depth of the reservoir does not inhibit bubble formation. Note that by causing the stirrer to 'vibrate' rather than rotate smoothly one can actually assist in the nucleation of gas bubbles.

then filled with oil to a depth of 15 cm, with care being taken to keep oil off the upper walls of the tube. It was immediately evacuated and reheated to ensure that any gasses that had dissolved during the transfer were removed.

The temperature dependence of the density of the oil was measured by observing the height of the oil column (no pressure difference between the two tubes) as a function of temperature. This dependence[6] is less than 1 part in 10^3 per degree C. ^{4}He pressures up to 10 Torr were admitted to the manometer but no detectable change in the density of the oil due to the dissolution of gas was observed. At no time during or after the baratron calibration was the pressure allowed to rise more than 40% above full scale. No gasses other than ^{4}He were admitted to this system during these experiments.

The baratron gauge was allowed to reach thermal equilibrium and then calibrated against the height of the column of oil in the manometer as different pressures of ^{4}He gas were admitted to the system. Measurements of the height of the oil column were made with a Geartner Scientific Corporation cathetometer with an accuracy of 0.05 mm. Pressures were determined using the local acceleration due to gravity. Care was taken to investigate possible errors due to wetting of the glass surfaces by the oil as well as hysteretic effects: none were observed. A linear[7] least squares fit (60 data points) to the calibration data over the entire operating range of the Baratron was performed in order to determine the calibration between the capacitance gauge output voltage V_B and the measured pressure P:

$$P = \kappa \times V_B + \text{Constant} \tag{D.2}$$

[6]Throughout the calibration run the temperature of the oil was maintained constant to within 0.1 C of the temperature at which the density of the oil was measured.

[7]The zero of this type of gauge drifts with time, however the calibration constant (κ) does not appear to be measurably affected. During each experimental run the zero reading of the Baratron output was measured and subtracted from the data before using κ to convert to the true pressure.

No systematic deviations from this fit were observed and thus fits to higher order polynomials were not used. The rms deviation of the data from the fit was 4 mTorr. This is less than the measurement error associated with the height of the oil column. The relative error in the calibration constant κ due to statistical fluctuations was 0.16%.

D.2 ^{4}He wand and temperature regulation

Pressure measurements above the ^{4}He bath were made through a thin wall 0.953 cm diameter stainless steel tube. This diameter is sufficient to limit temperature corrections due to thermomolecular pressure gradients[93] to 0.6% at 1.0 K. This correction drops to 0.2% at 1.1 K and 0.05% at 1.2 K. A sliding o-ring seal allowed the wand to be moved to arbitrary heights above the liquid ^{4}He bath. Typically the wand was placed within 2 cm of the ℓ-^{4}He surface. No corrections have been made for the pressure head of ℓ-^{4}He above the experimental cell. The lower end of the tube was tapered down to a short 0.635 cm diameter section terminating in a knife edge in order to inhibit superfluid film flow (see figure D.1). Several turns of AWG 40 manganin wire were wrapped around the outside of the tube just above the knife edge and held in place with GE varnish. The free ends of this heater wire were passed carefully back over the knife edge and 50 cm up the inside of the wand where a transition was made to AWG 32 brass wire. A small current passed through this 'film burner' during pressure measurements was sufficient to stop the flow of superfluid ^{4}He up the inside of the wand.

The analogue output of the Baratron gauge was fed to a differential amplifier with a variable reference potential. The error signal from the output of this amplifier was then fed to a PID temperature regulator which in turn drove a resistive heater inside the ℓ-^{4}He bath. This system allowed us to set and regulate the pressure reading to within 0.1 mTorr of a desired value. At 1 K this translates into a temperature stability of $\pm$0.1 mK.

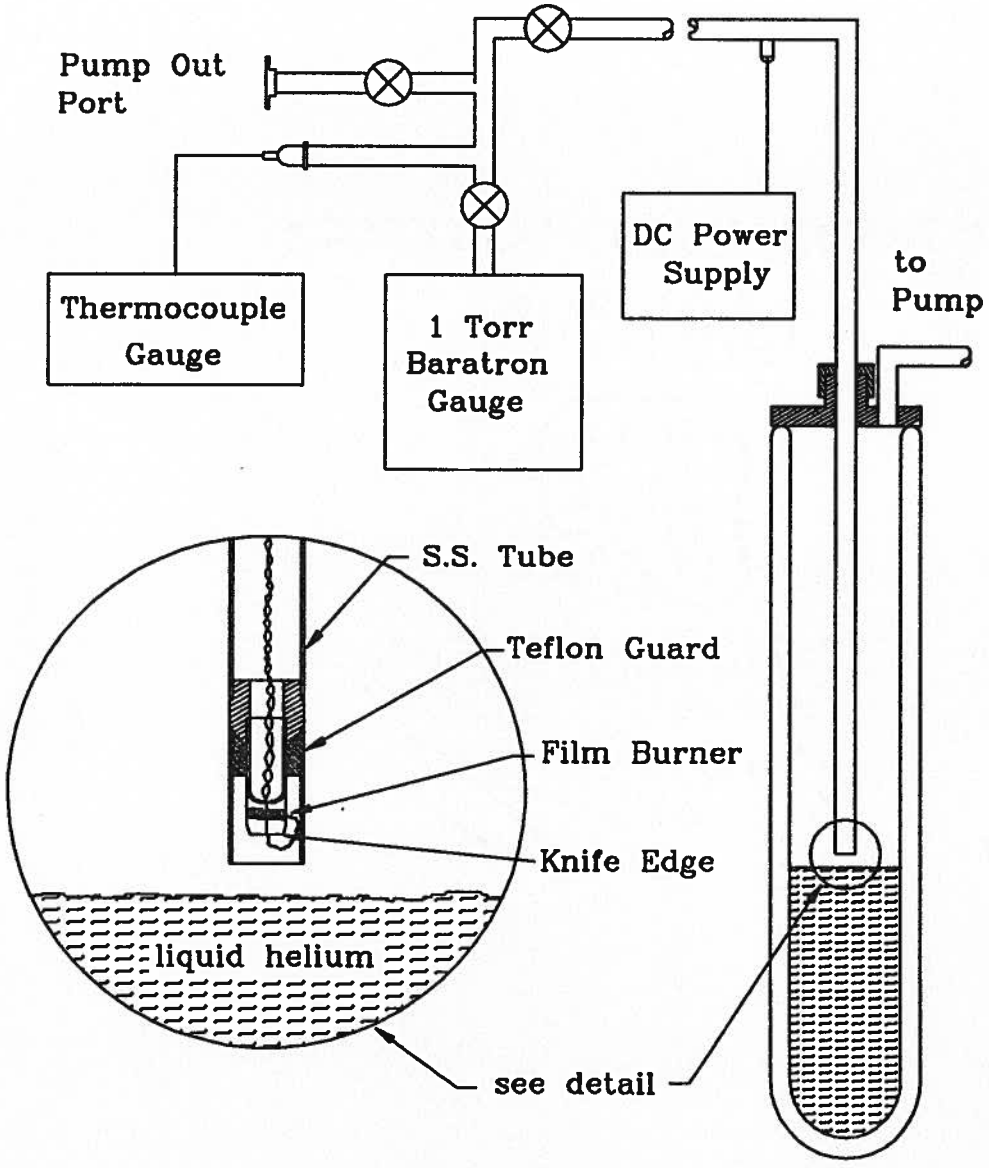

Figure D.1: A schematic diagram detailing the method used to measure ^{4}He vapour pressures above the ℓ-^{4}He cooling bath used in the experiments with H, D mixtures. Details are discussed in the text.

At 1.2 K the implied stability is about 5 times better due to the increased ^{4}He density.

The film burner was tested by applying varying amounts of power and monitoring the (unregulated) baratron reading. As the power was increased an abrupt drop in the pressure reading was observed at around 0.5 mW. This pressure drop was typically less than 1 mTorr or about 1 mK at 1K. Further increases in power did not influence the reading measurably until considerably higher power levels were reached and the entire ℓ-^{4}He bath was warmed. Under all operating conditions 1 mW of power was sufficient to burn off the film without causing a significant heat load.

D.3 Characterization of the measurement system

In order to establish the practical limitations of this method of measuring and regulating temperatures we undertook two experiments using the split-ring resonator described in chapter 6. These measurements are described below.

D.3.1 The superconducting transition of Al

Al undergoes a superconducting transition at a temperature T_c near 1.2 K and is thus a useful fixed point temperature reference for the work described in chapters 6 and 7. Microwave absorption measurements on superconducting materials using split-ring resonators are routine in this laboratory[117]. These measurements can be used to determine T_c. A 99.9999% pure Al disc (0.6 cm diameter, 1 mm thick) containing several large crystalline grains was attached to a thin strip of Cu with GE Varnish. This strip was then attached to the inner wall of the Cu housing for the 1.4 GHz split-ring resonator such that the clean face of the sample was normal to the radius of the split-ring and located about 3 mm away from its outer wall. The azimuthal location of the sample was about 90 degrees away from the gap in the split-ring. This location and means of mounting

the sample was chosen simply to make the mounting procedure as simple as possible without disturbing any components of the resonator and housing. No attempt was made to optimize the filling factor for the sample or the sensitivity of the measurement.

This assembly[8] was cooled to temperatures around 1.2 K and the resonator Q was measured in reflection as a function of the ℓ-^{4}He bath vapour pressure. Values of Q were determined by fitting the reflected power from a swept frequency measurement of the cavity resonance to a single Lorentzian lineshape with a second order background. In figure D.2 we plot the inverse quality factor of the resonator and sample as a function of the ^{4}He bath vapour pressure (squares). This data has been normalized to an arbitrary value Q_0 determined as the average Q 'far' from the data near 600 mTorr. The data consists of two temperature scans in opposite directions. No evidence of hysteresis is visible. The data in the wings[9] is quite flat in comparison to the feature near 600 mTorr. As the temperature of the sample is decreased from above 1.2 K, the microwave loss due to the combined resonator and sample first drops by a few percent before rising to a value which is slightly above the high temperature value. The decrease in absorption occurs at the onset of the superconducting transition. The sample and the sample mount were capacitively coupled to the resonator in such a way, that as the loss associated with the Al dropped, the microwave currents flowing through the sample holder increased. This is reflected in the data as an increase in the microwave loss part way through the transition.

Also shown in figure D.2 are two results (diamonds) from a measurement of T_c for Al by Cochrane and Mathoper [118]. The point at lower pressure represents their determination of $T_c = 1.196(4)$ K based upon a fit of their measurement of the critical field H_c as a function of temperature to the BCS theory [119]. We have plotted this value in equivalent ^{4}He vapour pressure units. Near T_c their fit deviates from their data.

[8]The Al sample was immersed in the ℓ-^{4}He bath in this geometry.
[9]Additional measurements extend to higher and lower pressures but are not shown.

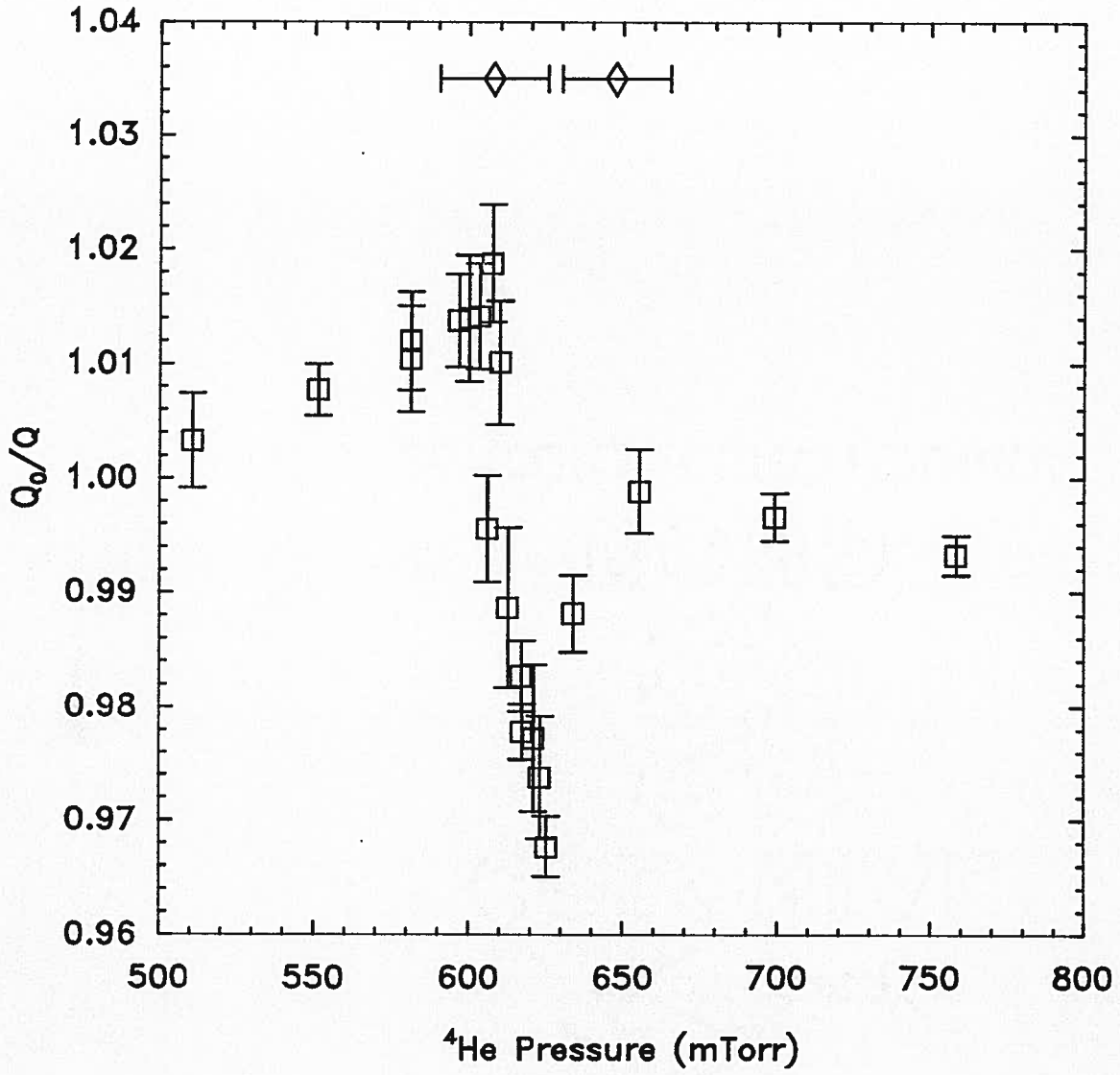

Figure D.2: The inverse quality factor (1/Q) of the 1420 MHz split-ring resonator loaded with an Al sample (squares) as a function of the vapour pressure of the ^{4}He cooling bath. This data has been normalized to an arbitrary value Q_0=415. The onset of the superconducting transition appears to be at about 640(10) mTorr (1.203(3) mK). Also shown (diamonds) are two determinations of T_c for Al using critical field data obtained by Cochrane and Mathoper [118]. The lower value (1.196(4) K) is obtained from a fit to their data. The upper value (1.205(4) K) is the actual temperature to which their data extrapolates.

The second point indicated by a diamond (at higher pressure) is our extrapolation of their actual data to zero field in order to determine $T_c = 1.203(4)$ K. Our results are in excellent agreement with these earlier results.

D.3.2 The ^{4}He buffer gas shift: Temperature stability

In chapter 7 we presented a new measurement of the ^{4}He buffer gas shift of the a-c hyperfine transition of atomic hydrogen. This shift is proportional to the ^{4}He density and is thus a strong function of temperature near 1 K. In order to place a practical limit on the temperature stability of the actual experimental bulb containing the atomic gasses, we monitored the frequency of a series of FID's taken at a constant ^{4}He pressure over a period of 40 minutes. This measurement was done at a pressure of 144.0(2) mTorr. The techniques outlined in Appendix A were used to determine the frequency of the FID's with respect to the Rb frequency reference. The results of this measurement are shown in figure D.3. No detectable drift in the frequency of the FID is seen above the scatter in the data. The standard deviation of the frequency from the mean is 13.5 mHz which is comparable to the fluctuations we would expect due to the fractional frequency stability of the Rb clock. The rate of change of the ^{4}He buffer gas shift with respect to temperature at this pressure is about -80 Hz/K. This data indicates that the pressure regulation of the system was stable enough to maintain the temperature of the experimental bulb containing the H constant to within better than 0.2 mK during the measurement. This result is in agreement with the measured fluctuations in pressure over this period.

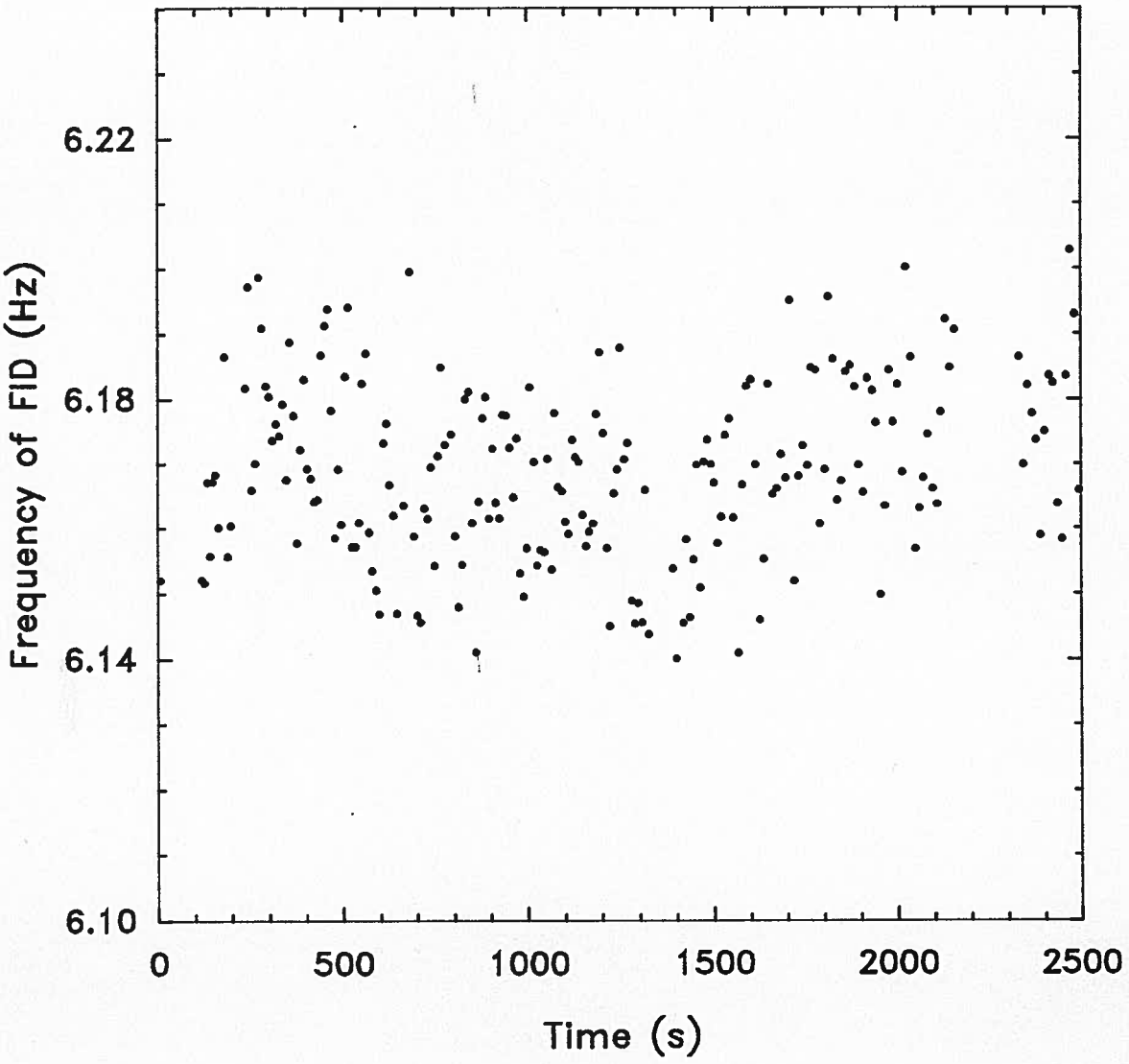

Figure D.3: The frequency of a FID with respect to a local oscillator (LO) near the a-c hyperfine transition of atomic hydrogen as a function of time at a ^{4}He pressure of 144.0(2) mTorr. The scatter in the data is consistent with the fractional frequency stability of the Rb frequency reference used to generate the LO. The ^{4}He buffer gas shift is expected to change by -80 Hz/K at this temperature. This implies that the temperature stability in the experimental cell is better than 0.2 mK.

Appendix E

Molecular Energy Levels of H_2, D_2 and HD just below Dissociation

Spectroscopic measurements of the weakly bound levels of the various molecules of H and its isotopes have been made by several authors. These molecular states play an important role in determining the strength of various interatomic interactions such as molecular recombination and spin-exchange at low temperatures. Reynolds [22] has compiled tables from the literature listing all known levels within 300 K of the dissociation energy for H_2, D_2 and HD. We reproduce his tabulation here for the sake of completeness.

In each case the original data was reported in energy units of cm^{-1}. Here we use the more convenient temperature units where 1 K is equivalent to 0.69502 cm^{-1}. The dissociation energy of the homonuclear species H_2 and D_2 were measured by Herzberg [120] who obtained values of 51967.0(4) K and 52381.2(6) K respectively. LeRoy and Barwell [121] measured a value of 52874.29(43) K for the HD molecule. The energies of the various molecular levels with respect to the ground state were measured by Dabrowski (H_2 [122]), Bredohl and Herzberg (D_2 [123]), and Dabrowski and Herzberg (HD [124]). These results are combined and tabulated in tables E.1, E.2, and E.3. in order of increasing binding energy. In these tables v refers to the vibrational quantum number of the state while J refers to the angular momentum quantum number. Note that for the (14,4) level of the H_2 molecule which lies extremely close to dissociation, a refined dissociation energy of 51967.4(7) K was used. This value was obtained by Stwalley [125] who reanalyzed the data of Herzberg [120] paying special attention to the weakly bound levels.

v	J	D_0 (K)
14	4	0.7
12	10	19.7
3	27	29.2
6	22	62.0
14	3	72.5
13	7	74.0
14	2	136.9
14	1	183.9
14	0	208.5
11	12	208.9
13	6	286.7

Table E.1: Dissociation energies of the rovibrational levels of molecular H_2 close to the dissociation threshold.

v	J	D_0 (K)
21	1	0.2
21	0	2.9
20	5	41.8
20	4	91.5
20	3	135.2
20	2	170.2
20	1	194.3
20	0	206.8

Table E.2: Dissociation energies of the rovibrational levels of molecular D_2 close to the dissociation threshold.

v	J	D_0 (K)
17	1	0.14
17	0	6.9
16	5	50.9
16	4	135.9
15	8	155.1
16	3	212.1
16	2	273.5

Table E.3: Dissociation energies of the rovibrational levels of molecular HD close to the dissociation threshold.